Utilization of Steel Industry LD-slag for Environmental Applications

Niladri Shekhar Samanta

Utilization of Steel Industry LD-slag for Environmental Applications

Thesis submitted in partial fulfillment of the requirements

for the degree of

DOCTOR OF PHILOSOPHY

by

Niladri Shekhar Samanta

Roll No: 186152003

Centre for the Environment
Indian Institute of Technology Guwahati
Guwahati-781039, India

Dedicated to my Parents for

their faith, love,

understanding and support

Centre for the Environment
Indian Institute of Technology Guwahati
Guwahati 781039, India

CERTIFICATE

It is certified that the work reported in the thesis entitled “**Utilization of Steel Industry LD-Slag for Environmental Applications**”, by **Niladri Shekhar Samanta**, has been carried out under our supervision. The work documented in this thesis has not been submitted to any other University or Institute for the award of any degree or diploma.

MKPurkait

Dr. Mihir Kumar Purkait

Professor
Department of Chemical Engineering
Indian Institute of Technology Guwahati
Guwahati 781039, India
Date: 08-08-2023

Dr. Utpal Bora

Professor
Department of Biosciences and Bioengineering
Indian Institute of Technology Guwahati
Guwahati 781039, India
Date: 08-08-2023

Acknowledgements

I owe a debt of gratitude to many people who have helped me in completing this research work directly and indirectly. I would like to acknowledge them all. To begin with, I wish to express my deepest acknowledgment to my supervisors, **Dr. Mihir Kumar Purkait** and **Dr. Utpal Bora** for providing me with inspiring guidance throughout the entire course of this work. I am indebted to them for their useful suggestions and constant encouragement throughout the entire period. I am grateful to them for their great support, encouragement which helped me to finish this work on time. I always admire their advice, energy, and hard work for all their students. Besides this, I feel very fortunate that I got a chance to work with such experienced and enthusiastic supervisors, whom I will admire throughout my career.

I would like to thank my doctoral committee members, **Prof. Subrata Kumar Majumder**, **Prof. Chandan Das** (Department of Chemical Engineering), and **Prof. Pranab Kumar Ghosh** (Civil Engineering Department) for their valuable suggestions and constructive criticism during the project evolutions, which helped me to make necessary improvements in various stages of my research work. I would especially like to thank **Prof. Subrata Kumar Majumder** for the rigorous and remarkable questions that he raised during the seminar presentations which helped me a lot in understanding many facts related to my work.

I am also thankful to all the faculty members of the Centre for the Environment for their encouragement and help at various stages during my stay in this Centre. In this regard, I would especially like to mention the name of **Dr. Chandan Das.**

I must thank all the technical staff of my Centre especially, **Dr. Deepmoni Deka**, **Mr. Partha Protim Bakal, Mr. Kaustubh Rakshit,** and other office staff. The experimental works presented in this thesis would never have been possible without the help of these proficient technicians. I am also very thankful to **Mr. Debajit Borah** (Technical

Superintendent, Department of Chemical Engineering), who helped me with the XRD analysis.

I am thankful to the **Central Instrument Facility** of IIT Guwahati for allowing me to utilize their experimental resources. I am also thankful to the **instrument facility** in our Centre for helping me in the fabrication part of my experimental setup which was essential in my research work.

I was fortunate enough to get excellent lab mates like, **Somnathda, Piyalda**, **Deepti, Pranjal, Simons, Ankush, Anweshan, Mukesh,** and **Satish**. Thanks to all of them for their friendly support, timely assistance, and cooperation throughout my research work. I am also thankful to **Gourav, Subrata, Sayantan, and Prabhat** for their friendly behavior and assistance.

I have no words to thank **GOD** who is my strength and wisdom.

I also wish to extend my loving thanks to my father **Mr. Bishnu Prasad Samanta** and my mother **Mrs. Chhaya Rani Samanta** for their constant moral support. Their love, affection, blessings, and sacrifices made me stronger to overcome my hurdles and achieve my goal. I express my humble regards to my parents-in-law and acknowledge their love and blessings. Also, I would like to give my love to my sweet niece **Shreya**. A special thanks to **Soma and Himadri** (my elder sister and brother) for their caring efforts for me and my family during these years.

Finally, I express my enormous gratitude and indebtedness to my wife, **Puja** for her utmost care, unlimited patience, and constant endorsement at all stages of this work during these four years. This work would not have been possible without her support.

Niladri Shekhar Samanta

Abstract

This thesis focuses on the usage and reduction of LD-slag by producing zeolite-like potential adsorbents using conventional techniques, and the synthesis of calcium carbonate minerals via CO_2 sequestration. Several types of zeolite synthesis from LD-slag and their applications for environmental protection have been discussed. Firstly, zeolite-like material was prepared from Linz-Donawitz (LD) process slag of the steel industry for the Removal of Fe^{3+} from Drinking water. Secondly, zeolite A and FAU-type zeolite X was prepared from LD-slag via fusion-assisted hydrothermal treatment to examine the physico-chemical and adsorption studies. Thirdly, zeolite type-Y was synthesized from LD-slag by ultrasonic facilitated hydrothermal route and the prepared zeolite nanoparticles were coated on a polysulfone (PSf) membrane and used to remove several contaminants from groundwater sample. Fourth, the CO_2 sequestration experiments were carried out using LD-slag, which yields value-added materials such as precipitated calcium carbonate. The details of the abstract are subsequently discussed.

Cubical-shaped zeolite A was synthesized from the Linz-Donawitz (LD) process slag of the Steel Industry, utilizing conventional fusion-assisted hydrothermal treatment. Morphological and Physico-chemical characterizations were performed by various characterization techniques. A weight ratio of 1:1.2 (LD-slag: NaOH) was maintained during fusion, which provides a better binding effect with better mechanical stability to the zeolite framework. Fe^{3+} adsorption studies were performed at 273, 298, 303, and 308 K, respectively, within the range of 10-40 mg/L Fe^{3+} ion concentration for kinetic and isotherm studies. A maximum adsorption capacity of 27.55 mg/g was obtained at a 1.4 g/L adsorbent dosage, with 99.99% Fe^{3+} ion removal. Moreover, the Fe^{3+} adsorption study obeyed the pseudo-second-order kinetic model, whereas multistage diffusion controlled the adsorption process. Langmuir isotherm model best fitted the equilibrium data suggesting the highly negative charge over the adsorbent surface played a vital role in the electrostatic attraction of Fe^{3+} ions. Isomorphic replacement of silicon by aluminum ion imparted a highly negative charge over the zeolite surface in the primary structure unit. For real-life sample drinking water, the Fe^{3+} ion removal efficiency increases to 97.7%.

The sodium-rich zeolite A and zeolite X (FAU-type) samples were synthesized from LD-slag via fusion-assisted hydrothermal treatment. The physicochemical and thermal stability of the prepared samples were examined with the help of various characterization techniques namely Fourier Transform Infrared (FTIR) Spectroscopy, X-ray diffraction (XRD), and thermogravimetric analysis (TGA) analysis at three different pH conditions and treatment time. Moreover, the sustainability of the crystalline phase and the corresponding zeolite network was evaluated from XRD, FTIR, TGA, and Field-Emission Scanning Electron Microscopy (FESEM) analysis. Zeolite A depicts a unique cubical structure and is thermally more stable as compared to zeolite type X. Also, zeolite A showed the highest dye removal efficiency of 98.13%, as compared to 94.47% for zeolite X, along with equilibrium sorption capacities of 25.30 and 23.57 mg/g, respectively. In addition, the study proposes that both the synthesized adsorbents are effective and economically sustainable for cationic methylene blue adsorption. Furthermore, methylene blue adsorption was regulated by a multistage diffusion process that agreed with a pseudo-second-order kinetic model (R^2 = 0.999 and 0.996 for A and X-type zeolites). The Langmuir isotherm model best suited the equilibrium data, with monolayer adsorption capacities of 20 and 25.40 mg/g, respectively.

Faujesite type zeolite Y was prepared via ultrasonic energy facilitated hydrothermal technique using Linz-Donawitz (LD) process slag as a precursor material. The surface modification of the PSf membrane was conducted with the as-synthesized zeolite powder in the presence of N-methyl pyrrolidone (NMP) solvent. The synthetic zeolite nanoparticles

(ZNPs) were sonicated by mixing them in NMP solvent before spreading over the membrane surface. The ZNPs layered flat sheet membrane was fabricated via dry-cast technique followed by phase inversion. The optimization of drying temperature and time was studied along with the variation of ZNPs wt.% to obtain defect-free membranes. The developed ZNPs layered membranes were characterized for membrane morphology, surface roughness, mechanical strength, thermal stability, functional group analysis, and surface hydrophilicity. The chemical characterization of all fabricated membranes was examined by X-ray photoelectron spectroscopy (XPS). An increased water flux of 28.83 L/m^{2}h was obtained whereas the fluoride concentration was reduced to 1.47 mg/L (~ 50.33% reduction) for the optimized PSf/Zeolite-1wt.% membrane. Moreover, other contaminants namely chromium (Cr^{6+}) and manganese (Mn^{2+}) were removed very significantly by utilizing the modified PSf/Zeolite-1wt.% membrane. The regeneration experiment was conducted utilizing an HCl solution through dead-end filtration. The flux recovery of membrane PSf/Zeolite-1wt.% was found to be 85.43%.

The waste Linz-Donawitz (LD) slag produced in the steel industries is known to have high calcium oxide (CaO) content along with other inorganic salts. There is an untapped potential for the valorization of the waste LD-slag, where the constituent calcium oxide can be converted to valuable calcium carbonate and subsequently contributes to the sequestration of carbon dioxide. In this study, commercial sugar was introduced as a promoter to enhance the conversion of CaO to $CaCO_3$. The valorization of the LD-slag process was conducted in a CO_2 atmosphere by varying the temperature over 25-55°C. The highest calcium oxide conversion was found at 55°C. Various techniques were employed in order to assess the crystal growth, textural properties, and thermal behavior of the synthetic $CaCO_3$ formed. The calcite phase is dominated in a temperature range of 25-55°C, whereas unstable vaterite was identified at 45°C. Further, at higher temperature ~55°C, the needle-like aragonite phase was found to dominate. The reaction kinetic data are well-fitted with the pseudo-second-order model ($R^2 = 0.99$) as compared to other models. The whiteness of the obtained samples was measured via UV-spectrometer and the PCC sample achieved at 55°C showed significant whiteness characteristics among others. The CO_2 sequestration efficiency in this study was found to be ~17%. It was estimated that 500 g of CO_2 could sequestrate by 1 kg of LD-slag. Moreover, the “t” value obtained from the hypothesis test is 49.92, which reveals that the presence of commercial sugar in the reaction, leads to a higher $Ca(OH)_2$ concentration.

Research Publications

Publication related to thesis work

Journal:

1. **N.S. Samanta,** S. Banerjee, P. Mondal, Anweshan, U. Bora, M.K. Purkait, Preparation and characterization of zeolite from waste Linz-Donawitz (LD) process slag of steel industry for removal of Fe^{3+} from drinking water, ***Adv. Powder Technol.*** 32 (2021) 3372–3387. https://doi.org/10.1016/j.apt.2021.07.023.
2. **N.S. Samanta,** P.P. Das, P. Mondal, U. Bora, K. Mihir, Physico-chemical and adsorption study of hydrothermally treated zeolite A and FAU-type zeolite X prepared from LD (Linz-Donawitz) slag of the steel industry, ***Int. J. Environ. Anal. Chem.*** 00 (2022) 1–23. https://doi.org/10.1080/03067319.2022.2079082.
3. **N.S. Samanta**, Anweshan, P. Mondal, U. Bora, M.K. Purkait, Synthesis of precipitated calcium carbonate from LD-slag using CO_2, ***Mater. Today Commun***. 36 (2023) 106588. https://doi.org/https://doi.org/10.1016/j.mtcomm.2023.106588.
4. **N.S. Samanta**, P. Mondal, S. Dhara, U. Bora, M.K. Purkait, Fabrication of LD-slag derived zeolite Y coated polysulfone (PSf) membrane for decontamination of groundwater, ***Chem. Eng. J.*** (Under review).
5. **N.S. Samanta,** P.P. Das, P. Mondal, M. Changmai, M.K. Purkait, Critical review on the synthesis and advancement of industrial and biomass waste-based zeolites and their applications in gas adsorption and biomedical studies, ***J. Indian Chem. Soc.*** 99 (2022) 100761. https://doi.org/https://doi.org/10.1016/j.jics.2022.100761.
6. **N.S. Samanta,** P.P. Das, S. Dhara, M.K. Purkait, An Overview of Precious Metal Recovery from Steel Industry Slag : Recovery Strategy and Utilization, ***Ind. Eng. Chem. Res.*** (2023). https://doi.org/10.1021/acs.iecr.3c00604.

Book Chapter:

1. **N.S. Samanta,** P. Mondal, Nanofiltration technique for the treatment of industrial wastewater, Volume: Advanced Application of Nanotechnology to Industrial Wastewater, Publisher: Springer, https://doi.org/10.1007/978-981-99-3292-4_9, (2023).
2. Ankush D. Sontakke, Deepti, **N.S. Samanta**, Smart nanomaterials in the medical industry, Volume: Advances in Smart Nanomaterials and their Applications, Publisher: Elsevier, https://doi.org/10.1016/B978-0-323-99546-7.00025-2, (2023).
3. Mukesh Sharma, P. P. Das, **N.S. Samanta,** Use of Biochar for the Remediation of Heavy-Metal-Contaminated Soil, Volume: Designer Biochar Assisted Bioremediation of Industrial Effluents, Publisher: CRC, ISBN: 9781003203438, (2023).
4. **N.S. Samanta**, P. Mondal, Waste-based zeolites and their advanced composites for wastewater and environmental remediation applications, Volume: Advances in Material Research and Technology, Publisher: Springer, (2023).
5. **N.S. Samanta**, Mukesh Sharma, Recycle of water treatment plant sludge and its utilization for wastewater treatment Volume: Resource Recovery in Drinking Water Treatment, Publisher: Elsevier (2023).

Book:

Waste-based zeolites: synthesis and environmental applications authored by, Mihir Kumar Purkait, P. Mondal, N. S. Samanta, P. P. Das, Imprint: Elsevier (ongoing), ISBN: 9780443223167.

Publication from other work

Journal:

1. S. Dhara, **N.S. Samanta,** R. Uppaluri, M.K. Purkait, High-purity alkaline lignin extraction from Saccharum ravannae and optimization of lignin recovery through response surface methodology, ***Int. J. Biol. Macromol***. (2023) 123594. https://doi.org/https://doi.org/10.1016/j.ijbiomac.2023.123594.
2. P. Mondal, **N.S. Samanta**, V. Meghnani, M.K. Purkait, Selective glucose permeability in presence of various salts through tunable pore size of pH responsive PVDF-co-HFP membrane, ***Sep. Purif. Technol.*** 221 (2019) 249–260. https://doi.org/https://doi.org/10.1016/j.seppur.2019.04.001.
3. P. Mondal, **N.S. Samanta**, A. Kumar, M.K. Purkait, Recovery of H_2SO_4 from wastewater in the presence of NaCl and $KHCO_3$ through pH responsive polysulfone membrane: Optimization approach, ***Polym. Test.*** 86 (2020) 106463. https://doi.org/10.1016/j.polymertesting.2020.106463.
4. S. Dhara, **N. Shekhar Samanta**, P.P. Das, R.V.S. Uppaluri, M.K. Purkait, Ravenna Grass-Extracted Alkaline Lignin-Based Polysulfone Mixed Matrix Membrane (MMM) for Aqueous Cr(VI) Removal, ***ACS Appl. Polym. Mater.*** (2023). https://doi.org/10.1021/acsapm.3c00999.
5. S. Dhara, **N.S. Samanta**, .P.P. Das, Potential of lignin as a biofuel substrate, ***Int. J. Biol. Macromol***. (Submitted).
6. P.P. Das, S. Dhara, **N.S. Samanta**, Recent progress on ozonation process for wastewater treatment: A review, ***Sep. Purif. Technol.*** (Submitted).

Book Chapter:

1. P. P. Das, **N.S. Samanta**, S. Dhara, Biofuel Production from Algal Biomass, Volume: Green Approach to Alternative Fuel for a Sustainable Future, Publisher: Elsevier, https://doi.org/10.1016/B978-0-12-824318-3.00009-6, (2023).
2. P. P. Das, Ankush D. Sontakke, **N.S. Samanta**, Emerging Contaminants in Wastewater: Eco-Toxicity and Sustainability Assessment, Volume: Industrial Wastewater Reuse, Publisher: Springer, https://doi.org/10.1007/978-981-99-2489-9_4, (2023).
3. **N.S. Samanta**, Anweshan, Techniques in Removal of organics and emerging contaminants from wastewater for water reuse application, Volume: Advances in Industrial Wastewater Treatment Technologies: Removal of Contaminants and Recovery of Resources, Publisher: Elsevier, https://doi.org/10.1016/B978-0-323-95684-0.00009-9, (2023).
4. **N.S. Samanta**, P. P. Das, Performance of Anammox Process for Wastewater Treatment, Publisher: Elsevier (accepted).
5. **N.S. Samanta**, S. Dhara, P. P. Das, Nanotechnology in Microbial Electrochemical Systems, Publisher: Elsevier (accepted).
6. Mukesh Sharma, **N.S. Samanta**, Simultaneous treatment of industrial wastewater and resource recovery using microbial fuel cell, Volume: Resource Recovery in Industrial Waste waters, Publisher: Elsevier (accepted).
7. S. Dhara, **N.S. Samanta**, P. P. Das, Potential of biochar and microalgae for bioremediation of emerging contaminants (accepted).
8. P. P. Das, S. Dhara, **N.S. Samanta**, Advancements in ozonation process for the treatment of wastewater contaminants, (accepted).

9. P. P. Das, S. Dhara, **N.S. Samanta**, Microbial fuel cell for wastewater treatment and energy recovery, Publisher: ACS (accepted).
10. S. Dhara, **N.S. Samanta**, P. P. Das, Biological nitrogen removal and recovery from wastewater, Publisher: ACS (accepted).
11. **N.S. Samanta**, P. P. Das, S. Dhara, Hybrid processes for the removal of emerging contaminants from wastewater, Publisher: ACS (accepted).

Conference/Presentations

1. Presented paper in "**International Conference on Functional Materials (ICFM-2020)**" held at IIT Kharagpur on 6th - 8th January 2020.
2. Presented paper in "**Research and industrial conclave integration 2022**" held at IIT Guwahati on 20th – 23rd January 2022.

CONTENTS

CHAPTER 3 **Physico-chemical and adsorption study of hydrothermally treated zeolite A and FAU-type zeolite X prepared from LD (Linz-Donawitz) slag of the steel industry** **71−121**

CHAPTER 5 **Synthesis of precipitated calcium carbonate from LD-slag using CO_2** **189−243**

LIST OF FIGURES

LIST OF FIGURES

LIST OF FIGURES

LIST OF TABLES

Nomenclature

Notations

Q_t	Adsorption uptake at time t (mg/g)
Q_e	Adsorption uptake at equilibrium (mg/g)
C_0	Concentration at the initial time (mg/L)
C_e	Concentration at equilibrium phase (mg/L)
$C(t)$	Concentration at any contact time t (mg/L)
V	Volume of feed (mL)
W	Mass of adsorbent (g)
K_1	Reaction rate constant for pseudo-first-order (1/minute)
K_2	Reaction rate constant for pseudo-second-order (g/(mg.minute))
t	Time (minute)
C	Film thickness of the boundary layer
B_t	Solute adsorbed at any time t according to Boyd kinetic model
Q_m	Maximum amount of solute adsorbed (mg/g)
K_L	Langmuir rate constant (L/mg)
R_l	Nature of adsorption isotherm
K_F	Freundlich rate constant (mg/g) $(L/mg)^{1/n}$
R	Universal gas constant (J/mole K)
K_4	Diffusion-chemisorption constant
T	Temperature (K)
ΔG_0	Gibbs free energy (KJ/mole)
ΔS_0	Entropy (LJ/mole K)
ΔH_0	Enthalpy (KJ/mole)
ε	Total porosity

Nomenclature

ω_1	Weight of the wet membrane (mg)
ω_2	Weight of the dry membrane (mg)
A	Area of membrane (m^2)
l	Membrane thickness (µm)
d_w	Density of water (g/cm^3)
Q	Water flux (m^3/s)
ΔP	transmembrane pressure in equations (kPa)
r_m	Mean pore radious (nm)
η	Viscosity of water (Pa s)
J	pure water flux (L/m^2h)
J_{w1}	initial water flux (L/m^2h)
J_{w2}	water flux in second run (L/m^2h)
Δt	working time (hour)
P	pressure (bar)
R_{ir}	Irreversible fouling
R_r	Reversible fouling
R_t	Total fouling
C_F	Concentration in the feed (mg/L)
C_p	Concentration in permeate (mg/L)

Abbreviations

ZNPs	Zeolite nanoparticles
GO	Graphene oxide
FTIR	Fourier transform infrared spectroscopy
XRD	X-ray diffraction

TGA	Thermogravimetric analysis
XPS	X-ray photoelectron spectroscopy
AFM	Atomic force microscopy
AAS	Atomic adsorption spectrophotometer
ATR	Attenuated total reflectance
EWC	Equilibrium water content
FESEM	Field emission scanning electron microscope
FETEM	Field emission transmission electron microscopy
SAED	Selected Area Electron Diffraction
EDS	Energy-dispersive X-ray spectroscopy
FTIR	Fourier transform infrared
NMP	N-methyl-2-pyrrolidone
PSF	Polysulfone
PEG	Polyethylene glycol
PAN	Polyacrylonitrile
PWF	Pure water flux
SEM	Scanning electron microscope
TMP	Transmembrane pressure
UF	Ultrafiltration
USD	United States dollar
EAFS	Electric-arc furnace slag
BFS	Blast furnace slag

Chapter 1

Introduction

This chapter discusses a brief summary of the fundamentals involved in steel slag production. It summarizes the state-of-the-art in the production of Linz-Donawitz (LD) slag, its composition, and its utilization. The chapter subsequently presents a literature review in detail that includes the utilization of LD-slag, slag-derived materials, and problems associated with the synthesis of valuable products from slag. Finally, the research scope and the objectives of the present work are highlighted in this chapter.

1.1. Steel slag Background

Steel slag (SS) is a by-product of the steel manufacturing process. It is formed when iron ore or scrap metal is melted in a blast furnace with limestone and coke to make molten iron. Impurities in the iron ore react with the fluxing agents (limestone and coke) during the smelting process to generate liquid slag. Steel slag is mostly made of calcium, iron, and silicon oxides, with trace quantities of manganese, phosphorus, and sulfur. The physical and chemical properties of steel may vary depending on the steelmaking process and raw material composition. The molten slag is rapidly cooled after being tapped from the furnace, causing it to harden into a glassy, granular phase. This granulated slag is then further treated, often by drying and grinding, to generate ground granulated blast furnace slag (GGBFS).

1.1.1. Classification of steel slag

Steel slag is classified into several categories based on its production processes and properties. The integrated steel industry uses two types of converter namely electric arc

---

Content of this chapter is published as below:
N.S. Samanta, P.P. Das, P. Mondal, M. Changmai, M.K. Purkait, Critical review on the synthesis and advancement of industrial and biomass waste-based zeolites and their applications in gas adsorption and biomedical studies, J. Indian Chem. Soc. 99 (2022) 100761. https://doi.org/https://doi.org/10.1016/j.jics.2022.100761.

furnace (EAF) and basic oxygen furnace (BOF), which generate three miscellaneous steel slag: EAF, BOF, and LD-slag. EAF slag is produced during the steelmaking process utilizing electric arc furnaces. It is made up of oxides, fluxes, and impurities. EAF slag is typically air-cooled and can be utilized as a building material or processed into products like lightweight aggregate. BOF slag is a mixture of fluxes, impurities, and oxidized steel that is produced during the steelmaking process in a basic oxygen furnace. It is extensively utilized in construction as road bases, fill materials, and aggregates. On the other hand, further purification of purified liquid steel through a ladle creates LD-slag. Because of the oxygen infusion, contaminants such as carbon, silicon, and phosphorus oxidize and create liquid slag. The LD-slag is predominantly constituted of calcium, iron, silicon oxides, and other elements found in the raw materials utilized. Figure 1.1 depicts the process flow diagram of different steel slag production.

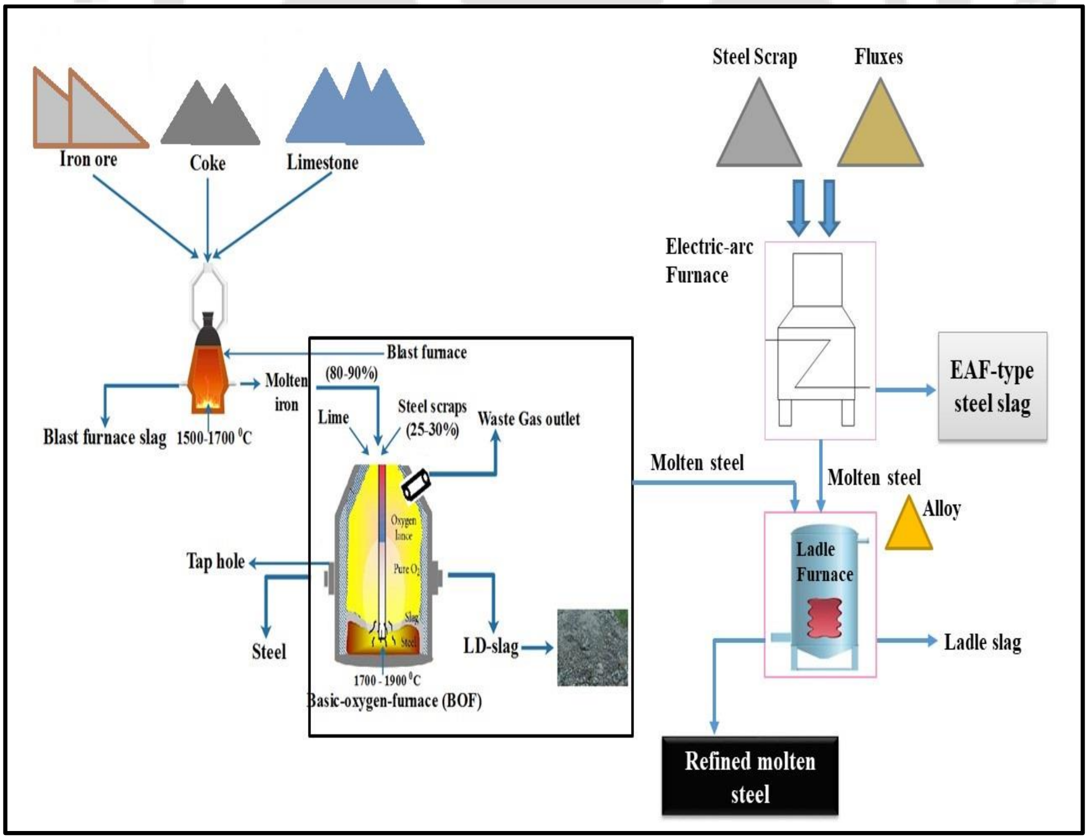

Figure 1.1: Process flow chart of different types of steel slag production.

Table 1.1 illustrates the chemical composition of various types of steel slag. From Table 1.1 it can be seen that for every slag sample, the CaO content is very much higher than other metallic oxides. In LD-slag the CaO was found the highest. The high amount of CaO in LD-slag can be attributed to the raw materials used in the steelmaking process and the reactions that occur during steel production. The compounds like CaO, SiO_2, and Al_2O_3 make the steel-processed slags more potential for valuable material synthesis which helps in reducing the environmental threat.

Table 1.1: Compositional analysis of different types of slag.

Chemical composition (wt. %)	**Slag type**			**References**
	EAF slag	**BOF slag**	**LD-slag**	
CaO	29.5	36.4-45.8	45-52	[1][2]
SiO_2	16.1	10.7-15.2	13-16	[1][2]
Al_2O_3	7.6	1-3.4	0.9-1.7	[1][2]
Fe_2O_3	32.56	-	1-8	[1][2]
TiO_2	0.78	-	0.4-0.9	[1][2]
MnO	4.5	2.7-4.3	4-7	[1][2]
MgO	5	4.1-7.8	4-5	[1][2]
V_2O_5	-	-	-	[1][2]
P_2O_5	0.6	1-1.5	1.6-2.1	[1][2]

1.1.2. Utilization of various types of steel slag

1.1.2.1. Utilization of electric arc furnace (EAF) slag

Worldwide, EAF slag is the principal source of silica (SiO_2) and alumina (Al_2O_3). The chemical composition is impacted by numerous mineral sources as well as the steel-making process. According to Italian road sector technical requirements, EAF slag exhibits superior mechanical properties in road applications when compared to natural aggregates in the base course and asphalt concrete for flexible pavements [3]. EAF slag offers high density, low organic content, and durability as an aggregate in subbase and engineering fill material for roadwork applications, according to Maghool et al. [4]. The EAF slag aggregate has been utilized as ballast material in railroad applications [5]. It was discovered that the EAF slag's robust modulus was greater than that of natural (granite) aggregates [6]. The EAF slag exhibits a macro-scale behavior that suggested its particle sharpness and crushing strength was higher than those of the granite aggregates, leading to a higher shear strength. Several literatures demonstrate the uses of EAF slag as aggregates in concrete [7]. The EAF slag performed exceptionally well in terms of compressive and flexural strengths attributed to its crushing resistance and high surface friction. Additionally, slag may be utilized in geopolymer concretes as a binder that is activated by alkali solutions. In a study, Gobetti et al. [8] employed EAF slag as a natural aggregate and suggested that the EAF slag could be replaced in epoxy screed construction. They revealed that slag composite has a greater flexural modulus than sand one with a high filler percentage. The findings also demonstrate that with the same %v/v, sand composites are stiffer and more brittle when compared to slag composites. In another study, Singh et al. [9] found EAF slag as a sustainable construction material by changing it to fresh EAF slag via a sequential water leaching experiment taking HCl as a leaching agent. Results reveal that EAF slag aggregates have excellent mechanical characteristics.

Aside from its usage as a construction and road material, researchers have discovered EAF slag to be a promising source of adsorbent materials. The constituents like silica and alumina of EAF slag make it a more useful precursor for zeolite-like mineral synthesis [10].

1.1.2.2. Utilization of basic oxygen furnace (BOF) slag

Previous literature surveys revealed that solid waste EAF slag was utilized for various purposes ranging from construction material to adsorbent for wastewater treatment. However, several studies focused on the preparation of cementitious material from waste BOF slag [11–13]. Recent studies focus on the preparation of geopolymer-like adsorbent material for wastewater treatment. In a recent study, Sun et al. [14] examined the feasibility of BOF slag by incorporating it into the geopolymer. Results achieved from the findings reveal that the addition of BOF aggregate prolongs the stability and strength. This study proved and stated that the production of metakaolin-geopolymer and BOF slag-like concrete material would be a promising solution for the re-utilization of steel slag and that proportionally alleviate the environmental impacts. In a geopolymer preparation study, Sithole et al. [15] used BOF slag as a supplement, fly ash (FA) as a silica source, and NaOH as a reagent. The solid/liquid (S/L) ratio was maintained at 20%, while the blending ratio was set at 10% FA. Using H_2O_2 as a blowing agent, the FA/BOFS-based geopolymer's porosity was increased. The synthesized geopolymer was used to treat Acid Mine Drainage (AMD) and remove metals, sulfates, and acidity.

In another avenue, carbon dioxide (CO_2) capturing techniques were built up in terms of greenhouse gas reduction as well as environmental protection. Several studies were explored for CO_2 storage as well as its capturing by employing potential adsorbent, biosorption, chemical looping, and membrane-based separation process. Among the techniques, ex-situ rapid carbonation using alkaline metal oxide and/or silicates will produce stable carbonate phases. However, the use of natural elements in the process of collecting CO_2 results in poor efficacy and significant energy use throughout the pre-treatment process [16,17].

Due to great mineralogy, availability, low process cost, and chemical properties, the use of steel industry slag as a CO_2 sorbent material is one viable option. Additionally, the slag's highly alkaline state is advantageous for the CO_2-capturing mechanism [18]. It is assumed that one ton of treated raw steel can produce 300-400 kg of BOF slag. The BOF slag was made up of a number of constituents, namely CaO, Fe_2O_3, Al_2O_3, SiO_2, and MgO. The size, pore shape, and surface heterogeneity of BOF slag will significantly increase its potential to absorb CO_2 [19]. In a recent study, Winayu et al. [20] utilized steel-processed BOF slag as a potential adsorbent for CO_2 adsorption in a fluidized bed reactor. The findings obtained calcium carbonate ($CaCO_3$) as a value-added product after the carbonation process. The investigation reveals that calcium oxide (CaO) content in solid slag plays a significant role in CO_2 capture at high temperatures. The effect of particle size on adsorption efficiency was also examined and results achieved from the study demonstrate that the sorption capacity goes down from 24.8 to 24.5% when the particle size ranged between 150-300 and 75-106 µm, respectively. On the other hand, researchers also synthesized BOF-based adsorbent for wastewater treatment. Mahamudur and other co-authors [21] have prepared polypyrrole (PPy)/BOF slag nanocomposite for phosphate removal from contaminated water.

1.1.2.3. Utilization of Linz-Donawitz (LD) slag

The disposal of LD-slag has increased dramatically over the past ten years due to high disposal prices, large-scale production, and other restrictions, including the reduction in the quantity of landfill space that is available and its unsuitability in cement-making processes due to its high calcium oxide concentration. Nowadays, researchers are found some sustainable ways to the utilization of LD-slag that can reduce environmental risk. Several studies focused on the re-utilization of LD-slag by making different composite and bricks type products, ceramic membranes, and geopolymer-like potential adsorbents. Mallik et al. [22] have synthesized glass-ceramic composite material with different amounts of glass waste and waste LD-slag via the powder metallurgy technique. The results demonstrated that after sintering at higher temperatures, the constructed composite material exhibited good hardness and tensile strength. Several studies have also looked at the production of sustainable bricks using LD-slag as raw material [23]. Singh et al. [24] prepared paver blocks by mixing 20% bricks bat with 50% powder LD-slag. The mixture of the following mass ratio was found to be best to make the high-strength paver blocks. Water absorption capacity results revealed that LD-slag-based prepared blocks have more water absorption capacity when compared to the natural aggregates-based blocks.

Another promising route for recycling steel industry-processed LD-slag was found to be ceramic membrane preparation. In this context, Deepti et al. [25] prepared ceramic microfiltration (MF) membranes using modified LD-slag as starting material. To create the MF membrane, two distinct forms of LD-slag were employed, one of which was untreated LD-slag and another one was treated. The modification of LD-slag was conducted to manufacture the crack-free ceramic membrane. Because, according to a report, a high free CaO content causes structures to hydrate and break [26]. The modified slag was obtained after a reaction with the acetic acid in a CO_2 environment, resulting in the formation of $CaCO_3$ which acts as a binding material in membrane fabrication and adversely reduce the effects of CaO. The as-synthesized MF membrane was used to treat the cold rolling mill (CRM) wastewater, which is the residue of the steel-making process. The treated water obtained after the membrane filtration showed that all parameters like pH, Dissolved oxygen, Chemical oxygen demand (COD), iron (Fe), chromium (Cr), etc., were within the permissible limit according to the Environmental protection agency (EPA).

On the other hand, various research has also found LD-slag as a suitable candidate for geopolymer synthesis. Sarkar et al. have synthesized a low-cost potential LD-slag geopolymer (LDSGP)-like adsorbent. In the typical geopolymer preparation technique, LD-slag was washed and dried at room temperature. The sodium silicate powder and 10 M NaOH solution were combined in a magnetic stirrer for 24 hours at a weight ratio of 1:1 to create the alkaline activator solution [27]. The alkaline activator and cleaned LD-slag were mechanically combined in a 2:1 weight-to-weight ratio to create a colloid paste, which was then transferred to a polyethylene cylindrical mold with a 35 cm radius and 30 cm height. The colloid paste was removed from the mold using a sonicator for 5 minutes, and it was then dried at 25°C for 3 days so that geopolymerization could take place. The final product was then washed with 0.1 N HCl in order to remove excess alkaline material followed by washing with Deionized (DI) water and dried at 105°C for 6 hours. The as-synthesized LDSGP was employed for Ni^{2+} decontamination from wastewater. The highest adsorption capacity was found as 85.29 mg/g. In another adsorption experiment, Zn^{2+} was successfully removed from wastewater with a maximum adsorption capacity of 86 mg/g over the LD-slag-derived geopolymer [28]. In another study, catalytic assessment of LD-slag derived MIL-53(Fe)/SiO_2 composite was used for methylene blue (MB) degradation with various working conditions [29]. The hexagonal nanorod-shaped composite was prepared via a facile single-step hydrothermal process. The synthesized composite material shows a good BET surface area of 149.1 m^2/g which was comparatively higher than the raw LD-slag surface area (4.85 m^2/g). The highest MB degradation was found to be 66.3% with the following experimental conditions as follows: initial MB condition: 5 mg/L; dosage of photo-catalyst: 0.5 g/L; pH: 10. The produced composite catalyst and its behavior during degradation were found to be the best among comparable photo-catalysts.

In another avenue, Zn^{2+} and Ni^{2+}-modified LD-slag-based geopolymer was found to be a potential adsorbent for fluoride removal, according to Sarkar et al. [30]. Bivalent metallic ions Zn^{2+} and Ni^{2+} independently have changed LD-slag geopolymeric adsorbent (LDSGP), resulting in the creation of Zn-LDSGP and Ni-LDSGP adsorbents, respectively. In the modification experiment, a simple bivalent ion exchange approach was used in the chemical modification procedure that involved combining 5 g of LDSGP powder with either 100 mL of 1M $ZnCl_2$ or 100 mL of 1M $NiCl_2$ solutions, separately, and stirring both solutions for 16 hours in magnetic stirrer. The obtained samples were then removed from the solutions of zinc chloride and nickel chloride, rinsed with distilled water, and evaporated at 105°C. The micro-petal morphological structured modified adsorbent was employed for the de-fluoridation study. Modified Zn-LDSGP adsorbent was found to have maximum fluoride uptake capacity (60 mg/g) among others. The study demonstrates that LD-slag-derived nanocomposites could be utilized as potential adsorbents for toxic metals removal in wastewater treatment. According to Sarkar et al. [31], the modified LD-slag exhibited good adsorbent characteristics during the water decontamination process. The modification of LD-slag was carried out via acid treatment followed by a microwave irradiation process. After modification, the BET surface area of the modified slag sample was enhanced to 81.18 m^2/g. The prepared adsorbent was employed for phenol adsorption and the highest uptake capacity was found to be 3.4 mg/g at 25°C.

The preceding sections comprehensively discussed an overview of steel slag, its classifications, chemical compositions, and other characteristics. The discussion mainly focused on three types of primary steel slags such as EAF, BOF, and LD-slag, and emphasized their uses in environmental remediation. It is anticipated that various studies utilized steel industry processed waste slag for preparing potential adsorbents, ceramic materials, and membranes via several conventional and chemical synthesis routes.

Adsorbents and their composites have recently been discovered to be a potential candidate for wastewater treatment.

1.2. State of the art

This section provides a brief overview of current research before outlining the study findings from various literature to suggest a few prospective research subjects that should be included in this thesis. The state-of-the-art depicts the potential uses of LD-slag for environmental applications.

1.2.1. Preparation of zeolite-like adsorbent

1.2.1.1. Overview of zeolite

The aluminosilicate family of minerals includes zeolites, which can be created artificially or naturally. They stand out for having a crystalline, porous structure made up of linked channels and cages. Zeolites are beneficial in various industrial and commercial applications due to their distinctive characteristics, which provide them with a variety of valuable features. Zeolite has a high affinity towards the cations and positively charged ions and hence, it absorbs and exchanges them selectively. Zeolites are useful in operations such as water purification because of their capacity to remove heavy metals and other contaminants from the water via ion exchange. According to Figure 1.2, the tetrahedral structure is linked by shared oxygen atoms, resulting in cavities or cages, and connected by either rings or pore holes, which dictate the zeolite's size and form.

Coal, biomass ash, steel slag, and other industrial waste have been discovered to be potential sources for zeolite synthesis due to the presence of aluminosilicate and silicate phases. Scientific reports on the creation of zeolite from solid waste, such as steel slag are very scant, while several studies on the creation of zeolite from CFA and biomass ash have been reported. The following sections provide details on zeolite synthesis from various steel industry-produced slags.

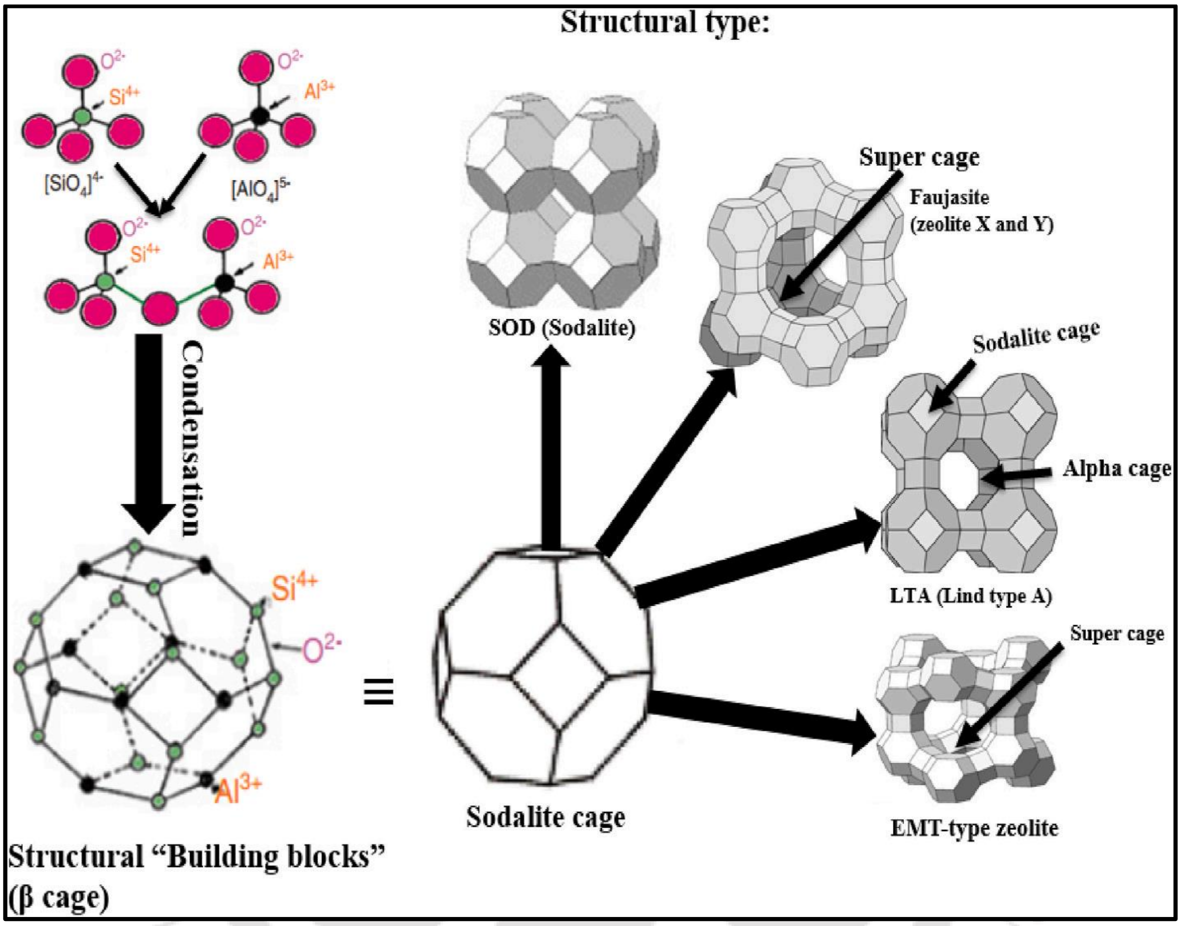

Figure 1.2: Step-by-step development of different zeolite structures (reproduced with permission from Samanta et al. ©Elsevier [32]).

1.3. Synthesis of zeolites from blast furnace slag (BFS)

Blast furnace slag is a by-product of the iron manufacturing process in a steel furnace. It is a granulated non-metallic substance formed by the melting and solidification of iron ore, limestone, and coke ash in the furnace. Blast furnace slag is mostly silicates and aluminosilicates. It comprises calcium oxide (CaO), silica (SiO_2), alumina (Al_2O_3), and trace quantities of other elements. The presence of silica and alumina in the BF slag makes it more precious for zeolite-like mineral synthesis. A few works of literature on zeolite synthesis from BF slag are listed below:

1.3.1. Literature survey

In a study, Kuwahara et al. [33] prepared Linde-type zeolite A (LTA) from blast furnace slag via a conventional hydrothermal synthesis route at 100°C for 6 hours. High crystalline synthetic zeolite A exhibits a significant water adsorption capacity of 247 mg/g. By employing the same synthesis technique Guo et al. [34] have prepared A-type zeolite using BFS as starting material. The adsorption behavior of the synthesized zeolite was examined by removing ammonia from wastewater with a maximum sorption capacity of 83.3 mg/g. According to Liu et al. [35], only zeolite P (gismondine-type zeolite) was produced during the CO_2 mineralizing process using blast furnace slag as the starting material. The well-crystallized zeolite P was produced in a brief period by hydrothermal treatment at a high temperature. The work synthesized spherical-shaped hydroxycancrinite zeolite and comprehensively evaluated the impacts of numerous operational parameters such as alkaline dose, crystallization duration, and temperature on zeolite crystal structure during zeolite production. Wajima et al. [36] attempted to create zeolite-like material by fusing it at high temperatures with the addition of NaOH as an alkaline source utilizing iron-steel industrial solid waste BFS as silica and alumina source. They attempted to demonstrate the influence of EDTA during the zeolitization process. Without the addition of EDTA, a combination of hydroxyl sodalite and calcite phases was obtained, whereas zeolite A and zeolite X were created following the addition of EDTA. In another experiment, Hu et al. [37] produced Medium Pore Framework Type I (MFI) and faujasite (FAU)-type zeolites from titanium (Ti)-enriched BF slag by a conventional hydrothermal route at various working conditions. The surface area of the obtained zeolite samples in this study was found to be 325.2 and 663.2 m^2/g, respectively. Both synthetic zeolites were employed to evaluate the photocatalytic activity under Ultraviolet (UV) irradiation and it was found that zeolite Ti-ZSM-5 (MFI) exhibited higher photocatalytic behavior as compared to Ti-containing zeolite X due to the presence of TiO_2 support in the zeolite ZSM-5 network.

1.3.2. Possible scope of work

The above scientific reports emphasized various types of zeolite synthesis by conventional techniques using steel industry solid waste BF slag as a precursor material. It is also seen that the synthesized zeolites were utilized for different environmental remediation processes namely wastewater treatment and gas adsorption. It is assumed that no study has been conducted on the synthesis of zeolites utilizing silica and alumina-riched Linz-Donawitz converter-generated slag or LD-slag as a precursor material and zeolite-like material can be prepared.

1.4. Synthesis of zeolites from EAF slag

Like BF slag, EAF slag also comprised zeolite precursor silica and alumina. Researchers nowadays, demonstrate the synthesis of various types of zeolite via conventional techniques using EAF slag. Few examples are given in the literature survey.

1.4.1. Literature survey

Zeolite type-A and hydroxy sodalite were produced by Li et al. [10] utilizing EAF slag as a silica and alumina source. In addition, they methodically examined the impact of hydrothermal temperature, treatment duration, $n(H_2O)/n(Na_2O)$, $n(SiO_2)/n(Al_2O_3)$ molar ratios, on the crystal phase and microstructure of the produced zeolite. Highly crystalline and cubical-shaped LTA with $n(H_2O)/n(Na_2O)$ of 100:1 and $n(SiO_2)/n(Al_2O_3)$ of 2:1 ratios were found at an operating temperature of 40°C and reaction time of 3 hours, respectively. The change from metastable zeolite A to high-framework-density hydroxy sodalite zeolite has been observed by reducing the $n(H_2O)/n(Na_2O)$ ratio to 40:1 and increasing the hydrothermal duration and temperature to 12 hours and 160°C, respectively. Both materials were evaluated for Cu^{2+} ion removal, and it was found that zeolite type-A manufactured at 120°C had much higher metal adsorption capacity (1.346 mmol/g) than sodalite (0.673 mmol/g) treated at 160°C.

1.4.2. Possible scope of work

It may be seen from the above literature that although lots of works have reported on the synthesis of various kinds of zeolites from steel industry processed slags and their environmental applications. It is envisaged that no research work has been focused on zeolite synthesis using Linz-Donawitz converter-generated slag or LD-slag as precursor material. So, keeping the main objective of the preparation of zeolite, this thesis focuses on the preparation of the zeolite via different techniques, their characterization, and their application towards environmental remediation. Zeolite synthesis from various steel slag has been summarized in Table 1.2.

Table 1.2: Zeolite synthesis using different steel slags and process description.

Slag type	NaOH (M)	Crystallization condition		Zeolite produced	Remarks	References
		T (°C)	t (h)			
EAFS	-	Desired temperature	Several hours	Zeolite A and hydroxysodalite (HSOD)	A hydrothermal synthesis technique was used, Na_2SiO_3 and $NaAlO_2$ were separated and used as precursors.	[10]
BFS	Varied from 0.5 to 5	Desired temperature	Several hours	Mixture of zeolite P1, FAU, and hydroxyapatite	A hydrothermal synthesis technique was employed, Higher NaOH concentration	[38]

					reduce the crystallization of the zeolite P1	
BFS	2	Varied from 50 to 150°C	4	Hydroxyapatite and FAU-type zeolite	Hydrothermal technique, hydroxyapatite appeared at 150°C, whereas FAU-type was formed at 90 and 120°C	[39]
BFS	4	100°C	6	Zeolite A and X	Hydrothermal treatment technique, Residual silica of BFS was used as zeolite precursor	[33]
BFS		100	5	Zeolite-type A	Hydrothermal method, H_2O/NaOH molar ratio results in a larger crystal size	[34]
BFS	-	120	2-4	Zeolite P	Octahedron shape was found, and zeolite was synthesized during the CO_2 mineralization process	[35]
BFS	0.375	100	6	HSOD, Zeolite A, and X	0-0.5 M of EDTA as an aging agent	[36]
BFS	0.1	100	8	FAU-type and ZSM-5	Hydrothermal process used for zeolite synthesis	[37]

1.5. Zeolite-based polymeric membrane for wastewater treatment

A zeolite-integrated membrane is a membrane with zeolite particles or zeolite-based compounds inserted into its structure. The addition of zeolites to a membrane can improve its performance and usefulness in a variety of applications. Depending on the individual design and required qualities, the zeolite particles can be scattered throughout the membrane matrix or coated onto the membrane surface. Zeolite membranes may be employed to separate carbon dioxide from methane in natural gas purification or to capture volatile organic compounds (VOCs) from air or industrial emissions. Nowadays, water purification and desalination applications have been examined using zeolite-incorporated membranes. Heavy metals, organic pollutants, and microbes can be adsorbed and removed from water streams by zeolite particles. Researchers, in recent times, focused on the fabrication of zeolite-membrane composites and their utilization for water decontamination and gas separation processes. Several studies related to zeolite-based composite membrane synthesis and their uses are provided in the literature survey section.

1.5.1. Literature survey

In a mixed matrix membrane (MMM) fabrication technology, Saranya and their research team [40] synthesized ZSM-5 embedded polyphenylsulfone (PPSU) membrane via the phase inversion process and employed it for lignin extraction. In this investigation, PPSU was combined with functionalized zeolites like Cu-ZSM-5 (Cu-Z) and Fe-ZSM-5 (Fe-Z) in the presence of N-methyl pyrrolidone (NMP) solvent. For a PPSU membrane with 0.5 wt.% of zeolite nanoparticles inserted, an increased pure water flow of 62 L/m^{2}h and the maximum lignin retention of 85.2% were recorded. The zeolite's 3D porous structure encouraged the augmentation of flux during the separation of water and lignin. But adding functionalized zeolite nanoparticles had a significant impact on the rise in the maximum lignin rejection to

88.5%. Based on their ability to reject organic components, synthetic MMMs have been assessed for their effectiveness and anti-fouling capacity. Zeolite and Cu-zeolite-included MMMs showed more preferred permeability and significant lignin rejection at the same time. In another experiment, Rodríguez et al. [41] fabricated polysulfone (PSf)/zeolite LTA MMM by dip coating followed by a phase inversion technique. For the purpose of creating MMMs, the organic free LTA zeolite was added as fillers at loadings of 10 and 20 weight percent to the polysulfone polymer matrix. The N_2 adsorption study was conducted over the as-synthesized membrane matrixes. The findings stated that increases in filler amount in the membrane network enhance the N_2 permeability. According to various scientific articles, a specific quantity of filler in the polymer matrix at least reduces membrane surface roughness and this effect is dependent on the filler's hydrophilic qualities [42]. Based on the statement, these findings reveal that the incorporation of functionalized zeolite LTA has exhibited a greater effect on the formation membrane surface and its structure. Yurekli [43] has prepared a zeolite/PSf composite membrane matrix via a nonsolvent-induced phase separation technique to reject lead (Pb^{2+}) and nickel (Ni^{2+}) from synthetic aqueous solution with an adsorption capacity of 682 and 122 mg/g, respectively. Hydrothermally synthesized zeolite X accompanied by membrane enhances the water permeability and adsorption capacity at the end of 60 minutes filtration process.

From the literature, it is concluded that lab-grade silica and alumina-derived zeolite were used to prepare different composite membranes. But, zeolite synthesis using silica-alumina enriched solid waste and their application to the fabrication of polymeric composite membrane matrix is very scarce. However, several scientific reports are available on waste-based zeolite production and their particular uses in mixed matrix membrane preparation for wastewater treatment. Some examples are given below in the literature survey.

1.6. Waste-derived Zeolites and their composite polymeric membrane for wastewater treatment

1.6.1. Literature survey

In order to remove lead (Pb^{2+}) from synthetic wastewater, Zhu et al. [44] created a homogeneous and narrow-sized Al_2O_3-NaA zeolite composite membrane from solid waste coal fly ash with a 99.9% removal efficiency at 0.1 MPa transmembrane pressure (TMP). In this common experiment, hydrothermally produced zeolite type-A was combined with an Al_2O_3 hollow fiber substrate to create a composite hollow fiber membrane that maintained a Si/Al ratio of 1.07. Li and others [45] fabricated two-dimensional (2D) zeolitic imidazolate frameworks (ZIFs) imprinted polyvinylidene fluoride (PVDF) ultrafiltration membrane for organic dye removal from wastewater under a low-pressure TMP of 1bar. The prepared membrane showed high organic dye removal efficiency (98%) along with a significant permeability flux of 290 L/m^2h. The desalinization rate was found to be in the range of 50-70% over the synthetic membranes with high anti-fouling properties. Habiba et al. [46] created a unique advanced chitosan/polyvinyl alcohol (PVA)/zeolite nanofibrous composite membrane using an electrospinning technique. In this experiment, chitosan was combined with hydrolyzed NaOH before being mixed with 1% zeolite in the presence of various aqueous PVA concentrations. When stored in distilled water, acidic and basic media for 20 days, the resulting composite membrane film had a considerable influence on mechanical and chemical stability. Over the constructed composite membrane, metal ions such as Ni^{2+}, Fe^{3+}, and Cr^{6+} were removed. The Cr^{6+}, Fe^{3+}, and Ni^{2+} adsorption capacities were 0.17, 0.11, and 0.03 mmol/g, respectively. Figure 1.3 depicts the schematic representation of wastewater treatment over zeolite-based polymeric MMMs.

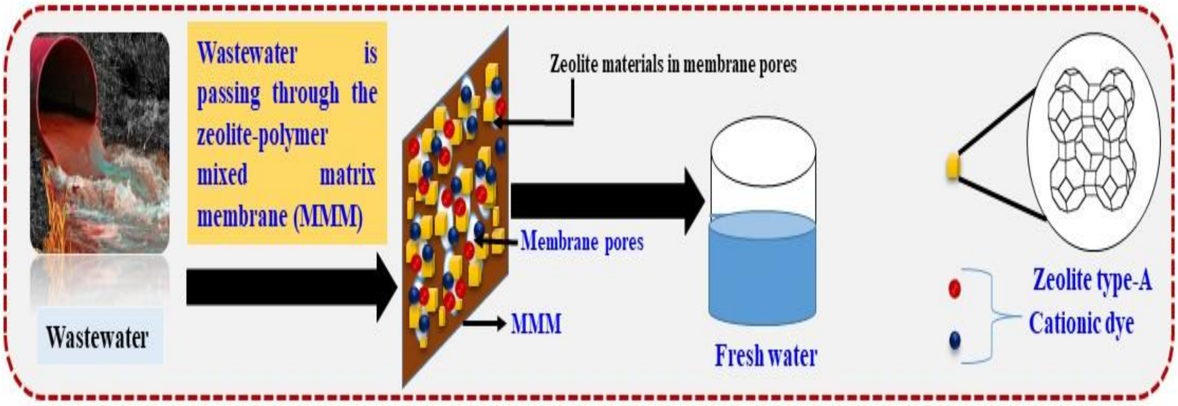

Figure 1.3: Zeolite-embedded mixed matrix membrane for wastewater treatment.

1.6.2. Possible scope of work

From the aforementioned literatures, it is envisaged that several studies have demonstrated zeolite-contained polymeric mixed matrix membrane fabrication and their utilization for different environmental remediation purposes. Some literature emphasized on zeolite-MMMs preparation, where solid waste fly ash was considered as a zeolite precursor instead of consuming lab-grade silica and alumina source. The utilization of silica and alumina-contained waste for zeolite synthesis reduces chemical consumption and enhances economic and environmental sustainability. It is also seen that zeolite synthesis from the steel industry processed slag and their uses for polymeric MMM synthesis are very scant. Moreover, slag-derived zeolite and its nanolayered polymeric membrane fabrication for wastewater treatment have not been done yet. Therefore, in this section of the thesis, zeolite was synthesized from LD-slag, and the prepared zeolite was layered on the PSf membrane by spray coating technique. This work focused on the synthesis and characterization of zeolite-coated membranes. The heavy metals removal study was conducted by the zeolite nanolayered membrane to examine the membrane efficiency. The increasing water flux was observed after the addition of hydrophilic zeolite on the membrane substrate.

1.7. CO_2 fixation with steel industry processed slag for the production of cementitious material and lowering CO_2 emission

The process of trapping and transforming carbon dioxide (CO_2) emissions into stable and ecologically safe forms inside the steel slag material is referred to as "CO_2 fixation in steel slag." Numerous minerals, including calcium, magnesium, and iron, can combine with CO_2 to generate stable carbonates in steel slag. Steel slag is subjected to CO_2, which interacts with calcium and magnesium ions to produce calcium and magnesium carbonates. This reaction efficiently stops CO_2 emissions by permanently locking CO_2 inside the slag's crystalline structure. Few scientific reports on CO_2 fixation with steel slag are discussed in the literature survey.

1.7.1. Literature survey

Rui et al. [47] prepared cementitious-like material by fixing CO_2 gas in steel-making slag. The calcium-containing ore phase is converted into calcium carbonate when the steel slag powder is cured by CO_2 from the cement kiln flue gas. The nucleating action of calcium carbonate encourages the early hydration process and raises the ionic concentration and pH of the liquid phase. Additionally, when employing bacteria and steel slag for CO_2 sequestration, the remaining bacteria can have a favourable impact. The low-carbon supplementary cementitious material created by the synergistic CO_2 fixation of bacteria and steel slag powder has been discovered to have larger application potential in cement-based products, according to long-term performance monitoring. The results achieved from the findings revealed that cement-based slag possesses higher mechanical and physical characteristics as compared to untreated slag. In another study, Cheng et al. [48] produced $CaCO_3$ using CaO enrich steel slag (SS) by CO_2 sequestration. The two-step leaching (TSL) technique was found to be the potential for SS and CO_2 reduction. This approach used two NH_4Cl solutions in series for two leaching operations on SS, significantly increasing the Ca leaching rate. When compared to the traditional one-step leaching (CSL) approach, TSL may enhance the activated Ca^{2+} leaching rate by 26.9% and achieve 223.15 kg CO_2 capture/ton SS. According to the findings, TSL is capable of performing up to 8 cycles of CO_2 sequestration and this proposed strategy has been found potential while reducing CO_2 emission and recycling of steel slag. Mineral carbonation with titanium-bearing blast furnace slag (TBFS) may provide a sustainable approach to the reduction of CO_2 emissions while also maximizing solid waste reuse, according to He et al. [49]. Using TBFS and copperas as feedstocks, this study presented a new method combining CO_2 mineral sequestration with rutile beneficiation. TBFS and copperas were roasted at 550-750°C to convert calcium and magnesium into matching sulfates, while titanium in the TBFS was beneficiated to rutile. The roasted slag was then carbonated before recovering rutile and hematite using flotation and magnetic separation, respectively. The impacts of process factors were thoroughly investigated. The addition of Na_2SO_4 considerably improved Ti conversion efficiency (from 53% to 98%). The process indicated that the addition of Na_2SO_4 increased the development of molten $Na_3Fe(SO_4)_3$, resulting in significantly quicker and more efficient gas-liquid-solid transitions. According to the carbonation findings of sulfated TBFS, the ideal CO_2 storage capacity can reach 187 kg/ton TBFS. Two solid wastes were used in this method for CO_2 mineralization, realizing the combined benefits of CO_2 emission reduction, solid waste disposal, and valuable by-product recovery.

1.7.2. Possible scope of work

From the above literature survey, it may be found that several authors have reported CO_2 fixation by sequestrating it to the SS which results in the formation of carbonate of calcium and magnesium that is considered as a cementitious material. But, CO_2 sequestration with

LD-slag and the formation of precipitated calcium carbonate (PCC) have not been explored yet. So, keeping the main objective of lowering the CO_2 emission and reduction of solid waste LD-slag, this part of the thesis focused on CO_2 sequestration and preparation of cementitious PCC. The addition as well as effects of commercial sugar on the yield of PCC formation was examined and the entire reaction mechanism was developed thereon. The prepared PCC was characterized by different characterization techniques to examine the phase identification, purity, and physical properties.

1.8. Objectives of thesis work

Based on the above state of the art, the present PhD thesis incorporates the following main objectives

- Preparation and characterization of zeolite from waste Linz-Donawitz (LD) process slag of steel industry for removal of Fe^{3+} from drinking water
- Physico-chemical and adsorption study of hydrothermally treated zeolite A and FAU-type zeolite X prepared from LD (Linz–Donawitz) slag of the steel industry
- Fabrication of LD-slag derived Zeolite Y coated Polysulfone (PSf) membrane for decontamination of groundwater
- Synthesis of precipitated calcium carbonate from LD-slag using CO_2

1.9. Organization of the thesis

Chapter 1 addresses the background of steel slag, the types of slag and their chemical characteristics, and the importance of slag. The utilization technique of slags in making value-added products was also elucidated comprehensively which can provide a sustainable way to reduce the waste slag. The objectives of the present work are also highlighted in this chapter. **Chapter 2** illustrates a comprehensive discussion on the preparation and characterization of zeolite-like adsorbent using LD-slag as a precursor material for Fe^{3+} removal from drinking water. **Chapter 3** presents the adsorption study of LD-slag-derived FAU-type zeolite X and zeolite A. Apart from these results, the thermal and physico-chemical stability of as-synthesized zeolite minerals were investigated at three different pH conditions and treatment times. **Chapter 4** provides a comprehensive idea of zeolite Y synthesis via ultrasonic irradiation followed by fusion-assisted hydrothermal treatment and their uses to fabricate nanolayered-based PSf membranes. The application of zeolite-coated membrane for the decontamination of groundwater was also studied and explained in this chapter. **Chapter 5** discusses the preparation and characterization of precipitated calcium carbonate by CO_2 sequestration in LD-slag using commercial sugar as a promoter. This chapter also provides an in-depth conclusion on the role of sugar in the formation of a variety of polymorphs of PCC samples. **Chapter 6** summarized the inferences drawn from this work and provided some suggestions for future research.

References

[1] I.Z. Yildirim, M. Prezzi, Chemical, mineralogical, and morphological properties of steel slag, Adv. Civ. Eng. 2011 (2011). https://doi.org/10.1155/2011/463638.

[2] Y.-S. Li, The use of waste basic oxygen furnace slag and hydrogen peroxide to degrade 4-chlorophenol, Waste Manag. 19 (1999) 495–502. https://doi.org/https://doi.org/10.1016/S0956-053X(99)00239-1.

[3] M. Pasetto, N. Baldo, Experimental evaluation of high performance base course and road base asphalt concrete with electric arc furnace steel slags, J. Hazard. Mater. 181 (2010) 938–948. https://doi.org/10.1016/j.jhazmat.2010.05.104.

[4] C. Maharaj, D. White, R. Maharaj, C. Morin, Re-use of steel slag as an aggregate to asphaltic road pavement surface, Cogent Eng. 4 (2017). https://doi.org/10.1080/23311916.2017.1416889.

[5] B.G. Delgado, A. Viana da Fonseca, E. Fortunato, A. Paixão, R. Alves, Geomechanical assessment of an inert steel slag aggregate as an alternative ballast material for heavy haul rail tracks, Constr. Build. Mater. 279 (2021). https://doi.org/10.1016/j.conbuildmat.2021.122438.

[6] F. Maghool, A. Arulrajah, Y.-J. Du, S. Horpibulsuk, A. Chinkulkijniwat, Environmental impacts of utilizing waste steel slag aggregates as recycled road construction materials, Clean Technol. Environ. Policy. 19 (2017) 949–958. https://doi.org/10.1007/s10098-016-1289-6.

[7] Y. Biskri, D. Achoura, N. Chelghoum, M. Mouret, Mechanical and durability characteristics of High Performance Concrete containing steel slag and crystalized slag as aggregates, Constr. Build. Mater. 150 (2017) 167–178. https://doi.org/https://doi.org/10.1016/j.conbuildmat.2017.05.083.

[8] A. Gobetti, G. Cornacchia, G. Ramorino, A. Riboldi, L.E. Depero, EAF slag as

alternative filler for epoxy screeds, an example of green reuse, Sustain. Mater. Technol. 29 (2021) e00324. https://doi.org/https://doi.org/10.1016/j.susmat.2021.e00324.

[9] S.K. Singh, P. Vashistha, R. Chandra, A.K. Rai, Study on leaching of electric arc furnace (EAF) slag for its sustainable applications as construction material, Process Saf. Environ. Prot. 148 (2021) 1315–1326. https://doi.org/https://doi.org/10.1016/j.psep.2021.01.039.

[10] Y. Li, T. Peng, W. Man, L. Ju, F. Zheng, M. Zhang, M. Guo, Hydrothermal synthesis of mixtures of NaA zeolite and sodalite from Ti-bearing electric arc furnace slag, RSC Adv. 6 (2016) 8358–8366. https://doi.org/10.1039/c5ra26881h.

[11] Y. Li, H. Mehdizadeh, K.H. Mo, T.-C. Ling, Co-utilization of aqueous carbonated basic oxygen furnace slag (BOFS) and carbonated filtrate in cement pastes considering reaction duration effect, Cem. Concr. Compos. 138 (2023) 104988. https://doi.org/https://doi.org/10.1016/j.cemconcomp.2023.104988.

[12] A.S. Reddy, R.K. Pradhan, S. Chandra, Utilization of Basic Oxygen Furnace (BOF) slag in the production of a hydraulic cement binder, Int. J. Miner. Process. 79 (2006) 98–105. https://doi.org/https://doi.org/10.1016/j.minpro.2006.01.001.

[13] E. Belhadj, C. Diliberto, A. Lecomte, Characterization and activation of Basic Oxygen Furnace slag, Cem. Concr. Compos. 34 (2012) 34–40. https://doi.org/10.1016/j.cemconcomp.2011.08.012.

[14] K. Sun, X. Peng, S.H. Chu, S. Wang, L. Zeng, G. Ji, Utilization of BOF steel slag aggregate in metakaolin-based geopolymer, Constr. Build. Mater. 300 (2021) 124024. https://doi.org/https://doi.org/10.1016/j.conbuildmat.2021.124024.

[15] N.T. Sithole, F. Ntuli, F. Okonta, Fixed bed column studies for decontamination of acidic mineral effluent using porous fly ash-basic oxygen furnace slag based

geopolymers, Miner. Eng. 154 (2020) 106397. https://doi.org/https://doi.org/10.1016/j.mineng.2020.106397.

[16] Z. Ma, H. Liao, F. Cheng, Synergistic mechanisms of steelmaking slag coupled with carbide slag for CO2 mineralization, Int. J. Greenh. Gas Control. 105 (2021) 103229. https://doi.org/10.1016/j.ijggc.2020.103229.

[17] R. Baciocchi, G. Costa, M. Di Gianfilippo, A. Polettini, R. Pomi, A. Stramazzo, Thin-film versus slurry-phase carbonation of steel slag: CO2 uptake and effects on mineralogy, J. Hazard. Mater. 283 (2015) 302–313. https://doi.org/10.1016/j.jhazmat.2014.09.016.

[18] Q. Zhao, X. Chu, X. Mei, Q. Meng, J. Li, C. Liu, H. Saxén, R. Zevenhoven, Co-treatment of Waste From Steelmaking Processes: Steel Slag-Based Carbon Capture and Storage by Mineralization, Front. Chem. 8 (2020) 1–7. https://doi.org/10.3389/fchem.2020.571504.

[19] Y. Xue, H. Hou, S. Zhu, Characteristics and mechanisms of phosphate adsorption onto basic oxygen furnace slag, J. Hazard. Mater. 162 (2009) 973–980. https://doi.org/10.1016/j.jhazmat.2008.05.131.

[20] B. Narindri Rara Winayu, N.-Y. Shen, H. Chu, Valuable reutilization of Basic Oxygen Furnace (BOF) slag for the CO2 sorption from oxy-fuel combustion in a fluidized bed reactor, J. CO2 Util. 66 (2022) 102280. https://doi.org/https://doi.org/10.1016/j.jcou.2022.102280.

[21] M. Islam, S. Mishra, S.K. Swain, R. Patel, R.K. Dey, M. Naushad, Evaluation of Phosphate Removal Efficiency from Aqueous Solution by Polypyrrole/BOF Slag Nanocomposite, Sep. Sci. Technol. 49 (2014) 2668–2680. https://doi.org/10.1080/01496395.2014.933981.

[22] M. Mallik, S. Hembram, D. Swain, G. Behera, Potential utilization of LD slag and

waste glass in composite production, Mater. Today Proc. 33 (2020) 5196–5199. https://doi.org/https://doi.org/10.1016/j.matpr.2020.02.881.

[23] J. Yang, W.M. Shaban, K. Elbaz, B.S. Thomas, J. Xie, L. Li, Properties of concrete containing strengthened crushed brick aggregate by pozzolan slurry, Constr. Build. Mater. 247 (2020) 118612. https://doi.org/https://doi.org/10.1016/j.conbuildmat.2020.118612.

[24] P. Singh, A. Sharma, A.B. Danie Roy, Utilization of Linz-Donawitz slag and brick bat for the production of sustainable paver blocks, Mater. Today Proc. (2023). https://doi.org/https://doi.org/10.1016/j.matpr.2023.04.044.

[25] Deepti, A. Sinha, P. Biswas, S. Sarkar, U. Bora, M.K. Purkait, Utilization of LD slag from steel industry for the preparation of MF membrane, J. Environ. Manage. 259 (2020) 110060. https://doi.org/https://doi.org/10.1016/j.jenvman.2019.110060.

[26] S. Chand, B. Paul, M. Kumar, An Overview of Use of Linz-Donawitz (LD) Steel Slag in Agriculture, Curr. World Environ. 10 (2015) 975–984. https://doi.org/10.12944/cwe.10.3.29.

[27] T.W. Cheng, M.L. Lee, M.S. Ko, T.H. Ueng, S.F. Yang, The heavy metal adsorption characteristics on metakaolin-based geopolymer, Appl. Clay Sci. 56 (2012) 90–96. https://doi.org/https://doi.org/10.1016/j.clay.2011.11.027.

[28] C. Sarkar, J.K. Basu, A.N. Samanta, Synthesis of mesoporous geopolymeric powder from LD slag as superior adsorbent for Zinc (II) removal, Adv. Powder Technol. 29 (2018) 1142–1152. https://doi.org/https://doi.org/10.1016/j.apt.2018.02.005.

[29] C. Sarkar, J.K. Basu, A.N. Samanta, Synthesis of MIL-53(Fe)/SiO2 composite from LD slag as a novel photo-catalyst for methylene blue degradation, Chem. Eng. J. 377 (2019) 119621. https://doi.org/10.1016/j.cej.2018.08.007.

[30] C. Sarkar, J.K. Basu, A.N. Samanta, Experimental and kinetic study of fluoride

adsorption by Ni and Zn modified LD slag based geopolymer, Chem. Eng. Res. Des. 142 (2019) 165–175. https://doi.org/https://doi.org/10.1016/j.cherd.2018.12.006.

[31] C. Sarkar, J.K. Basu, A.N. Samanta, Microwave Activated LD Slag for Phenolic Wastewater Treatment : Multi- Microwave Activated LD Slag for Phenolic Wastewater Treatment : Multi-parameter Optimization , Isotherms , Kinetics and Thermodynamics, (2017). https://doi.org/10.3303/CET1757047.

[32] N.S. Samanta, P.P. Das, P. Mondal, M. Changmai, M.K. Purkait, Critical review on the synthesis and advancement of industrial and biomass waste-based zeolites and their applications in gas adsorption and biomedical studies, J. Indian Chem. Soc. 99 (2022) 100761. https://doi.org/https://doi.org/10.1016/j.jics.2022.100761.

[33] Y. Kuwahara, T. Ohmichi, T. Kamegawa, K. Mori, H. Yamashita, A novel conversion process for waste slag : synthesis of a hydrotalcite-like compound and zeolite from blast furnace slag and evaluation of adsorption capacities, (2010) 5052–5062. https://doi.org/10.1039/c0jm00518e.

[34] I.W.A. Publishing, W. Science, NaA zeolite derived from blast furnace slag : its application for ammonium removal Hongwei Guo , Lizhen Tang , Bingji Yan , Kang Wan and Peng Li, (2017) 1140–1149. https://doi.org/10.2166/wst.2017.294.

[35] W. Liu, T. Aldahri, C. Xu, C. Li, S. Rohani, Synthesis of sole gismondine-type zeolite from blast furnace slag during CO2 mineralization process, J. Environ. Chem. Eng. 9 (2021) 104652. https://doi.org/https://doi.org/10.1016/j.jece.2020.104652.

[36] T. Wajima, Synthesis of Zeolite from Blast Furnace Slag using Alkali Fusion with Addition of EDTA, (2014) 124–127. https://doi.org/10.4028/www.scientific.net/AMR.1044-1045.124.

[37] G. Hu, X. Duan, J. Yang, C. Yang, Q. Liu, S. Ren, J. Li, L. Teng, W. Liu, A novel conversion of Ti-bearing blast furnace slag into Ti-containing zeolites: Comparison

study between FAU and MFI type zeolites, Adv. Powder Technol. 33 (2022) 103559. https://doi.org/https://doi.org/10.1016/j.apt.2022.103559.

[38] G.U. Ryu, H.R. Khalid, N. Lee, Z. Wang, H.K. Lee, The effects of NaOH concentration on the hydrothermal synthesis of a hydroxyapatite–zeolite composite using blast furnace slag, Minerals. 11 (2021) 1–13. https://doi.org/10.3390/min11010021.

[39] F. Slag, materials The E ff ects of Temperature on the Hydrothermal Synthesis of Hydroxyapatite-Zeolite Using Blast Furnace Slag, (2019).

[40] R. Saranya, G. Arthanareeswaran, A.F. Ismail, N.L. Reddy, M. V. Shankar, J. Kweon, Efficient rejection of organic compounds using functionalized ZSM-5 incorporated PPSU mixed matrix membrane, RSC Adv. 7 (2017) 15536–15552. https://doi.org/10.1039/c6ra27314a.

[41] A. Jacas-Rodríguez, P. Rodríguez-Pascual, D. Franco-Manzano, L. Contreras, C. Polop, M.A. Rodriguez, Mixed matrix membranes prepared from polysulfone and linde type A zeolite, Sci. Eng. Compos. Mater. 27 (2020) 236–244. https://doi.org/10.1515/secm-2020-0022.

[42] V. Vatanpour, S.S. Madaeni, L. Rajabi, S. Zinadini, A.A. Derakhshan, Boehmite nanoparticles as a new nanofiller for preparation of antifouling mixed matrix membranes, J. Memb. Sci. 401–402 (2012) 132–143. https://doi.org/https://doi.org/10.1016/j.memsci.2012.01.040.

[43] Y. Yurekli, Removal of heavy metals in wastewater by using zeolite nano-particles impregnated polysulfone membranes, J. Hazard. Mater. 309 (2016) 53–64. https://doi.org/10.1016/j.jhazmat.2016.01.064.

[44] L. Zhu, J. Ji, S. Wang, C. Xu, K. Yang, M. Xu, Removal of Pb(II) from wastewater using Al2O3-NaA zeolite composite hollow fiber membranes synthesized from solid

waste coal fly ash, Chemosphere. 206 (2018) 278–284. https://doi.org/https://doi.org/10.1016/j.chemosphere.2018.05.001.

[45] T. Li, Y. Ren, D. Wu, W. Zhang, M. Shi, C. Ji, L. Lv, M. Hua, W. Zhang, A novel water-stable two-dimensional zeolitic imidazolate frameworks thin-film composite membrane for enhancements in water permeability and nanofiltration performance, Chemosphere. 261 (2020). https://doi.org/10.1016/j.chemosphere.2020.127717.

[46] U. Habiba, A.M. Afifi, A. Salleh, B.C. Ang, Chitosan /(polyvinyl alcohol)/ zeolite electrospun composite nanofibrous membrane for adsorption of Cr^{6+} , Fe^{3+} and Ni^{2+}, J. Hazard. Mater. 322 (2017) 182–194. https://doi.org/10.1016/j.jhazmat.2016.06.028.

[47] Y. Rui, C. Qian, CO_2-fixing steel slag on hydration characteristics of cement-based materials, Constr. Build. Mater. 354 (2022) 129193. https://doi.org/https://doi.org/10.1016/j.conbuildmat.2022.129193.

[48] C. Cheng, W. Huang, H. Xu, Z. Liu, X. Li, H. Shi, Y. Yu, Z. Qu, N. Yan, CO_2 sequestration and $CaCO_3$ recovery with steel slag by a novel two-step leaching and carbonation method, Sci. Total Environ. 891 (2023) 164203. https://doi.org/https://doi.org/10.1016/j.scitotenv.2023.164203.

[49] M. He, L. Teng, Y. Gao, S. Rohani, S. Ren, J. Li, J. Yang, Q. Liu, W. Liu, Simultaneous CO2 mineral sequestration and rutile beneficiation by using titanium-bearing blast furnace slag: Process description and optimization, Energy. 248 (2022) 123643. https://doi.org/https://doi.org/10.1016/j.energy.2022.123643.

Chapter 2

Preparation and Characterization of Zeolite from Waste Linz-Donawitz (LD) process slag of Steel Industry for Removal of Fe^{3+} from Drinking Water

In this chapter cubical-shaped zeolite A was synthesized from the Linz-Donawitz (LD) process slag of the steel industry, via fusion-facilitated hydrothermal treatment. Morphological and Physico-chemical characterizations were examined by various characterization techniques. The stability analysis of the as-synthesized zeolite A sample was assessed by field emission scanning electron microscope (FESEM) and X-ray diffraction (XRD) analysis. The specific surface area of the zeolite A sample was determined by Brunauer-Emmett-Teller (BET) analysis. Thermal stability measurement of the obtained zeolite was examined by Thermogravimetric analysis (TGA). Synthetic zeolite was employed for iron (Fe^{3+}) removal from synthetic as well as drinking water. Fe^{3+} adsorption studies were performed at 273, 298, 303, and 308K, respectively, within the range of 10-40 mg/L Fe^{3+} ion concentration for kinetic and isotherm studies.

2. Experimental methods

2.1. Materials

TATA Steel, Jamshedpur, India, supplied raw LD-slag which is a waste material from the process units. The XRF data of that sample are given in Table 2.1. Various oxides of metal ions are present in it, such as Ca, Fe, Mg, Mn, and our target material Si and Al. Hydrochloric acid (HCl), used for acid treatment, nonahydrate of sodium silicate ($Na_2O_3Si{\cdot}9H_2O$), and sodium aluminate ($Na_2O_3Al_2{\cdot}9H_2O$), used for maintaining the Si/Al ratio, sodium hydroxide

---

Content of this chapter is published as below:

N.S. Samanta, S. Banerjee, P. Mondal, Anweshan, U. Bora, M.K. Purkait, Preparation and characterization of zeolite from waste Linz-Donawitz (LD) process slag of steel industry for removal of Fe^{3+} from drinking water, Adv. Powder Technol. 32 (2021) 3372–3387. https://doi.org/10.1016/j.apt.2021.07.023.

(NaOH) as pellets and anhydrous ferric chloride ($FeCl_3$), used for the adsorption experiment, were all procured from Merck (Darmstadt, Germany).

Table 2.1: Elemental composition of LD-slag (Data provided by TATA steel industries ltd.).

Components	Weight (%)
CaO	41.92
SiO_2	12.69
Al_2O_3	1.71
MgO	2.33
Fe_2O_3	36.72
P_2O_5	2.27
Others	2.36

2.2. Zeolite A synthesis from LD-slag

Alkali fusion and subsequent hydrothermal treatment were performed on LD-slag to synthesize Zeolite A. The raw slag was rinsed with distilled water to eliminate any soluble impurities. It was then kept inside a muffle furnace operated at 800°C for 2 hours to expunge the unwanted volatile matter present in the sample. Furthermore, hydrochloric acid (10%, w/v) at 50-60°C was applied to LD-slag to improve its capacity for zeolite framework formation [1]. After cooling down, the sample was taken out to prepare a homogenous fusion mixture of treated LD-slag and NaOH in the ratio of 1:1.2 (w/w), respectively, by proper grinding. The mixture was kept at 550°C for 2 hours in a muffle furnace for the fusion to occur. Distilled water was added in a 1:10 ratio to the fused mass after cooling it to ambient temperature. The slag solution was mixed with sodium silicate. Sodium aluminate was then added simultaneously to the resulting slurry to obtain the desired Si/Al ratio. The slurry was stirred continuously during the mixing using a magnetic stirrer. After 24 hours, the slurry sample was allowed to crystallize by hydrothermal treatment at 90°C for 8 hours in an autoclave reactor. The resultant sample was filtered, rinsed thoroughly with distilled water, and kept for drying at 100°C for 6 hours in a hot air oven to recover crystallized zeolite A. Figure 2.1 shows the flow chart of fusion-assisted hydrothermal treatment for zeolite A.

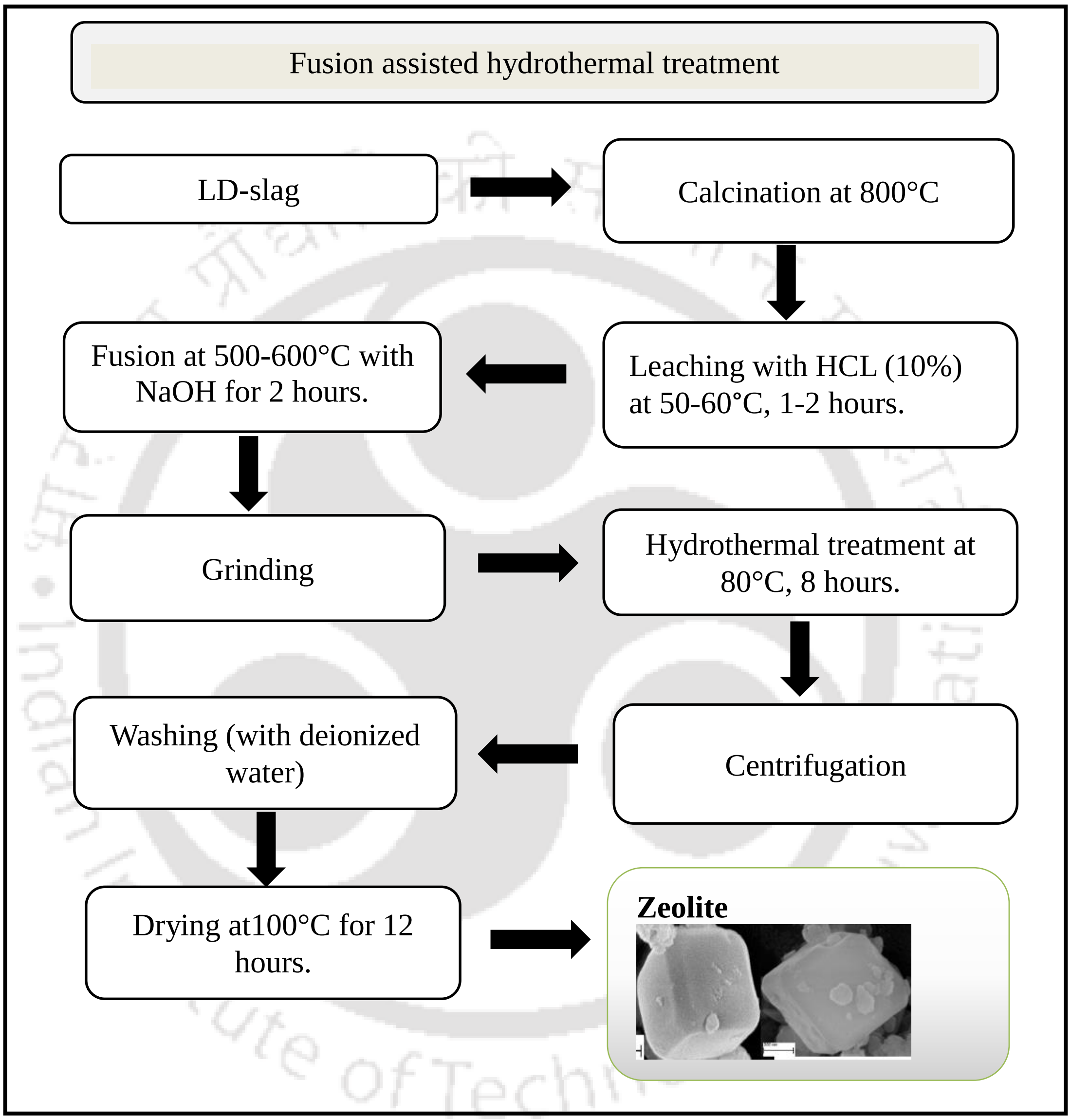

Figure 2.1: Process flow chart of Zeolite synthesis from LD-slag via fusion-assisted hydrothermal treatment.

2.3 Characterization techniques

The determination of characteristic attributes of both LD-slag and Zeolite A was accomplished using well-established techniques. The pore size and specific surface area analysis were performed using the BET apparatus Autosorb iQ (Quantachrome Instruments, USA). The surface morphology study was carried out using an EDX-equipped FESEM Sigma 300 (ZEISS, Germany). The crystal structure was studied using a transmission electron microscope JEM-2100F (JEOL, Japan) and x-ray diffraction patterns were obtained using XRD D8 Advance Model (Bruker, USA) equipped with monochromatic Cu Kα radiation having $\lambda = 0.154$ nm. The 2θ value was scanned from 10° to 80° with a step time of 0.5 s. FTIR analysis on both LD-slag and synthetic zeolite was performed using the IRAffinity-1 (Shimadzu, Japan). Wavenumbers from 400-4000 cm^{-1} were scanned with a 10 cm/s scanning rate.

The glass transition temperature (T_g) of the obtained zeolite sample was determined via Differential Scanning Calorimetry (DSC 1, Mettler Toledo, Switzerland). The scanning temperature was from 25°C to 450°C at a heating rate of 5°C/minute purgings with nitrogen gas. The thermogravimetric analysis of the prepared zeolite sample was performed by TGA instrument (TG209 F1, NETZSCH, Germany), type of crucible: DSC/TGA pan Al_2O_3. Argon was used as both protective and purge gas at the flow rate of 20 mL/minute and 60 mL/minute, respectively. The temperature program was set from 25 to 1000°C at an increment of 10°C/minute.

The isoelectric point of the synthesized zeolite was determined using the Dynamic Light Scattering (DLS) instrument (Litesizer 500, Anton Paar, Austria).

Analyzing the concentration of Fe^{3+} ion was performed using Atomic Absorption Spectrophotometer (AAS) (Model No.: Spectra AA 220 FS; Make: M/s Varian, Netherland).

2.4. Adsorption experiments

Fe^{3+} adsorption onto the synthesized zeolite A adsorbent was performed in a batch system (50 mL of Fe^{3+} solution in 250 mL conical flask, agitated in a fixed temperature mechanical shaker at 200 rpm). The adsorption kinetics was performed with several different experimental conditions to check the influence of those experimental parameters such as temperature (293, 298, 303, and 308K), adsorption dosage (from 0.01 to 0.07 g), contact time, and initial Fe^{3+} concentration (from 10 to 40 mg/L). Solution pH was fixed to a point above the isoelectric point of zeolite A throughout the experiment to maximize the adsorption capacity [2]. Concentration was measured using atomic absorption spectroscopy. Fe^{3+} adsorption uptake at the equilibrium, Q_e (in mg/g), was calculated by using equation (2.1) [3].

$$Q_e = \frac{(C0-Ce)V}{W} \tag{2.1}$$

Fe^{3+} adsorption uptake Q_t, at time t, was calculated by using equation (2.2) [2]

$$Q_t = \frac{(C0-C(t))V}{W} \tag{2.2}$$

Where C_0, C_e, and C(t) are Fe^{3+} concentrations at an initial time, equilibrium phase, and at any contact time t respectively, in mg/L. V is the volume of the mother solution in L, and W (g) is the mass of the adsorbent zeolite A

Removal efficiency (%) of Fe^{3+} on the adsorbent was calculated from equation (2.3)

$$\text{Removal efficiency (\%)} = \frac{(C_0-C_t)V}{C_0} \times 100 \tag{2.3}$$

2.5. Real-life water sample analysis

Drinking water obtained from the IIT Guwahati Campus, India was spiked with Fe^{3+} ion and three different concentration of 2.5 mg/L, 5 mg/L, and 10 mg/L was attained. The optimized zeolite A dosage was then utilized for treating the real-life sample waters and the concentration of Fe^{3+} ion was analyzed using the AAS instrument.

2.6. Results and Discussion

2.6.1. Zeolitization

Generally, three necessary steps of geochemical reactions were involved in the process of zeolitization of LD-slag. Firstly, the LD-slag went through an alkali fusion treatment (i.e., LD-slag to NaOH ratio of 1 to 1.2 with a very high temperature). This alkali fusion helped to extract the Si^{4+} and Al^{3+} ions from SiO_2 and Al_2O_3, respectively present in the LD-slag. The amount of Si^{4+} ions was more as compared to Al^{3+} because the LD-slag has a high Si/Al ratio. This helped to maintain the required Si/Al ratio for zeolite A. The lower Si/Al ratio also ensures suitable crystallinity of the zeolite. Moreover, a low Si/Al ratio provides a hydrophilic zeolite surface and enhances the interaction between adsorbate and polar molecules (water in the present study) which leads to the higher adsorption capacity of the material. On the contrary, zeolite with a high Si/Al ratio causes the surface to be hydrophobic which diminishes the molecular interaction and may lead to less adsorption capacity of the synthesized material [4]. However, the sodium hydroxide was used as an activator of the Si^{4+} and Al^{3+} ions and helped to maintain the required Na amount in the starting material. These active Si^{4+} ions formed a tetrahedral unit of silicate (SiO_4), which again react with NaOH to form sodium silicate. Also, the Al^{3+} reacted with sodium hydroxide to produce sodium aluminate. The probable reactions involved with LD-slag are shown in equations (2.4), (2.5), and (2.6).

$$NaOH \rightarrow Na^{+} + OH^{-} \tag{2.4}$$

$$Na^{+} + SiO_4 \rightarrow Na_{2,}SiO_3 \tag{2.5}$$

$$NaOH + Al^{3+} + H_2O \rightarrow NaAl(OH)_4 \tag{2.6}$$

In the next step, the above NaOH fused LD-slag was mixed with sodium silicate and sodium aluminate (20 to 30 wt.% of LD-slag, to balance the Si/Al ratio), which helped to initiate the zeolitization process by copolymerization of the resultant mass. The probable reaction mechanism is given in reaction no (2.7).

$$NaAl(OH)_4 + Na_2SiO_3 + NaOH \rightarrow [NA_p(AlO_2)q(SiO_2)rNaOH.H_2O](gel) \qquad (2.7)$$

The last step is the hydrothermal treatment of the polymeric gel produced in the reaction (2.8) for crystallization of the zeolite A. The chemical formula of zeolite A has been taken from the literature [5]. The crystallization process is given in reaction (2.8).

$$\left[NA_p(AlO_2)q(SiO_2)rNaOH.H_2O\right](gel) \rightarrow Na_2O.Al_2O_3.2SiO_2.4-5H_2O(zeolite\ A) \quad (2.8)$$

Simultaneously, calcium oxide (CaO) reacts with the water molecule present in the sample and produces calcium hydroxide $Ca(OH)_2$, which again decomposed into Ca^{2+} and OH^-. These Ca^{2+} get attached to some of the silicate ions to produce complex salt of calcium [6].

2.6.2. Characterization

2.6.2.1. XRD analysis

The XRD pattern of the LD-slag in Figure 2.2 has a lot of overlapping, which describes that a bulk amount of minerals can be present in the sample. The phases were characterized as major and minor phases based on the intensity of the peaks. High-intensity peaks were observed at 18.09°, 29.62°, and 34.03°, which mainly represent the presence of major phases of different oxides of calcium. Several other peaks represent the presence of minor phases of oxide forms of silica and alumina [7]. The peaks present in the XRD pattern of zeolite A refer that a highly crystalline phase was present in the synthesized product. Diffraction peaks at a 2θ angle of 7.18°, 10.16°, 12.58°, 16.1°, 20.4°, 21.66°, 23.98°, 26.1°, 27.09°, 29.94°, 32.54°, 34.18°, 39.49°, 44.18°, 45.3°, 47.29°, 52.58°, and 54.23°, matched with commercial zeolite 4A [8], International Zeolite Association (IZA) data [9], and also with fly ash based zeolite A [10]. It also demonstrated that the zeolite was enriched with Na, which helped to provide the crystalline structure of zeolite A. Crystalline planes of zeolite A are tabulated in Table 2.2, exactly matched with zeolite A synthesized by Tepamat et al. [11]. The crystalline particle with lattice fringe can be assigned to (1 0 0) the face of the cubic structure of zeolite A (Figure 2.2, inset) [1].

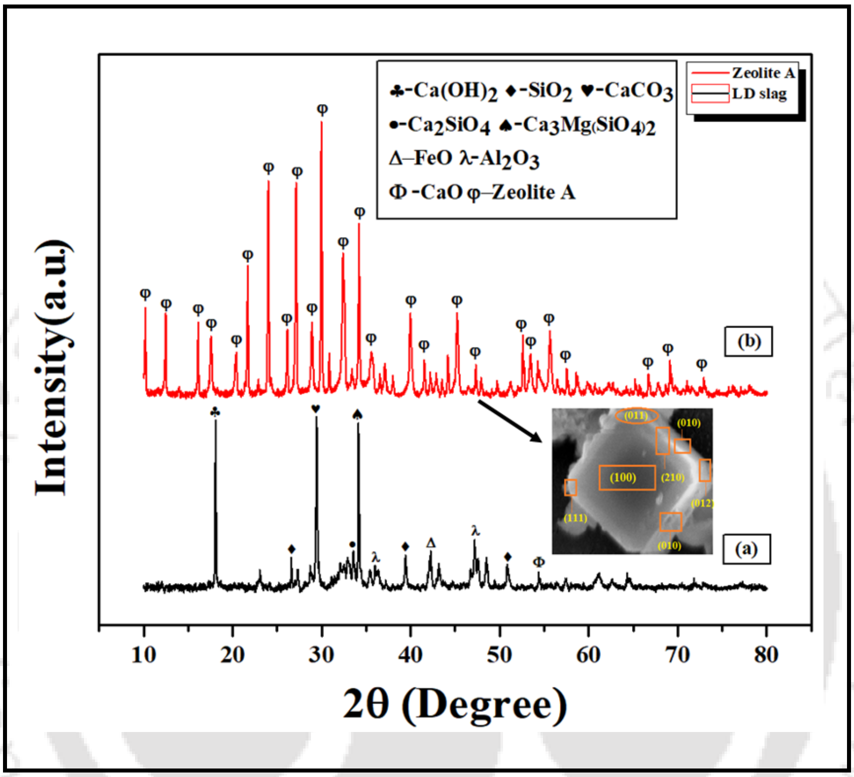

Figure 2.2: XRD analysis of (a) LD-slag (b) synthesized zeolite A.

Table 2.2: Crystalline plane of zeolite A from XRD analysis.

2θ	Crystal plane	2θ	Crystal plane	2θ	Crystal plane
7.2	(1 0 0)	23.98	(3 1 1)	39.49	(4 3 2)
10.16	(1 1 0)	26.1	(3 2 0)	44.18	(4 4 2)
12.58	(1 1 1)	27.09	(3 2 1)	45.3	(6 2 2)
16.1	(2 1 0)	29.94	(4 1 0)	47.29	(6 2 1)
20.4	(2 2 0)	32.54	(4 2 0)	52.58	(5 5 0)
21.66	(3 0 0)	34.18	(3 3 2)	54.23	(7 2 0)

2.6.2.2. FTIR analysis

FTIR of synthesized zeolite A was performed using infrared radiation in the wavelength range of 4000 to 400 cm^{-1} to detect the functional group present in the zeolite A. FTIR spectrum (Figure 2.3) shows a band at 1660 cm^{-1} is attributed to the flexion vibration of the OH group presence in adsorbed water molecules. The asymmetric and symmetric stretching vibrations incorporated with tetrahedral units of SiO_4 and AlO_4 were reported at around 710, and 1030 cm^{-1}, respectively. The absorption band at about 450 cm^{-1} was attributed to Si-O, and Al-O bonds present in the zeolite A framework. The peaks that appeared at 553 and 668 cm^{-1} were assigned for the zeolite A double four-ring framework (D4R). The presence of hydrous metal oxides and hydroxides was represented by the bending vibrational peak at 1430 cm^{-1} [12]. The spectrum also demonstrated that the stretching vibration of -OH groups present in zeolite A was confirmed in the range of 3300-3700 cm^{-1} [13].

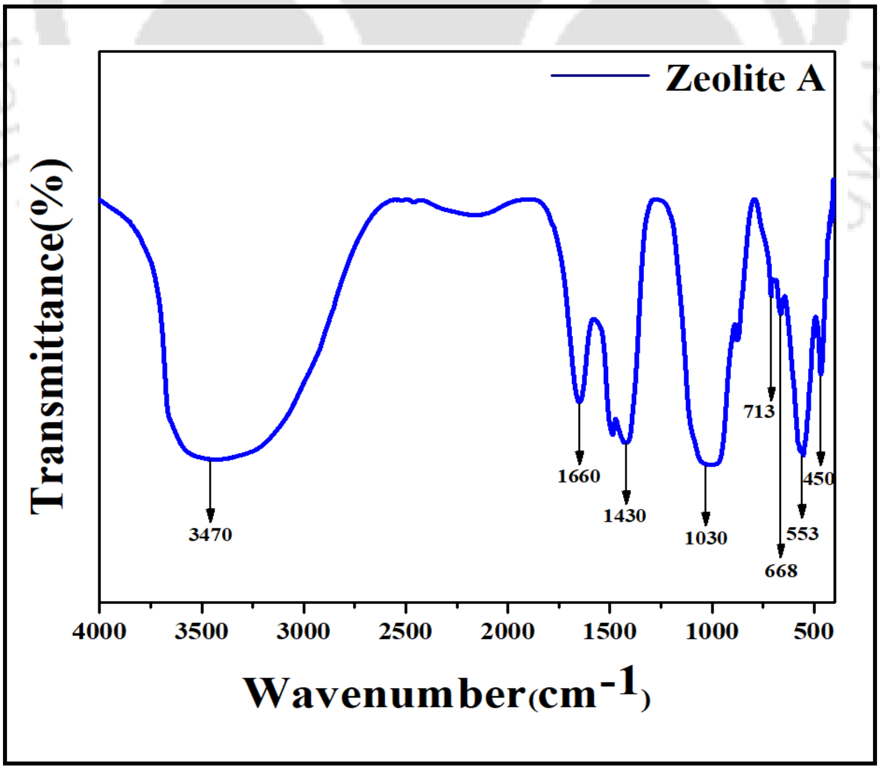

Figure 2.3: FTIR spectrum of zeolite A.

2.6.2.3. FESEM analysis

The structural morphology of the synthesized product was analyzed by FESEM and FETEM. FESEM images of the prepared sample and spent sample have been shown in Figure 2.4a, from which it was clear that the geometric structure of the obtained zeolite was cubical (inset Figure 2.4a). The crystalline cubical structure of the resultant sample can be identified as zeolite A [8]. Figure 2.5a depicts the surface texture of the spent sample after the adsorption study. It was revealed that the adsorbent shrank, and agglomeration occurred after the adsorption reaction. Somewhere brittle type sample was also found. The agglomerated form may be due to the presence of adsorbate particles on the zeolite surface. Figures 2.4b and 2.5b illustrated the TEM images of the prepared and spent sample. Figure 2.4b revealed the same cubical shape structure and a well-organized zeolite framework. However, more agglomerated species were found in Figure 2.5b. The HRTEM analysis for both samples revealed that the synthesized and used sample formed a polycrystalline structure in nature, i.e., crystalline and amorphous structures co-existed in the samples.

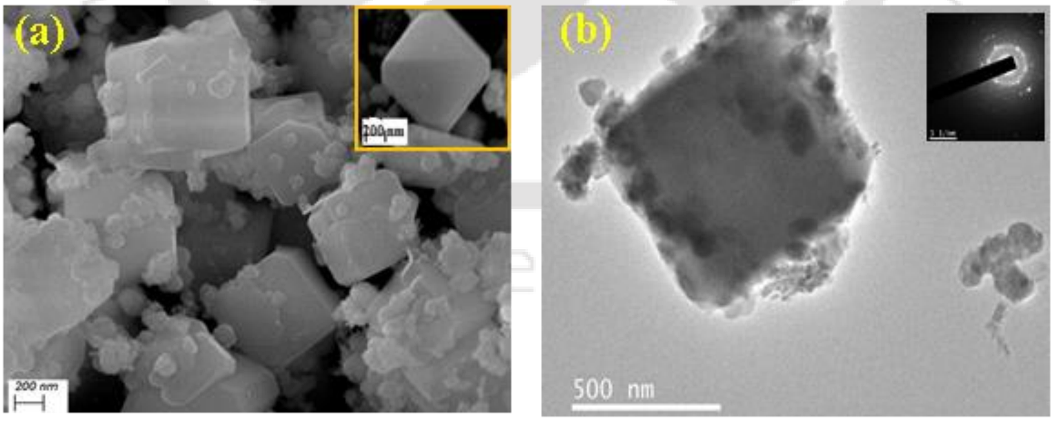

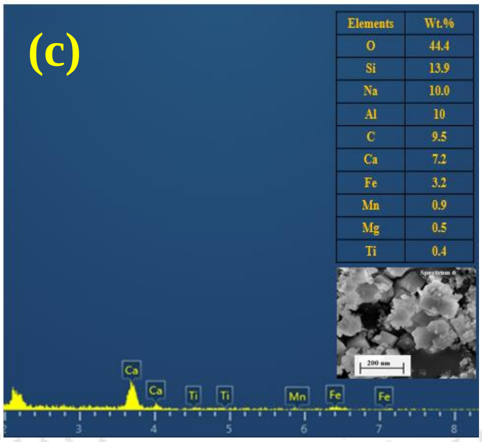

Elements	Wt.%
O	44.4
Si	13.9
Na	10.0
Al	10
C	9.5
Ca	7.2
Fe	3.2
Mn	0.9
Mg	0.5
Ti	0.4

Figure 2.4: (a) FESEM (b) TEM, and (c) EDX analysis of the prepared zeolite A.

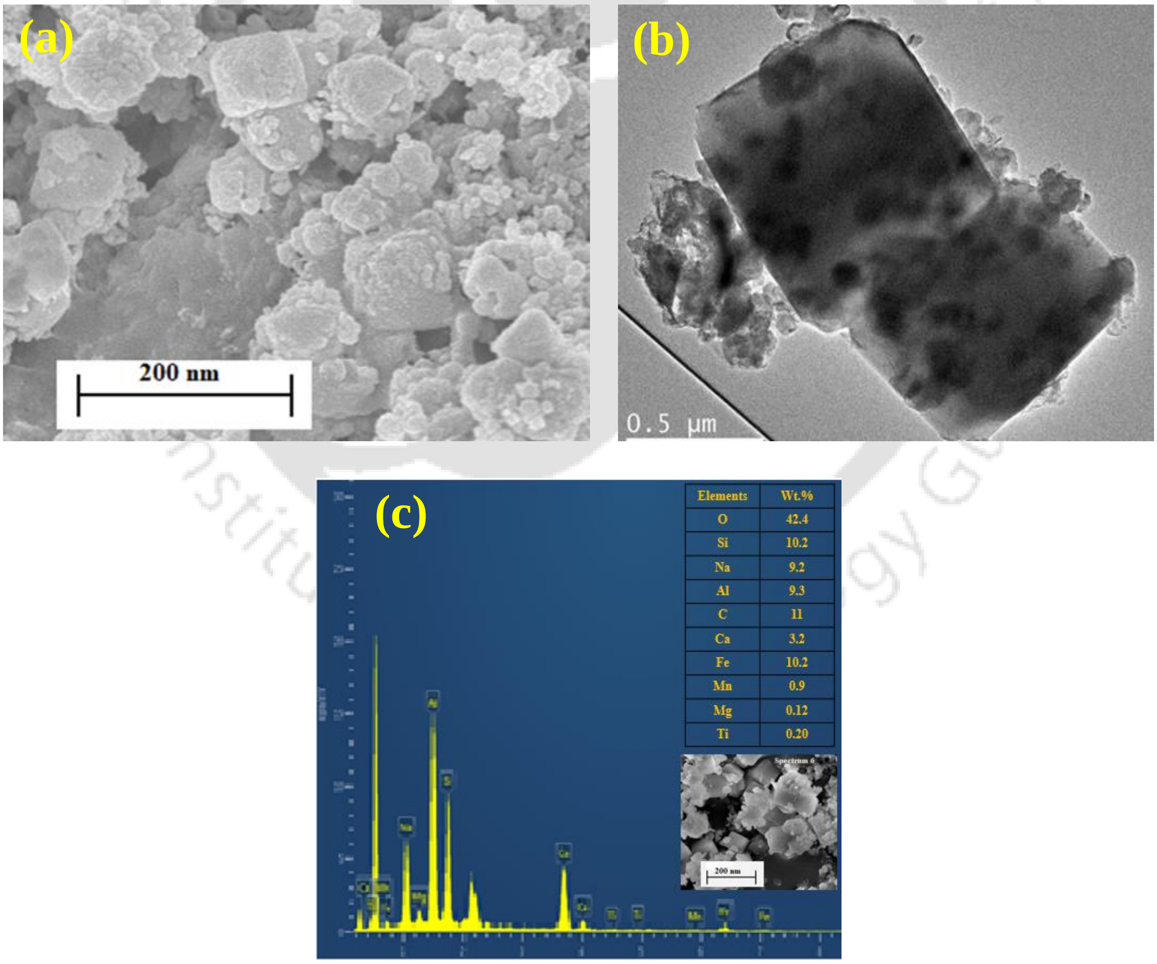

Elements	Wt.%
O	42.4
Si	10.2
Na	9.2
Al	9.3
C	11
Ca	3.2
Fe	10.2
Mn	0.9
Mg	0.12
Ti	0.20

Figure 2.5: (a) FESEM (b) TEM, and (c) EDX analysis of zeolite A after iron removal study.

2.6.2.4. EDS analysis

The elemental analysis of synthesized zeolite A before and after the adsorption study was examined through energy-dispersive X-ray spectroscopy (EDS) equipped with the scanning electron microscope (FESEM-EDS), shown in Figure 2.4c and 2.5c, respectively. Results obtained for elements like Al, Fe, Mg, Na, Ca, O, and Si showed that oxygen (O) was present in abundance amount in the product sample. Also, it was shown that the weight percentage of Si was more than Al, which maintains the Si/Al ratio near about 1.1. From the Si/Al ratio, it was identified as type A zeolite [8]. Also, the Si/Al ratio of the sample after adsorption was found to be fixed, but the amount of Fe (wt.%) increased as shown in Figure 2.5c, which suggested that Fe^{3+} was adsorbed on the adsorbent surface.

2.6.2.5. BET analysis

The nitrogen adsorption and desorption isotherm for synthesized type A zeolite with surface area and pore size analysis results were reported in Figure 2.6a. A comparison study for BET surface area, micropore surface area, and pore volume of zeolite A has been tabulated in Table 2.3. By investigating more closely Figure 2.6a then, it showed us a hysteresis loop. It is undeniable that adsorption-desorption isotherm, followed by zeolite A is almost similar to the IUPAC Type II isotherm curve, from which we can recognize it as a mesoporous sample [8]. The pore size distribution calculated with Barrett-Joyner-Halenda's (BJH) equation is shown in Figure 2.6a, inset. It was observed that the pore size for prepared zeolite was between 2-5 nm. So, the result confirmed mesoporous type zeolite was formed after the hydrothermal process.

In this present study, the BET-surface area of LD-slag-based zeolite A exhibits a substantially high value because, during zeolite preparation, a high amount of Sodium aluminate (20-30 wt.% of LD-slag) was added with the modified LD-slag to maintain the Si/Al ratio in the zeolite structure. It is also suggested that the addition of aluminium atoms offers nucleation sites that favour the formation of zeolite structure and pore formation in the zeolite network [14]. The BET-surface area of prepared zeolite A was measured to be 15.1025 m^2/g.

2.6.2.6. TGA analysis

Many authors have performed experiments with raw LD-slag and reported a weight loss of about 5 to 6% due to moisture evaporation from the external surface [6]. The TGA-DTA curve of LD-slag-based zeolite A is presented in Figure 2.6b. The thermographs revealed that moisture loss from LD-slag-based zeolite A was started between 35 and 50°C, and continued up to shortly above 900°C. In the three-stage TGA curve, the first was caused by the evolution of bound water (130-266°C) and the second by strongly bound water (266-500°C). The percentage weight loss of moisture was observed at 17.80% from the component. The thermograph of cubical-type zeolite A indicated the desorption of physically adsorbed water inside the zeolite pores in the temperature range of 35-945°C [15].

The DTA curve (at inset) of zeolite shows one prominent endothermic signal and one strong exothermic peak between (150 and 370°C).

2.6.2.7. Isoelectric point (zeta potential)

The isoelectric point or zero point is known as the pH of the sample at which the surface charge of a sample becomes zero, i.e., molecules of the sample carry no charge on its surface, or we can say electrically neutral at that pH. For this experiment, six different pH samples were prepared with zeolite A and distilled water by adjusting them with 0.1M HCl and NaOH solution. We measure the zeta potential of those samples and plot the result, shown in Figure 2.6c, to get the isoelectric point of the zeolite A. From the plot, one can easily understand the isoelectric point of the sample is 6.3, i.e., below 6.3 pH; it will carry a positive charge while above 6.3 pH will result in carrying a negative charge.

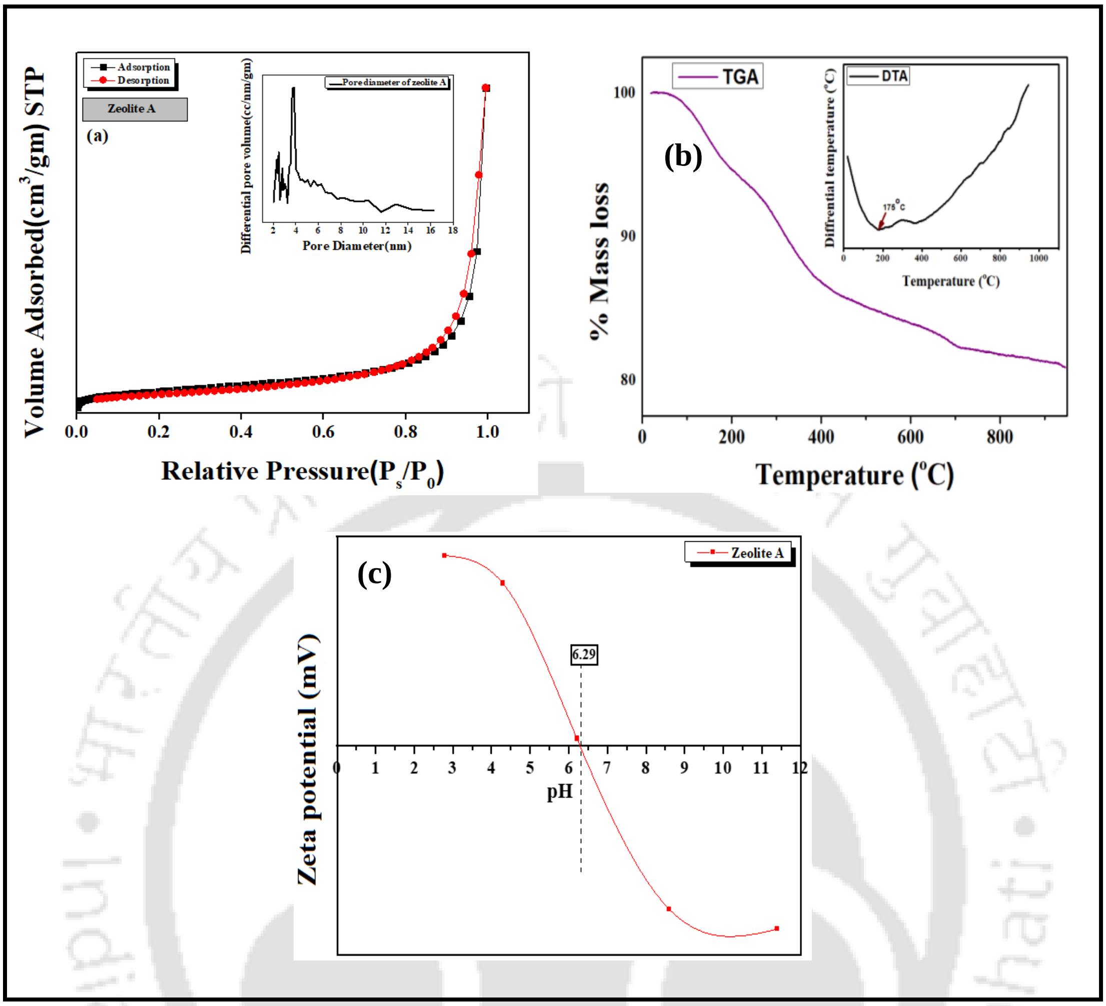

Figure 2.6: (a) N_2 adsorption/desorption isotherm of synthesized zeolite A (b) BJH pore size distribution of zeolite, prepared by alkali fusion assisted hydrothermal treatment (c) Isoelectric point of zeolite A.

2.7. Stability analysis of synthetic zeolite A

Generally, industrial wastewater contains a variety of chemicals depending on the types of industries, which results in wastewater with a wide range of pH. To analyze the stability of the synthesized zeolite A in different pH conditions, an experiment was performed by keeping the zeolite sample in a variety of pH for varying periods. In each pH of 2 (highly acidic), 7 (moderate), and 12 (highly basic) zeolite samples were kept for 1 day, 2 days, and 3 days to check the stability. Characterization of these samples was done by XRD, FTIR, and FESEM analysis.

Table 2.3: Textural analysis of zeolite A with other synthesized zeolite.

Sample	BET surface area (m^2 g^{-1})	Micropore surface area (m^2 g^{-1})	Micropore volume (cm^3 g^{-1})	Reference
Commercial zeolite 4A	7.3738	0.6201	0.000227	[16]
Zeolite A	3	0.5	0.001	[17]
Zeolite A	13.37	3.37	0.0011	[11]
Zeolite A	11.9	-	-	[18]
Synthesized zeolite A	**15.1025**	**0.1748**	**0.000038**	**Present work**

2.7.1. Powder XRD

The XRD patterns of the resultant zeolite A samples were represented in Figure 2.7 (a, b, and c). Zeolite, kept in a highly acidic nature, showed a small reduction in the intensity of peaks on the first day, but on the second day and third days, there was some major reduction of peak intensities of zeolite A and also (1 0 0), and (1 1 0) planes (responsible for zeolite framework) intensity reduced, i.e., some crystal morphology is changing at this point Figure 2.7g. All samples were subjected to XRD analysis in the range of 4-10°. According to the XRD pattern displayed in Figure 2.8, the distinct peak was reached at 7.18°. The (1 0 0) crystalline plane, which refers to the cubical topology of the material, is shown by the first peak in the XRD pattern of zeolite A at 7.18° [1]. The same geometry was observed in the FESEM analysis, as shown in Figure 2.4a. The breakdown of the tetrahedral unit in the zeolite cage might be because of dealumination, which occurs due to its exposure to the highly acidic medium for over 3 days of treatment. The dealumination procedure was carried out in an acidic solution, resulting in the formation of novel groups such as Si-OH and Al-OH, which would increase with treatment time, potentially lowering the crystallinity of the zeolite framework. At low pH, a similar pattern can be seen, as illustrated in Figure 2.8b. The figure shows that the equivalent peak at 7.18° has disappeared, implying that the material changes to an amorphous character after 3 days of treatment. However, samples kept at pH 7 showed a negligible reduction of peak intensities of zeolite A with the variation of time, i.e., there might be a small change in the crystalline phase. For pH 12, the intensity of peaks remains almost the same as the originally synthesized zeolite A with almost no change in the crystalline plane. After verifying the peaks in Figure 2.7 (a, b, and c) with the initially prepared product, we conclude that zeolite A is stable for a long time in a higher pH range, but in a lower pH range is stable for a short period.

2.7.2. FTIR spectroscopic analysis

FTIR patterns of the synthesized zeolite A in different pH were shown in Figure 2.7d-f. A consecutive reduction in the absorption bands at around 460 cm^{-1} and 701 cm^{-1} is attributed to Si-O-Al, SiO_4, and AlO_4 respectively, and becomes negligible with time for a lower pH. This was because bonds at 450 cm^{-1} broke down completely after 1 day, and the metal hydroxide bond intensity decreased maybe because of the H^+ ion present in acidic conditions reacting with the OH^- ions and the oxygen released from the Si-O and Al-O group. It may be assumed that, with increasing pH, the metal hydroxide group is becoming sharp, because the OH^- ions present in the base solution contribute to form bonds with metal ions of zeolite A. FTIR pattern in pH 12 and pH 7 shows a comparatively good result and almost every band were present in the sample. The stability analysis reported good results at higher pH, but it is not stable for a longer time in the lower pH range.

2.7.3. Surface analysis

To check the structural and geometrical stability, synthesized zeolite A was kept at different pHs for 3 days. SEM images of those samples were presented in Figure 2.7g-i. It was observed that zeolite A shrank due to the breaking of the Si-O-Al bond when it was kept at an extremely acidic solution (pH 2) for 3 days of treatment time, as shown in Figure 2.7g. The possible reason may be that at the above-mentioned pH, the dealumination occurs in the zeolite framework and as a consequence, the formation of a silanol group (Si-OH) creates an internal pressure that allows water molecules to flow from β-cage to α-cage. Furthermore, Na^+ ions in the zeolite cage attract OH^- ions, which make up NaOH and migrate out with water molecules, resulting in the breakdown or shrinking of the tetrahedral unit of the zeolite framework [19]. Also, an uneven distribution of crystal size was noted in the product sample. Zeolite A kept at pH 7, showed no major changes in the crystal structure, which is also syncing with the XRD and FTIR results in Figure 2.7a-c and 2.7d-f, respectively. There were no significant changes in the structural properties in highly basic conditions, i.e., the geometrical structure was cubical only. This cubical-shaped zeolite is also known as double 4 rings (D4R) structure zeolite. In acidic conditions, most of the metal hydroxides and metal oxides completely broke down and reacted with H^+ ions present in the acidic condition. This might be the reason behind the fractures present in the crystal surface at lower pH.

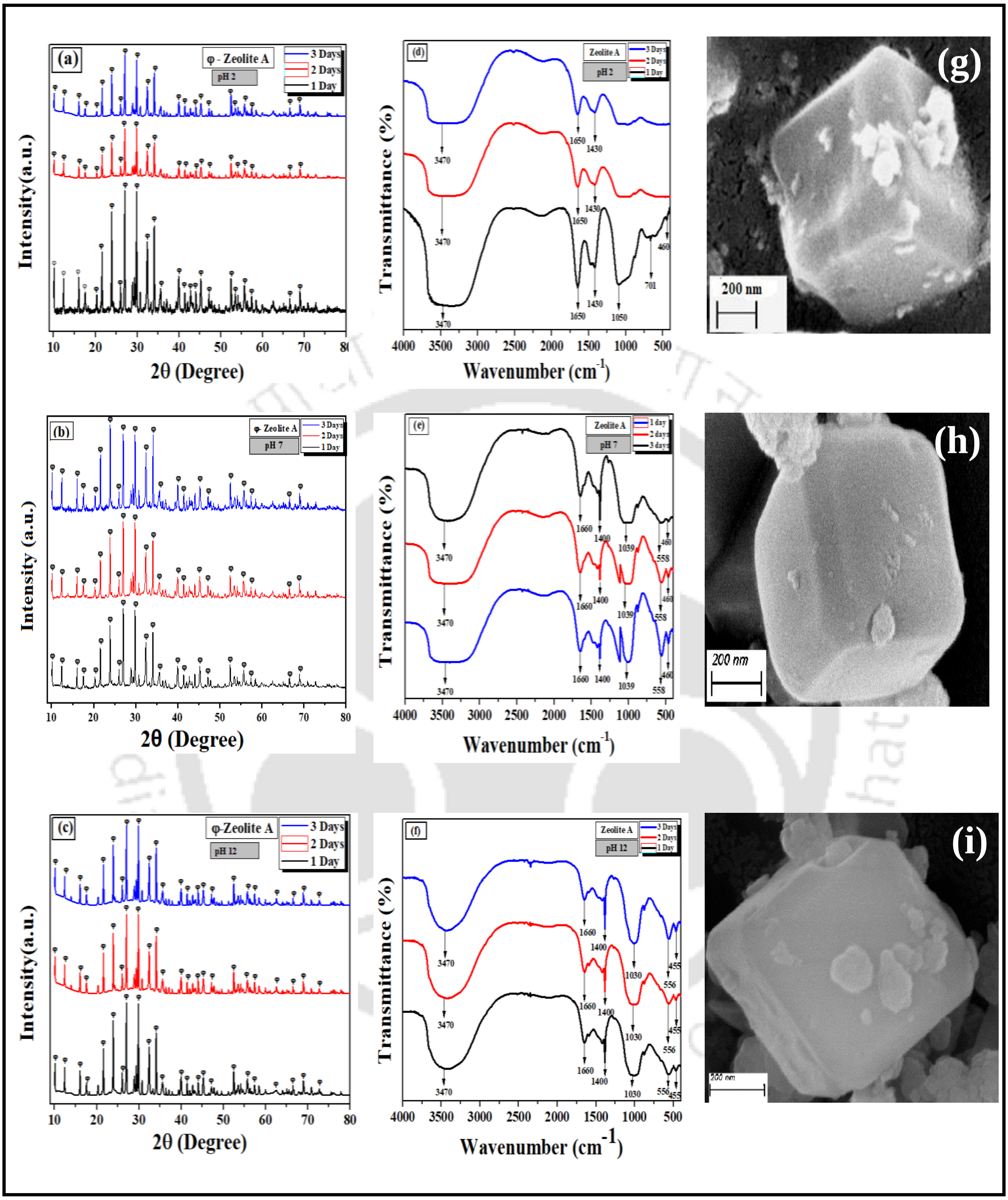

Figure 2.7: XRD analysis of zeolite A at (a) pH 2 (b) pH 7 (c) pH 12. FTIR analysis of zeolite A at (d) pH 2 (e) pH 7 (f) pH 12. FESEM images of zeolite A at (g) pH 2 (h) pH 7 (i) pH 12.

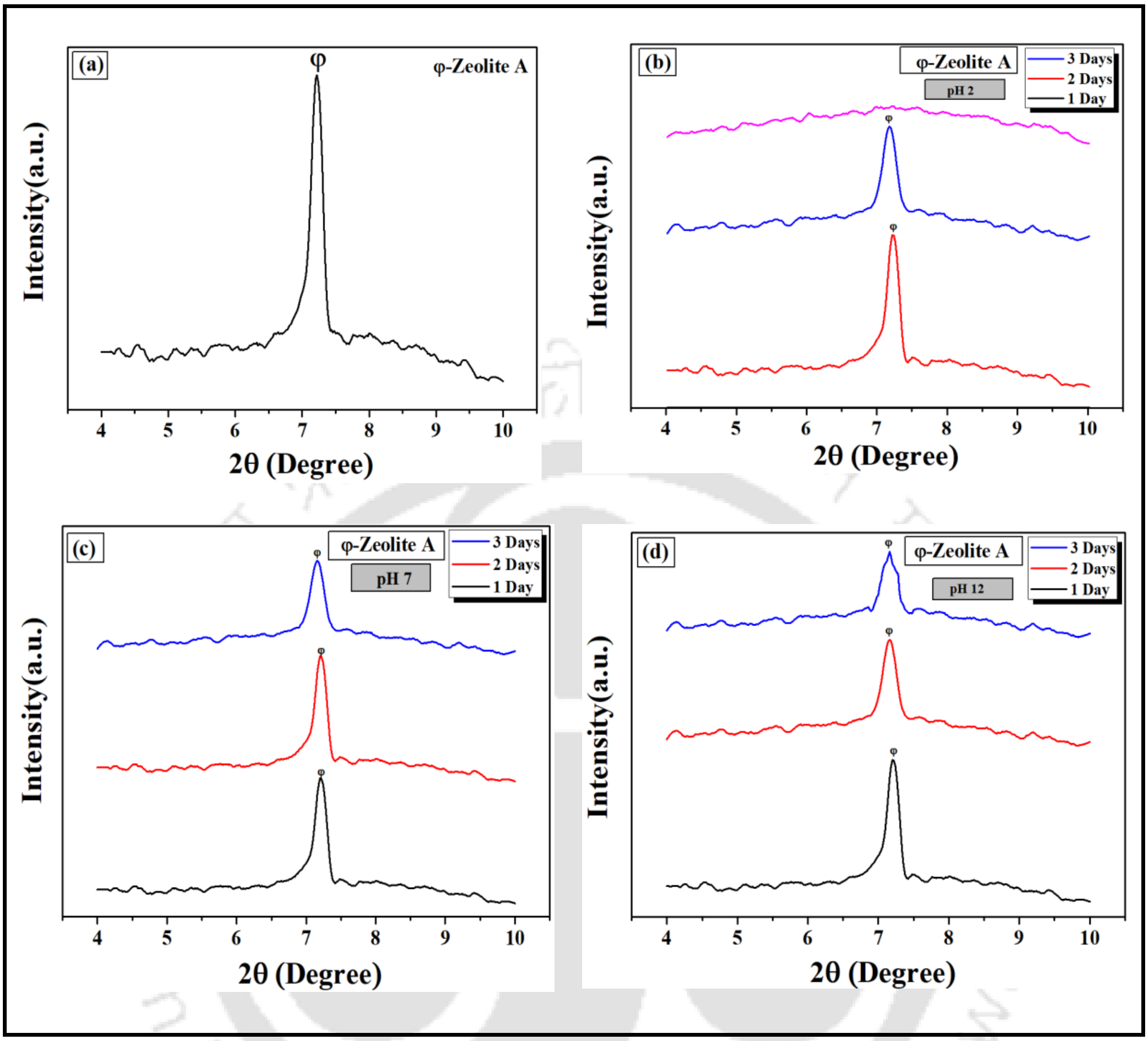

Figure 2.8: (a) XRD pattern of synthesized zeolite A at 2θ range of 4-10°. (b)-(d) XRD pattern of synthesized zeolite A at 2θ range of 4-10° at pH 2, pH 7, and pH 12, respectively.

2.8. Adsorption optimization

The adsorption capacity of Fe^{3+} on raw LD-slag and synthesized LD-slag-based zeolite A was investigated to compare the adsorption rates, with varying times by keeping other parameters constant. From Figure 2.9a, it is undeniable that the rate of adsorption was very rapid for the first 40 to 50 minutes. Nevertheless, after that, the rate of adsorption slowed down gradually and eventually diminished as the adsorption reaches equilibrium at about 90 to 100 minutes. Fe^{3+} adsorption uptake (Q_t) increases with the increase in contact time for both LD-slag and zeolite A. 99.99% adsorption of Fe^{3+} was achieved on zeolite A but, on LD-slag, the rate was a bit low. The initial rate of adsorption on both LD-slag and zeolite A was high because of the high concentration gradient of adsorbate and adsorbent in the test sample [20]. Also, maybe, initially, the active sites present on the adsorbent were high, which accelerated the adsorption rate. With time, these active sites were blocked by the Fe^{3+} molecules. For both LD-slag and zeolite A, it was perhaps difficult for the Fe^{3+} molecules to diffuse deeper on the adsorbent surface beyond the equilibrium point. As the active sites get filled by the Fe^{3+} molecules, surface resistance increases, which neglects the influence of contact time.

The Fe^{3+} adsorption capacity of zeolite A was studied with various adsorbent doses of 0.01 g, 0.02, 0.03, 0.04, 0.05, 0.06, and 0.07 g to find the optimum adsorbent dosage. Other operating parameters such as initial concentration, temperature, and contact time were kept constant. From Figure 2.9b it is very clear that percentage removal increases with an increase in adsorbent dosage, while Fe^{3+} adsorption uptake (Q_e) get decreases rapidly. The experimental result showed an increase in adsorption capacity from 55.11 to 99.99% by increasing the adsorbent dosage from 0.01 to 0.05 g. At a higher dosage of adsorbent quantity, more active sites were present for the Fe^{3+} ion. The adsorption capacity was decreased from 27.55 to 7.14 mg/g when the adsorbent dosage increases from 0.01 to 0.07 g. The decay in Fe^{3+} adsorption rate with the increase in adsorbent dosage may be due to unsaturated active sites of adsorbent [21]. This adsorbent dosage optimization is crucial for economical operation. Our present study will carry forward an optimum adsorbent dosage of 0.05 g for the feasibility of the process.

The effect of temperature on zeolite A was examined at 293, 298, 303, and 308K. The adsorption operated for 2 hours (to reach equilibrium) with an adsorbent dose of 0.05 g and an initial concentration of 10 mg/L. The percentage removal improved from 94.25 to 99.95%

as the temperature increased from 293 to 308K, Figure 2.9c. This is maybe due to the increase in surface activity with an increase in temperature, suggesting an endothermic process of adsorption between Fe^{3+} and zeolite A. To make the process feasible, our further study will be operated at 303K.

The effect of initial Fe^{3+} concentration on adsorption capacity in the adsorption experiment was investigated and shown in Figure 2.9d. Several different initial concentrations of Fe^{3+} ions were prepared in the range of 10 to 50 mg/L and were examined at 303K with 0.05 g of zeolite A for 12 hours to accommodate enough time to reach the equilibrium state. The effect of higher Fe^{3+} concentrations in the range of 45 to 50 mg/L on adsorption capacity was also studied, as demonstrated in Figure 2.9d. The higher Fe^{3+} adsorption capacity (Q_e) was measured at 27.55 mg/g for a starting concentration of 40 mg/L, according to the figure. However, when the initial Fe^{3+} concentration was raised from 45 to 50 mg/L, the adsorption capacity did not rise and reached equilibrium, indicating that the iron adsorption capacity reaches the saturation point of 27.55 mg/g with an initial Fe^{3+} concentration of 40 mg/L and above. As the initial concentration increased from 10 to 45 mg/L, the rate of adsorption decreases rapidly. However, the net adsorption capacity was higher for 40 mg/L Fe^{3+} concentration. Mass transfer theory can explain this behavior. As the initial concentration increased, the concentration gradient also increased, which helped overcome diffusion resistance on the surface of zeolite A. Also, the interaction between the Fe^{3+} molecule and zeolite A increased with an increase in initial adsorbate concentration. The percentage removal of Fe^{3+} was 99.99% for the initial concentration of 10 mg/L, which reduced to 69.89 to 54.89% for the initial concentration of 40 to 50 mg/L, respectively. The comparison study of Fe^{3+} ion removal using different types of zeolite is provided in Table 2.4, which shows that the prepared zeolite A from waste LD-slag was better than the previously reported works.

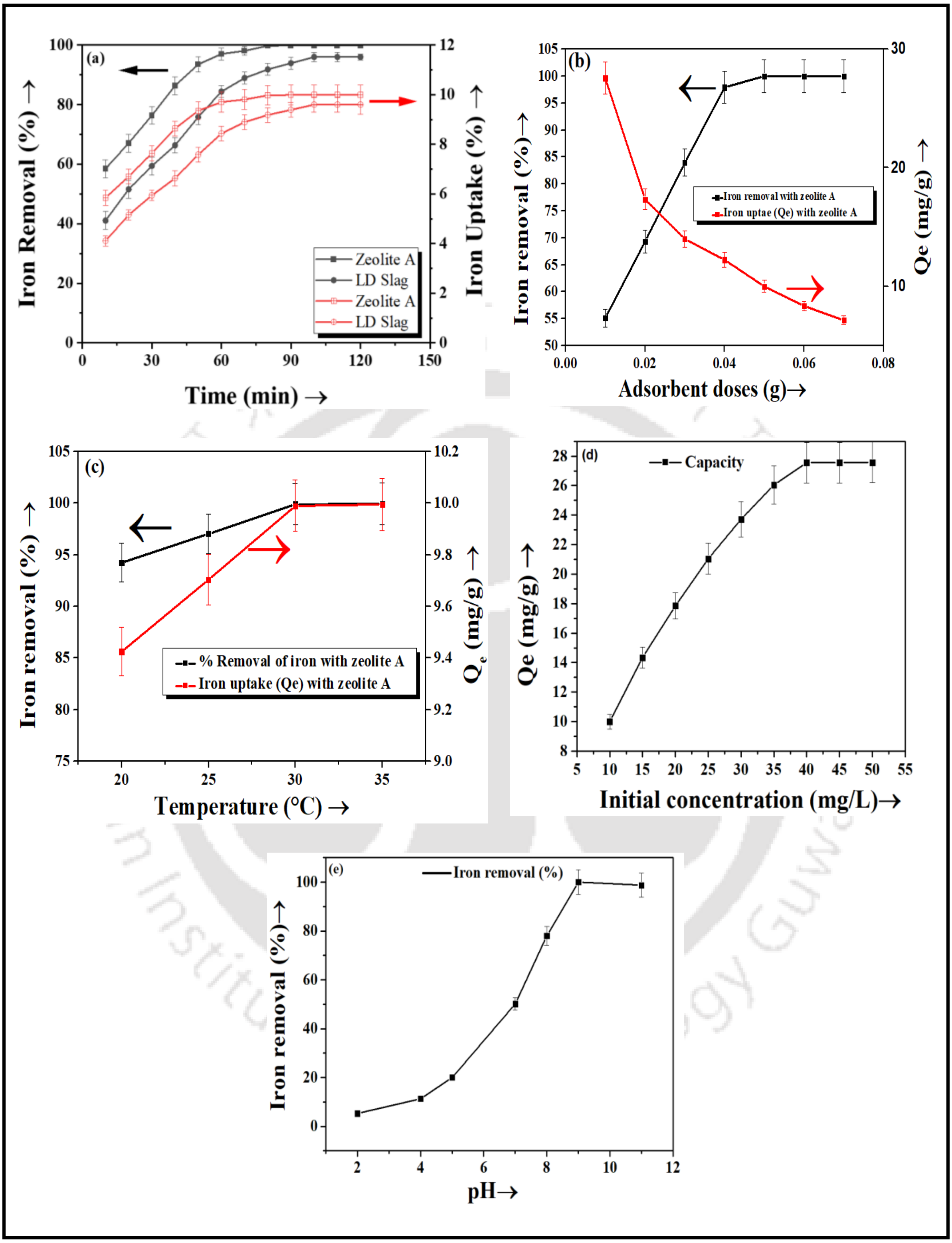

Figure 2.9: (a) Effect of contact time on iron removal (T=30°C, adsorbent dosage=0.05g, initial concentration=10 mg/L) (b) Effect of adsorbent dosage on iron removal (T=30°C, contact time=120 minutes, initial concentration=10 mg/L) (c) Effect of temperature on iron removal (adsorbent dosage=0.05g, initial concentration=10 mg/L, contact time=120 minutes) (d) Effect of initial concentration of adsorbate on iron removal (adsorbent

dosage=0.05g, T=30˚C, contact time=120 minutes) (e) Effect of initial pH on iron removal (T=30˚C, adsorbent dosage=0.05g, initial concentration=10 mg/L).

Table 2.4: Comparison study of iron removal using different types of zeolite.

Zeolite material	Type	Adsorption capacity (mg g^{-1})	Percentage removal (%)	Reference
Zeolite Y	Synthetic	0.220	98.00	[22]
Zeolite A	Synthetic	12.13	99.98	[23]
Zeolite A	Synthetic	20.02	99.00	[24]
Zeolite	Synthetic	8.24	99.34	[6]
Zeolite	Commercial	6.49	74.00	[6]
Zeolite A	Synthetic	5.62	87.60	[25]
Zeolite A	Synthetic	10.02	99.90	[26]
Zeolite A	**LD-slag**	**27.55**	**99.99**	**Present work**

2.8.1. Effect of pH on iron removal

The effect of iron removal with a fixed amount of Fe^{3+} concentration (10 mg/L) and adsorbent dose (0.05 g) varying with pH has been illustrated in Figure 2.9e. It's well known that for every adsorption process, the zero point charge (pH_{zpc}) is considered an essential parameter. It was observed that the removal efficiency of Fe^{3+} ion increased with pH from acid to basic condition. However, the highest Fe^{3+} removal was found at pH 9. The reason could be when pH falls below pH_{zpc} (6.45 in this study), the adsorbent site gets protonated, resulting in an excess positive charge on the adsorbent surface which leads to a repulsive tendency between adsorbate-adsorbent molecules [27]. On the contrary, the zeolite surface carried an excess negative charge at pH level more than the pH_{zpc} which develops a good adherence of positively charged Fe^{3+} ion towards the zeolite surface and shows a good removal efficiency of the synthesized zeolite.

2.9. Adsorption model design

2.9.1. Adsorption kinetics

Adsorption kinetic study is critical to explain the controlling mechanism, which is a fundamental parameter for mass transfer of Fe^{3+}, adsorption rate, and as well as equilibrium contact time for adsorption. Two models, pseudo-first-order and pseudo-second-order, were applied to investigate the kinetics of the Fe^{3+} adsorption process by zeolite A. The pseudo-first-order model assumed that the change in Fe^{3+} adsorption rate is directly proportional to the deviation between the saturated concentration and the quantity of Fe^{3+} uptake with time. The pseudo-second-order was used to find out the nature of the adsorption process. Typically, the linear equation for both models can be expressed as equations (2.9) and (2.12), respectively

$$Q_t = Q_e(1 - e^{-k_1 t}) \tag{2.9}$$

Or,

$$\ln (Q_e - Q_t) = \ln Q_e - K_1 t \tag{2.10}$$

$$Q_t = \frac{Q_e^2 K_2 t}{(1 + Q_e K_2 t)} \tag{2.11}$$

Or,

$$\frac{t}{Q_t} = \frac{1}{K_2 Q_e^2} + \frac{t}{Q_e} \tag{2.12}$$

Where K_1 (1/min) and K_2 (g/mg min) are the reaction rate constant for pseudo-first-order and pseudo-second-order models, respectively. Q_t (mg/g) and Q_e (mg/g) are the Fe^{3+} adsorption capacity of zeolite A, at any time t (minute) and equilibrium state, respectively. The kinetic parameters of the pseudo-first-order and pseudo-second-order model were calculated from the linear plot of ln(Q_e-Q_t) vs. t (Figure 2.10a) and ($\frac{t}{Q_t}$) vs. t, respectively (Figure 2.10b), and listed in Table 2.5, from which, it was clear that, at different concentrations of Fe^{3+}, the pseudo-second-order model had a higher correlation coefficient (R^2 = 0.99) than the pseudo-first-order model (R^2 = 0.87), along with lower error values. Moreover, the pseudo-second-order model had a better agreement for $Q_{e(exp)}$ with $Q_{e(cal)}$ obtained from the plot. From the results in Table 2.5, it was apparent that pseudo-second-order can explain all the adsorption data and represent the process that involves chemisorption. On the other hand, the pseudo-first-order model is limited to the initial time range only, which resulted in a poor fit of the adsorption data and deviation in the $Q_{e(cal)}$ and $Q_{e(exp)}$ [28].

2.9.2. Adsorption mechanism

To understand the adsorption of Fe^{3+} on solid zeolite A, it is imperative to gather some knowledge about the adsorption mechanism. Usually, the adsorption process can be illustrated in several steps: (i) diffusion of the target material from the bulk solution to the film surrounded by the adsorbent surface; (ii) diffusion through the film (film diffusion) to the external solid surface of the adsorbent; (iii) penetration within the pores (pore diffusion) and (iv) sorption and desorption of the target material within the pores and solid surface [18,29]. Steps (ii) and (iii) are responsible for the rate determination of the adsorption process because these two steps are considered the slowest steps. Whereas the other two are rapid steps. The Weber–Morris intraparticle diffusion [30], Boyd model [31], and Diffusion-Chemisorption models were employed to investigate the diffusion mechanism.

Webber-Morris intraparticle diffusion model was used to predict the transport property of Fe^{3+} from the bulk solution to the solid surface film, and it can be expressed as equation (2.13):

$$Q_t = K_3 t^{0.5} + C \tag{2.13}$$

Where Q_t (mg/g) is the amount of Fe^{3+} adsorbed at any time t, K_3 is the intraparticle diffusion rate constant (mg/g $min^{0.5}$), and C (mg/g) denotes the film thickness of the boundary layer. If a plot between Q_t and $t^{0.5}$ gives a straight line, then the adsorption process would be solely controlled by the intraparticle diffusion mechanism. On the other hand, if the plot exhibits multilinear curve nature, it can be assumed that more than one step influences the adsorption process. The intraparticle diffusion model can be subdivided into three different steps: (a) adsorption of Fe^{3+} through the external surface; (b) intraparticle diffusion, and (c) equilibrium phase build-up where lack of Fe^{3+} concentration in solution will lead to the lower effectiveness of intraparticle diffusion [32]. Here, Figure 2.10c illustrates the Webber-Morris intraparticle diffusion model plot. Two straight lines (i.e. (i) in the time range of 3 to 7 minutes and another (ii) in the 7 - 9 minutes range) were detected in the plot, from which it is pronounced that adsorption of Fe^{3+} is not solely controlled by intraparticle diffusion. The intraparticle diffusion was responsible for the first line segment, while the second line segment implied the building up of the equilibrium phase. As shown in Figure 2.10c, the intercept of the plot did not pass through the origin (i.e. (0, 0) point), which implies that the effect of the boundary layer cannot be neglected over intraparticle diffusion [30]. So it also can be suggested that multistage diffusion is occurring during the adsorption process.

Many authors reported that the Boyd equation could be applied to determine the rate-controlling step for any adsorption process. The equations involved can be expressed as equations (2.14) and (2.15):

$$F = 1 - \left(\frac{6}{\pi^2}\right) \exp(-B_t) \tag{2.14}$$

B_t can be expressed as a mathematical function of F, and F is the fraction of Fe^{3+} adsorbed at any contact time t. The F value can be calculated from the following expression:

$$F = \frac{Q_t}{Q_e} \tag{2.15}$$

Where Q_t and Q_e are the amount of Fe^{3+} adsorbed into zeolite A at any time t and equilibrium state, respectively. The B_t values for several times (t) can be calculated from equation (2.16):

$$B_t = -0.4977 - \ln(1 - F) \tag{2.16}$$

The Boyd model suggested that if a linear plot of B_t vs. t (minute) passes through the origin, then the adsorption process is controlled by the particle diffusion method, else film diffusion can be considered as a rate-determining step for the process [30]. A plot between B_t and t (minute) is reported in Figure 2.10d, which shows that the line did not pass through the origin, which suggested that the process is film diffusion controlled.

The diffusion-Chemisorption model was used to describe the Fe^{3+} adsorption on heterogeneous adsorbent zeolite A. The model can be expressed as equation (2.17):

$$\frac{t^{0.5}}{Q_t} = \frac{1}{K_4} + \frac{t^{0.5}}{Q_e} \tag{2.17}$$

Where K_4 is known as the diffusion-chemisorption constant. A plot between $\frac{t^{0.5}}{Q_t}$ vs $t^{0.5}$ is reported in Figure 2.10e to explain the diffusion-chemisorption model and all the kinetic parameters are tabulated in Table 2.5. The R^2 value obtained from the diffusion-chemisorption model confirmed the adsorbate molecules (Fe^{3+} ions) are diffused into the zeolite A pore channel. It is also suggested that positively charged Fe^{3+} ions are attracted on a highly negative charge-contained zeolite A surface due to electrostatic force [30]. After comparing the correlation coefficient values from Table 2.5, for the above three models, it is reasonable to consider the diffusion-chemisorption model ($R^2 = 0.98$) would be most suitable to illustrate the Fe^{3+} adsorption process mechanism.

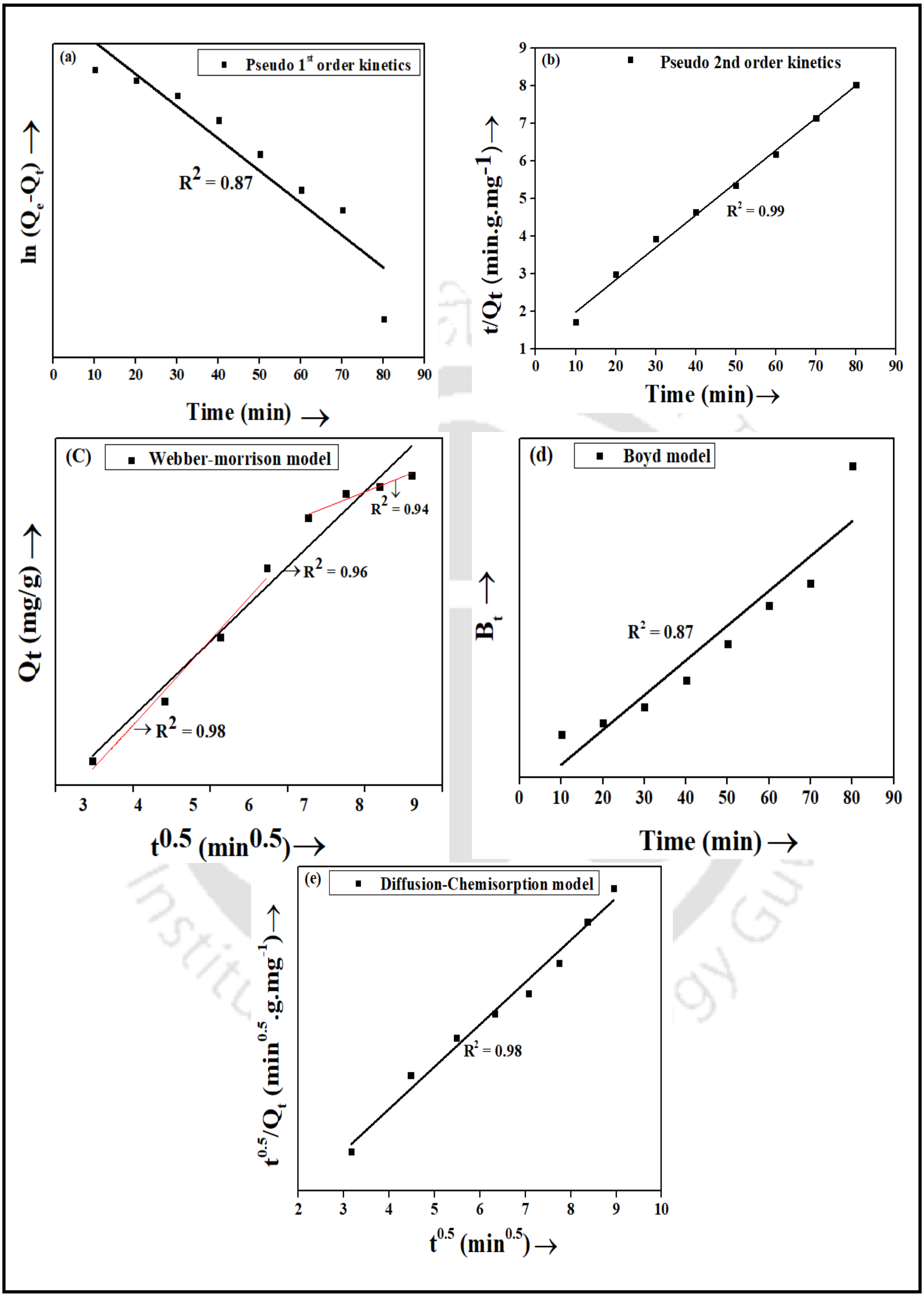

Figure 2.10: Adsorption kinetic models (a) pseudo-first-order (b) pseudo-second-order (c) Webber-Morrison intra-particle diffusion model (d) Boyd model (e) Diffusion-Chemisorption model at(adsorbent dosage=0.05g, contact time=120 minutes, initial concentration=10 mg/L, T=30˚C).

Table 2.5: Adsorption model parameters at (adsorbent dosage=0.05g, Initial concentration=10 mg/L, contact time=120 minutes, T=30˚C).

Adsorption process modelling Parameters		
Model	**Parameters**	**Values**
Weber–Morris intra-particle diffusion	K_3 (mg/g min$^{0.5}$)	0.78
	C (mg/g)	3.48
	R^2	0.96
Boyd	Slope	0.072
	Intercept	-0.96
	R^2	0.87
Diffusion-Chemisorption	$Q_{e(exp)}$(mg/g)	9.99
	$Q_{e(cal)}$(mg/g)	18.22
	K_4(mg/g min$^{0.5}$)	2.55
	R^2	0.98
Langmuir isotherm	Q_m (mg/g)	28.63
	K_L (L/mg)	1.192
	R_l	0.08
	R^2	0.99
Freundlich isotherm	K_F ((mg/g)(L/mg)$^{1/n}$)	18.73
	n	9.63
	R^2	0.84
Temkin isotherm	B	2.97
	A (L/g)	16.14
	B (J/mole)	848.36
	R^2	0.72
Pseudo-first-order	$Q_{e(exp)}$ (mg/g)	9.99
	$Q_{e(cal)}$ (mg/g)	15.88
	K_1 (1/min)	0.072
	R^2	0.87
Pseudo-second-order	$Q_{e(exp)}$(mg/g)	9.99
	$Q_{e(cal)}$ (mg/g)	11.6
	K_2 (g/(mg min))	0.006
	R^2	0.99

2.9.3. Adsorption isotherm study

The graphical representation of Fe^{3+} adsorption capacity at the equilibrium of LD-slag-based zeolite A has been shown in Figure 2.11, where zeolite A showed a superior Fe^{3+} adsorption capacity. It was expected that the zeolite surface has a high negative surface charge density (-

56.7 mV), which causes the Fe^{3+} ion to have an electrostatic affinity on the zeolite surface. Moreover, the low Si/Al ratio in zeolite A causes the surface to be hydrophilic, which leads to good interaction between zeolite surface and iron molecule in aqueous media, which again consequently may influence a better removal efficiency of the synthesized zeolite [4]. To gather insight into the adsorption isotherm, the experimental Fe^{3+} adsorption update data (i.e., Q_e, mg/g) has been correlated with the equilibrium concentration (C_e, mg/L) data at a fixed temperature of 303K. The Langmuir [33], Freundlich [30], and Temkin [16] adsorption isotherm model was used to study the isotherm nature of the Fe^{3+} adsorption process on zeolite A.

The Langmuir adsorption isotherm model assumes that one adsorbate molecule will only occupy one active site on the adsorbent surface, i.e., maximum adsorption is related to a saturated monolayer of adsorbate molecule on the active site of the adsorbent. The homogeneous surface-based Langmuir isotherm [20] can be explained by equation (2.19):

$$Q_e = \frac{Q_m K_L C_e}{1+K_L C_e} \tag{2.18}$$

Or,

$$\frac{C_e}{Q_e} = \frac{1}{Q_m K_L} + \frac{C_e}{Q_m} \tag{2.19}$$

Where Q_e (mg/g) and C_e (mg/L) are the amount of Fe^{3+} ions adsorbed, and the Fe^{3+} concentration at equilibrium state, Q_m (mg/g) is the maximum amount of Fe^{3+} adsorbed, K_L (L/mg) is the Langmuir rate constant which describes the affection of active sites and the free energy of biosorption. A linear plot between $\frac{C_e}{Q_e}$ and C_e has been reported in Figure 2.11a. The isotherm parameters obtained from the plot are tabulated in Table 2.5. The Langmuir monolayer adsorption capacity was calculated from the slope of the plot (i.e., Q_m = 28.63 mg/g) at 303K with 0.05 g zeolite A loading. The affinity between the adsorbent and adsorbate has been established by a separation factor (R_l) which was expressed in equation (2.20) [33]:

$$R_l = \frac{1}{1+K_L C_0} \qquad (2.20)$$

The value of R_l describes the nature of adsorption isotherm, whether the isotherm either linear ($R_l = 1$), favourable ($0 < R_l < 1$), unfavourable ($R_l > 1$), or irreversible for $R_l = 0$. In the present study, the value of the separation factor ($R_l = 0.08$) is between 0 and 1, which indicates the adsorption of Fe^{3+} on zeolite A is favourable.

The Freundlich isotherm model is not limited to monolayer adsorption. This model is useful to describe non-ideal heterogeneous adsorption systems. Many functional groups may present on the adsorbent surface, which causes the non-ideal heterogeneous nature of any system. The Freundlich isotherm model was expressed by equation (2.22).

$$Q_e = K_F C_e^{\frac{1}{n}} \qquad (2.21)$$

Or,

$$\ln Q_e = \ln K_F + \frac{1}{n} \ln C_e \qquad (2.22)$$

Where, Q_e (mg/g) and C_e (mg/L) are the concentration of Fe^{3+} adsorbed and the Fe^{3+} concentration at the equilibrium state, respectively. K_F ((mg/g)(L/mg)$^{1/n}$) is the Freundlich rate constant that describes the adsorption capacity and n is another rate constant. A plot of ln(Q_e) vs. ln(C_e) is shown in Figure 2.11b and all the isotherm parameters are tabulated in Table 2.5. The R^2 value from the Freundlich isotherm was 0.84, so the curve is not well fitted. It also suggests that no physisorption is involved in this adsorption process. The obtained 'n' value of 9.63 from the Freundlich model ranges from 1 to 10, which means that the only adsorption phenomenon taking place on the zeolite A surface was synthesized by the fusion-assisted hydrothermal method [17,34]. After comparing the R^2 values for both the isotherm model from Table 2.5, it is evident that the Langmuir isotherm ($R^2 = 0.99$) is better fitted for the adsorption data than the Freundlich isotherm model, which indicates the Fe^{3+} ions are chemically adsorbed on the surface of highly negative charged prepared zeolite due to electrostatic attraction [28].

Figure 2.11c depicts the Temkin isotherm model. R^2 value 0.72 from this isotherm suggests that the adsorption isotherm was not purely a chemisorption model. Now the order of equilibrium adsorption models that fitted best to the experimental data was: Langmuir > Freundlich > Temkin

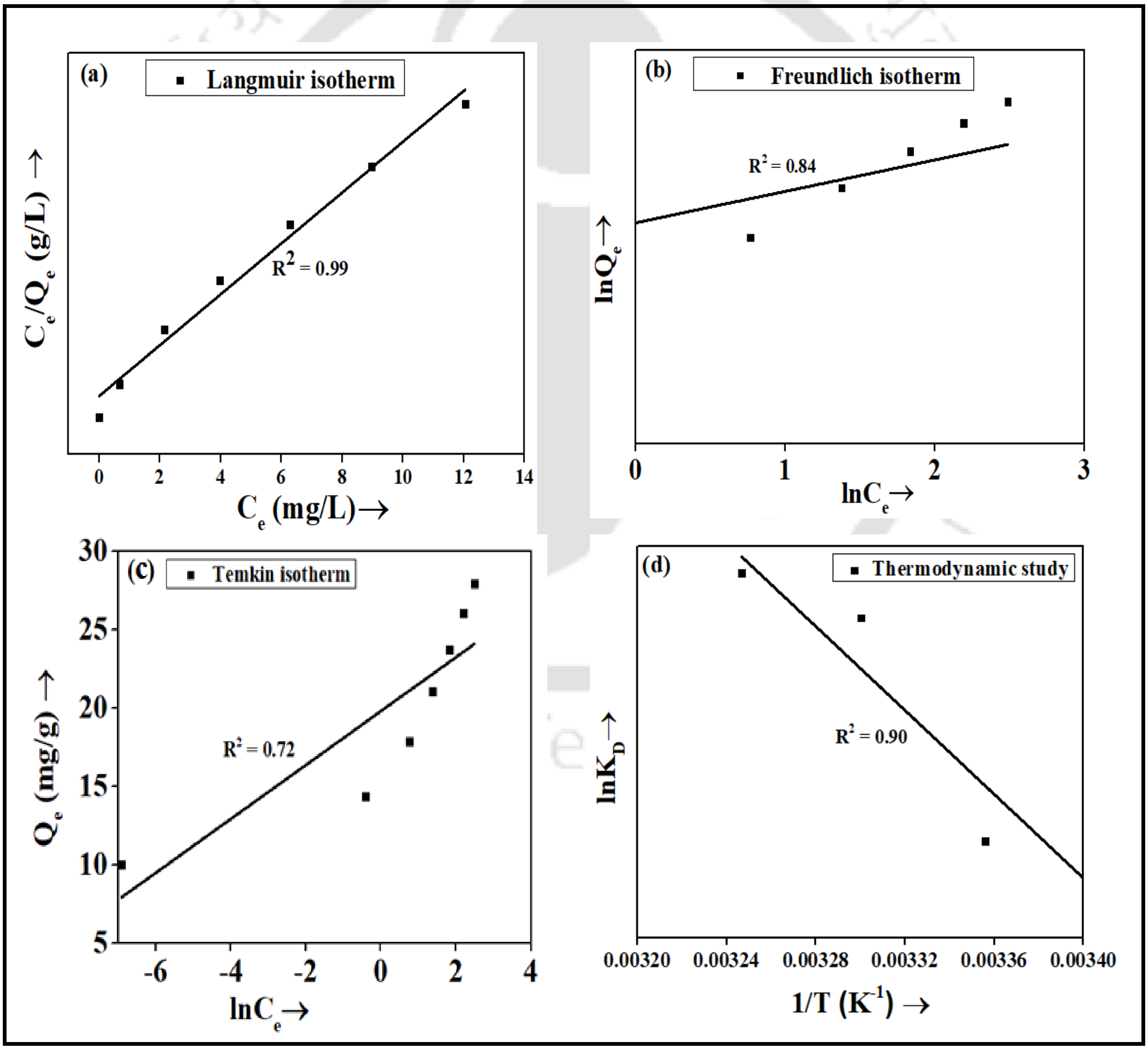

Figure 2.11: Plot of adsorption isotherms for iron on synthesize zeolite A (a) Langmuir (b) Freundlich (c) Temkin model and (d) Thermodynamics study.

2.9.4. Adsorption thermodynamics

In general, the adsorption process is associated with temperature, i.e., the rate of adsorption is dependent on temperature, which can be explained by the thermodynamic properties of the given system. These thermodynamic properties are related to each other by some thermodynamic relations. Those relations are as follows equations (2.23) and (2.24):

$$\Delta G_0 = -RT \ln K_D \tag{2.23}$$

$$\ln K_D = -\frac{\Delta G_0}{RT} = \frac{\Delta S_0}{R} - \frac{\Delta H_0}{RT} \tag{2.24}$$

Where R (8.314 J/mole K) is known as the universal gas constant and T is the solution temperature in K. ΔG_0 is the change in Gibbs free energy, ΔH_0 is known as an enthalpy change in the system, ΔS_0 is the measure of randomness of the system or the change in entropy, K_D is the distribution coefficient for adsorbate, i.e., Fe^{3+} and adsorbent, i.e., zeolite A and can be expressed as equation (2.25):

$$K_D = \frac{Q_e}{C_e} \tag{2.25}$$

Thermodynamic study for Fe^{3+} adsorption on zeolite A, at a temperature of 293, 298, 303, and 308K, have been reported in Figure 2.11d, where $\ln(K_D)$ has been plotted with (1/T). Thermodynamic parameters obtained from the plot in Figure 2.11d have been tabulated in Table 2.6. The change in Gibbs free energy (ΔG_0) values was found to be negative for the Fe^{3+} adsorption process at all temperatures, which suggested that the adsorption process be spontaneous. The ΔS_0 was estimated using the intercept of the plot $\ln(K_D)$ vs (1/T) and a value of 0.94 kJ/mole K was achieved, which indicated the process as an irreversible process. The standard enthalpy change (ΔH_0) was obtained as a positive value, i.e. the Fe^{3+} adsorption on zeolite A is an endothermic process. If we increase the process temperature, the rate of adsorption and equilibrium conversion (for chemisorption only) will also increase.

Table 2.6: Thermodynamic parameters at (adsorbent dosage=0.05g, Initial concentration=10 mg/L, contact time=120 minute).

Thermodynamic parameters					
ΔH_0 (KJ/mole)	ΔS_0 (KJ/mole K)	ΔG_0 (KJ/mole)			
		293K	298K	303K	308K
267.46	0.94	-8.79	-12.66	-17.36	-22.08

2.9.5. Application toward real-life drinking water samples

The prepared zeolite A obtained from waste LD slag when utilized towards the drinking water samples obtained from the IIT Guwahati campus, spiked with various Fe^{3+} concentrations showed promising results. For 2.5 mg/L Fe^{3+} ion solution, the removal percentage was ~97.7% whereas for 5 mg/L, and 10 mg/L the removal percentage decreases to 95.3% and 93.5% respectively when a 1.4 g/L dosage of zeolite A was utilized. The decrease in removal % could be attributed due to the presence of several other ions present in the drinking water which increases the competition between the Fe^{3+} ions and others towards adsorption onto zeolite A. Moreover the active sites for adsorption decreases with an increase in Fe^{3+} ion concentration, hence with increasing Fe^{3+} ion concentration removal percentage decreases. From the obtained results it could be attributed that the prepared zeolite A can efficiently improve the water quality by removing excess Fe^{3+} ions in drinking water which is injurious to human health.

Summary

Steel industry by-product, LD-slag, was found to be a potential candidate for zeolite type-A synthesis via fusion-assisted hydrothermal route. The stability performance of the obtained zeolite was conducted at different pH and treatment periods. The structural deformation was observed at low pH. At neutral and basic pH conditions no structural changes were noticed. The prepared zeolite A was employed as an adsorbent and has shown a significant Fe^{3+} adsorption efficiency from synthetic and Fe^{3+} spiked groundwater sample.

References

[1] S. Mintova, N.H. Olson, V. Valtchev, T. Bein, Mechanism of zeolite A nanocrystal growth from colloids at room temperature., Science. 283 (1999) 958–960. https://doi.org/10.1126/science.283.5404.958.

[2] F. Collins, A. Rozhkovskaya, J.G. Outram, G.J. Millar, A critical review of waste resources, synthesis, and applications for Zeolite LTA, Microporous Mesoporous Mater. 291 (2020) 109667. https://doi.org/https://doi.org/10.1016/j.micromeso.2019.109667.

[3] M. Ghaedi, S. Hajati, M. Zaree, Y. Shajaripour, A. Asfaram, M.K. Purkait, Removal of methyl orange by multiwall carbon nanotube accelerated by ultrasound devise: Optimized experimental design, Adv. Powder Technol. 26 (2015) 1087–1093. https://doi.org/10.1016/j.apt.2015.05.002.

[4] C. Wang, S. Leng, H. Guo, J. Yu, W. Li, L. Cao, J. Huang, Quantitative arrangement of Si/Al ratio of natural zeolite using acid treatment, Appl. Surf. Sci. 498 (2019) 143874. https://doi.org/10.1016/j.apsusc.2019.143874.

[5] J. Pal, P. Chaudhary, M. Goswami, Utilisation of LD slag - An overview, J. Metall. Mater. Sci. 45 (2003) 61–72.

[6] A. bin Jusoh, W.H. Cheng, W.M. Low, A. Nora'aini, M.J. Megat Mohd Noor, Study on the removal of iron and manganese in groundwater by granular activated carbon, Desalination. 182 (2005) 347–353. https://doi.org/https://doi.org/10.1016/j.desal.2005.03.022.

[7] D. Ruen-ngam, D. Rungsuk, R. Apiratikul, D. Ruen-ngam, D. Rungsuk, Zeolite Formation from Coal Fly Ash and Its Adsorption Potential Zeolite Formation from Coal Fly Ash and Its Adsorption Potential, 2247 (2012). https://doi.org/10.3155/1047-3289.59.10.1140.

[8] F. Zamani, M. Rezapour, S. Kianpour, Immobilization of L-Lysine on zeolite 4A as an organic-inorganic composite basic catalyst for synthesis of α,β-unsaturated carbonyl compounds under mild conditions, Bull. Korean Chem. Soc. 34 (2013) 2367–2374. https://doi.org/10.5012/bkcs.2013.34.8.2367.

[9] No Title, (n.d.). http://asia.iza-structure.org/IZA-SC/framework.php?STC=LTA.

[10] V. Volli, M.K. Purkait, Selective preparation of zeolite X and A from flyash and its use as catalyst for biodiesel production, J. Hazard. Mater. 297 (2015) 101–111. https://doi.org/https://doi.org/10.1016/j.jhazmat.2015.04.066.

[11] T. Tepamat, C. Mongkolkachit, T. Wasanapiarnpong, Synthesis of zeolite NaA and activated carbon composite from rice husk, Suranaree J. Sci. Technol. 21 (2013) 119–123.

[12] H. Panda, N. Tiadi, M. Mohanty, C.R. Mohanty, Studies on adsorption behavior of an industrial waste for removal of chromium from aqueous solution, South African J. Chem. Eng. 23 (2017) 132–138. https://doi.org/10.1016/j.sajce.2017.05.002.

[13] P.K. Raul, R.R. Devi, I.M. Umlong, S. Banerjee, L. Singh, M. Purkait, Removal of fluoride from water using iron oxide-hydroxide nanoparticles., J. Nanosci. Nanotechnol. 12 (2012) 3922–3930. https://doi.org/10.1166/jnn.2012.5870.

[14] Y. Gao, B. Zheng, G. Wu, F. Ma, C. Liu, Effect of the Si/Al ratio on the performance of hierarchical ZSM-5 zeolites for methanol aromatization, RSC Adv. 6 (2016) 83581–83588. https://doi.org/10.1039/C6RA17084F.

[15] I. Blanco, P. Molle, L.E. Sáenz de Miera, G. Ansola, Basic Oxygen Furnace steel slag aggregates for phosphorus treatment. Evaluation of its potential use as a substrate in constructed wetlands., Water Res. 89 (2016) 355–365. https://doi.org/10.1016/j.watres.2015.11.064.

[16] P. Wang, Q. Sun, Y. Zhang, J. Cao, Synthesis of zeolite 4A from kaolin and its

adsorption equilibrium of carbon dioxide, Materials (Basel). 12 (2019) 1–12. https://doi.org/10.3390/ma12091536.

[17] W.F. Monteiro, F.M. Diz, L. Andrieu, F.B. Morrone, R.A. Ligabue, K. Bernardo-Gusmão, M.O. de Souza, A.J. Schwanke, Waste to health: Ag-LTA zeolites obtained by green synthesis from diatom and rice-based residues with antitumoral activity, Microporous Mesoporous Mater. 307 (2020) 110508. https://doi.org/https://doi.org/10.1016/j.micromeso.2020.110508.

[18] Y. Kuwahara, T. Ohmichi, T. Kamegawa, K. Mori, H. Yamashita, A novel conversion process for waste slag: synthesis of a hydrotalcite-like compound and zeolite from blast furnace slag and evaluation of adsorption capacities, J. Mater. Chem. 20 (2010) 5052–5062. https://doi.org/10.1039/C0JM00518E.

[19] J. Perez-Carbajo, S.R.G. Balestra, S. Calero, P.J. Merkling, Effect of lattice shrinking on the migration of water within zeolite LTA, Microporous Mesoporous Mater. 293 (2020) 109808. https://doi.org/10.1016/j.micromeso.2019.109808.

[20] M.K. Purkait, S. DasGupta, S. De, Determination of design parameters for the cloud point extraction of congo red and eosin dyes using TX-100, Sep. Purif. Technol. 51 (2006) 137–142. https://doi.org/https://doi.org/10.1016/j.seppur.2005.12.027.

[21] F. Taghizadeh, M. Ghaedi, K. Kamali, E. Sharifpour, R. Sahraie, M.K. Purkait, Comparison of nickel and/or zinc selenide nanoparticle loaded on activated carbon as efficient adsorbents for kinetic and equilibrium study of removal of Arsenazo (III) dye, Powder Technol. 245 (2013) 217–226. https://doi.org/https://doi.org/10.1016/j.powtec.2013.04.020.

[22] L. Järup, Hazards of heavy metal contamination, Br. Med. Bull. 68 (2003) 167–182. https://doi.org/10.1093/bmb/ldg032.

[23] S. Chaturvedi, P.N. Dave, Removal of iron for safe drinking water, Desalination. 303

(2012) 1–11. https://doi.org/https://doi.org/10.1016/j.desal.2012.07.003.

[24] D. Ghosh, H. Solanki, M.K. Purkait, Removal of Fe(II) from tap water by electrocoagulation technique, J. Hazard. Mater. 155 (n.d.) 135–143. https://doi.org/DOI:101016/jjhazmat200711042.

[25] No Title, (n.d.). https://doi.org/https://doi.org/10.1201/b15579.

[26] L. Stęgpniak, U. Kęgpa, E. Stańczyk-Mazanek, The research on the possibility of ultrasound field application in iron removal of water, Desalination. 223 (2008) 180–186. https://doi.org/https://doi.org/10.1016/j.desal.2007.01.212.

[27] V.L. Dhadge, C.R. Medhi, M. Changmai, M.K. Purkait, House hold unit for the treatment of fluoride, iron, arsenic and microorganism contaminated drinking water., Chemosphere. 199 (2018) 728–736. https://doi.org/10.1016/j.chemosphere.2018.02.087.

[28] W.A. Khanday, G. Kabir, B.H. Hameed, Catalytic pyrolysis of oil palm mesocarp fibre on a zeolite derived from low-cost oil palm ash, Energy Convers. Manag. 127 (2016) 265–272. https://doi.org/https://doi.org/10.1016/j.enconman.2016.08.093.

[29] W.A. Khanday, S.A. Majid, S. Chandra Shekar, R. Tomar, Dynamic adsorption of DMMP over synthetic zeolite-Alpha, Arab. J. Chem. 7 (2014) 115–123. https://doi.org/10.1016/j.arabjc.2013.06.026.

[30] P. Mondal, M.K. Purkait, Preparation and characterization of novel green synthesized iron–aluminum nanocomposite and studying its efficiency in fluoride removal, Chemosphere. 235 (2019) 391–402. https://doi.org/https://doi.org/10.1016/j.chemosphere.2019.06.189.

[31] X. Shen, G. Qiu, C. Yue, M. Guo, M. Zhang, Multiple copper adsorption and regeneration by zeolite 4A synthesized from bauxite tailings., Environ. Sci. Pollut. Res. Int. 24 (2017) 21829–21835. https://doi.org/10.1007/s11356-017-9824-5.

[32] Y. Sasaki, W. Shimizu, Y. Ando, H. Saka, Microstructure analysis with TEM for zeolite layer formed in pore of porous alumina substrate, Microporous Mesoporous Mater. 40 (2000) 63–71. https://doi.org/https://doi.org/10.1016/S1387-1811(00)00231-6.

[33] N.M. Musyoka, L.F. Petrik, E. Hums, A. Kuhnt, W. Schwieger, Thermal stability studies of zeolites A and X synthesized from South African coal fly ash, Res. Chem. Intermed. 41 (2015) 575–582. https://doi.org/10.1007/s11164-013-1211-3.

[34] F. Gorzin, M.M. Bahri Rasht Abadi, Adsorption of Cr(VI) from aqueous solution by adsorbent prepared from paper mill sludge: Kinetics and thermodynamics studies, Adsorpt. Sci. Technol. 36 (2017) 149–169. https://doi.org/10.1177/0263617416686976.

Chapter 3

Physico-chemical and adsorption study of hydrothermally treated zeolite A and FAU-type zeolite X prepared from LD (Linz-Donawitz) slag of the steel industry

The sodium-rich zeolite A and zeolite X (FAU-type) samples were synthesized from LD-slag via fusion-assisted hydrothermal treatment. The physicochemical and thermal stability of the prepared samples were examined with the help of various characterization techniques namely Fourier Transform Infrared (FTIR) Spectroscopy, X-ray diffraction (XRD), and thermogravimetric analysis (TGA) analysis at three different pH conditions and treatment times. Moreover, the sustainability of the crystalline phase and the corresponding zeolite network was evaluated from XRD, FTIR, TGA, and Field-Emission Scanning Electron Microscopy (FESEM) analysis. Methylene blue (MB) adsorption performance of both zeolite samples were examined at different MB concentration and pH. The cost analysis is evident in the economic sustainability of the LD-slag-derived zeolites.

3.1. Experimental

3.1.1. Materials

The LD-slag utilized in this study was obtained from TATA Steel Industry Ltd., Jamshedpur, India. Hydrochloric acid (37%), sodium hydroxide pellets (98%), sodium aluminate (99.99%), and sodium silicate (99%) were procured from Sigma Aldrich Pvt. Ltd. and were employed in zeolite synthesis to maintain the Si and Al ratio.

Methylene blue (MB) with chemical formula: $C_{16}H_{18}CIN_3S.3H_2O$ and molecular weight: 319.86 g/mol was procured from analytical reagent (AR) grade from Merck (Darmstadt, Germany) and used without any further purification. An aqueous stock solution of methylene

---

Content of this chapter has been submitted for publication as below:

N.S. Samanta, P.P. Das, P. Mondal, U. Bora, K. Mihir, Physico-chemical and adsorption study of hydrothermally treated zeolite A and FAU-type zeolite X prepared from LD (Linz-Donawitz) slag of the steel industry, Int. J. Environ. Anal. Chem. 00 (2022) 1–23. https://doi.org/10.1080/03067319.2022.2079082.

blue concentration (1000 mg/L) was made in distilled water for the adsorption experiment. The desired concentration for all working solutions was prepared by consecutive dilution.

3.1.2. Zeolite synthesis

LD-slag-based zeolite A and X were prepared through fusion-assisted followed by alkaline hydrothermal treatment. The unburnt carbon along with volatile materials was removed by calcination of LD-slag at 800°C for 2.5 hours. The acid leaching was conducted with calcined slag and 0.1M hydrochloric acid (1:5, w/v ratio) at 80°C for 2 hours during zeolitization in order to enhance the phase purity of zeolites. The solution pH was found to be 6.8 after acid leaching. In this treatment, NaOH (7.5 g) facilitated LD-slag (5 g) (1:1.5 w/w ratio of slag/NaOH) was fused at 550°C for 1 hour to fabricate Na-rich zeolite type A and X zeolite. The obtained fusion mixture was cooled, crushed, and combined with de-ionized water (1:10, w/v ratio) and kept for 12 hours at room temperature for stirring, followed by aging. A very small amount of sodium silicate was then mixed with the resulting slag solution. Simultaneously, sodium aluminate was added to the resulting slurry to maintain the synthesized zeolite's Si/Al ratio [1,2]. The slurry was agitated continuously for 24 hours at room temperature. After 24 hours, the obtained slurry was poured into an autoclave for crystallization at 90°C for 8 hours. The resulting sample was then filtered and washed several times with de-ionized water to reduce the number of unwanted metal oxides and also to fix the solution pH at 9-10. Subsequent drying was carried out at an elevated temperature of 100°C for 12 hours in a hot air oven to recover zeolite A and X respectively. The zeolite synthesis procedure is illustrated in Figure 3.1.

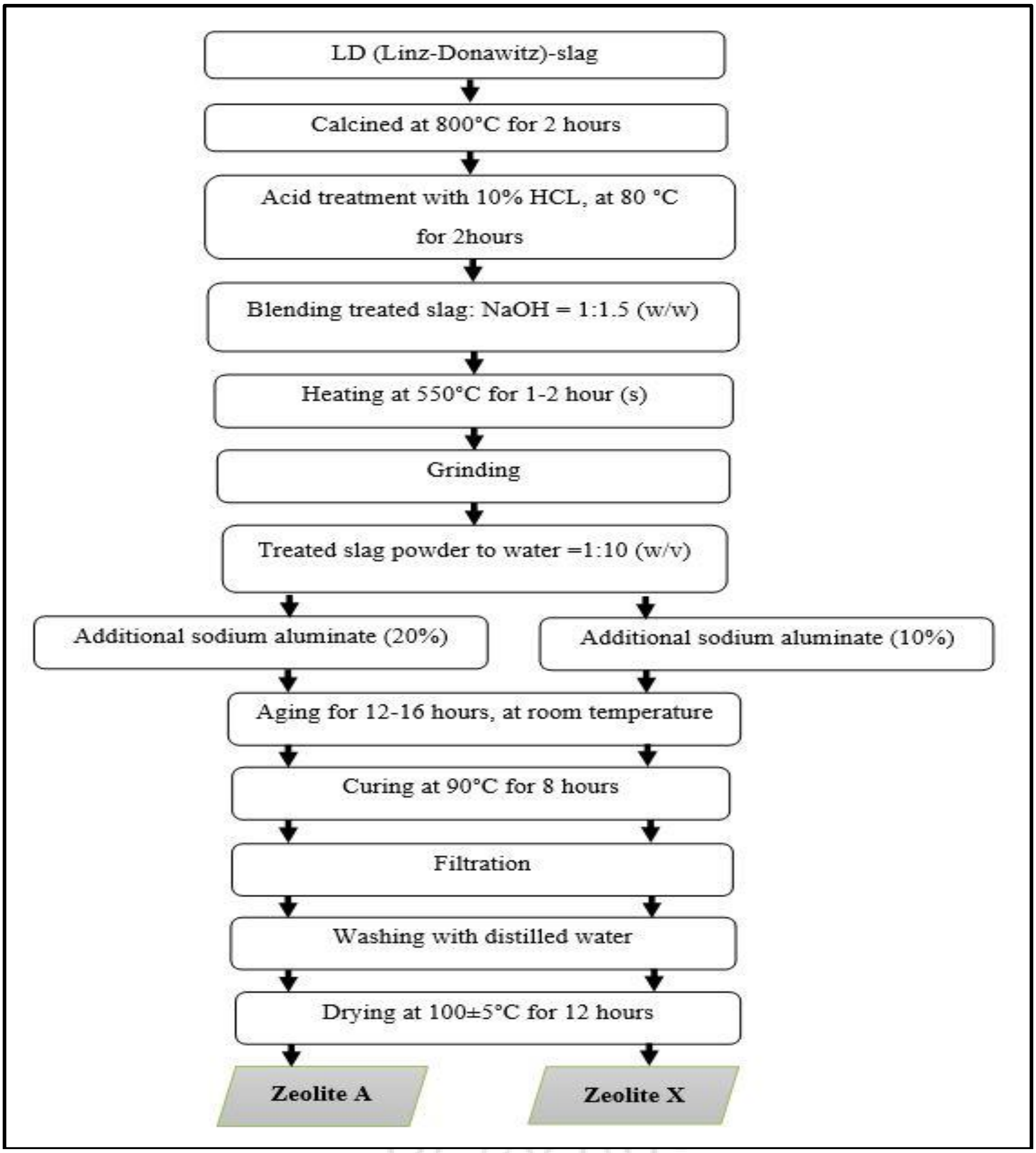

Figure 3.1: Flowchart of zeolite synthesis from LD-slag via Fusion-assisted followed by hydrothermal treatment.

3.1.3. Advantages and disadvantages of the method

The fusion-assisted hydrothermal treatment is a conventional way to prepare zeolite-type minerals from synthetic wastes. However, this technique has some benefits and limitations which are illustrated below.

Advantages: (i) The pre-fusion treatment promotes the zeolite structure and crystallinity; (ii) Allows a high amount of synthetic waste and alkaline material to form a higher concentration of silicate and aluminosilicate that leads to more zeolite formation [3].

Disadvantages: (i) The pre-fusion treatment may increase the cost of the following method due to the high temperature required (500-600°C) [4]; (ii) The high-temperature fusion may cause the generation of greenhouse and harmful gases [3].

3.1.4. Adsorption studies

An initial concentration of 15 mg/L MB synthetic solution was prepared by dissolving 15 mg of MB in 1 L of de-ionized water for conducting the adsorption experimental studies on both the synthesized zeolites (zeolite A and zeolite X) for the evaluation of their adsorption ability. The synthetic MB mixture was prepared with a concentration somewhat higher than that seen in textile effluent (10 mg/L). The adsorption experiment was carried out using a series of batch methods in a 100 mL conical flask at ambient temperature (25°C). A mixture of 0.08 g of zeolite A and 50 mL of 15 mg/L MB was supplied to a 100 mL conical flask and agitated at 300 rpm for 3 hours. After a time interval of 1 hour, the dye solution was taken out, filtered, and analyzed with the help of a UV-visible spectrometer at a fixed characteristic wavelength of 663 nm. From the calibration curve, the Methylene blue (MB) concentration was determined at different time intervals. For zeolite A and X, the equilibrium period for MB adsorption was 120 and 135 minutes, respectively. The removal efficiency (R) of MB and adsorption capacity (Q_t) of the prepared zeolites at varying treatment times were estimated by the following equations:

$$Q_t = \frac{(C0-Ct)V}{W} \tag{3.1}$$

$$R = \frac{(C0-Ce)}{C0} \times 100\ (\%) \tag{3.2}$$

The initial and final concentrations of Methylene blue (MB) were represented by C_0 and C_e respectively where C_t in equation (3.1) denotes the dye concentration after a regular time interval [5].

3.2. Characterization methods

X-ray diffraction analysis was carried out using the Bruker D8 Advance model. Scanning was performed in a 2θ range between 10 to 60° and at a speed of 0.05°/sec in continuous mode. The XRD profiles were obtained using radiation of Cu Kα = 0.15406 nm. The X-ray source was operated at 40 kV and 5 mA.

FESEM was performed for determining the morphological analysis of the treated samples. The internal and external surface morphology of the samples was investigated by the FESEM (ZESIS, Model 1430 VP) instrument. Before the analysis, the treated samples were dried between 70 to 80°C in a hot air oven and were coated with gold plating on their surface before the analysis.

EDX analysis equipped with FESEM was carried out to observe the EDX spectra. EDX was performed to determine the elemental composition of the treated samples. The sample preparation for EDX was kept similar to the FESEM analysis.

FTIR analysis of the samples was conducted using Shimadzu IR Affinity-1. The instrument is equipped with a ceramic infrared (IR) source. The scanning range of the instrument varied from 400-4000 cm^{-1} with a maximum resolution of 0.5 cm^{-1}.

Thermal durability analysis of the synthesized zeolite was conducted with the help of a TGA instrument (Make: NETZSCH, Model: TG209 F1). Type of crucible used: DSC/TG pan Al_2O_3. At a flow rate of 20 mL/minute, argon was employed as an inert gas. The analysis temperature was adjusted in the range of 25°C to 1000°C at a heating rate of 10 K/minute.

Differential Thermal Analysis (DTA) (Make: NETZSCH, Model: TG209 F1) analysis was performed to determine the melting or degradation temperature of the prepared zeolites. The temperature program was set at a rate of 10 K/minute from 25°C to 1000°C.

N_2 adsorption-desorption isotherms of the prepared zeolites were recorded at -196°C with a Quanta chrome (Model: AutosorbiQ) gas sorption analyzer. The samples were degassed at 150°C for 12 hours in an ultrahigh vacuum environment before the analysis. Brunauer-Emmett-Teller (BET) and Barrett-Joyner-Halenda (BJH) techniques were applied to determine the specific surface area (S_{BET}) and pore size distribution.

The quantitative estimation of adsorbate concentration in the liquid sample was performed through ultraviolet-visible (UV-Vis) (Model: UV-2600 240 V EN) spectroscopy at room temperature. Adsorptions were determined using a 4 s integration time in a wavelength range of 200-800 nm.

3.3. Results and discussion

3.3.1. Characterization of Zeolite type-A and X

3.3.1.1. XRD analysis

The XRD pattern of the synthesized zeolites for instance zeolite A and zeolite X utilizing LD-slag as the waste source is shown in Figure 3.2 and Figure 3.3, respectively, which exhibits the structural characteristics of the zeolite phase. The crystalline plane of the final sample of zeolite A, zeolite X, and LD-slag was also investigated. The sharp peaks of the slag along with the product samples of zeolite A and zeolite X were observed at different diffraction angles, having the same 2θ degree ranging from 10 to 80°. Moreover, 2θ angle at 10.18°, 12.54°, 16.06°, 20.28°, 21.88°, 24.04°, 27.72°, 30.04°, 32.66°, 34.14°, 39.58°, 44.18°, 45.24°, 47.34°, 52.58°, 53.5°, 54.26°, 58.56°, 69.19° confirmed the crystalline planes (1 1 0), (1 1 1), (2 1 0), (2 2 0), (3 0 0), (3 1 1), (3 2 1), (4 1 0), (4 2 0), (3 3 2), (4 3 2), (4 4 2), (3 1

1), (4 4 3), (5 4 3), (5 5 1), (6 4 1), (6 4 3), (8 3 3) which corresponds to zeolite A [6–8]. On the other hand, the diffraction peaks observed at10°, 15.76°, 20.08°, 21.50°, 23.12°, 26.99°, 32.98°, and 34.20° indicate the crystalline planes (2 2 0), (3 3 1), (4 4 0), (5 3 1), (4 4 2), (1 1 2), (6 6 4) and (9 1 3) for zeolite X [9]. The characteristic peaks confirm that the synthesized zeolites are zeolite A and zeolite X. Furthermore, the sharp peaks detected at 18.04°, 26.6°, 29.5°, 33.64°, 34.16°, 39.48°, 42.12°, 47.2°, and 50.88° also reveals the crystalline nature of LD-slag [10].

Figure 3.4a-c and Figure 3.5a-c show the X-ray diffraction pattern of the fabricated zeolites which evaluates the stability of zeolite A and zeolite X samples at different pH conditions. The results indicated that no drastic change in crystalline phases has been found at different pH conditions, however, a decrease in the peak intensity was observed for the zeolite A sample at pH 2, treated for 2 and 3 days, respectively, as compared to other pH conditions treated for the same number of days. The reason may be attributed to the presence of less crystallinity in the prepared sample under the acidic condition at a diffraction angle of 30.04° as shown in Figure 3.4a. In addition, noticeable changes in peak intensity have not been observed at pH 12 for zeolite A, however, peaks at 10.16° and 12.58° were almost invisible after 3 days of treatment time which corresponds to the crystalline plane of (1 1 0) and (1 1 1). The result refers to the breaking or deformation of the zeolite A cage, the FESEM images depicted in Figure 3.6c(i) verified the XRD analysis. The same characteristic has also been observed for the zeolite X sample at low pH conditions (Figure 3.5a). Moreover, the FESEM images shown in Figures 3.6a(i) and a(ii) verified the XRD analysis.

It was found from the XRD patterns that, the final products still maintained the zeolitic structure, ranging from high to low pH conditions. The analysis report also reveals that the synthesized samples may show stability under any pH range except for very acidic pH conditions (pH 2), at which a less crystalline nature was observed with regard to both the synthesized samples.

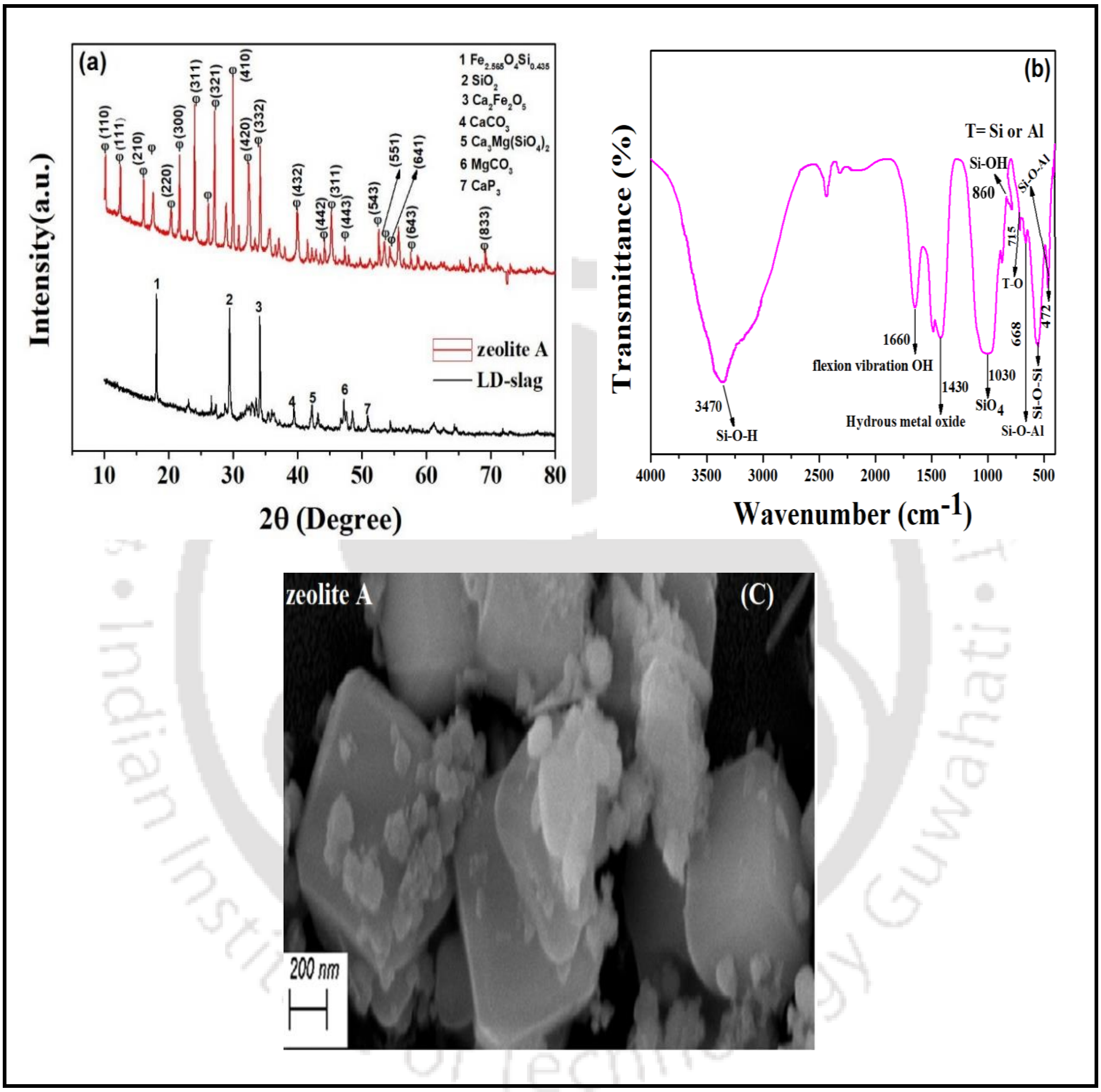

Figure 3.2: (a) XRD pattern, (b) FTIR spectrum, and (c) FESEM micrographs of synthetic zeolite type-A.

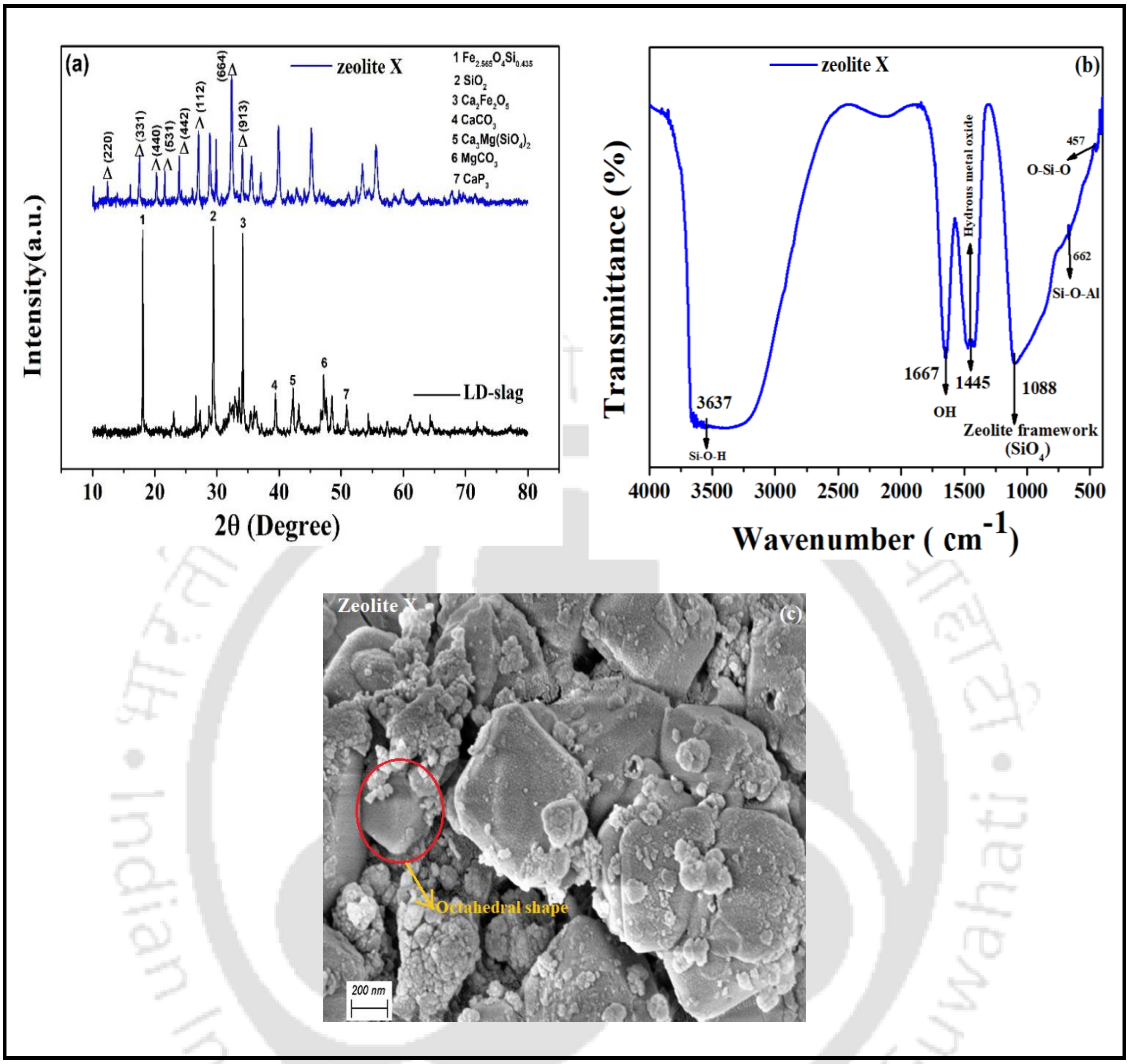

Figure 3.3: (a) XRD pattern, (b) FTIR spectrum, and (c) FESEM images of the synthesized zeolite X.

3.3.1.2. Fourier transform infrared spectroscopy

The IR-spectra of the synthesized zeolite A and zeolite X samples are shown in Figure 3.2 and Figure 3.3, respectively. Almost similar spectra were observed for both synthesized samples. The adsorption peak bands at 457-472 cm^{-1}, 662-668 cm^{-1}, 1030-1088 cm^{-1}, 1660-1667 cm^{-1}, and 3470-3637 cm^{-1} signify Si-O or Al-O (T-O) bending vibration [11], symmetric stretching of Si-O-Al, symmetric and asymmetric stretching of SiO_4 and AlO_4,

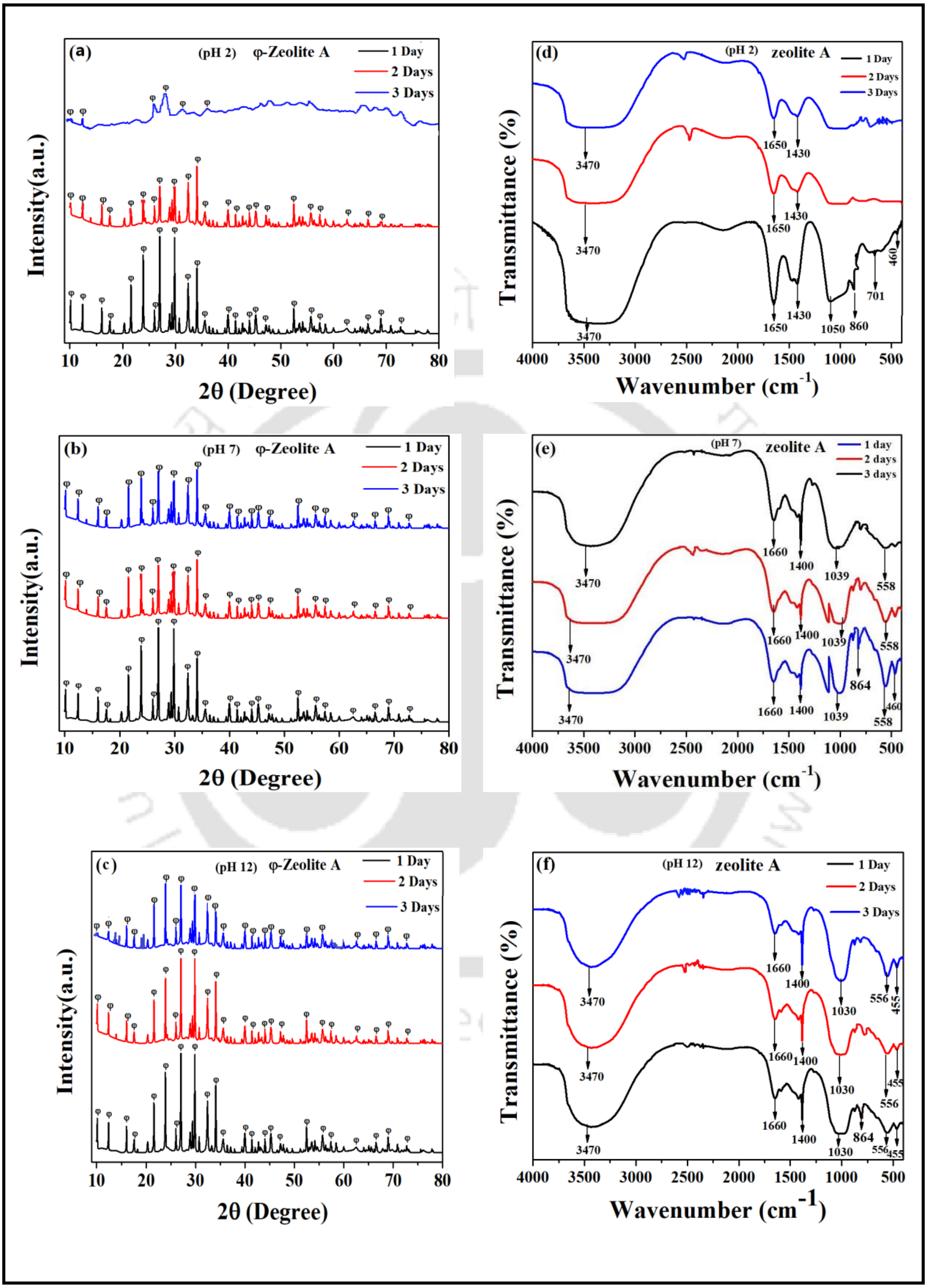

Figure 3.4: (a)-(c) XRD pattern and (d)-(f) FTIR spectrum of synthesized zeolite A at different pH conditions and different treatment periods of 1-3 days.

flexion vibration of O-H group, and hydrogen-bonded Si-OH groups respectively [12]. In addition to that, the broad band that appeared at 860 cm^{-1} depicts the presence of stretching of the Silanol (Si-OH) group related to silicon atoms bonded with the hydroxyl (-OH) group [12,13].

As shown in Figure 3.4d-f and Figure 3.5d-f, a comparative study of zeolite A and X has been established through FTIR spectroscopy analysis performed within the range of 500-4000 cm^{-1}. Figure 3.4d and Figure 3.5d depict the IR spectrum of zeolite A and X, respectively at pH 2. In Figure 3.4d, a broad peak appeared at 1650 cm^{-1}, which is assigned to the flexion vibration of the OH group in the zeolite A sample. The same band was shifted towards a slightly higher frequency of 1654 cm^{-1} for the zeolite X sample. In the case of zeolite A, the small vibrational peaks noticed at 460 cm^{-1} and 701 cm^{-1} for pH 2 are assigned to the asymmetric and symmetric stretch of T-O (T=Si, Al) and TO_4, respectively. However, the same peaks were found to be negligible after a period of 2-3 days, when the zeolite A sample was treated under the same pH condition. It was also observed that at highly acidic conditions the Si-OH band hasn't arrived but the same band was shifted towards a slightly higher frequency of 864 cm^{-1} for neutral and highly basic conditions, respectively. On the other hand, for the zeolite X sample, the asymmetric and symmetric stretch of T-O (T=Si, Al) and TO_4 were observed at 460 and 715 cm^{-1}, respectively. FTIR spectrum of the zeolite X sample also demonstrated a sharp and very prominent peak at 555 cm^{-1}, which refers to the symmetric stretching vibrations of the bridge bonds Si-O-Si and bending vibrations O-Si-O at the same pH condition, however, no prominent vibrational peak was observed within this range for zeolite A sample [14].

Figure 3.4e and Figure 3.4e illustrated the IR spectrum of the final product sample zeolite A and zeolite X at pH 7, respectively. The asymmetric and symmetric stretch of T-O (T=Si, Al) and TO_4, flexion vibration of OH group, symmetric stretching vibrations of bridge bonds Si-

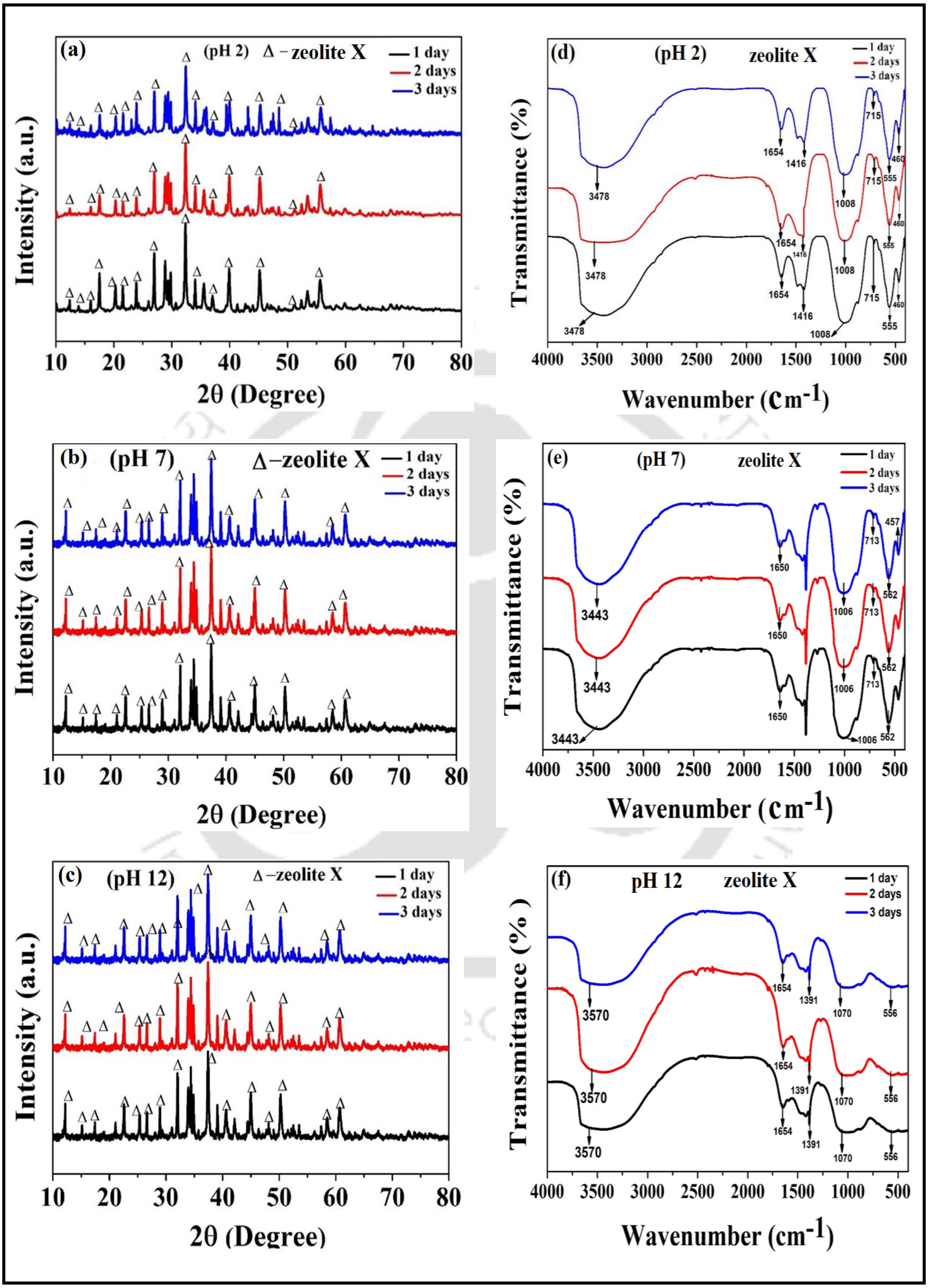

Figure 3.5: (a)-(c) XRD pattern and (d)-(f) FTIR spectrum of synthesized zeolite X sample at pH 2, 7, and 12, respectively at various treatment periods of 1-3 days.

O-Si and bending vibrations O-Si-O, asymmetric stretching vibrations of bridge bonds Si-O(Si) and Si-O (Al), hydrous metal oxides and OH^- bond were observed at 460, 1660, 558, 1006 and 1400 cm^{-1} frequency, respectively for the synthesized zeolite A sample [15]. However, the same vibrational peaks for zeolite X appeared at 457, 1650, 552, 1006, and 1400 cm^{-1} bands. Figure 3.4e reveals a decreasing trend in the peak intensity of the band at 558 cm^{-1} when the sample was dipped at pH 7 for 2-3 days. This is due to the presence of weaker Si-O-Si and O-Si-O bonds in the zeolite sample. Similarly, Figure 3.4f and Figure 3.5f display the IR spectrum for synthesized zeolite A and X, respectively, at highly basic conditions (pH 12). The well-defined IR bands at 1660, 1400, 1006, 556, and 455 cm^{-1} are assigned to water deformation mode (flexion vibration of OH), hydrous metal oxides and OH^- bond, asymmetric stretching vibrations of bridge bonds Si-O (Si) and Si-O (Al), symmetric stretching vibrations of bridge bonds Si-O-Si and bending vibrations O-Si-O and T-O vibration of the SiO_4 and AlO_4 internal tetrahedral respectively for zeolite A. For zeolite X, the bonds appeared at 1654, 1391, 1070, and 556 cm^{-1}, where the disappearance of the T-O vibration band is also observed. The band ranging from 3470 to 3570 cm^{-1} are assigned to hydroxyl groups (hydrogen-bonded Si-OH groups) in zeolite cages. The distinct band at ~ 1660 cm^{-1} is attributed to the bending vibration of the OH group which coexists with OH stretching vibration at ~ 3470 to 3570 cm^{-1} [16].

3.3.1.3. SEM analysis

The microscopic images of zeolite A and zeolite X are shown in Figure 3.2c and Figure 3.3c, respectively. The SEM micrographs in both figures demonstrate that the synthesized zeolite A sample showed a much smoother and cubical surface as compared to the synthesized zeolite X. However, the octahedral crystal shape of X-type zeolite has been observed, as shown in Figure 3.3c.

After being treated at various pH (2, 7, and 12) for 3 days, the surface morphologies of both the prepared zeolites (zeolite A and zeolite X) were studied with the help of FESEM analysis, as displayed in Figure 3.6. It was seen from Figure 3.6a(i) that the cubic shape of the zeolite A sample gets distorted when it was kept at pH 2 for a maximum treatment time of 3 days. This is because highly acidic solution protons (H^+ ions) attack the Si-O-Al bonds which get hydrolyzed, resulting in the dealumination and splitting of the bonds into more stable Si=OH and Al=OH structures [17]. This causes an internal pressure in the zeolite cage due to which the water present in the β cage of zeolite A will move out to the α cage. In addition, the Na^+ ion present in the zeolite cage gets attacked by OH^- ions, thereby forming NaOH and moving out with the water molecules, which in turn results in the disintegration of the tetrahedral unit of the zeolite network [5]. Figure 3.7 illustrates the stepwise deformation mechanism of the zeolite framework. On the other hand, brittle, agglomerated, and uneven surface texture distribution was observed for the zeolite X sample at the same pH condition. The reason may be due to the breaking down of metal hydroxide and metal oxide under acidic conditions. Also, as shown in Figure 3.6b(i), no major changes in the geometrical structure of zeolite A were observed at pH 7, however, some ruptures on the surface of zeolite X were noticed under the same pH condition, as displayed in Figure 3.6b(ii). Figure 3.6c(i) and c(ii) also confirmed that there was no significant shift in both the types of zeolite structures under highly basic conditions (i.e. pH 12), though the presence of agglomerated particles on the surface of zeolite X was observed, as shown in Figure 3.6c(ii).

As such, it was confirmed from the FESEM images that, at low pH conditions zeolite samples appear to be unstable; whereas no structural change has been observed at neutral and highly basic conditions. The result also implies that synthesized zeolite A and X are more stable at pH 7 and 12 rather than at pH 2.

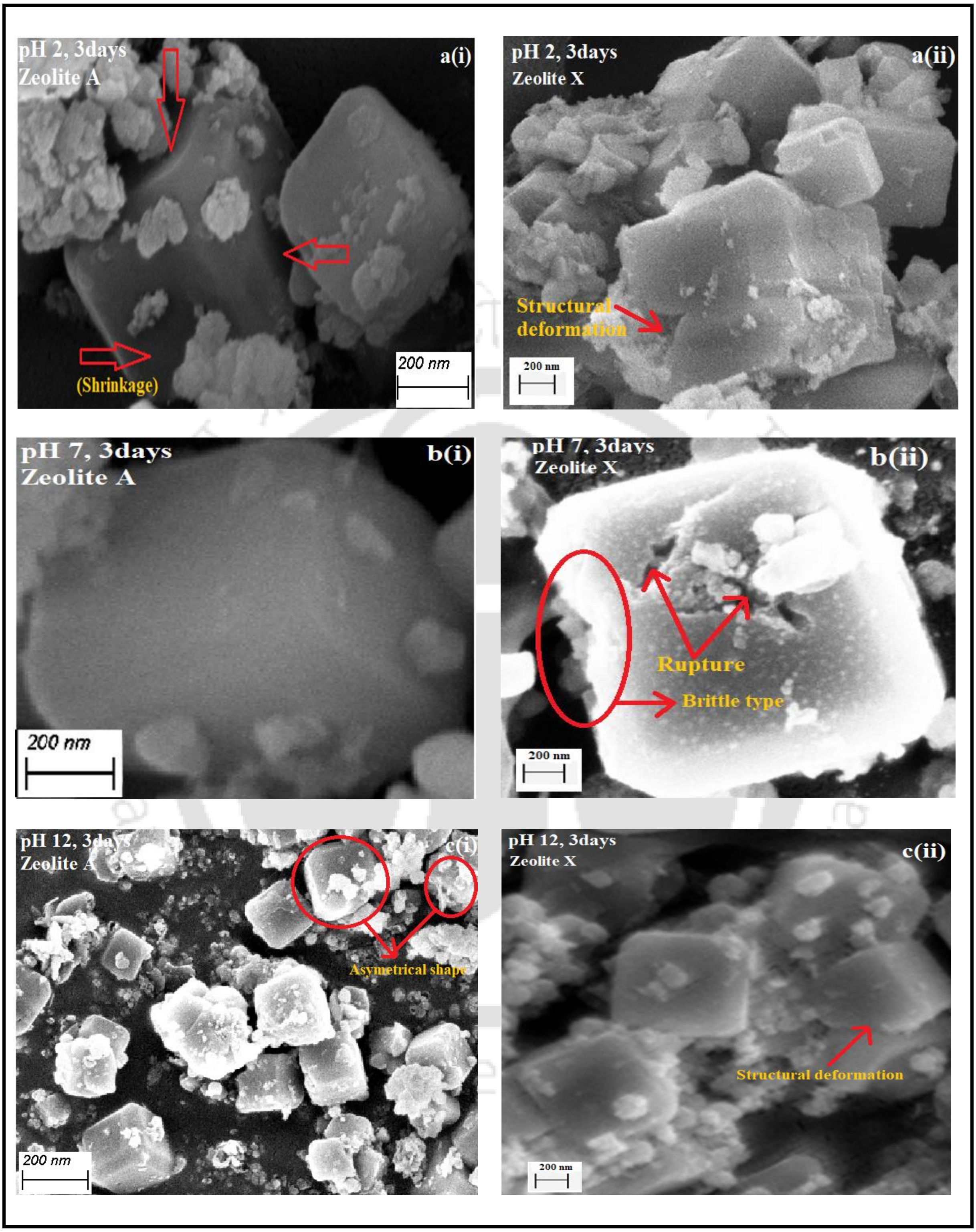

Figure 3.6: a(i)-c(i) and a(ii)-c(ii) SEM analysis of synthesized zeolite A and zeolite X at pH 2, pH 7, and pH 12, respectively for 3 days.

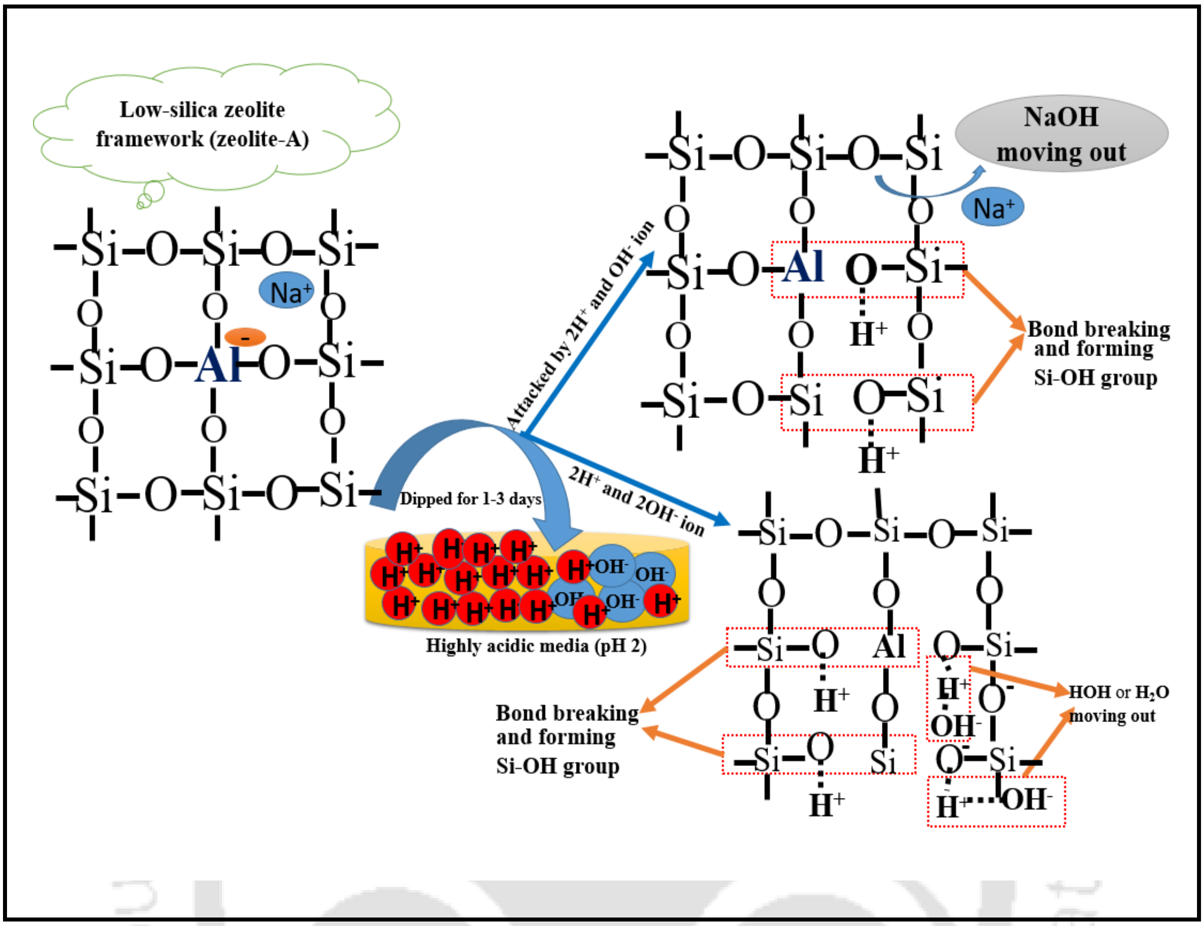

Figure 3.7: Stepwise mechanism of structural deformation of the low-silica zeolite framework.

3.3.1.4. Thermo-gravimetric analysis

The comparative TGA-DTA graph of LD-slag processed zeolite A and X is shown in Figure 3.8. The LD-slag-based zeolites were synthesized to understand the limitation of thermal stability, as synthesized zeolites may be used during adsorption or catalytic processes where heat treatment is the basic requirement for regeneration processes. The multi-stage mass losses from both LD-slag-based zeolites were observed at different temperature ranges for all pH conditions. The thermograph shown in Figure 3.8a illustrates the dehydration characteristics of the zeolite A sample. It was noticed that dehydration of zeolite A sample leads to its splitting at 4 different stages under acidic pH 2 after a period of 3 days. A mass loss percentage of 1.03% occurs at the initial stage between 23.8 and 70.03°C. However, a

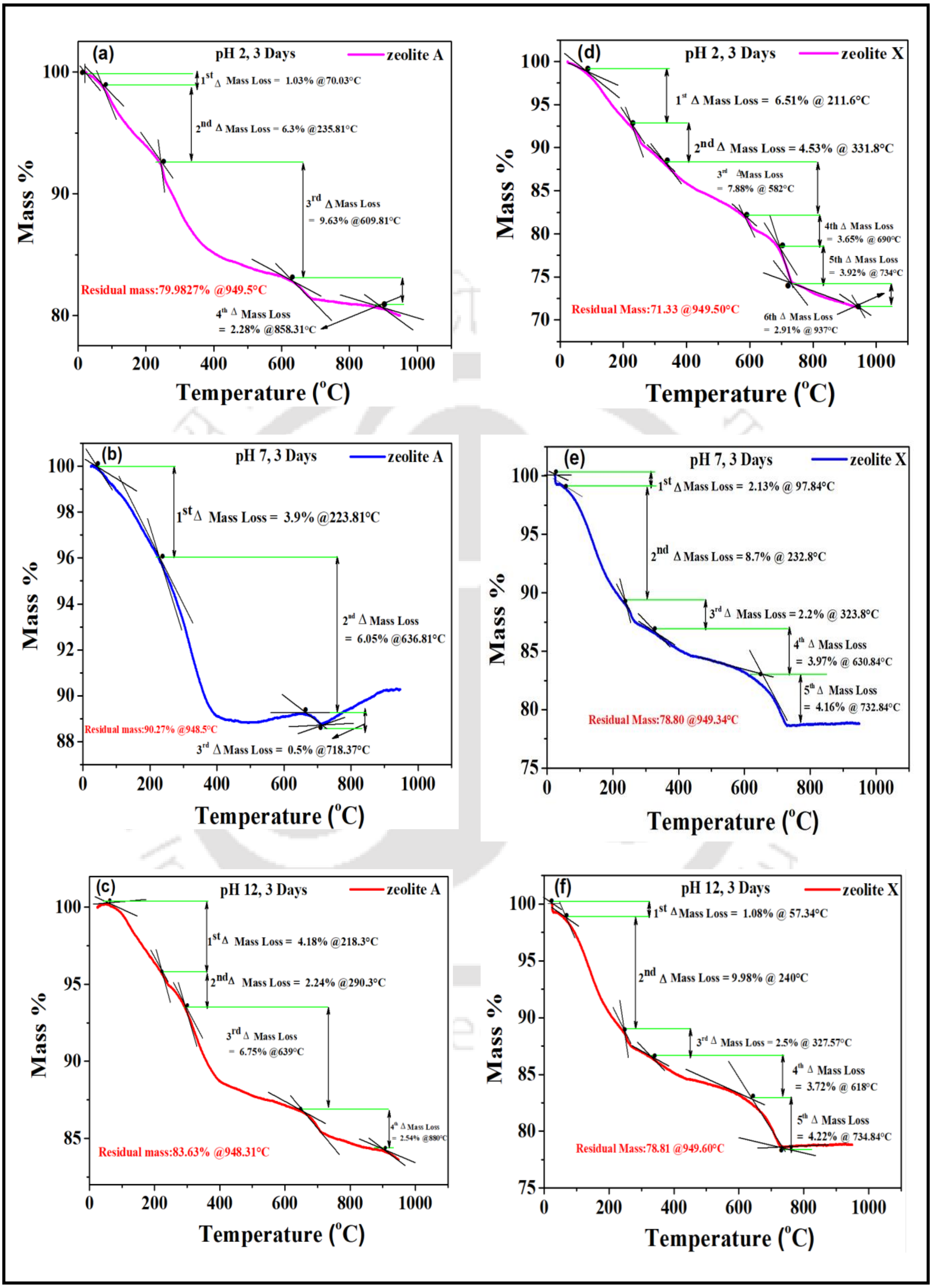
(a)
pH 2, 3 Days
zeolite A
1st Δ Mass Loss = 1.03% @70.03°C
2nd Δ Mass Loss = 6.3% @235.81°C
3rd Δ Mass Loss = 9.63% @609.81°C
4th Δ Mass Loss = 2.28% @858.31°C
Residual mass:79.9827% @949.5°C
Mass %
Temperature (°C)
100
90
80
0
200
400
600
800
1000
(d)
pH 2, 3 Days
zeolite X
1st Δ Mass Loss = 6.51% @ 211.6°C
2nd Δ Mass Loss = 4.53% @ 331.8°C
3rd ΔMass Loss = 7.88% @ 582°C
4th Δ Mass Loss = 3.65% @ 690°C
5th Δ Mass Loss = 3.92% @ 734°C
6th Δ Mass Loss = 2.91% @ 937°C
Residual Mass:71.33 @949.50°C
Mass %
Temperature (°C)
100
95
90
85
80
75
70
0
200
400
600
800
1000
(b)
pH 7, 3 Days
zeolite A
1st Δ Mass Loss = 3.9% @223.81°C
2nd Δ Mass Loss = 6.05% @636.81°C
3rd Δ Mass Loss = 0.5% @718.37°C
Residual mass:90.27% @948.5°C
Mass %
Temperature (°C)
100
98
96
94
92
90
88
0
200
400
600
800
1000
(e)
pH 7, 3 Days
zeolite X
1st Δ Mass Loss = 2.13% @ 97.84°C
2nd Δ Mass Loss = 8.7% @ 232.8°C
3rd Δ Mass Loss = 2.2% @ 323.8°C
4th Δ Mass Loss = 3.97% @ 630.84°C
5th Δ Mass Loss = 4.16% @ 732.84°C
Residual Mass:78.80 @949.34°C
Mass %
Temperature (°C)
100
95
90
85
80
75
0
200
400
600
800
1000
(c)
pH 12, 3 Days
zeolite A
1st Δ Mass Loss = 4.18% @218.3°C
2nd Δ Mass Loss = 2.24% @290.3°C
3rd Δ Mass Loss = 6.75% @639°C
4th Δ Mass Loss = 2.54% @880°C
Residual mass:83.63% @948.31°C
Mass %
Temperature (°C)
100
95
90
85
0
200
400
600
800
1000
(f)
pH 12, 3 Days
zeolite X
1st Δ Mass Loss = 1.08% @ 57.34°C
2nd Δ Mass Loss = 9.98% @ 240°C
3rd Δ Mass Loss = 2.5% @ 327.57°C
4th Δ Mass Loss = 3.72% @ 618°C
5th Δ Mass Loss = 4.22% @ 734.84°C
Residual Mass:78.81 @949.60°C
Mass %
Temperature (°C)
100
95
90
85
80
75
0
200
400
600
800
1000

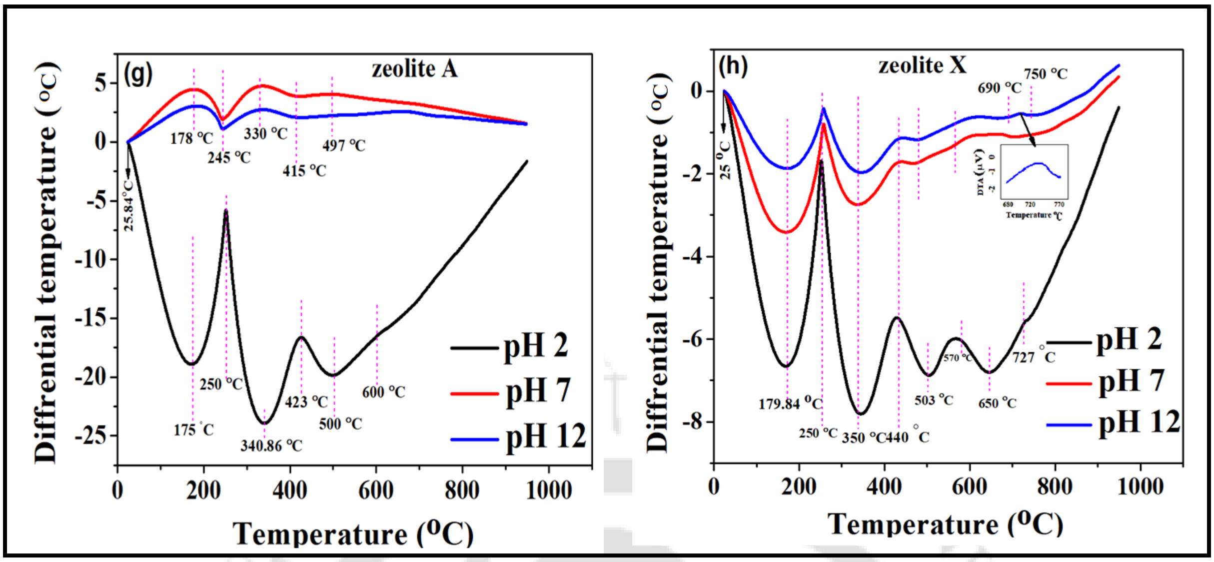

Figure 3.8: (a)-(c) and (d)-(f) TGA, (g) and (h) DTA analysis of synthesized zeolite A and X at pH 2, 7, and 12, respectively for a treatment time of 3 days.

major mass loss of 9.63% was observed during the third stage at a temperature range of 235 to 609.81°C. The reason may be due to the mesoporosity as well as water entrapment in the mesoporous pores of the zeolite framework, which eventually gets evaporated during the above-mentioned temperature range. Moreover, Figure 3.8b indicates a mass loss of 3.9% at a temperature range of 40.8 to 223.81°C, during the initial stage. As the experiment proceeds further, it can be seen that the highest mass loss of 6.05% occurred within a temperature range of 223.81 and 636.81°C under neutral pH conditions (pH 7). Similarly, Figure 3.8c depicts a mass loss of 4.18% initially at a temperature range of ~ 60 to 218.3°C, followed by a subsequent mass loss of 6.75% between 290.3 to 639°C, respectively. From the three figures, it was inferred that the mass loss occurrence at pH 7 is less compared to the mass loss at pH 2 and 12.

The TGA thermograph shown in Figures 3.8d-f indicates the thermal study of zeolite X. It was observed from Figure 3.8d that, the mass loss for zeolite X under acidic pH 2 occurs at six different stages, of which a mass loss of 7.88% during the third stage was found to be highest between a temperature range of 331.8 and 582°C. Furthermore, the mass loss that occurs during the initial stage was found to be 6.51% at a temperature between 60 to 211.6°C. However, at the temperature range of 734-937°C, the mass loss was found to be minimal (2.91%). Similarly, at pH 7 (Figure 3.8e), the mass loss during the initial stage was found to be 2.13%, whereas, a maximum mass loss of 8.7% occurred within the temperature range of 97.84-232.8°C. Moreover, at pH 12 (Figure 3.8f) it was noticed that the maximum (9.98%), and minimum (1.08%) mass losses were observed at the temperature range of 25-57.34°C and 57.34-240°C, respectively.

From Figure 3.8, it is apparent that the highest residual mass of 89.55% and 78.80% were achieved for zeolite A and zeolite X samples respectively under neutral pH conditions (pH 7) and a temperature of 949°C. However, a less residual mass percentage was found at pH 2 and 12 for both samples. The TGA analysis also revealed that the residual mass of zeolite A was higher at all the pH conditions, as compared to zeolite X. The maximum weight loss or moisture loss from the zeolite network indicated the dissociation of Si-O and weaker Al-O bonds present in the zeolite framework. Generally, the water adsorption capacity of highly crystalline zeolite A and X is usually >26% and >32%, respectively. Moreover, mesopores in X-type zeolite framework could lead to cage deformation at high temperature, resulting in loss of moisture as well as volatile components present in the synthetic zeolite [18], which could be a valid reason for less residual mass of zeolite X at all pH conditions compare to zeolite type-A. The FESEM images confirmed the above findings as shown in Figure 3.6a(i), a(ii) and c(i), c(ii), which designates the shrinkage and structural deformation of zeolite crystal obtained under highly acidic (pH 2) and basic (pH 12) conditions after a treatment time of 3 days. As a consequence, a high amount of mass loss was observed due to evaporation during thermal analysis. The detailed thermal analysis report of both the synthesized samples is summarized in Table 3.1.

Table 3.1: TGA analysis of synthesized zeolite types A and X.

Zeolite A				Zeolite X			
Stage no.	**Mass loss (%)**	**Temperature (°C)**	**Total mass loss (%)**	**Stage no.**	**Mass loss (%)**	**Temperature (°C)**	**Total mass loss (%)**
Thermal analysis at pH 2				**Thermal analysis at pH 2**			
1st	1.03	23.8-70.3	**19.2**	1st	6.51	60-211.6	**29.4**
2nd	6.3	70.3-235.8		2nd	4.53	211.6-331.8	
3rd	9.63	235.8-609.8		3rd	7.88	331.8-582	
4th	2.28	609.8-858.3		4th	3.65	582-690	
-	-	-		5th	3.92	690-734	
-	-	-		6th	2.91	734-937	
Thermal analysis at pH 7				**Thermal analysis at pH 7**			
1st	3.9	40.8-223.8	**10.45**	1st	2.13	25-97.84	**21.16**
2nd	6.05	223.8-636.8		2nd	8.7	97.84-232.8	
3rd	0.5	636.8-718.3		3rd	2.2	232.8-323.8	
-	-	-		4th	3.97	323.8-630.8	
-	-	-		5th	4.16	630.84-732.8	
Thermal analysis at pH 12				**Thermal analysis at pH 12**			
1st	4.18	60-218.3	**15.71**	1st	1.08	25-57.34	**21.32**
2nd	2.24	218.3-290.3		2nd	9.98	57.34-240	
3rd	6.75	290.3-639		3rd	2.5	240-327.57	
4th	2.54	639-880		4th	3.72	327.57-618	
-	-	-		5th	4.22	618-734.84	

The similarities of TGA results were supported by the corresponding DTA graphs for both zeolite A and X as shown in Figure 3.8g and 3.8h, respectively**.** The sharp endothermic peaks were only observed near 175°C, 340.86°C, and 500°C for pH 2, whereas for pH 7 and 12, the peaks occurred at 245°C and 415°C, respectively for zeolite A. This can be attributed to the desorption of water molecules, which leads to shrinkage in the unit cell to form a new anhydrous phase at the above-mentioned temperature. However, no exothermic peak was observed during the DTA analysis, which suggested that less structural deformation was observed for the zeolite A sample. Moreover, the endothermic peak characteristic of dihydroxylation was found to be within the temperature range of 25°C-250°C, 250°C-440°C, and 440°C-570°C for zeolite X sample in all pH conditions after a treatment time of 3 days as shown in Figure 3.8h. Furthermore, an exothermic peak seen between 690°C to 750°C can be attributed to the structural disintegration of zeolite X, thereby resulting in the arrangement of an amorphous phase, as observed in Figure 3.8h inset [19].

It is apparent from the preceding thermal study that the residual mass of the zeolite A sample is higher as compared to zeolite X for all pH conditions. That indicates that type-A zeolite is more thermally stable than another sample (zeolite X). The reason can be explained as temperature increased the dissociation of weaker Al-O bond and Si-O bond in zeolite X network occurred that resulting in the elimination of a higher amount of moisture as well as other volatiles substituents with respect to zeolite type A.

3.3.1.5. BET analysis

The N_2 adsorption-desorption and pore size distribution of raw LD-slag and slag-based fabricated zeolite A and FAU (X-type zeolite) are depicted in Figures 3.9a and 3.9b, respectively. The surface area, pore volume, and BJH pore diameter are displayed in Table 3.2. Both the synthesized zeolites showed type II adsorption-desorption isotherm with H3 type hysteresis loop, thereby indicating the presence of mesopores. Zeolite A and X were found to have surface areas of 27.61 and 14.17 m^2/g, respectively, and total pore volumes of 0.086 and 0.131 cm^3/g (Table 3.2). The Barrett, Joyner, and Halenda (BJH) pore size distribution revealed that the majority of the pore size lies within the range of 1.98 to 4.22 nm for zeolite A, on the contrary, the majority of the pore size for zeolite X lies within the range of 3.37 to 4.21 nm, respectively, as depicted in Figure 3.9b. Therefore, it is apparent from the above study that the obtained zeolites were mesoporous in nature [20]. However, the BET surface area of raw slag was found to be 6.11m^2/g with BJH pore size in the range of 3.32 to 4.57 nm. The results suggested that the pores in the raw slag were mesoporous in nature. From the BET analysis, it was suggested that the synthesized zeolite A was found to be highly porous compared to zeolite X. The findings also demonstrated that for both samples the BET surface area is higher as compared with raw LD-slag. Table 3.3 shows a comparative analysis of BET surface area and pore volume of synthetic LD-slag-based zeolite A and zeolite X with other types of commercial and synthesized zeolite.

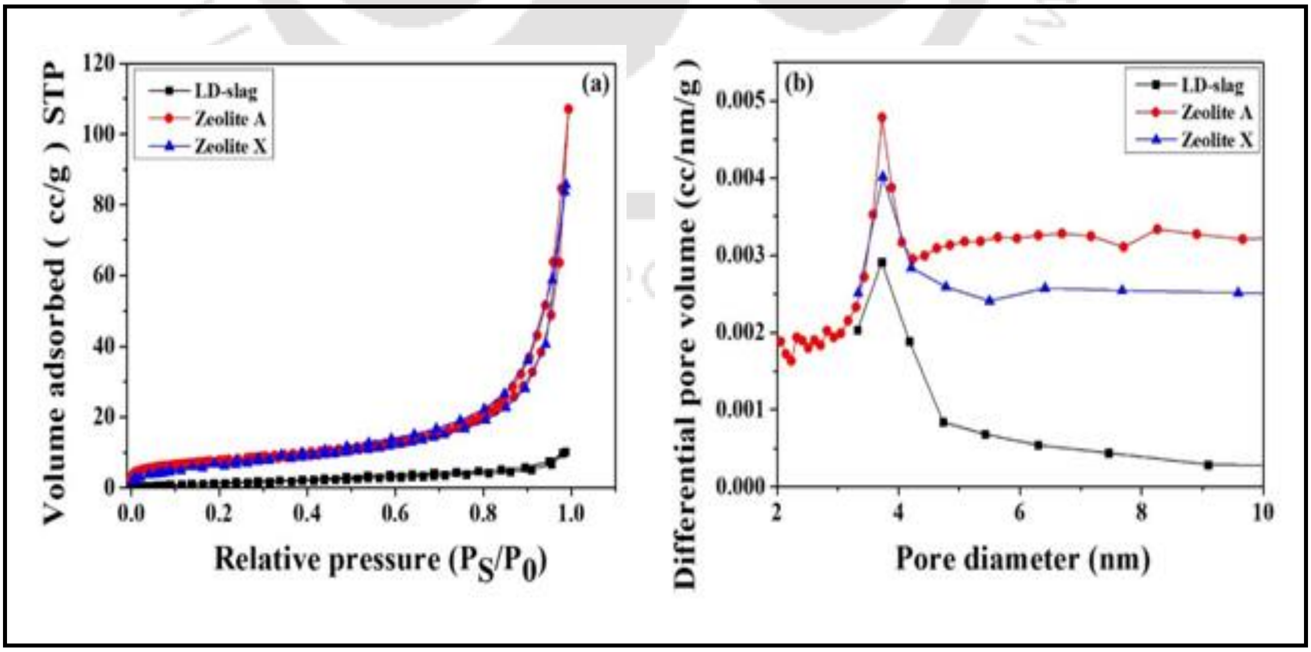

Figure 3.9: (a) BET isotherms and (b) BJH pore-size distributions of LD-slag and synthesized zeolites.

Table 3.2: BET analysis of raw LD-slag and slag-modified zeolite type-A and X.

Sample	BET surface area (m^2/g)	Pore volume (cm^3/g)	BJH Pore diameter (nm)
Raw LD-slag	6.11	0.015	3.32-4.57
Zeolite A	27.61	0.086	1.98-4.22
Zeolite X	14.17	0.131	3.37-4.21

Table 3.3: A comparison study on BET analysis of LD-slag-based zeolite A and X with zeolites from other sources.

Sample	Type	BET surface area (m^2/g)	Pore volume (cc/g)	References
Zeolite A	Synthesized	3.00	0.001	[35]
Zeolite A	Synthesized	13.37	0.0011	[36]
Zeolite A	Synthesized	11.90	-	[37]
Zeolite 4A	Commercial	7.37	0.00022	[36]
Zeolite 4A	Synthesized	13.37	0.00114	[36]
Zeolite A	Synthesized (CFA-based)	<3	-	[38]
Cancrinite	Synthesized (CFA-based)	11.90	-	[8]
Zeolite	Natural	11.40	0.06035	[39]
Zeolite Na-P1	Synthesized (CFA-based)	4.311	0.077	[40]
Zeolite	Commercial	13.83	-	[34]
Zeolite A	Synthesized (BFA-based)	12.00	0.004	[41]
Zeolite A	**Synthesized (LD-slag-based)**	**27.61**	**0.086**	**Present work**
Zeolite X	**Synthesized (LD-slag-based)**	**14.17**	**0.131**	**Present work**

3.3.1.6. Zeta potential and isoelectric point of prepared zeolites

The zeta potential value obtained confirms the surface charge of the synthesized zeolites. The two synthesized zeolites (A and X) showed a highly negative surface charge, as both consist of a high silica-enrich framework (where silica atoms were substituted by an aluminium atom with the sharing of oxygen atoms). This resulted in a negatively charged zeolite framework. It was also proposed that the higher the number of aluminum atoms associated with silicon atoms or zeolite framework, the more will be the surface negative charge density of zeolite A [21]. As more amount of sodium aluminate is used to maintain the Si/Al ratio of zeolite A, it resulted in a high negative surface charge. The surface charge for zeolite A and zeolite X was obtained at -52.60 and -43.90 mV, respectively at pH 8.9±0.1. Particles with zeta potentials more positive than +30 mV or more negative than -30 mV are normally considered stable particles [22,23]. Therefore, zeolite A and zeolite X particles are very stable at pH 8.9.

The isoelectric point of synthesized zeolite A and zeolite X was found at pH 5 and 5.5 respectively. For instance, at a pH below 5, zeolite A carries a positive charge, whereas a negative charge was obtained at a pH higher than 5. However, zeolite X showed a positive surface charge below pH 5.5 and gets negatively charged above the same pH condition as depicted in Figure 3.10a.

3.4. Methylene Blue (MB) removal study

As already mentioned, this work is mainly focused on the synthesis of zeolites along with their sustainability with respect to physiochemical, and thermal stability under acidic, neutral, and highly basic conditions, at different treatment times. The surface charge analysis confirmed the high negative charge of both zeolites, which can be effectively used as cation exchange agents. Therefore, to establish its ability towards cation exchange both zeolites were employed for cationic dye removal.

3.4.1. Adsorbent dose optimization

To investigate the optimum zeolite dose on MB adsorption at an initial concentration of 15 mg/L, the following protocol has been employed: 50 mL of MB solution and 0.02, 0.04, 0.06, 0.08, 0.1, 0.12 g of each zeolite (zeolite A and zeolite X) were mixed to prepare 6 different synthetic solutions of zeolite A and zeolite X at room temperature (25°C) and stirred for a duration of 12 hours. At an optimum zeolite dose of 0.08 g, the maximum MB sorption was found to be 98.13% and 94.47% for zeolite A and zeolite X, respectively within 3 hours (Figure 3.10b). However, dye concentration was varied from 15-50 mg/L to find the effect on adsorption capacity and dye rejection efficiency.

3.4.2. Effect of initial concentration of MB

Initially, the MB concentration was set to 15-50 mg/L to investigate the percent removal of dye and equilibrium adsorption capacity onto 0.08 g of prepared zeolite A and X, as shown in Figure 3.10e. Percent removal of dye was reduced with higher MB concentration (40-50 mg/L), meanwhile, equilibrium sorption capacity gets increased up to a certain MB concentration range and reached equilibrium at higher dye concentration (Figure 3.10e) and this is because the driving force for mass transfer rises as the dye concentration increases. There will be vacant active sites on the adsorbent's surface at low concentrations. But, at a high concentration, there will be lacking an active site for adsorption, indicating that with an initial MB concentration of 35 mg/L and above the sorption capacity did not rise and reached equilibrium [2,24].

3.4.3. Effect of contact time on dye removal and adsorption capacity of zeolites

It was observed that during the initial period, the MB removal and adsorption capacity increases exponentially until an equilibrium is reached after 120 minutes for zeolite A and 135 minutes for zeolite X. This is probably due to the electrostatic attraction between the anionic zeolite surface and cationic dye molecules. However, it was also proposed that the presence of a large number of active sites significantly influences the binding of adsorbates on the adsorbent surface, thereby leading to a higher MB removal by zeolite A as compared to zeolite X [25]. The effect of contact time on MB removal and sorption capacity is depicted in Figures 3.10c and 3.10d, respectively. The relative adsorption capacity was found to be 25.30 and 23.57 mg/g with MB removal efficiency of 98.13% and 94.47% on zeolite A and X surfaces, respectively. Table 3.4 depicts a comparison study of MB cationic dye removal utilizing various types of zeolite, revealing that the produced zeolite A and X from waste LD-slag performed better than previously published studies.

3.4.4. Effect of solution pH on MB removal and sorption capacity

It is widely known that dye adsorption is considerably influenced by solution pH [30]. The solution pH resulted in a higher degree of cation adsorption when comes in contact with the adsorbent surface. Figure 3.11 illustrates the effect of solution pH (2 to 12) on MB removal by LD-slag-based synthesized zeolites. It was observed that variation in pH causes an irregular change in the MB removal efficiency along with its adsorbed amount (mg/g). As shown in Figures 3.11a and 3.11b the threshold pH value was found to be 4.9±0.3 and 5.5±0.3 for synthesized A and X-type zeolites, respectively. This threshold pH can be described by the value of zero point charge, as shown in Figure 3.10a. This indicates that the prepared samples will carry positive and negative charges before and after the threshold pH value respectively.

Table 3.4: Comparison study of MB removal by various types of zeolites reported in the different literature.

Adsorbent	Type	MB concentration (mg/L)	Adsorption capacity (mg/g)	MB removal (%)	References
Zeolite	Commercial	18	11.21	95	[26]
Zeolite	Fly ash-based	9.6	0.225	82	[27]
Zeolite	Natural	72	3.25	-	[28]
Zeolite	Commercial	25	8.67	98.22	[29]
Zeolite	Natural	11.35	23.50	-	[30]
Zeolite P1	Fly ash-based	50	9.12	~100	[31]
Zeolite X	Synthetic	10	2.04	99	[32]
Zeolite A	Synthetic	15	0.0067	-	[33]
Zeolite X	Synthetic	15	0.1543	-	[33]
Zeolite	Bagasse-based	63.97	14.296	96	[34]
ZSM-5	Synthetic	10	6.21	-	[35]
Zeolite	Fly ash-based	-	12.64	-	[36]
Zeolite A	**LD-slag-based**	**15**	**25.30**	**98.13**	**This study**
Zeolite X	**LD-slag-based**	**15**	**23.57**	**94.47**	**This study**

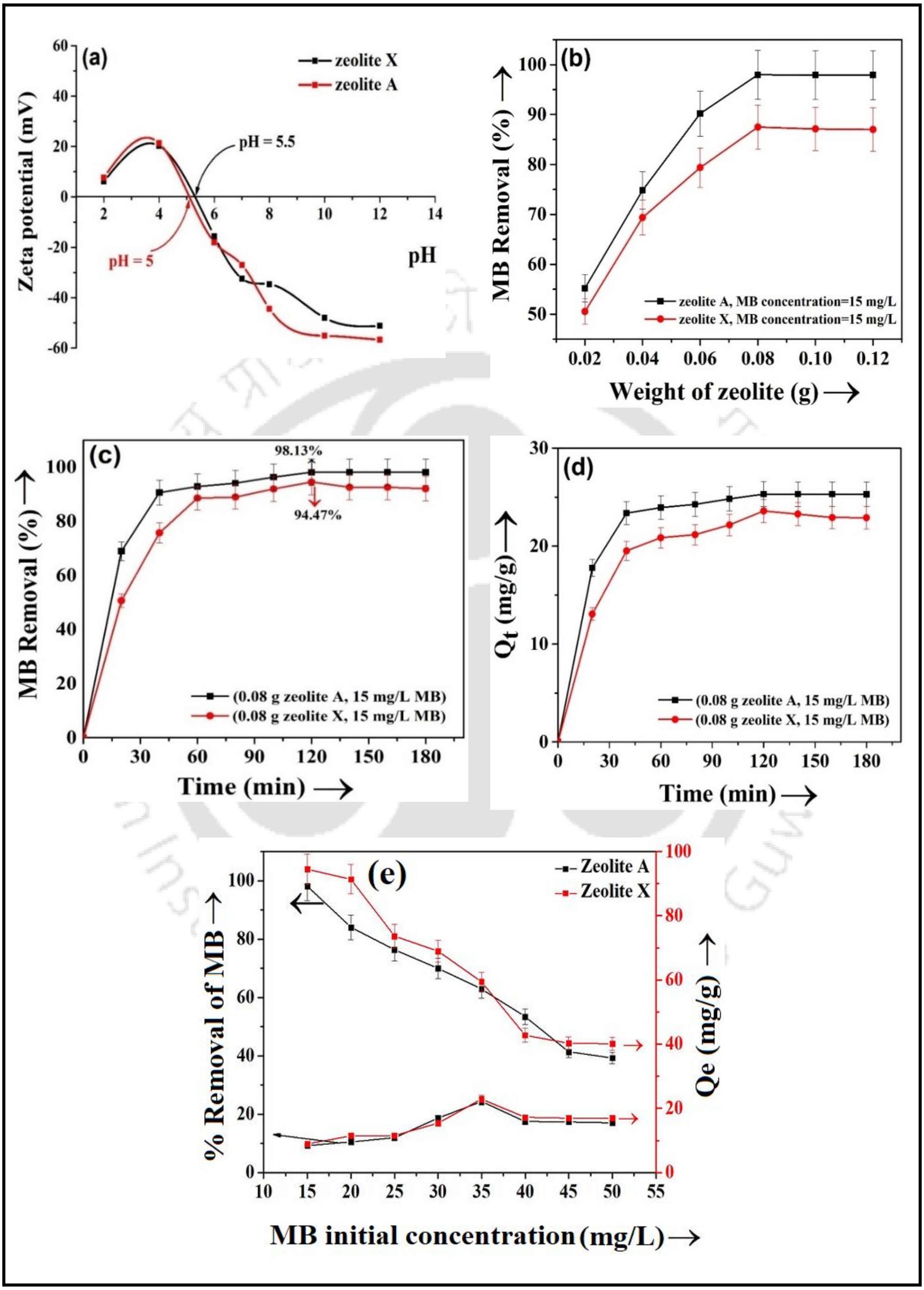

Figure 3.10: (a) Isoelectric point, (b) effect of zeolite amount and (c) time on MB sorption, (d) adsorption capacity with respect to time of synthesized zeolites, (e) effect of MB initial concentration on % dye extraction and equilibrium sorption capacity.

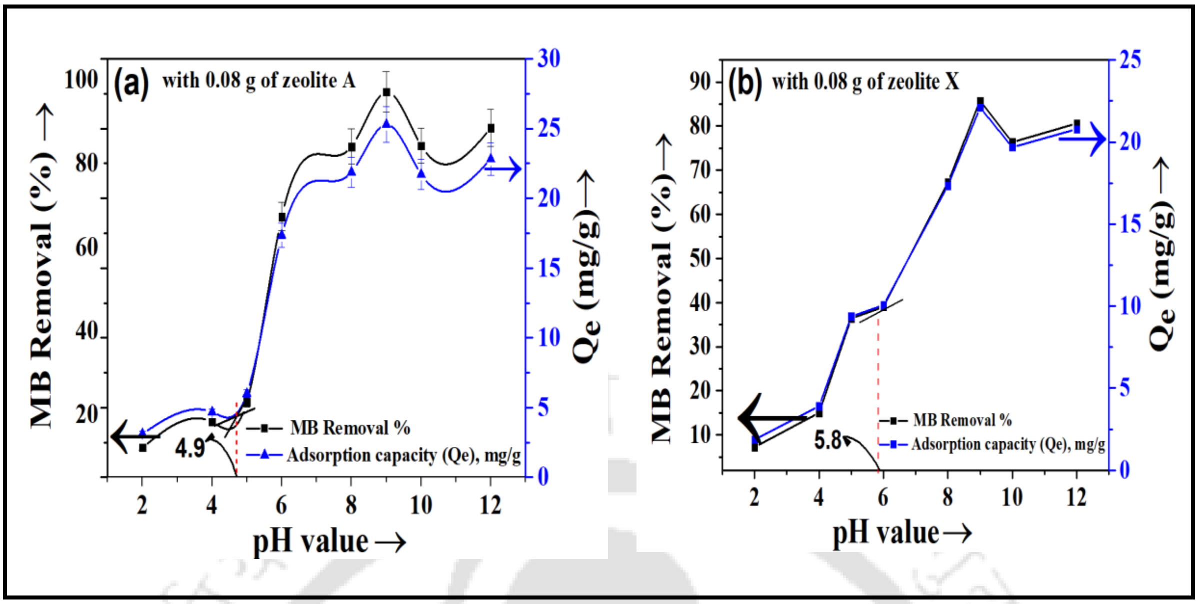

Figure 3.11. pH effect on MB removal and adsorption capacity (a) for zeolite A and (b) for zeolite X.

As depicted in Figures 3.11a and 3.11b, an increasing trend of adsorption capacity was observed immediately after the threshold pH, with maximal sorption capacity of 25.29 and 22.50 mg/g (which are very close to obtained adsorption capacity, shown in Figure 3.10d) obtained at pH 8.5±0.5 for zeolite A and zeolite X sample, respectively. The positively charged adsorbent surface at lower pH results in the generation of more H^+ ions to compete effectively with the cationic dye, thereby reducing the MB concentration. The adsorbent surface, on the other hand, will be negatively charged at higher pH (pH>pHzpc), which causes the electrostatic force of attraction of cationic dye to move towards the anionic sorbent surface, resulting in higher MB uptake capacity [37]. As seen in Figure 3.11, the amount of MB adsorbed is considerably reduced after pH 9, and a drastic reduction was observed at pH 10.9 ~ 11, followed by a slight increase up to pH 12 by both the adsorbents. The reduction in MB adsorption capacity and MB removal at a pH range of 9-11, may be attributed to the increase in repulsive forces that exist between the functional groups present on the adsorbent surface and dye anions [25,26,28]. Mainly, MB and other cationic dyes dissociate into strong molecular cations (C^+) and reduced CH^+ ions upon dissolution in water, and as a consequence, the adsorbent surface gets negatively charged at higher pH, and as such provides greater adsorption capacity [31,32].

It is apparent from the adsorption studies that zeolite A offers a significant adsorption capacity as compared to zeolite X. The possible reasons could be: (i) zeolite A exhibits a highly negative charge in water and as such the electrostatic attraction will favor the affinity of basic dye molecules towards the zeolite surface; (ii) the number of pores and its size may also influence the adsorption process. As zeolite A has a higher specific surface area than zeolite X, the number of pores will be more in zeolite A. In addition, the methylene blue and zeolite pore sizes are found to be 13.82 A° (1.382 nm) and 18.20-60 A° (1.82-6 nm), respectively. These values suggest that the dye molecules can be easily absorbed into the pores due to the high concentration gradient and active functional group present in the pores.

3.5. Adsorption isotherm analysis

Figure 3.12 illustrates MB adsorption equilibrium data at pH 8.5 (±0.2) and a temperature of 25°C. Results achieved from the study revealed that slag-modified zeolites have a higher adsorption affinity towards methylene blue. To investigate the adsorption behavior, Langmuir, Freundlich, and Temkin isotherm models (Table 3.5) were employed. Table 3.5 shows the associated parameters generated from the previous equations. The experimental findings are well in agreement with Langmuir model Figure 3.12 (R^2>0.99) rather than other models for both synthesized adsorbents. The order of equilibrium adsorption models that best fit the experimental data was: Langmuir >Freundlich>Temkin. The Langmuir isotherm model, in which C_e (mg/L) and Q_e (mg/g) represent adsorbate concentration and sorption capacity at equilibrium, respectively; whereas K_L (L/mg) is equilibrium adsorption constant and Q_m represents adsorption capacity in monolayer, expressed by (mg/g).

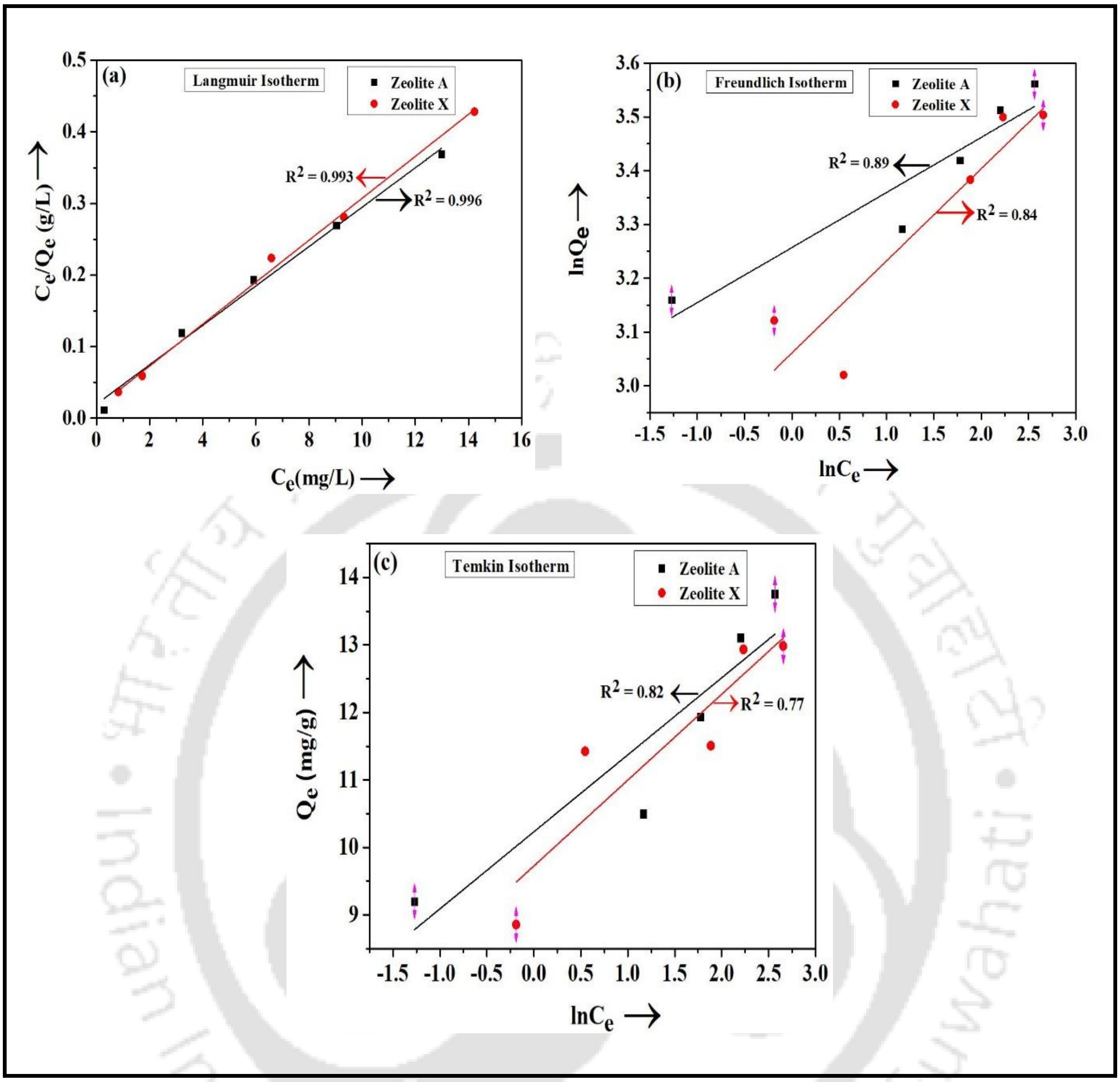

Figure 3.12: (a) Langmuir, (b) Freundlich, and (c) Temkin model plot for dye adsorption study onto synthesized zeolites.

In the same way, Table 3.5 displays the Freundlich isotherm model, where C_e and Q_e have the same meanings as mentioned before, and n and K_F are empirical constants. At 298K with 0.08 g prepared zeolites, the Langmuir monolayer sorption capacity was estimated to be 20 and 25.44 mg/g, respectively. The separation factor with no dimensions (R_L) is a crucial parameter in the Langmuir model [38,39], which may be described as follows:

$$R_L = \frac{1}{1+K_L C_0} \tag{3.3}$$

K_L represents the Langmuir constant whereas C_0 denotes the initial MB concentration. R_L implies the isotherm's character, such as (a) unfavourable when larger than 1 (b) if $R_L = 1$, the result is linear (c) R_L in a range of 0-1, indicates it is advantageous (d) when R_L equals to zero (0), it is irreversible.

In our current investigation, R_L was determined to be in the 0 to 1.0 working range (0.085 and 0.11, respectively, Table 3.5) of MB concentration, implying that MB adsorption onto the LD-slag modified zeolite A and X was favourable under the experimental circumstances. The Langmuir adsorption model also implies that each adsorbate molecule occupies just one active site on the surface of the adsorbent, therefore the highest sorption is associated with a saturated monolayer of adsorbate molecules on the active site of FAU-type zeolite X and zeolite A, respectively.

The Freundlich isotherm model may be applied to more than only monolayer adsorption. Non-ideal heterogeneous sorption systems can be described using this approach. The presence of many functional groups on the adsorbent surface produces the non-ideal heterogeneous character of any system. The R^2 value from the Freundlich isotherm model (Figure 3.12a) was recorded to be 0.89 and 0.84 for zeolite A and zeolite X, respectively, indicating that the curve is not well fitted. It also implies that there is no physisorption in this adsorption process. The derived 'n' values of 9.98 and 5.88 from the Freundlich model span from 1 to 10, indicating that the sorption process took place on active sites of the synthesized adsorbents [40–42]. In literature, similar isotherm results were obtained for various clay-dye systems [43,44].

Table 3.5: Different isotherm variables for MB sorption at 298K over zeolite A and X originated from LD-slag.

Values		
Parameters	**Langmuir isotherm model: $Q_e = \frac{Q_m K_L C_e}{1+K_L C_e}$**	
	Zeolite A	**Zeolite X**
Q_m (mg/g)	20	25.40
R_L	0.085	0.11
K_L (L/mg)	0.70	0.52
R^2	0.996	0.993
Parameters	**Freundlich isotherm model: $Q_e = KFC_e^{\frac{1}{n}}$**	
KF (mg/g)(L/mg)$^{1/n}$)	25.15	21.32
n	9.99	5.88
R^2	0.89	0.84
Parameters	**Temkin isotherm model: $Q_{e = a+blogC_e}$**	
a (L/mg)	2.92	3.25
b (J/Mol)	26.19	24.19
R^2	0.82	0.77

The Temkin isotherm model is shown in Figure 3.12c. This isotherm's R^2 values of 0.82 and 0.77 indicate that the sorption isotherm was not solely a chemisorption model.

When the R^2 values for both the isotherm models from Table 3.5 are compared, it is clear that the Langmuir isotherm (R^2 = 0.99) better fits the sorption data than the Freundlich and Temkin isotherm, indicating that the dye molecules are chemically adsorbed on the surface of extremely negative charged synthesized zeolites due to electrostatic force [45–47].

3.6. Design of Adsorption model

3.6.1. Adsorption Mechanism

To comprehend the adsorption of methylene blue on synthesized zeolite type-A and X, some knowledge of the adsorption mechanism is required. In most cases, the adsorption process may be demonstrated in many steps: (i) diffusion of the target substance from the bulk solution to the sorbent surface-encircled film; (ii) diffusion through the film (film diffusion) to the adsorbent's exterior solid surface; (iii) pore diffusion or infiltration of the pores and (iv) The target material's sorption and desorption inside the solid surface and the pores [1]. Steps (i) and (ii) are crucial for the rate-determining of the sorption process because these two processes are the slowest. The other two, on the other hand, are quick steps. To assess the diffusion mechanism the Diffusion-Chemisorption model [1], Boyed model [1], and Weber–Morris intraparticle diffusion [1] models were used. The details investigation of the said models is demonstrated in the subsequent section.

3.6.2. Kinetic Data Analysis

The MB adsorption rate, mass transfer, and equilibrium contact period for adsorption are the controlling mechanism in the adsorption kinetic study, which is shown in Figure 3.17. For MB adsorption on synthesized zeolite minerals, Table 3.6 gives the various kinetic parameters of pseudo-first and second-order, Diffusion-chemisorption, Webber-Morrison, and Boyd kinetic models.

The kinetics of the methylene blue sorption process by A and X-type zeolite were examined using two empirical models: pseudo-first-order and pseudo-second-order. Where, K_1 (1/min), and K_2 (g (mg/min)) are rate constant, Q_t (mg/g) and Qe (mg/g) denote the quantity of MB

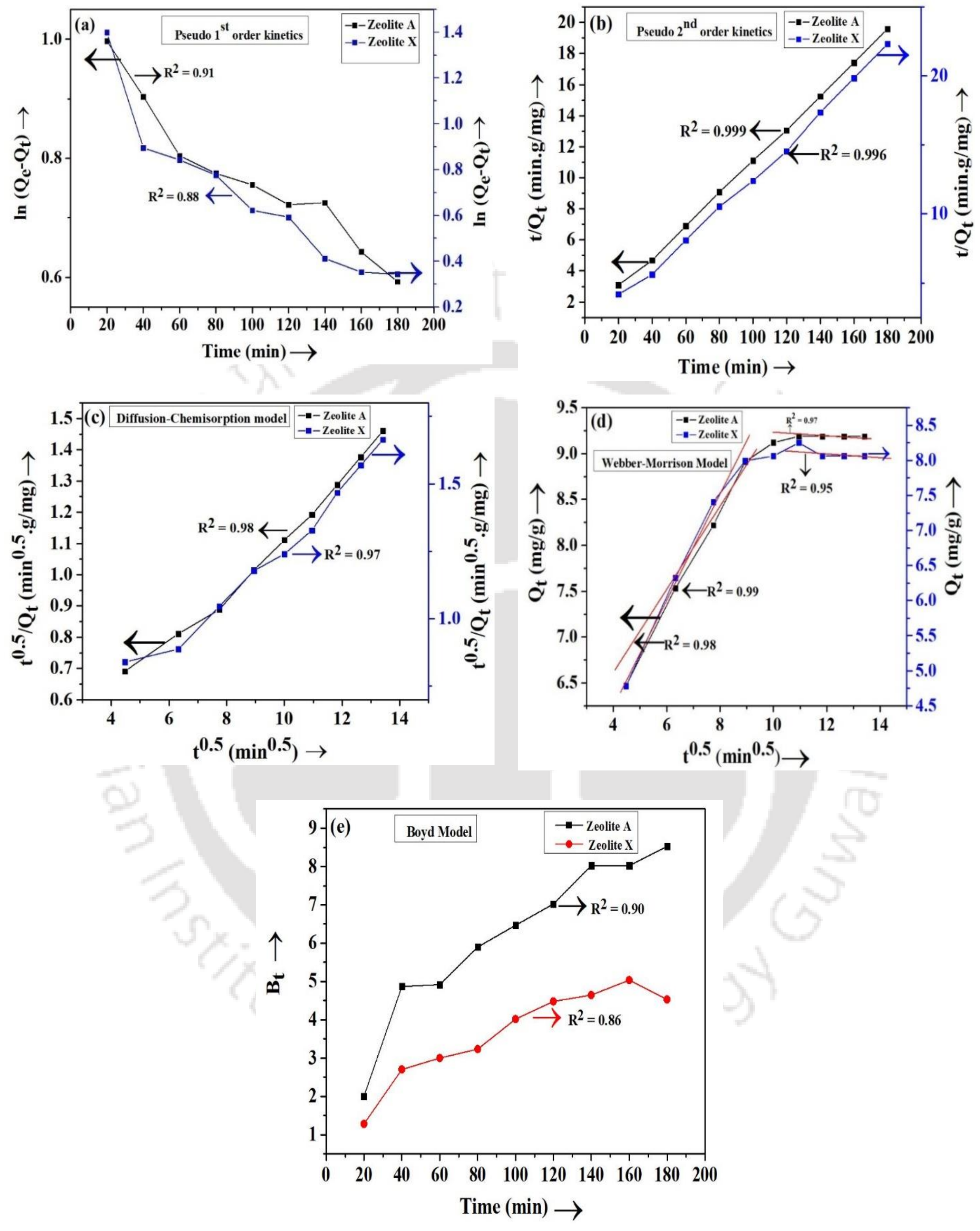

Figure 3.13: Kinetics models (a) Pseudo-first-order (b) Pseudo-second-order (c) Diffusion-Chemisorption model (d) Webber-Morrison, and (e) Boyd model at (Initial MB concentration = 15 mg/L, Adsorbents dosage = 0.08 g, Contact period = 180 minutes, Temperature = 25°C).

adsorbed at any time t (minute) and equilibrium state, respectively. From the liner plot ($\frac{t}{Q_t}$) vs t (Figure 3.13b) and $\ln(Q_e - Q_t)$ vs t (Figure 3.13a) the kinetic variables of pseudo-second and pseudo-first-order models were estimated and enlisted in Table 3.6.

Table 3.6: Different kinetics variables for MB sorption at 298K onto zeolite A and X prepared from LD-slag with an initial MB concentration of 15 mg/L.

Values		
Parameters	**Pseudo-first-order kinetic equation: $Q_t = Q_e(1 - e^{-k_1 t})$**	
	Zeolite A	**Zeolite X**
Q_e (mg/g)	9.18	8.83
K_1 (1/min)	0.002	0.005
R^2	0.91	0.88
Parameters	**Pseudo-second-order kinetic model: $Q_t = \frac{Q_e^2 K_2 t}{(1+Q_e K_2 t)}$**	
Q_e (mg/g)	9.18	8.83
K_2 (g/(mg min))	0.114	0.104
R^2	0.999	0.996
Parameters	**Diffusion-Chemisorption kinetic equation: $\frac{t^{0.5}}{Q_t} = \frac{1}{K_4} + \frac{t^{0.5}}{Q_e}$**	
Q_e	9.18	8.83
K_4((mg/g) min$^{0.5}$)	0.090	0.095
R^2	0.98	0.97
Parameters	**Webber-Morrison kinetic equation: $Q_t = K_3 t^{0.5} + C$**	
C (mg/g)	5.61	3.27
K_3((mg/g) min$^{0.5}$)	0.301	0.406
R^2	0.99	0.98
Parameters	**Boyd kinetic equation: $\log(1 - F) = -\left(\frac{K_R}{2.303}\right) t$**	
K_R	0.035	0.020
Intercept	2.62	1.61
R^2	0.90	0.86

The higher correlation coefficients were found to be $R^2 = 0.999$ and $R^2 = 0.996$ for pseudo-second-order rather than pseudo-first-order ($R^2 = 0.91$ and $R^2 = 0.88$) which refers that adsorption is controlled by chemisorption on the surface of zeolite A and X, respectively. Moreover, from Table 3.6 it is also clear that in the pseudo-second-order kinetic model, the sorption rate constant (K_2) for zeolite A (0.114 (g (mg/min))) is a bit higher than zeolite X (0.104 (g (mg/min))), results suggest that rate of MB adsorption towards A-type zeolite is higher than X-type zeolite that may be due to highly negatively charge presence on A-type zeolite (surface charge: -52.60 mV) rather than zeolite type-X (surface charge: -43.90 mV) which resulting in a higher interaction between adsorbate and adsorbent surface in aqueous media [48,49].

Figure 3.13c depicts the diffusion-chemisorption model that has been used to explain the MB adsorption on heterogeneous adsorbents. All kinetic parameters of the diffusion-chemisorption model are tabulated in Table 3.6. The R^2 value of 0.98 and 0.97 for synthesized adsorbents reveals that adsorbate molecules penetrate the pore channel of prepared zeolites. However, the adhesion of MB molecules towards the adsorbent's surface due to electrostatic attraction might be the other possibility for diffusion-chemisorption [47].

Similarly, in Table 3.6 the Webber-Morrison model equation is given along with other parameters where K_3 ((mg/g) $min^{0.5}$) and C (mg/g) represent the rate constant and boundary layer thickness, respectively. The intraparticle-diffusion model graph is shown in Figure 3.13d. From the plot, two distinct straight lines at different times were observed for both adsorbents, which in turn suggests that intraparticle diffusion does not fully control the adhesion of MB molecules. The first line segment was caused by intraparticle diffusion, whereas, the formation of the equilibrium phase was determined by the second line segment. In addition, the intercept of the graph did not pass through the origin (i.e. (0, 0) point), as shown in Figure 3.13d, signifying that the boundary layer impact cannot be ignored over intraparticle diffusion [37,47]. Therefore, diffusion may occur in multistage during the sorption operation.

In Boyd kinetic model (Table 3.6), F can be represented as F= $\frac{Q_t}{Q_e}$, where the significance of Q_e and Q_t have been discussed above. The model signifies that if a linear plot of B_t vs. t (minute) passes through the origin, the particle diffusion approach controls the adsorption process; otherwise, film diffusion can be regarded as a rate-determining phase for the process [2,50]. These results are consistent with the literature [22,51,52]. Figure 3.13e displays a plot of B_t and t (minute), which demonstrates that the line does not pass through the origin (intercept value in Table 3.6), implying that the process is regulated by film diffusion.

3.7. Effect of Si/Al ratio on MB adsorption

In the present study, contact time, pH, and zeolite dosage determine the MB adsorption in aqueous media. Many literatures have confirmed the influence of the Si/Al ratio (zeolite framework) on adsorption studies. It was also reported that zeolite with a low Si/Al ratio makes its surface hydrophilic, while a high Si/Al ratio causes the surface to be hydrophobic [53]. It was also demonstrated that zeolite with a low Si/Al ratio and high hydrophilicity exhibits greater interaction with the polar molecules (water in the present study). On the other hand, a high Si/Al ratio with high hydrophobicity displays weak interaction with the polar solvent, however, results in strong interaction with the non-polar molecules, e.g. volatile organic compounds (VOCs) [53]. Here, the Si/Al ratio was maintained at 1.009 and 1.486 for zeolite A and zeolite X samples, respectively (Figure 3.14). Hence, the zeolite A sample exhibits a strong interaction with cationic dye molecules present in water as compared to zeolite X. This resulted in a higher removal efficiency of zeolite A over zeolite X. A comparison study of LD-slag processed zeolite A and zeolite X is discussed in Table 3.7.

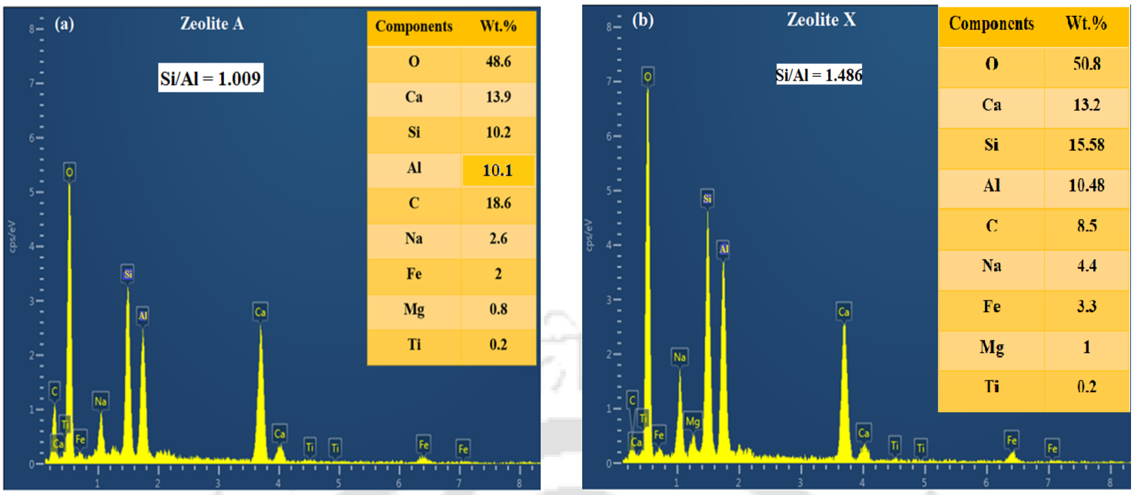

Figure 3.14: EDX analysis of (a) zeolite A and (b) zeolite X.

Table 3.7: Comparison study of zeolite A and FAU-type zeolite X from LD-slag solid waste, modified by conventional fusion-assisted hydrothermal treatment.

Analysis method	Zeolite A	Zeolite X
XRD	No drastic change in peak intensity was observed at pH 7 and 12 but peak intensity changes occurred at pH 2.	The same trend has been found for the Zeolite X sample. The reason may be due to decreasing Si/Al ratio in an acidic solution i.e. at pH 2.
FTIR	The weaker Si-O-Si bond at 558 cm^{-1} for pH 7 and decreasing trend in hydrous metal oxides and flexion vibrational OH bond at 1400 and 1660 cm^{-1} at pH 2 and 7, respectively with treatment time, which can be assigned to the deformation of TiO_4 network. However, no Si-O-Si bond was noted at pH 2.	At pH 2 it was noted that frequency bands were observed through all treatment times (1-3 days) in all pH conditions which confirmed the presence of all zeolite functional groups that indicate better stability than zeolite A. However, the absence of the Si-O-Si bond at pH 12 is associated with unit cell deformation in their structure, Figure 3.5f.
FESEM	Hydration of zeolite leads to shrinkage of their crystal lattice due to the dislodgement of aluminum from the zeolite framework [10] at low pH conditions, shown in Figure	It is noticeable that more structural deformation, brittleness, irregular shape, surface rupture, and distortion occurred in pH 2, 7, and 12, respectively

	3.6a(i). It can be also considered that nonhomogeneous and irregular or asymmetrical zeolite crystal shape was found under basic conditions but uniform and cubical crystal has observed under neutral conditions, as shown in Figure 3.6c(i) and 3.6b(i), respectively.	which can be inferred from the weak Si and Al bond in the zeolite network or maybe reducing the Si/Al ratio that effect on zeolite structure, depicted in Figure 3.6a(ii), b(ii), and c(ii).
TGA-DTA	The highest residual mass of 89.55% was achieved in pH 7 at 948.5°C. The order of residual mass in the zeolite A sample concerning different pH conditions at the relatively same temperature ~ 949°C was pH 7>pH 12>pH 2 with a residual mass of 89.55%, 83.63%, 79.98%, respectively, Figure 3.8a-c. No exothermic has been observed in all pH conditions while corresponding endothermic peaks arrived at different temperature ranges.	For the zeolite X sample, the order of residual mass at different pH was found in the sequence of pH 7>pH 12>pH 2. The highest residual mass was 78.80% at 949.34°C. Only a single exothermic peak has been observed in the temperature range of 690-750°C at pH 12.
BET-surface area	The obtained specific surface area for zeolite A was 27.61 m^2/g with both micro and mesoporous-type pores ranging from 2 to 4.22. The results can refer to the high pore volume present in the sample.	For zeolite X the BET-surface area was estimated to be 14.17 m^2/g with only mesoporous type pores, ranging from 3.37 to 4.21.
Surface charge	The zeolite A sample shows a better surface charge of -52.60 mV.	For zeolite X the surface charge was found to be -43.90 mV.
Adsorption studies	MB removal was found at 98.13% with an adsorption capacity of 25.30 mg/g over synthesized zeolite A.	For synthesized zeolite X, MB removal was estimated to be 94.47% with an adsorption capacity of 23.57 mg/g.

3.8. Cost estimation for zeolite A and X preparation

It is known that the effectiveness of any adsorbent can be determined by its surface properties and the cost involved during adsorbent preparation. The present study implies the synthesis, physicochemical properties, and stability of LD-slag-based zeolite A and X. However, the methylene blue removal efficiency and sorption capacity of both the prepared adsorbents have also been examined to ensure their respective feasibility. Instead of commercially available zeolites, LD-slag solid waste was employed for the synthesis of zeolite A and X. In the present study, 5 g of LD-slag was taken which yielded 3.98 g of zeolite A and X, respectively. The cost of adsorbent preparation was estimated using the methods described by Mukherjee et al. [54] and is presented in Table 3.8. It can be seen that the production cost of zeolite A and zeolite X were found to be 8.74 USD and 8.72 USD, respectively which are in close proximity to one another. It was also estimated that the preparation of 100 g of zeolite A and zeolite X zeolite requires a fabrication cost of 8.95 USD and 8.93 USD, respectively.

The cost estimation study showed that the production of zeolite A (8.74 USD) and zeolite X (8.72 USD) via conventional hydrothermal treatment has proved to be a cost-effective method as compared to the commercially available zeolite A (102.48 USD) and zeolite X (95.58 USD), respectively. Therefore, it was concluded that the synthesis of zeolite A and zeolite X utilizing steel industry by-products (LD-slag) results in the production of high-value-added materials with low preparation costs.

Table 3.8: Cost estimation to synthesized zeolite type-A and X from solid LD-slag waste.

	Zeolite A			**Electric power consumption**			
Sl. no.	**Materials used**	**Weight taken**	**Price (in INR)**	**Instrument used**	**unit**	**Electric charge/Unit**	**Price (in INR)**
1.	**LD-slag**	5 g	0.00	Muffle Furnace	45.6	5.96	271.76
				Curing	14.4		83.44
2.	**NaOH**	7.5 g	4.42	Dryer	36		214.56
3.	**0.1N 20 mL HCl (37%)**	1.67 mL	0.74	HPMS	1.17		6.97
4.	**Sodium aluminate**	1.05 g	3.16				
			(a) Total= 8.32 INR				**(b)** Total= 576.73 INR
Overall cost for zeolite A production = (a+b) = 585.05 INR; Overhead charge = 10% of overall cost = 0.1×585.05 = 58.505 INR Net cost for zeolite A production = Overall cost + Overhead charge = 643.55 INR = 8.74 USD							
	Zeolite X			**Electric power consumption**			
Sl. no.	**Materials used**	**Weight taken**	**Price (in INR)**	**Instrument used**	**unit**	**Electric charge/Unit**	**Price (in INR)**
1.	**LD-slag**	5 g	0.00	Muffle Furnace	45.6	5.96	271.76
2.	**NaOH**	7.5 g	4.42	Curing	14.4		83.44
3.	**0.1N HCl (37%)**	1.67 mL	0.74	Hot air oven	36		214.56
4.	**Sodium aluminate**	0.5 g	1.47	HPMS	1.17		6.97
			(a) Total= 6.63 INR				**(b)** Total= 576.73 INR
Overall cost for zeolite X production = (a+b) = 583.36 INR; Overhead charge = 10% of overall cost = 0.1×583.36 = 58.336 INR Net cost for zeolite X production = Overall cost + Overhead charge = 641.696 INR = 8.72 USD							

USD: United States Dollar; HPMS: Hot plate magnetic stirrer

Summary

The zeolite-type A and faujasite-type zeolite X were prepared from steel industry LD-slag via fusion-facilitated hydrothermal treatment. Physico-chemical characteristics of both the zeolite samples were examined and it was found that zeolite A showed good thermal stability as compared to the zeolite X. The methylene blue adsorption study was conducted over the synthesized zeolites and results demonstrated that A-type zeolite exhibits better adsorption capacity than X-type zeolite. Overall, the utilization of waste LD-slag towards the zeolite like potential adsorbent synthesis may provide economic and environmental benefits.

References

[1] V. Volli, M.K. Purkait, Selective preparation of zeolite X and A from flyash and its use as catalyst for biodiesel production, J. Hazard. Mater. 297 (2015) 101–111. https://doi.org/10.1016/j.jhazmat.2015.04.066.

[2] N.S. Samanta, S. Banerjee, P. Mondal, Anweshan, U. Bora, M.K. Purkait, Preparation and characterization of zeolite from waste Linz-Donawitz (LD) process slag of steel industry for removal of Fe^{3+} from drinking water, Adv. Powder Technol. 32 (2021) 3372–3387. https://doi.org/10.1016/j.apt.2021.07.023.

[3] A. Khaleque, M.M. Alam, M. Hoque, S. Mondal, J. Bin Haider, B. Xu, M.A.H. Johir, A.K. Karmakar, J.L. Zhou, M.B. Ahmed, M.A. Moni, Zeolite synthesis from low-cost materials and environmental applications: A review, Environ. Adv. 2 (2020) 100019. https://doi.org/10.1016/j.envadv.2020.100019.

[4] S.S. Bukhari, J. Behin, H. Kazemian, S. Rohani, Conversion of coal fly ash to zeolite utilizing microwave and ultrasound energies: A review, Fuel. 140 (2015) 250–266. https://doi.org/10.1016/j.fuel.2014.09.077.

[5] P.K. Raul, R.R. Devi, I.M. Umlong, S. Banerjee, L. Singh, M. Purkait, Removal of fluoride from water using iron oxide-hydroxide nanoparticles., J. Nanosci. Nanotechnol. 12 (2012) 3922–3930. https://doi.org/10.1166/jnn.2012.5870.

[6] S.-Y. Pan, T.-C. Chung, C.-C. Ho, C.-J. Hou, Y.-H. Chen, P.-C. Chiang, CO2 Mineralization and Utilization using Steel Slag for Establishing a Waste-to-Resource Supply Chain, Sci. Rep. 7 (2017) 17227. https://doi.org/10.1038/s41598-017-17648-9.

[7] T.J.M. Fraga, M.P. da Silva, E.M.P. de Luna Freire, L.C. Almeida, M.A. da Motta Sobrinho, M.G. Ghislandi, M.N. Carvalho, Amino-functionalized graphene oxide supported in charcoal from the gasification of furniture scraps: From one-pot synthesis to wastewater remediation, Chem. Eng. Res. Des. 180 (2022) 109–122.

https://doi.org/10.1016/j.cherd.2022.02.006.

[8] Y. Li, T. Peng, W. Man, L. Ju, F. Zheng, M. Zhang, M. Guo, Hydrothermal synthesis of mixtures of NaA zeolite and sodalite from Ti-bearing electric arc furnace slag, RSC Adv. 6 (2016) 8358–8366. https://doi.org/10.1039/c5ra26881h.

[9] S.M. Al-Jubouri, S.M. Holmes, Hierarchically porous zeolite X composites for manganese ion-exchange and solidification: Equilibrium isotherms, kinetic and thermodynamic studies, Chem. Eng. J. 308 (2017) 476–491. https://doi.org/10.1016/j.cej.2016.09.081.

[10] S. Ashrit, R. V. Chatti, S. Sarkar, R. Venugopal, U.G. Nair, An infrared spectroscopic study of non-metallic portion of Linz-Donawitz slag fines generated at Tata Steel, Jamshedpur, Metall. Res. Technol. 115 (2018) 1–9. https://doi.org/10.1051/metal/2018024.

[11] M. Changmai, M. Pasawan, M.K. Purkait, A hybrid method for the removal of fluoride from drinking water: Parametric study and cost estimation, Sep. Purif. Technol. 206 (2018) 140–148. https://doi.org/10.1016/j.seppur.2018.05.061.

[12] Z. Ghasemi, H. Younesi, Preparation of free-template nanometer-sized Na-A and -X zeolites from rice husk ash, Waste and Biomass Valorization. 3 (2012) 61–74. https://doi.org/10.1007/s12649-011-9084-4.

[13] E.S. Behbahani, K. Dashtian, M. Ghaedi, Fe_3O_4-$FeMoS_4$: Promise magnetite LDH-based adsorbent for simultaneous removal of Pb (II), Cd (II), and Cu (II) heavy metal ions, J. Hazard. Mater. 410 (2021) 124560. https://doi.org/10.1016/j.jhazmat.2020.124560.

[14] W. Mozgawa, M. Król, K. Barczyk, FT-IR studies of zeolites from different structural groups, Chemik. 65 (2011) 671–674.

[15] V. Sivasankar, Zeolites from fireworks ash: synthesis and characterization through ftir

and xrd studies, (2014).

[16] P.P. Das, Anweshan, M.K. Purkait, Treatment of cold rolling mill (CRM) effluent of steel industry, Sep. Purif. Technol. 274 (2021) 119083. https://doi.org/https://doi.org/10.1016/j.seppur.2021.119083.

[17] A. Khaleque, M.M. Alam, M. Hoque, S. Mondal, J. Bin Haider, B. Xu, M.A.H. Johir, A.K. Karmakar, J.L. Zhou, M.B. Ahmed, M.A. Moni, Zeolite synthesis from low-cost materials and environmental applications: A review, Environ. Adv. 2 (2020) 100019. https://doi.org/https://doi.org/10.1016/j.envadv.2020.100019.

[18] Z. Latifi, M. Jalali, Measuring and Simulating Co(II) Sorption on Waste Calcite, Zeolite and Kaolinite, Nat. Resour. Res. 29 (2020) 967–981. https://doi.org/10.1007/s11053-019-09475-8.

[19] W.F. Monteiro, F.M. Diz, L. Andrieu, F.B. Morrone, R.A. Ligabue, K. Bernardo-Gusmão, M.O. de Souza, A.J. Schwanke, Waste to health: Ag-LTA zeolites obtained by green synthesis from diatom and rice-based residues with antitumoral activity, Microporous Mesoporous Mater. 307 (2020) 110508. https://doi.org/https://doi.org/10.1016/j.micromeso.2020.110508.

[20] Z. Liu, S. Li, L. Li, J. Wang, Y. Zhou, D. Wang, One-step high efficiency crystallization of zeolite A from ultra-fine circulating fluidized bed fly ash by hydrothermal synthesis method, 257 (2019). https://doi.org/10.1016/j.fuel.2019.116043.

[21] M.K. Purkait, S. DasGupta, S. De, Determination of design parameters for the cloud point extraction of congo red and eosin dyes using TX-100, Sep. Purif. Technol. 51 (2006) 137–142. https://doi.org/https://doi.org/10.1016/j.seppur.2005.12.027.

[22] O. Duman, S. Tunç, Electrokinetic and rheological properties of Na-bentonite in some electrolyte solutions, Microporous Mesoporous Mater. 117 (2009) 331–338.

https://doi.org/https://doi.org/10.1016/j.micromeso.2008.07.007.

[23] S. Tunç, O. Duman, B. Kancı, Rheological measurements of Na-bentonite and sepiolite particles in the presence of tetradecyltrimethylammonium bromide, sodium tetradecyl sulfonate and Brij 30 surfactants, Colloids Surfaces A Physicochem. Eng. Asp. 398 (2012) 37–47. https://doi.org/https://doi.org/10.1016/j.colsurfa.2012.02.006.

[24] N. Barka, S. Qourzal, A. Assabbane, A. Nounah, Y. Ait-Ichou, Removal of Reactive Yellow 84 from aqueous solutions by adsorption onto hydroxyapatite, J. Saudi Chem. Soc. 15 (2011) 263–267. https://doi.org/10.1016/j.jscs.2010.10.002.

[25] M.K. Purkait, S. DasGupta, S. De, Determination of thermodynamic parameters for the cloud point extraction of different dyes using TX-100 and TX-114, Desalination. 244 (2009) 130–138. https://doi.org/https://doi.org/10.1016/j.desal.2008.04.042.

[26] K. Rida, S. Bouraoui, S. Hadnine, Adsorption of methylene blue from aqueous solution by kaolin and zeolite Applied Clay Science Adsorption of methylene blue from aqueous solution by kaolin and zeolite, Appl. Clay Sci. 83–84 (2019) 99–105. https://doi.org/10.1016/j.clay.2013.08.015.

[27] D.A. Fungaro, M. Bruno, L.C. Grosche, Adsorption and kinetic studies of methylene blue on zeolite synthesized from fly ash, Desalin. Water Treat. 2 (2009) 231–239. https://doi.org/10.5004/dwt.2009.305.

[28] R. Han, Y. Wang, W. Zou, Y. Wang, J. Shi, Comparison of linear and nonlinear analysis in estimating the Thomas model parameters for methylene blue adsorption onto natural zeolite in fixed-bed column, J. Hazard. Mater. 145 (2007) 331–335. https://doi.org/10.1016/j.jhazmat.2006.12.027.

[29] X. Jin, M. Jiang, X. Shan, Z. Pei, Z. Chen, Journal of Colloid and Interface Science Adsorption of methylene blue and orange II onto unmodified and surfactant-modified zeolite, J. Colloid Interface Sci. 328 (2008) 243–247.

https://doi.org/10.1016/j.jcis.2008.08.066.

[30] S. Wang, Z.H. Zhu, Characterisation and environmental application of an Australian natural zeolite for basic dye removal from aqueous solution, 136 (2006) 946–952. https://doi.org/10.1016/j.jhazmat.2006.01.038.

[31] V. Prajaputra, Z. Abidin, Widiatmaka, D.T. Suryaningtyas, H. Rizal, Characterization of Na-P1 zeolite synthesized from pumice as low-cost materials and its ability for methylene blue adsorption, IOP Conf. Ser. Earth Environ. Sci. 399 (2019). https://doi.org/10.1088/1755-1315/399/1/012014.

[32] M. Shirani, A. Semnani, H. Haddadi, S. Habibollahi, Optimization of simultaneous removal of methylene blue, crystal violet, and fuchsine from aqueous solutions by magnetic NaY zeolite composite, Water. Air. Soil Pollut. 225 (2014). https://doi.org/10.1007/s11270-014-2054-2.

[33] W. Chunfeng, L.I. Jiansheng, W. Lianjun, S.U.N. Xiuyun, Adsorption of Dye from Wastewater by Zeolites Synthesized from Fly Ash : Kinetic and Equilibrium Studies *, Chinese J. Chem. Eng. 17 (2009) 513–521. https://doi.org/10.1016/S1004-9541(08)60239-6.

[34] B.A. Shah, A. V. Shah, H.D. Patel, Alkaline hydrothermal conversion of agricultural waste bagasse fly ash into zeolite: Utilisation in dye removal from aqueous solution, Int. J. Environ. Waste Manag. 7 (2011) 192–208. https://doi.org/10.1504/IJEWM.2011.037376.

[35] S. Prodinger, M.A. Derewinski, Erratum to: Recent Progress to Understand and Improve Zeolite Stability in the Aqueous Medium, Pet. Chem. 61 (2021) 1084. https://doi.org/10.1134/S0965544121090176.

[36] C.D. Woolard, J. Strong, C.R. Erasmus, Evaluation of the use of modified coal ash as a potential sorbent for organic waste streams, 17 (2002) 1159–1164.

[37] M. Ghaedi, S. Hajati, M. Zaree, Y. Shajaripour, A. Asfaram, M.K. Purkait, Removal of methyl orange by multiwall carbon nanotube accelerated by ultrasound devise: Optimized experimental design, Adv. Powder Technol. 26 (2015) 1087–1093. https://doi.org/https://doi.org/10.1016/j.apt.2015.05.002.

[38] S. Kanrar, S. Debnath, P. De, K. Parashar, K. Pillay, P. Sasikumar, U.C. Ghosh, Preparation, characterization and evaluation of fluoride adsorption efficiency from water of iron-aluminium oxide-graphene oxide composite material, Chem. Eng. J. 306 (2016) 269–279. https://doi.org/10.1016/j.cej.2016.07.037.

[39] M. Moghaddari, F. Yousefi, M. Ghaedi, K. Dashtian, A simple approach for the sonochemical loading of Au, Ag and Pd nanoparticle on functionalized MWCNT and subsequent dispersion studies for removal of organic dyes: Artificial neural network and response surface methodology studies, Ultrason. Sonochem. 42 (2018) 422–433. https://doi.org/10.1016/j.ultsonch.2017.12.003.

[40] F. Gorzin, M.M. Bahri Rasht Abadi, Adsorption of Cr(VI) from aqueous solution by adsorbent prepared from paper mill sludge: Kinetics and thermodynamics studies, Adsorpt. Sci. Technol. 36 (2017) 149–169. https://doi.org/10.1177/0263617416686976.

[41] M. Firoozi, Z. Rafiee, K. Dashtian, New MOF/COF Hybrid as a Robust Adsorbent for Simultaneous Removal of Auramine O and Rhodamine B Dyes, ACS Omega. 5 (2020) 9420–9428. https://doi.org/10.1021/acsomega.0c00539.

[42] T.J.M. Fraga, D.M.D.S.M. Fraga, T.C. da Silva, M.N. Carvalho, M.A. da M. Sobrinho, Adsorption of reactive dyes onto thermally treated waste from aluminum lamination, Water Pract. Technol. 13 (2018) 629–641. https://doi.org/10.2166/WPT.2018.076.

[43] O. Duman, S. Tunç, T. Gürkan Polat, Adsorptive removal of triarylmethane dye (Basic Red 9) from aqueous solution by sepiolite as effective and low-cost adsorbent,

Microporous Mesoporous Mater. 210 (2015) 176–184. https://doi.org/https://doi.org/10.1016/j.micromeso.2015.02.040.

[44] O. Duman, S. Tunç, T.G. Polat, Determination of adsorptive properties of expanded vermiculite for the removal of C. I. Basic Red 9 from aqueous solution: Kinetic, isotherm and thermodynamic studies, Appl. Clay Sci. 109–110 (2015) 22–32. https://doi.org/https://doi.org/10.1016/j.clay.2015.03.003.

[45] R.B. de Assis Filho, A.M.S. Baptisttella, C.M.B. de Araujo, T.J.M. Fraga, T.M.N. de Paiva, C.A.M. de Abreu, M.A. da Motta Sobrinho, Removal of textile dyes by benefited marine shells wastes: From circular economy to multi-phenomenological modeling, J. Environ. Manage. 296 (2021). https://doi.org/10.1016/j.jenvman.2021.113222.

[46] T.J.M. Fraga, M.N. Carvalho, D.M. dos S.M. Fraga, M. do C.L. da Silva, J.M. Ferreira, M.A. da Motta Sobrinho, Treated residue from aluminium lamination as adsorbent of toxic reactive dyes–a kinetic, equilibrium and thermodynamic study, Environ. Technol. (United Kingdom). 41 (2020) 669–681. https://doi.org/10.1080/09593330.2018.1508255.

[47] P. Mondal, M.K. Purkait, Preparation and characterization of novel green synthesized iron–aluminum nanocomposite and studying its efficiency in fluoride removal, Chemosphere. 235 (2019) 391–402. https://doi.org/https://doi.org/10.1016/j.chemosphere.2019.06.189.

[48] L. Abramian, H. El-Rassy, Adsorption kinetics and thermodynamics of azo-dye Orange II onto highly porous titania aerogel, Chem. Eng. J. 150 (2009) 403–410. https://doi.org/https://doi.org/10.1016/j.cej.2009.01.019.

[49] T.M.N. De Paiva, T.J.M. Fraga, D.C.S. Sales, M.N. Carvalho, M.A. Da Motta Sobrinho, Anomalocardia brasiliana shellfish shells as a novel and ecofriendly

adsorbent of Nylosan Brilliant Blue acid dye, Water Sci. Technol. 78 (2018) 1576–1586. https://doi.org/10.2166/wst.2018.434.

[50] M. Ghaedi, K. Dashtian, A.M. Ghaedi, N. Dehghanian, A hybrid model of support vector regression with genetic algorithm for forecasting adsorption of malachite green onto multi-walled carbon nanotubes: Central composite design optimization, Phys. Chem. Chem. Phys. 18 (2016) 13310–13321. https://doi.org/10.1039/c6cp01531j.

[51] E. Ayranci, O. Duman, Structural effects on the interactions of benzene and naphthalene sulfonates with activated carbon cloth during adsorption from aqueous solutions, Chem. Eng. J. 156 (2010) 70–76. https://doi.org/https://doi.org/10.1016/j.cej.2009.09.038.

[52] O. Duman, S. Tunç, T.G. Polat, B.K. Bozoğlan, Synthesis of magnetic oxidized multiwalled carbon nanotube-κ-carrageenan-Fe3O4 nanocomposite adsorbent and its application in cationic Methylene Blue dye adsorption, Carbohydr. Polym. 147 (2016) 79–88. https://doi.org/https://doi.org/10.1016/j.carbpol.2016.03.099.

[53] C. Wang, S. Leng, H. Guo, J. Yu, W. Li, L. Cao, J. Huang, Quantitative arrangement of Si/Al ratio of natural zeolite using acid treatment, Appl. Surf. Sci. 498 (2019) 143874. https://doi.org/10.1016/j.apsusc.2019.143874.

[54] S. Mukherjee, S. Barman, G. Halder, Fluoride uptake by zeolite NaA synthesized from rice husk: Isotherm, kinetics, thermodynamics and cost estimation, Groundw. Sustain. Dev. 7 (2018) 39–47. https://doi.org/10.1016/j.gsd.2018.03.003.

Chapter 4

Fabrication of LD-slag derived Zeolite Y coated Polysulfone (PSf) membrane for decontamination of groundwater

Faujesite type zeolite Y was prepared via ultrasonic energy facilitated hydrothermal technique utilizing Linz-Donawitz (LD) process slag as a precursor material. The surface modification of the PSf membrane was conducted with the as-synthesized zeolite powder in the presence of N-methyl pyrrolidone (NMP) solvent and discussed in this chapter. The morphology and structure of the obtained membranes were examined by a field emission scanning electron microscope (FESEM). Chemical analysis and electronic configuration of the membrane surface were examined by X-ray photoelectron spectroscopy (XPS). The permeation performances of the membranes were evaluated in terms of pure water flux (PWF), while hydrophilicity was evaluated in terms of porosity, equilibrium water content (EWC), and static water contact angle. The modified PSf membrane was used to remove detrimental elements like fluoride (F^-), manganese (Mn^{2+}), and chromium (Cr^{6+}) from the groundwater sample.

4.1. Experimental

4.1.1. Materials

LD-slag used in this study was kindly provided by TATA Steel Industry Ltd., Jamshedpur, India. Hydrochloric acid (37%), sodium hydroxide pellets (98%), sodium aluminate (99.99%), sodium silicate (99%) for zeolite production, polysulfone (Mw =35000 g/mol) and 1-Methyl-2-pyrrolidone (NMP) anhydrous (99.5%) was procured from Sigma Aldrich. Salts of different metal ions were purchased from Merck for preparation.

Content of this chapter has been submitted for publication as below:

N. S. Samanta, Piyal Mondal, S. Dhara, Utpal Bora, M.K. Purkait, Fabrication of LD-slag derived Zeolite Y coated Polysulfone (PSf) membrane for decontamination of groundwater, Chemical Engg. J.

4.1.2. Synthesis of zeolite Y nanoparticles

The Y-type zeolite synthesis experiment was conducted through a fusion-boosted hydrothermal process preceded by a sonochemical technique. The predetermined LD-slag was calcined and leached with 1M hydrochloric acid (HCl, 37%) to remove volatile and unwanted metal oxides before the fusion step. The synthesis experiment consisted of several steps. The acid-leached LD-slag and NaOH were mixed with a weight ratio of 1:1.2 and were ground by a mechanical mortar and further, the resultant mixture was heated for 1 hour at 550°C. The obtained solid mass was again ground and the obtained powder was mixed with de-ionized water (1:10 w/v ratio) and stirred for 12 hours wherein sodium aluminate and sodium silicate powder were added sequentially to maintain the Si/Al ratio of synthesized zeolite. The resulting mixture was then placed in an ultra-sonication bath (240 W; 35 KHz) for 1 hour and then pour into a Teflon lid stainless steel hydrothermal reactor (100 mL). The reactor was then placed in a hot air oven at 100°C for 24 hours. The resultant viscous solution was then filtered until pH ~8 was attained. The mixture was then evaporated overnight at 100°C to obtain the final product. The entire sonochemical preceded hydrothermal treatment for zeolite synthesis is depicted in Figure 4.1a.

4.1.3. Zeolite-coated membrane fabrication

Figure 4.1b depicts a step-by-step synthesis route for the synthesis of zeolite Y-coated nanolayered PSf membrane. As is shown in Figure 4.1b, a known quantity of zeolite nanopowder was mixed with NMP to get the desired solution and then sonicated for 30 minutes. The substrate polymer matrix (PSf) was pulled off on a glass plate using a glass rod and the zeolite-NMP solution was then sprayed over the film surface homogeneously. Thereafter, the resultant thin film matrix was kept at room temperature for 5 minutes and then placed in a hot air oven at 60°C for 30-45 minutes. The obtained zeolite-coated polymer matrix is then dipped into the de-ionized (DI) water (non-solvent) bath to obtain the final zeolite Y-coated nano-layered PSf membrane.

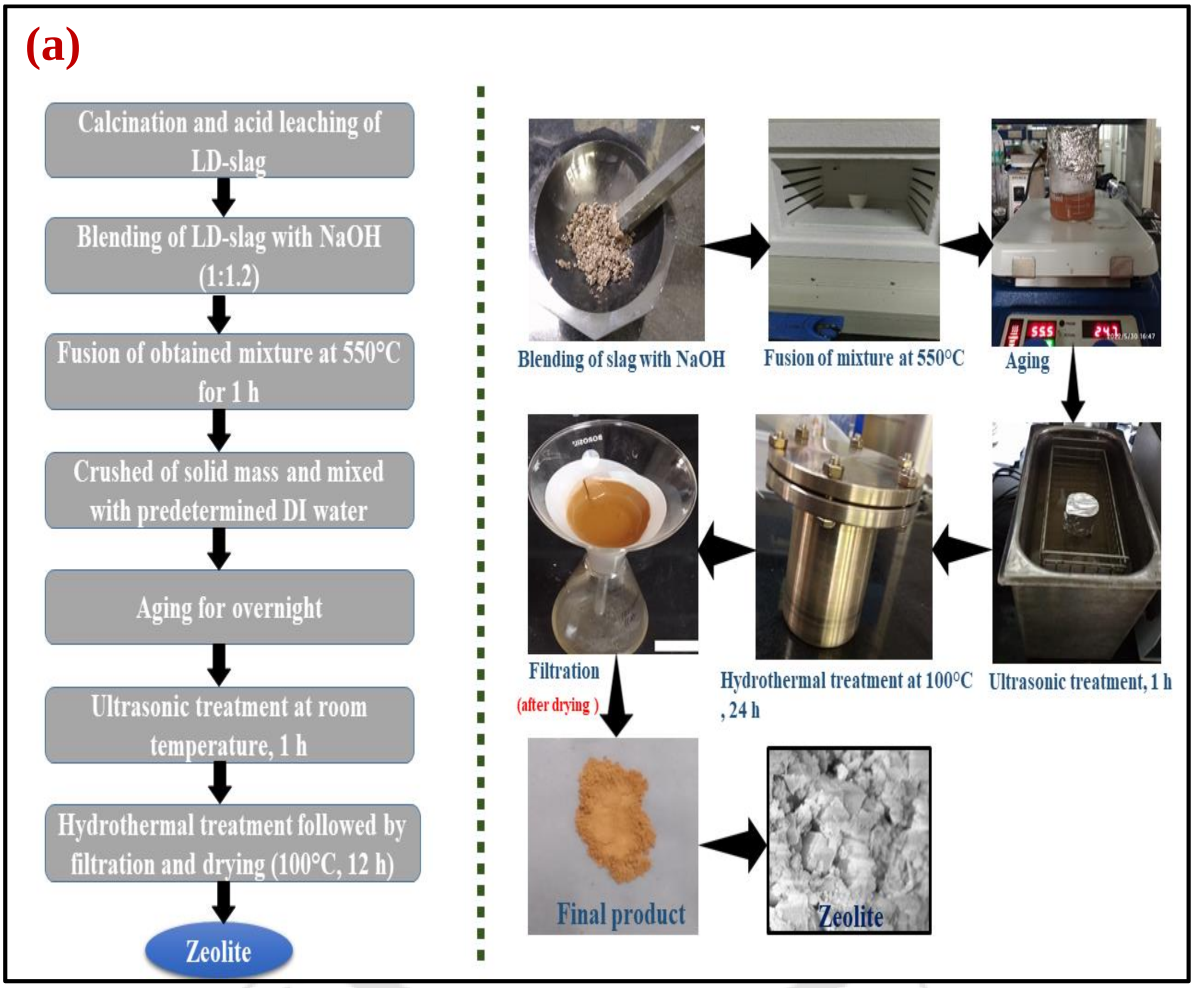

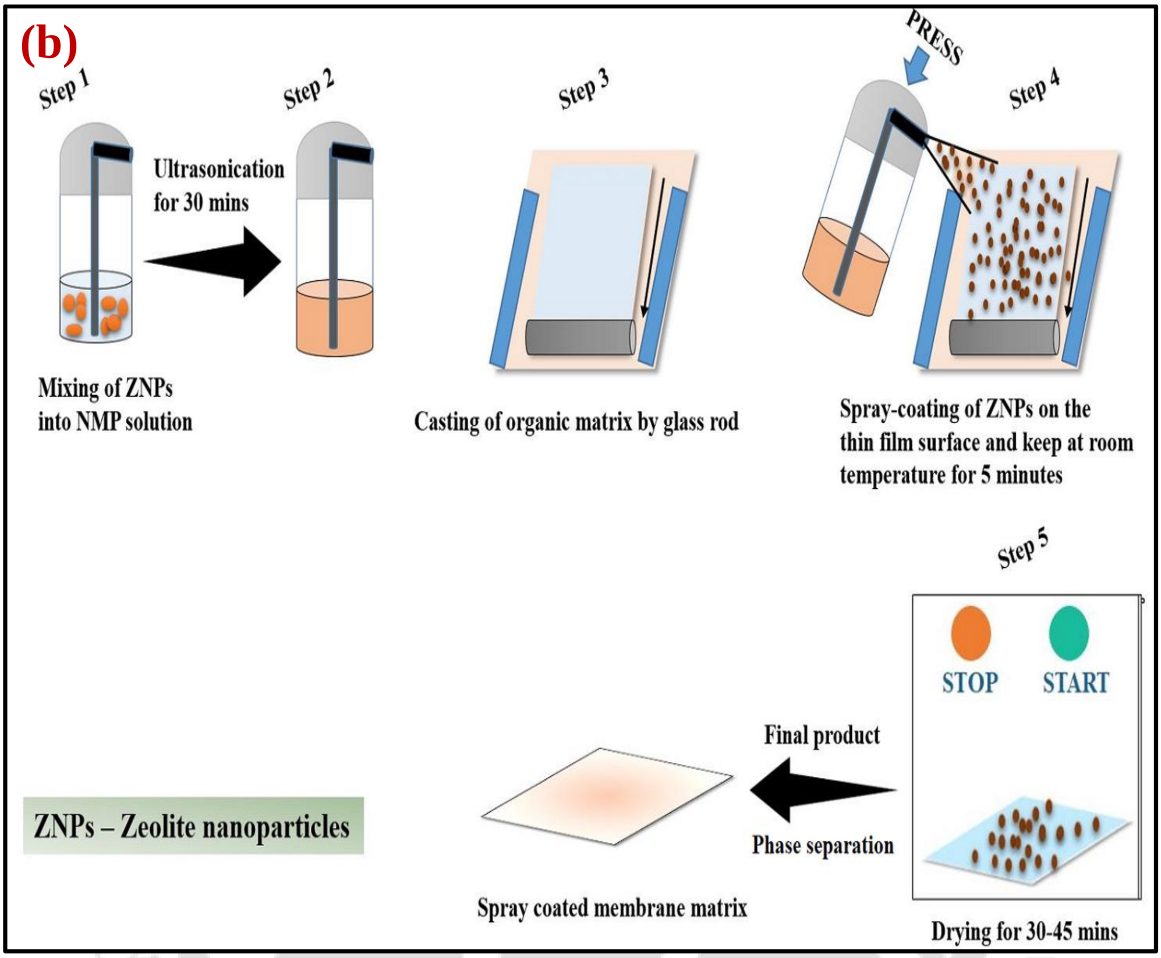

Figure 4.1: (a) Steps involved in the fabrication of zeolite and (b) zeolite-coated PSf membrane.

4.1.4. Zeolite Y and spray-coated membranes characterization

X-ray diffraction (XRD) analysis of prepared zeolite and membrane samples was conducted by the Bruker D8 Advance model. Scanning was done in continuous mode with a 2θ range of 10 to 60° and a speed of 0.05°/sec. The XRD profiles were obtained using Cu Kα = 0.15406 nm radiation. The X-ray source was set to work at 40 kV and 5 mA.

Attenuated total reflectance-Fourier transform infrared spectroscopy (ATR-FTIR) analysis of the ZNPs and membranes was conducted employing PerkinElmer Spectrum Two instrument. An infrared (IR) source made of ceramic is included with the device. The instrument's scanning range was from 400 to 4000 cm^{-1}, and its highest resolution was 0.5 cm^{-1}.

Field emission scanning electron microscopy (FESEM) was performed for determining the morphological analysis of the filler particles as well as MMMs. FESEM (ZESIS, Model 1430 VP) instrument was used to examine the materials' internal and exterior surface morphology. The treated samples were dried in a hot air oven between 70 to 80°C before analysis, and gold plating was applied to their surfaces. The Energy Dispersive X-ray (EDX) microscopic analysis was employed for chemical characterization/elemental study.

X-ray photoelectron spectroscopy (XPS) analysis of synthesized zeolite and composite membranes was carried out by RBD upgraded PHI-5000 Versa Probe III system (PerkinElmer) utilizing a monochromatic Al K-alpha x-ray source at pass energy of 55 eV.

Agilent, Model 5500 series equipped with Nanoscope IIIa controller was used in atomic force microscopy (AFM) to examine surface roughness values, topography as well as phase pictures. The characteristics of the film surface were assessed using phase-imaging and tapping modes. AFM images were used to assess the samples' root-mean-square roughness values. A frequency of 1.0 Hz and 256 scan lines per picture were used to take the height (topography) and phase images, respectively. Using the Gwyddion software, surface roughness images were captured.

The fluoride concentration in the aqueous solutions was measured using a fluoride meter (Model: Thermo Orion STAR A214).

An atomic adsorption spectrophotometer (AAS; Netherland; Varian; Spectra AA 220 FS) was used to detect and measure the concentration of heavy metals present in synthetic and groundwater samples.

The ion concentration like phosphate, sulphate, chloride, and nitrate was analyzed by ion meter (Make: Thermo Fisher Scientific, Model: Orion Star A214).

A thermal stability investigation of the synthesized membranes was performed using a TGA instrument (Make: NETZSCH, Model: TG209 F1). DSC/TG pan Al_2O_3 crucible was utilized. As an inert gas, argon was used at a flow rate of 20 mL/minute. With a heating rate of 10°C/minute, the analytical temperature was set between 25 and 900°C.

Static water contact angle measurement was applied to assess the membranes' hydrophilicity employing a digital camera (Nikkon Coolpix power shot at 7X optical zoom). Droplets of deionized water were put on membrane surfaces, and the contact angle between the water and membrane was monitored repeatedly until no change was observed. At least five measurements were carried out at various locations on the membrane matrix to verify the consistency of the results of the contact angle value. The tests were performed at ambient temperature.

The tensile strength of all prepared membrane samples was analyzed by a tensile testing instrument with a stretching rate of 2 mm/minute and a 5 KN load cell at an ambient atmosphere (25°C).

Using the gravimetric approach, the total porosity (ε) of the zeolite-coated composite membranes was determined using the following equation [1]:

$$\varepsilon = \frac{\omega_1 - \omega_2}{A \times d_w \times l} \times 100\% \qquad (4.1)$$

ω_1 and ω_2 are the weights of the wet and dry membrane, respectively, A is the area of membrane (m^2), where l defines the membrane thickness, and d_w is the density of water ($0.998\ g/cm^3$). To ensure that all of the membranes' pores are filled before measuring porosity, a portion of the membranes with a defined area must first be submerged in distilled water for at least 12 hours. After that, water on the membrane surface has been carefully wiped off and the sample was weighed. Following that, the samples are weighed again after being heated in an oven for 2 hours at 60°C to remove excess water from membrane pores.

The porosity of all prepared membranes was recorded to find out the mean pore radius (r_m) using Guerout–Elford–Ferry formula, as follows [1]:

$$\text{Pore radious } (r_m) = \sqrt{\frac{(2.9-1.75\varepsilon)\times 8\eta l Q}{\varepsilon\times A\times\Delta P}} \qquad (4.2)$$

Where l is the thickness of membranes, Q is the water flux (m^3/s), ΔP is the operation pressure (1.37 bar), and η is the viscosity of water (8.9×10^{-4} Pa s).

The EWC of all prepared membranes was estimated according to equation (4.3):

$$EWC = \frac{m_w - m_d}{m_w} \times 100 \qquad (4.3)$$

A membrane sample was first immersed in distilled water for 24 hours and then weight was marked as m_w. The membrane specimen was then evaporated at 60°C overnight and measured which is defined by m_d. For every sample, three measurements were taken, with a mean and corresponding standard deviation. The EWC value of the membrane does not signify the hydrophobicity or hydrophilicity of the membrane rather than indicates the amount of water withheld in the membrane pore, therefore it correlates with only the porosity of the membrane. The EWC increases when the porosity of the membrane enhances.

4.2. Permeation studies

4.2.1. Ultrafiltration test equipment

The permeation chamber used in this experiment is schematically depicted in Figure 4.2. The membrane was placed in a dead-end cell having an effective area of 22.89 cm^2. The feed fluoride solution was injected into the cylindrical container, and N_2 gas was pressurized to pass the feed solution through the membrane. The amount of permeation was measured at a time interval of every 10 minutes at room temperature. The transmembrane pressure (TMP) was maintained at 1.37 bar (20 psi) and the fluoride concentration was fixed at 5 ppm to assess the experimental results. The steady-state water flux was obtained after 60 minutes of operation and the initial water flux of every membrane was calculated as follows:

$$J = \frac{Q}{A \times \Delta t} \tag{4.4}$$

In this equation, J represents water flux (L/m^{2}h), Q is the volume of water, A and Δt are the area of membrane (m^2) and working time (h), respectively.

4.2.2. Flux recovery and antifouling performance of the prepared membrane

Membrane fouling is a physical phenomenon that occurred during membrane filtration and inhibits the membrane flux. Initially, the flux measurement was conducted with the deionized water (DI-water), and then with the groundwater sample. After the filtration the used membrane was washed with DI-water by rinsing three to four times and placed into the membrane holder to measure pure DI-water flux. The following equations (equation 4.5-4.8) calculated the flux recovery ratio (FRR) and the degree of the total flux losses due to overall fouling (R_t).

$$FRR\ (\%) = \left(\frac{J_{w2}}{J_w}\right) \times 100 \tag{4.5}$$

$$R_t\ (\%) = \left(1 - \frac{J_{w1}}{J_w}\right) \times 100 \tag{4.6}$$

$$R_r\ (\%) = \left(1 - \frac{J_{w2}}{J_w}\right) \times 100 \tag{4.7}$$

$$R_{ir}\ (\%) = (R_t - R_r) \tag{4.8}$$

Where J_{w1} is the pure water flux of the membrane after the ultrafiltration test of the contaminated groundwater sample at a particular transmembrane pressure of 1.37 bar, and J_{w2} is the water flux of the clean membrane after fouling at the same pressure. J_w is the pure water flux (L/m^{2}h) of clean water. R_r and R_{ir} denote the reversible and irreversible fouling ratios, respectively.

The F^- rejection percentage was measured by equation 4.9 which is given below:

$$R\ (\%) = \left(1 - \frac{C_P}{C_F}\right) \times 100 \tag{4.9}$$

Where C_P and C_F represent the F^- concentration in permeate and feed, respectively. A chromium and manganese adsorption isotherm study was conducted using a surface-coated membrane as an adsorbent to examine the surface properties and phenomena occurring at the interface. The Cr^{6+} and Mn^{2+} removal was estimated by equation 4.9.

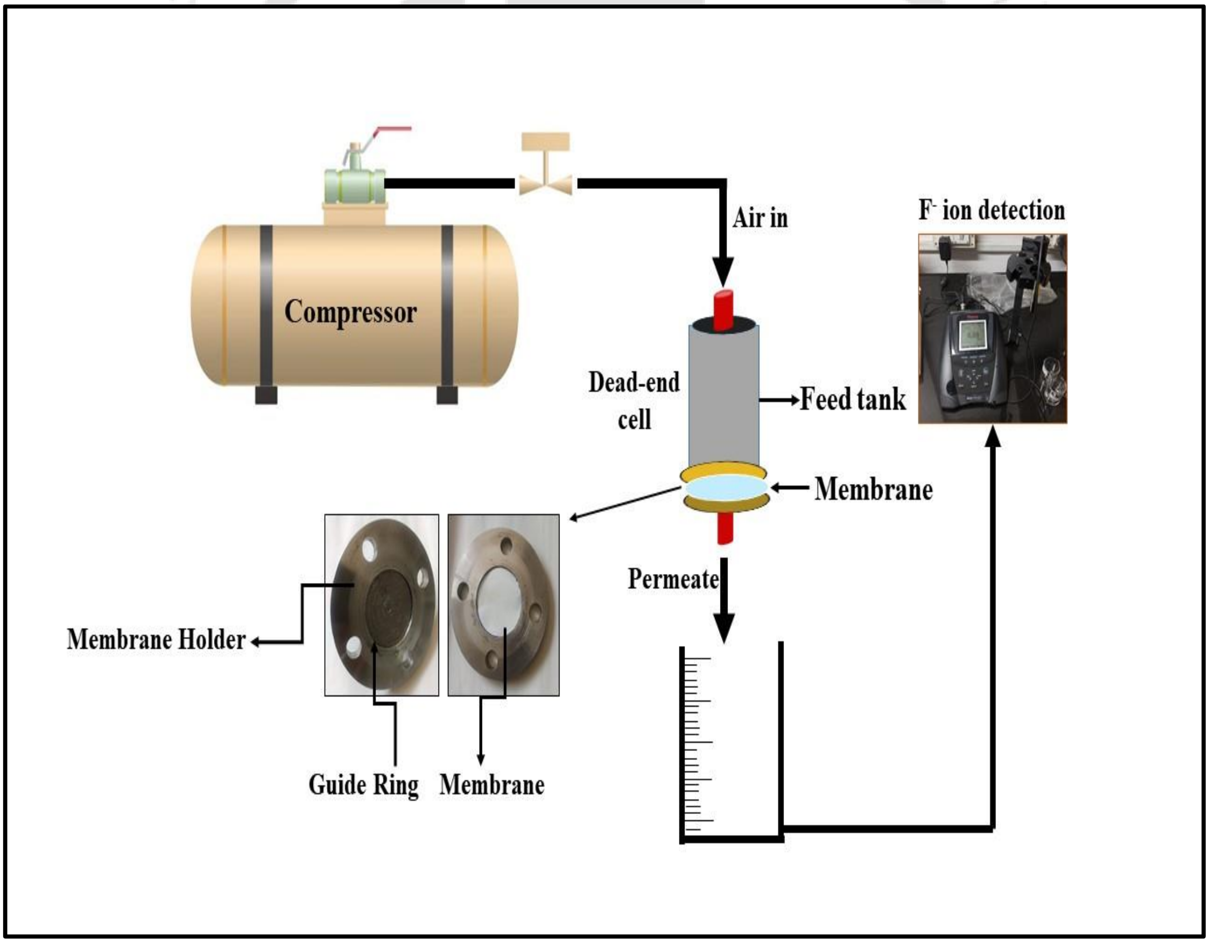

Figure 4.2: Schematic diagram of fluoride rejection and other contaminants removal dead-end ultrafiltration set-up.

4.3. Results and discussion

4.3.1. Characterization of zeolite Y

4.3.1.1. X-ray Diffraction Analysis

Figure 4.3 (a) depicts that the crystal planes in LD-slag mainly show peaks at 2θ = 18.046°, 29.46°, 34.14°, 39.37°, 42.10°, 47.11°, and 48.50° which attributes to the presence of iron, silicon oxide, coesite (SiO_2), brown millerite, calcite, merwinite, and calcium iron-molybdenum oxide. Figure 4.3 (a) shows more intense peak diffracted at 2θ = 6.2° (1 1 1), 10.11° (2 2 0), 11.88° (3 1 1), 18.6° (5 1 1), 20.31° (4 4 0), 23.64° (5 3 3), 27.00° (6 4 2), 30.7° (8 2 2), 32.43° (8 4 0), 34.46° (9 3 1), 39.99° (4 3 2), 45.26° (12 2 2), which attributes to zeolite Y and further, the peaks well matched with the JCPDS card no 039-1380 [2], which is provided in Figure 4.4.

4.3.1.2. ATR-FTIR analysis

ATR-FTIR spectrum of untreated LD-slag and synthesized zeolite sample has been depicted in Figure 4.3 (b). Peaks exhibited at a wavelength of 513 and 908 cm^{-1} corresponding portlandite ($Ca(OH)_2$) and periclase (MgO) [3] functional groups of LD-slag, meanwhile functional groups containing Al-O, Si-O, and T-O groups, which reveals the successful formation of zeolite Y [4]. The peak that appeared at 567 and 719 cm^{-1} are attributed to the bending and symmetric stretching vibrations of Si-O or Al-O bonds, respectively [4]. Moreover, the vibrational band appeared at 998 cm^{-1} is due to the presence of asymmetric vibrations of the Al-O groups [4–6]. The peak at 1645 cm^{-1} is assigned to the bending vibration of water molecules located at the zeolite cage [5,7]. Peak arrived within 457-462 cm^{-1} representing buckling vibration of the O-Si-O or Si-O-Si group in the zeolite cage [2]. Only a peak at 694 cm^{-1} is ascribed to the internal tetrahedral symmetric stretching mode in the zeolite network [8]. The large band exhibited at 3448 cm^{-1} as a result of O-H stretching vibration of the hydroxyl group [9] and hydrogen-bonded silanol groups [10,11]. The aforesaid vibration peaks all verify the successful preparation of zeolite Y using LD-slag as precursor material.

4.3.1.3. XPS analysis

The surface elements and bonding interactions were obtained using X-ray photoelectron spectroscopy (XPS). Figure 4.3c represents the XPS results obtained for the synthesized Y-type zeolite nanoparticles. The full scan of the zeolite Y sample is depicted in Figure 4.3c. The XPS binding energy of Si 2p and Al 2p in the same sample is shown in Figures 4.3d and 4.3e, respectively. After a Shirley background adjustment, all XPS spectra were fitted [12]. As shown in Figure 4.3c, the intensive peak observed at a binding energy of 530.35 eV is attributed to the presence of O 1s, meanwhile, a peak near 1073 eV ascribed the presence of Na 1s in sodium-enriched zeolite Y mineral [13]. The XPS signals at 101.75 and 153.0 eV are ascribed to Si $2p_{1/2}$ and Si $2s_{3/2}$ states of Si (IV) [13], as shown in Figure 4.3d. Similarly, the oxidized state of Al (III) has appeared at XPS binding energy of 74.5 and 118.0 eV which corresponds to Al $2p_{3/2}$ and Al $2s_{1/2}$ [13], respectively, as depicted in Figure 4.3e. Figure 4.3c exhibits that the generated sample has significantly positive shifted binding energy values, implying that O, Na, Si, and Al are not present as discrete oxides but as a single oxide constituent. The atomic weight percent of Si and Al in the zeolite Y network is enlisted in Table 4.1.

Table 4.1: XPS analysis of zeolite Y.

Component	Si	Al
Atomic wt.%	65.83	34.17

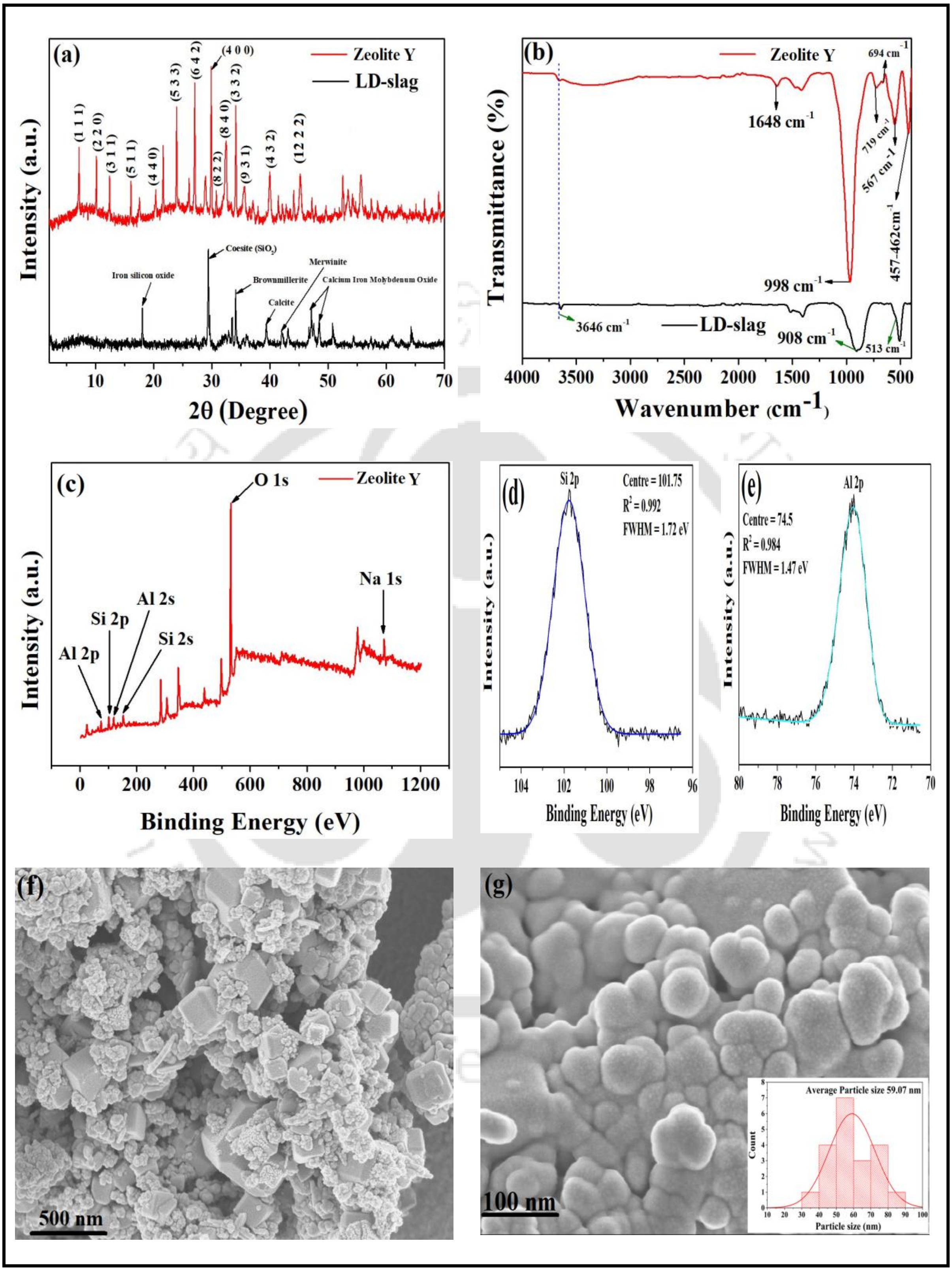
(a)
Zeolite Y
LD-slag
Intensity (a.u.)
2θ (Degree)
(1 1 1)
(2 2 0)
(3 1 1)
(5 1 1)
(4 4 0)
(5 3 3)
(6 4 2)
(4 0 0)
(8 2 2)
(8 4 0)
(3 3 2)
(9 3 1)
(4 3 2)
(12 2 2)
Iron silicon oxide
Coesite (SiO₂)
Brownmillerite
Merwinite
Calcite
Calcium Iron Molybdenum Oxide
(b)
Zeolite Y
LD-slag
Transmittance (%)
Wavenumber (cm⁻¹)
694 cm⁻¹
1648 cm⁻¹
719 cm⁻¹
567 cm⁻¹
457-462cm⁻¹
998 cm⁻¹
3646 cm⁻¹
908 cm⁻¹
513 cm⁻¹
(c)
O 1s
Zeolite Y
Na 1s
Al 2s
Si 2p
Si 2s
Al 2p
Intensity (a.u.)
Binding Energy (eV)
(d)
Si 2p
Centre = 101.75
R² = 0.992
FWHM = 1.72 eV
Intensity (a.u.)
Binding Energy (eV)
(e)
Al 2p
Centre = 74.5
R² = 0.984
FWHM = 1.47 eV
Intensity (a.u.)
Binding Energy (eV)
(f)
500 nm
(g)
100 nm
Average Particle size 59.07 nm
Count
Particle size (nm)

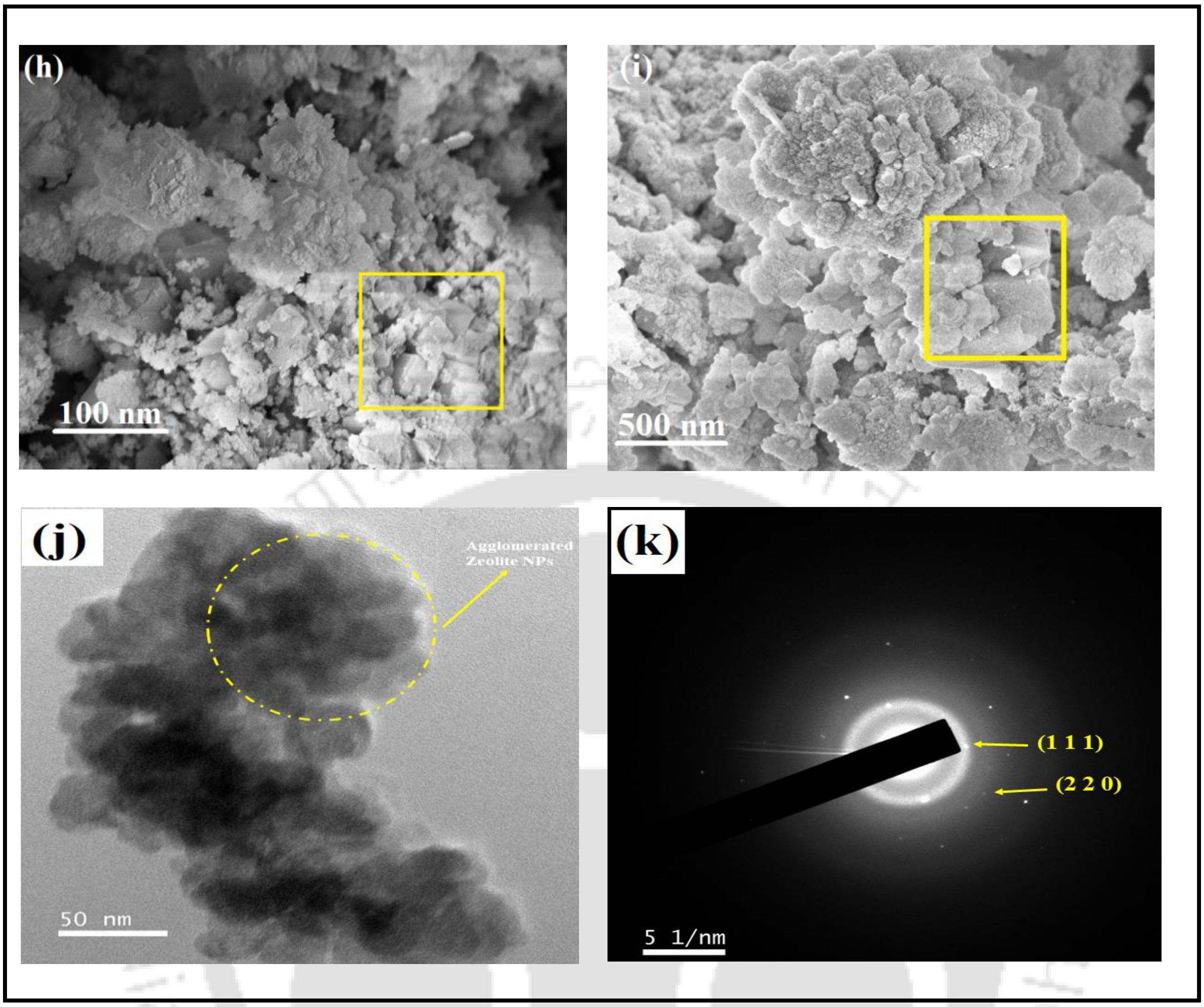

Figure 4.3: (a) XRD, (b) FTIR, (c) XPS spectra for zeolite Y, (d) and (e) Si-2p and Al-2p XPS binding energies of SiO_2 and Al_2O_3, (f)-(i) FESEM, (j) FETEM analysis and (k) SAED pattern of synthesized zeolite mineral.

4.3.1.4. FESEM and FETEM analysis of zeolite nanocrystals

The surface morphology of the synthetic zeolite was examined to confirm the surface characteristics. Figure 4.3f-i represents the surface morphology of the LD-slag-modified zeolite Y. As is shown in Figure 4.3f, irregular angular-shaped zeolite Y was formed and the result is in good agreement with the XRD result (Figure 4.3a) [14]. The agglomerated, nano-seeds, and non-uniform structure of zeolite Y crystal was observed with an average particle size of 59.07 nm, as displayed in Figure 4.3g (inset). Figure 4.3h exhibits the octahedral shape of zeolite nanopowder, along with grooves and abrasions features were also obtained as shown in Figure 4.3i [15].

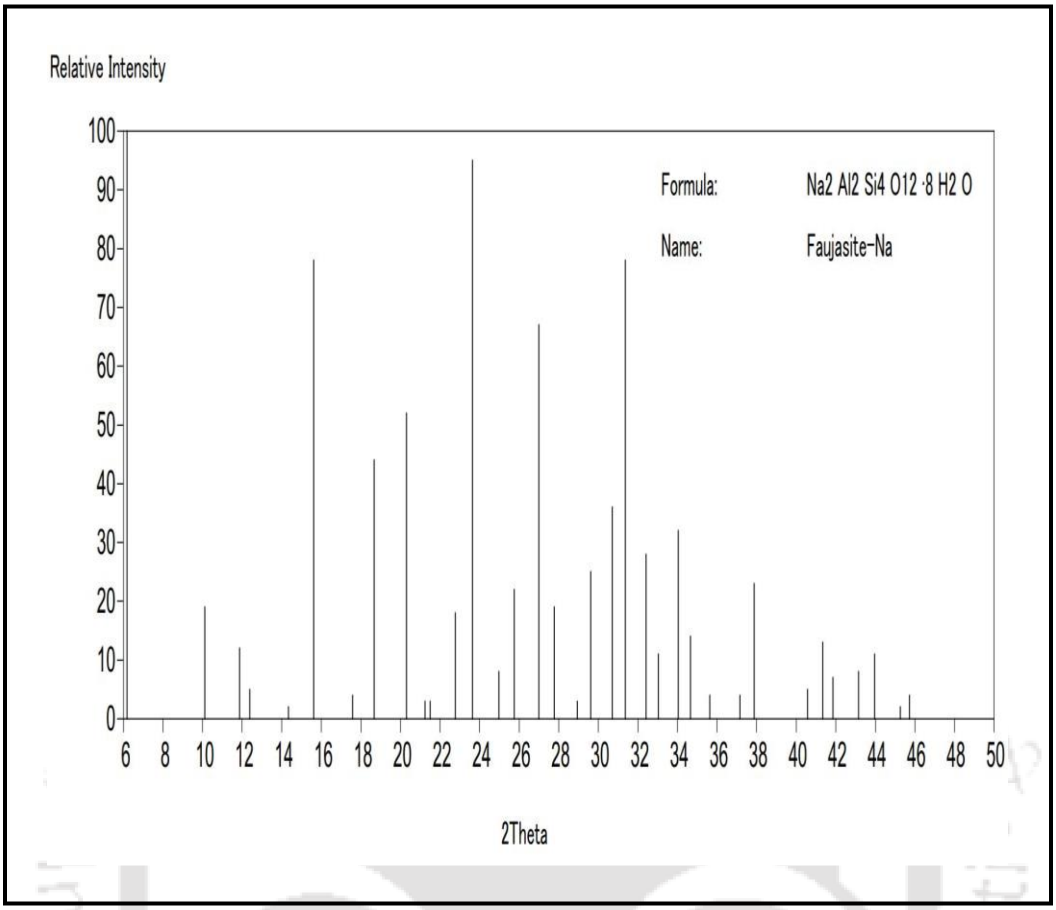

Figure 4.4: Standard XRD peaks of pure faujasite type zeolite Y (JCPDS No- 039-1380).

The results obtained from FESEM analysis confirmed that the presence of other elements in waste LD-slag inhibits zeolite formation as well as the transformation of zeolite crystals.

In order to identify the crystal structure and crystalline plane as well as the nature of zeolite particles the FETEM and SAED patterns were conducted and the results are depicted in Figure 4.3j and 4.3k, respectively. Agglomerated and irregular forms of zeolite NPs were seen, as shown in Figure 4.3j. Figure 4.3k displays the selected area electron diffraction (SAED) pattern where polycrystalline rings are observed. In addition to that, crystalline planes (1 1 1) and (2 2 0) were also detected in the SAED pattern which was in good agreement with the XRD result (Figure 4.3a). The elemental mapping was recorded to identify the Si and Al distribution of the prepared zeolite type-Y sample, as shown in Figure 4.5.

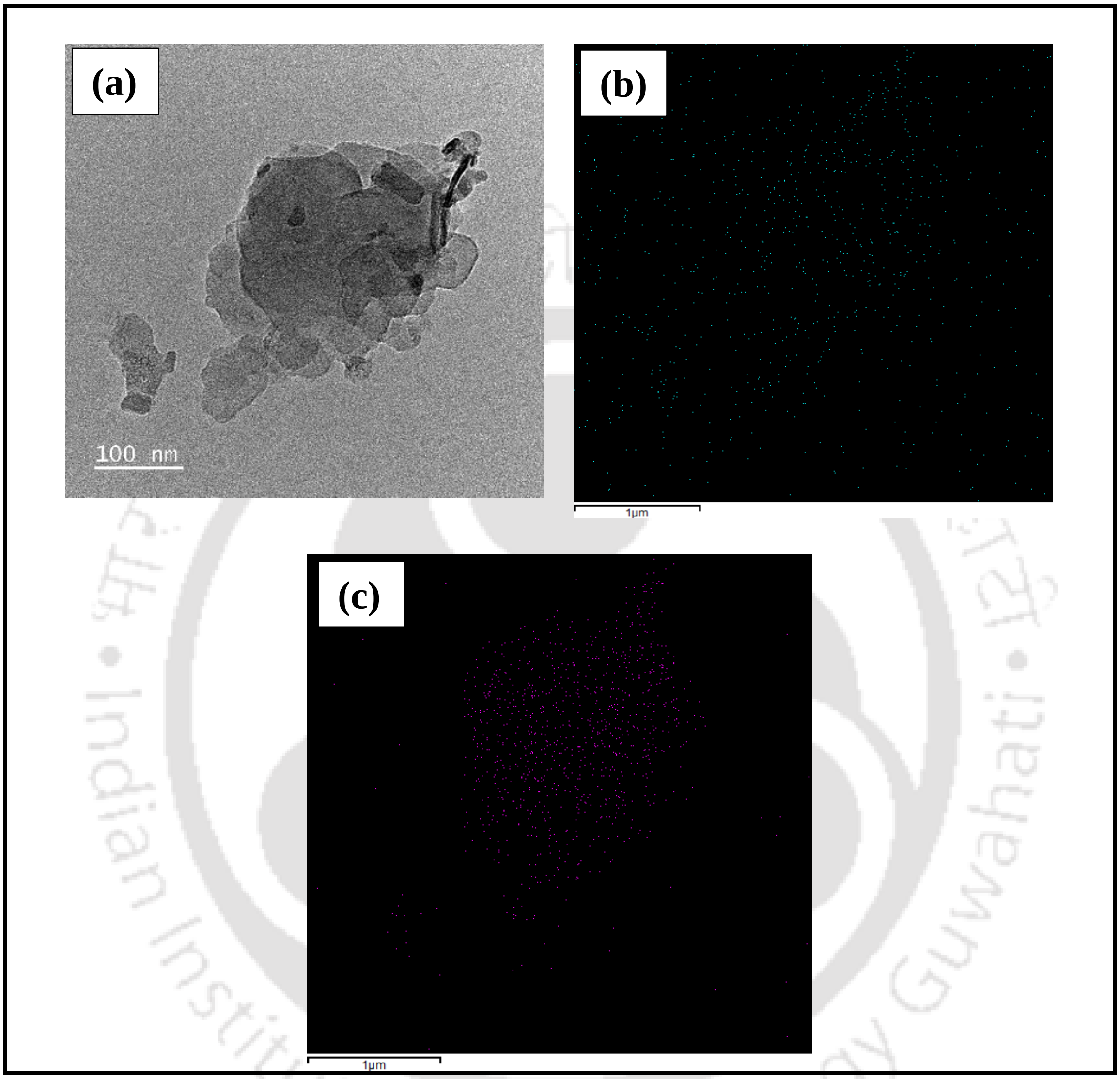

Figure 4.5: Elemental mapping by FETEM of Y-type zeolite synthesized by ultrasonic energy facilitated hydrothermal treatment (a) Electron image, (b) Si distribution, and (c) Al distribution.

4.4. Optimization of the membrane synthesis

For synthesizing defect-free PSf nanolayered coated membrane, the following factors were considered such as zeolite concentration, drying time, and the impact of drying temperature. The membrane surface was coated using various weights (%) of zeolite Y (0.01, 0.1, 1, and 2 wt.%, respectively). It was found that zeolite concentration beyond 1 wt.% constrained the ZNPs from being evenly distributed, which further prevents the layer formation on the polymer matrix and wreck the membrane fabrication. Hence, three different zeolite weights (%) were considered (0.01, 0.1, and 1 wt.%) for preparing the surface-modified membrane. The drying temperature and time optimization study was conducted utilizing the highest zeolite-wt (%) membrane. Four different drying temperature (20, 40, 60, and 80°C) was set for 30 minutes to find the optimized temperature for synthesis. The FESEM analysis clearly showed that at the lower temperature altostratus cloud and asymmetrical membrane surface were observed (Figure 4.6a and 4.6b, respectively) which might be due to less interaction between zeolite-NMP mixtures with polymeric gel substrate. The symmetrical flat sheet membrane was obtained when the temperature was set at 60°C (Figure 4.6c). It was also noted that beyond 60°C, the membrane surface got cracked (Figure 4.6d), which is presumably due to the vaporization of NMP solvent at 80°C and the leaching of non-vaporized solvent during phase inversion. The results revealed that 60°C is the acceptable temperature for membrane fabrication.

Figure 4.6e-h shows the membrane fabrication with optimized temperature with different drying times to optimize the membrane drying time. Huge membrane swelling, membrane disintegration, and uneven membrane surface were observed, according to Figures 4.6i and 4.6j. The defect-free membrane was produced after 45 minutes of drying time (Figure 4.6k).

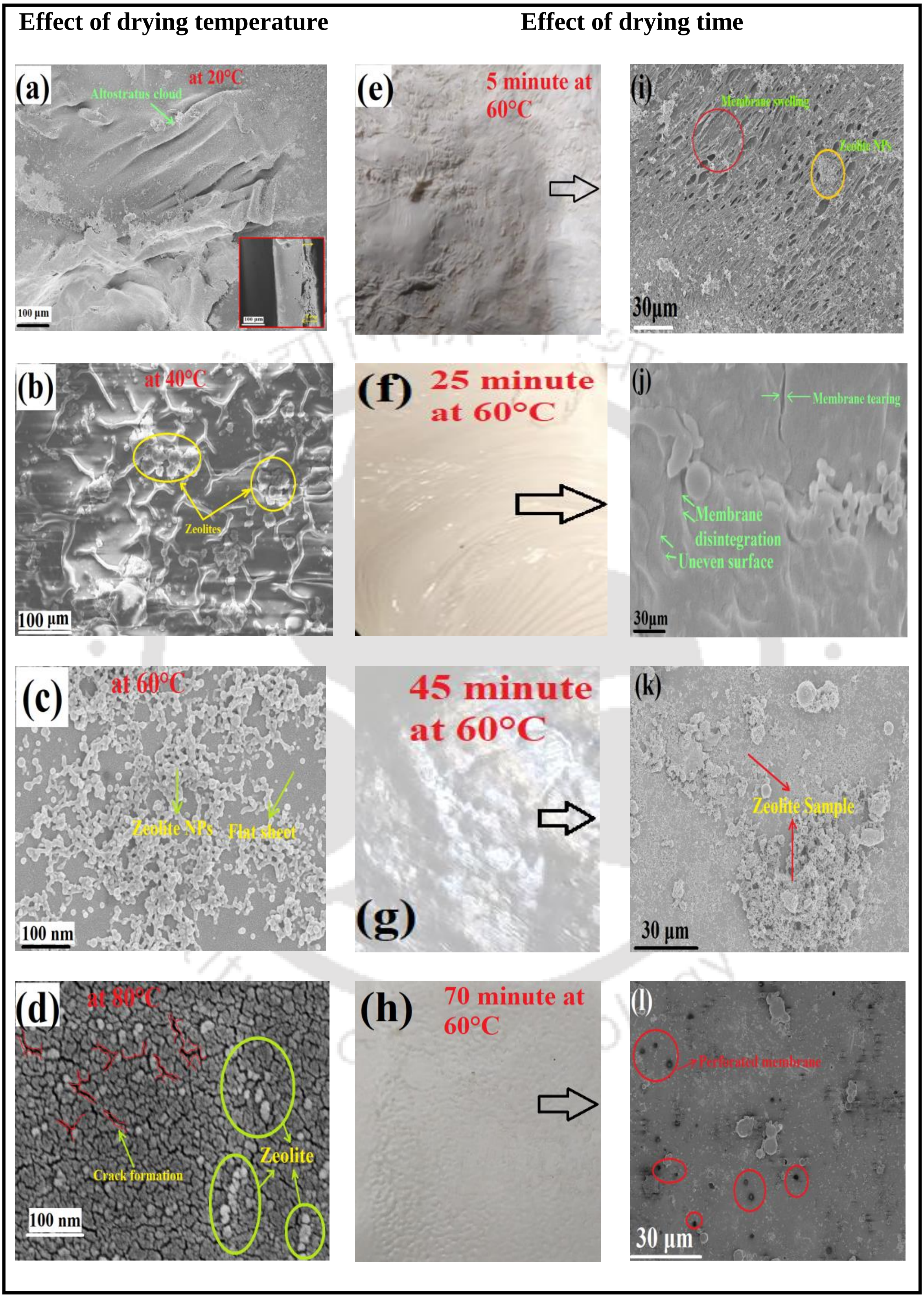

Figure 4.6: (a)-(d) membrane synthesized at different temperatures, (e)-(h) obtained membrane for various synthesis times at constant temperature i.e., 60°C, (i)-(l), and (m)-(p) their corresponding surface morphology.

On the other hand, a perforated membrane was seen after 70 minutes of drying time. This type of problem can lead to the degradation of membrane performance.

4.5. Membrane characterization

4.5.1. X-ray Diffraction Analysis

Figure 4.7a depicts the X-ray diffraction pattern of the resulting neat PSf and Zeolite Y-coated membranes. The amorphous structure of the PSf membrane is indicated by a large peak that was reached at 2θ = 17.69° [16]. The characteristic diffraction peak of zeolite at 2θ = 6.8° and 45.28° is attributed to the presence of (1 1 1) and (7 7 7) crystalline plane of faujasite type zeolite Y. The average interchain distance (d-spacing) of the membranes was measured using Bragg's equation ($n\lambda = 2d\sin\theta$, where λ and θ denote the X-ray wavelength and diffraction angle, respectively), and the values are reported in Table 4.2. It was seen from Table 4.2 that the peak position and d-spacing value (except PSf/zeolite-0.01wt.%) of the spray-coated membrane were displaced to a higher angle, revealing the internal electrostatic repulsion of the Y-type zeolite and polymer [17].

Table 4.2: Calculation of d-spacing value for as-synthesized zeolite-coated thin film matrix.

Membrane sample	Diffraction angle (2θ)	FWHM (°)	d-spacing (nm)
Neat PSf	17.69	10.17	0.140
PSf/Zeolite-0.01wt.%	23.11	6.29	0.09
PSf/Zeolite-0.1wt.%	18.03	8.3	0.193
PSf/Zeolite-1wt.%	18.13	7.16	0.218

4.5.2. ATR-FTIR Study of prepared membranes

The interaction between the polymer matrix and nanofiller was investigated using Fourier transform infrared spectroscopy. Figure 4.7b depicts the ATR-FTIR spectrum of pure PSf and zeolite encapsulated thin film. The results of the obtained functional groups are shown in Table 4.3.

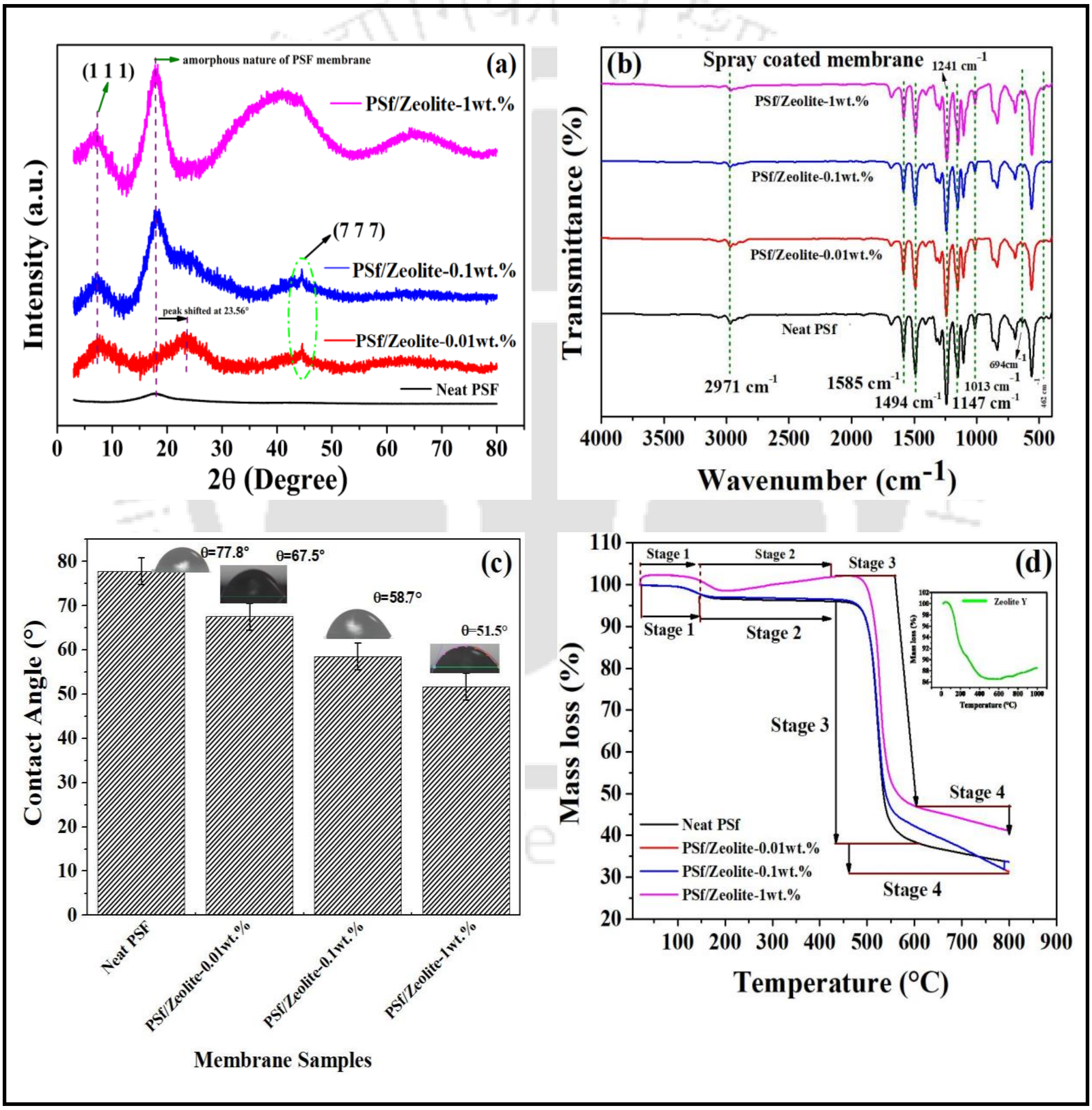

Figure 4.7: (a) XRD pattern, (b) FTIR spectrum, (c) contact angle, and (d) TGA analysis of neat PSf, PSf/zeolite-0.01wt.%, PSf/zeolite-0.1wt.%, and PSf/zeolite-1wt.% membrane sample, respectively.

Two prominent absorption spectra were detected at 1494 cm^{-1} and 1585 cm^{-1} wavelengths implying aromatic vibrational bonding of C=C in the polysulfone group. The strong vibrational bonding of O=S=O in the polysulfone structure was observed at 1147 cm^{-1} [18]. Furthermore, the C-O-C vibrational bond in the ether group was detected at 1241 cm^{-1}. The absorption band at 1014 cm^{-1} represents the asymmetric stretching of the C-O group [18]. The aromatic and aliphatic C-H stretching vibration in the polysulfone group was found at 2971 and 3060 cm^{-1}, respectively [19]. The band at 833 cm^{-1} was denoted to the C-H bending vibration. At 694 and 462 cm^{-1} the absorption bands represent the symmetric stretching of the TO_4 (T=Si and Al) in the zeolite framework which confirms that AlO_4 and SiO_4 are linked together [20] in the polymer matrix. The ATR-FTIR spectra of zeolite-incorporated polymeric membranes were comparable to that of pure PSf, with no band shifting or formation of new bands, revealing that there was no chemical interaction between PSf and nanoscale zeolite Y [21].

Table 4.3: Functional groups in the surface-coated synthesized membrane.

Frequency range (cm^{-1})	Functional group
2971, 3060	C-H stretching vibration
1494, 1585	Vibrational bonding of C=C in polysulfone
1241	Vibrational bond of C-O-C in ether group
1147	Vibrational bonding of O=S=O in PSf group
1014	C-O
833	C-H bending
694, 462	Internal tetrahedral of zeolite framework

4.5.3. Static water contact angle

The hydrophilicity capability of the polymer substrate was quantified as contact angle (θ) based on the degree of interaction of droplets of water on the membrane surface (wettability) at the interface. The hydrophilicity and hydrophobicity were considered when the contact angle is close to 0° and 90° or higher, respectively. It can be observed that as the zeolite concentration increased, the static contact angle of the neat PSf membrane (77.8°) decreased (Figure 4.7c). The intrinsic hydrophobicity of PSf polymer causes the lowest hydrophilicity of fresh PSf membrane [22]. The highest contact angle decrease was found at 51.5° with 1wt.% zeolite Y concentration. It is well known that the membrane hydrophilicity increased when the contact angle is decreased. The spontaneous liquid penetration into the pores, results in a decrease of contact angle. A decreasing trend of contact angle was noted (Figure 4.7c) while zeolite loading was increased from 0.01 to 1wt.%. This implies that the hydrophilicity of the membrane has enhanced due to the presence of hydroxyl groups on the membrane surface, which was induced by the zeolite mineral [22].

The above study reveals that zeolite Y-coated PSf membrane exhibits higher hydrophilicity compared to neat PSf, the reason is presumably due to the high aluminum content in the zeolite network [22]. It is also known that when the Si/Al ratio reaches 10, the zeolite becomes hydrophobic [23]. In this present study, Si/Al ratio was maintained at less than 2, and the zeolite could be noted as hydrophilic.

4.5.4. TGA analysis

The thermogravimetric analysis (TGA) results of all fabricated membranes and zeolite NPs (at inset) have been provided in Figure 4.7d. The weight loss of 66, 69, 68, and 58.5 wt.% was estimated for neat and zeolite-assembled PSf membranes. The mass loss of modified membranes occurred in the four stages phenomenon, as illustrated in Figure 4.7d. Stage 1 indicates the presence of residue solvent and removal of adsorbed water from the precursor which is occurred at below 200°C [24]. The thermal rearrangement of the as-synthesized membrane is observed in stage 2, meanwhile, the third stage denotes the initial decomposition of the polymer substrate towards the creation of the zeolite membrane. A sudden weight drop of approximately 6.5% from their original weight occurred at 436.21°C. It was also seen from Figure 4.7d that the lowest mass loss (~58.5 wt.%) observed for PSf/Zeolite-1wt.% membrane at the highest temperature as compared to other synthesized membranes, indicating the less possibility of melting when exposed at high temperature (heat treatment process). The reason is due to the presence of thermally stable silica and alumina in the zeolite framework. At high temperatures, long-chain polymer gets disintegrated and chain separation occurs which reacts with one another, and alters the polymer characteristics, contributing to high extraction efficiency [25]. It was also noted that ~5wt.% weight loss occurred for all the fabricated membranes in the range of 613 to 800°C.

4.5.5. XPS analysis

XPS was used in order to confirm the chemical compositions of the membrane surfaces, and the findings are given in Figure 4.8 and Table 4.4. The XPS C 1s core-level spectrum of all synthetic membranes has been shown in Figure 4.8b. For the nascent PSf membrane it was observed that the C 1s spectrum was curved-fitted into three peaks with binding energies (BEs) at 284.76, 285.29, and 286.03 eV, which were ascribed to C-H, C-N, and C-O, respectively. However, the following peaks were shifted for zeolite-coated membranes (Table 4.4). The XPS N 1s spectrum (Figure 4.8c) was curved-fitted into two peaks with the BEs at 399.92 and 400.3 eV, which were attributed to (C)-N=, and N^-, respectively [26]. The deconvolution O 1s (532.27 and 533.7 eV) showed the O=S=O and O-C-O chemical bonding (Figure 4.8d) for neat PSf membrane [27]. The existing peaks were varied for all modified membranes, as shown in Figure 4.8 and Table 4.4. Additionally, XPS Si 2P and Al 2p spectra were found at 102.31-101.93 eV and 74.41-74.45 eV, which is evident in the incorporation of zeolite nanoparticles on the modified membrane surfaces (Table 4.4).

4.5.6. Morphology analysis of neat and surface-coated PSf membranes

The surface and cross-sectional morphology of pure PSf and zeolite Y nanofiller-coated PSf membrane was examined by FESEM, as depicted in Figure 4.9. Figure 4.9a, c, e, and g represents the surface morphology of neat PSf, PSf/Zeolite-0.01wt.%, PSf/Zeolite-0.1wt.%, and PSf/Zeolite-1wt.% membrane, respectively. All of the images show a typical porous and uneven membrane structure with a dense top layer and a porous sub-layer. A porous PSf membrane with an average pore size of 11.80 nm is shown in Figure 4.9a inset. The accumulation of zeolite NPs at 0.1wt.% concentration was observed in Figure 4.9e. The surface characterization of all zeolite powder-coated membranes reveals the presence of zeolite particles on the surface of the PSf substrate. It was observed that zeolite particles are visible in the polymer matrix and tend to form aggregate at higher zeolite NPs concentrations (Figure 4.9g). Therefore, the fabrication of a nanoparticle-coated uniform polymer matrix is very crucial.

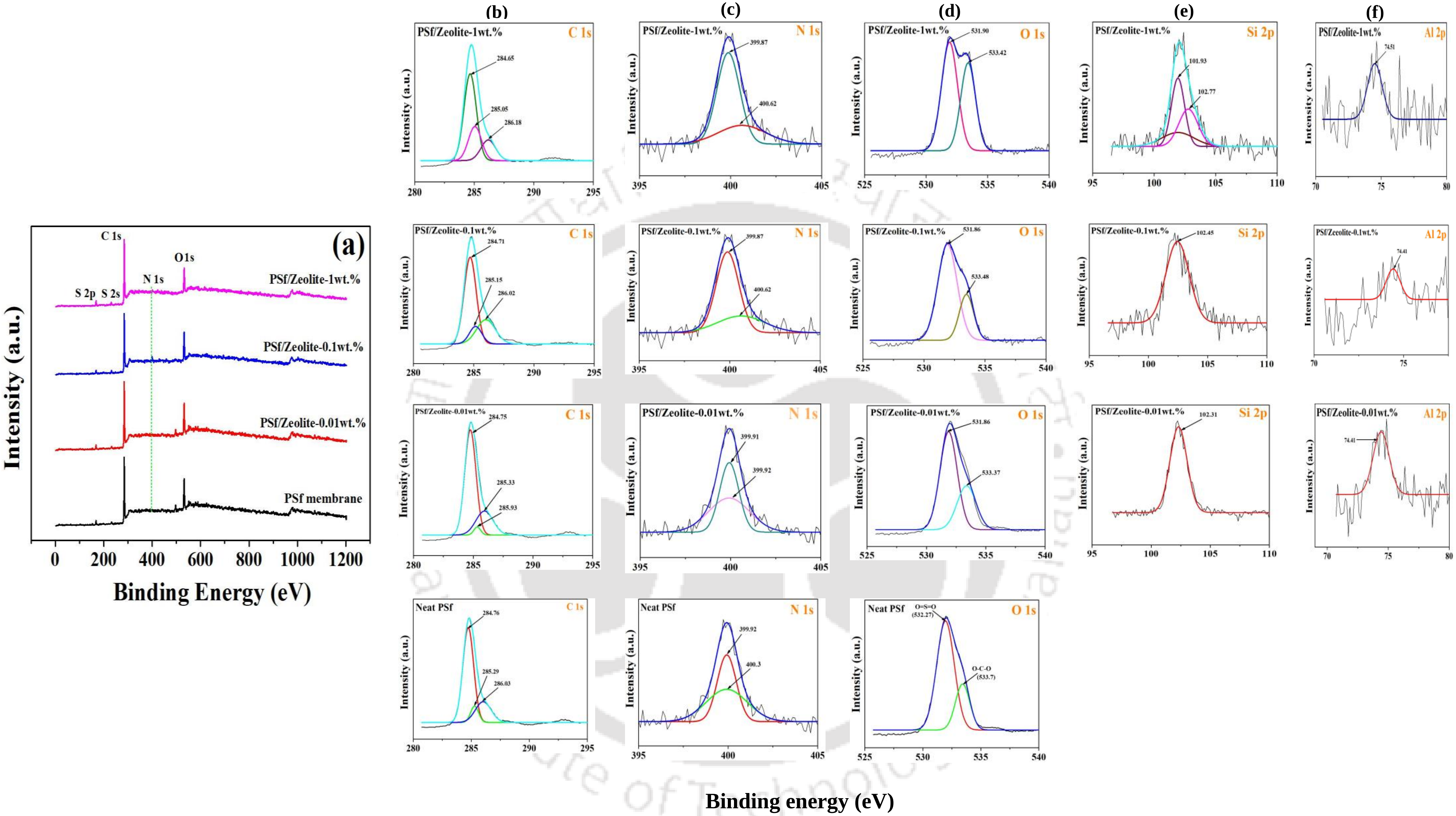

Figure 4.8: XPS survey spectra of prepared membranes: (a) wide scan, (b) C 1s core electron spectra, (c) N 1s spectra, (d) O 1s core electron spectra of all prepared membranes, (e) Si 2p core level spectra and (f) Al 2p core level spectra of zeolite modified PSf membrane.

Table 4.4: XPS binding energies (eV) for all synthesized membranes.

Spectra	**Functional Group**	**Membrane sample**			
		Neat PSf BEs (eV)	**PSf/Zeolite-0.01wt.% BEs (eV)**	**PSf/Zeolite-0.1wt.% BEs (eV)**	**PSf/Zeolite-1wt.% BEs (eV)**
C 1s	**C-H**	284.76	284.75	284.71	284.65
	C-N	285.29	285.33	285.15	285.05
	C-O	286.03	285.93	286.02	286.18
N 1s	**(C)-N=**	399.92	399.91	399.87	399.87
	N^-	400.3	399.92	400.62	400.62
O 1s	**$O=S=O/OH^-$**	532.27	531.86	531.86	531.90
	O-C-O	533.7	533.37	533.48	533.42
Si 2p		-	102.31	102.45	101.93, 102.77
Al 2p		-	74.41	74.41	74.45

Figures 4.9b, d, f, and h represent the cross-sectional morphology of all the fabricated membranes. For the PSf membrane, a large finger-like structure (Figure 4.9b) was observed which was attributed due to high affinity between solvent (NMP) and non-solvent (water) and sudden demixing during phase separation. Moreover, the finger-like structure turns into a honeycomb even porous structures for zeolite-coated PSf membranes. This is because of the thermal treatment of membranes before phase inversion. As the solvent gets evaporated during thermal treatment, it creates more void spaces and leads to the formation of a honeycomb-like porous structure. It was also seen that membrane thickness increased with zeolite concentration as compared to the pure PSf membrane which was attributed to the zeolite layer formation on the membrane surface.

Table 4.5 shows the porosity, equilibrium water content, and mean pore radius of all prepared membranes. The membrane porosity for neat PSf was found to be 46.09%, whereas, for zeolite-coated membrane, this value was within the range of 51.49% and 56.77%. The increment order of the fabricated membrane thickness was observed with zeolite concentration (Table 4.5 and Figure 4.9b, d, f, and h), indicating the existence of a zeolite-NMP layer on the membrane surface. It was noted that the porosity of all surface-coated membranes enhances as compared with unmodified membranes due to faster precipitation and exchange of solvent/non-solvent with the addition of nanoparticles [28]. On the other hand, faster demixing is also induced by the hydrophilic nature of nanopowder which leads to large pore size (Table 4.5) formation in the membrane. As represented in Table 4.5, the EWC value increased with membrane porosity and it was also stated that with higher zeolite concentration, the membrane porosity diminishes which reduces the EWC [22].

Table 4.5: Porosity, equilibrium water content, and mean pore radius of unmodified and surface-coated membrane matrix.

Membrane sample	Membrane thickness (μm)	Porosity (%)	EWC (%)	Mean pore radius, r (nm)
Neat PSf	121	46.09	6.46	2.66
PSf/Zeolite-0.01wt %	156.7	53.07	8.73	3.71
PSf/Zeolite-0.1wt %	187	51.49	8.14	5.09
PSf/Zeolite-1wt %	256	56.77	11.73	7.50

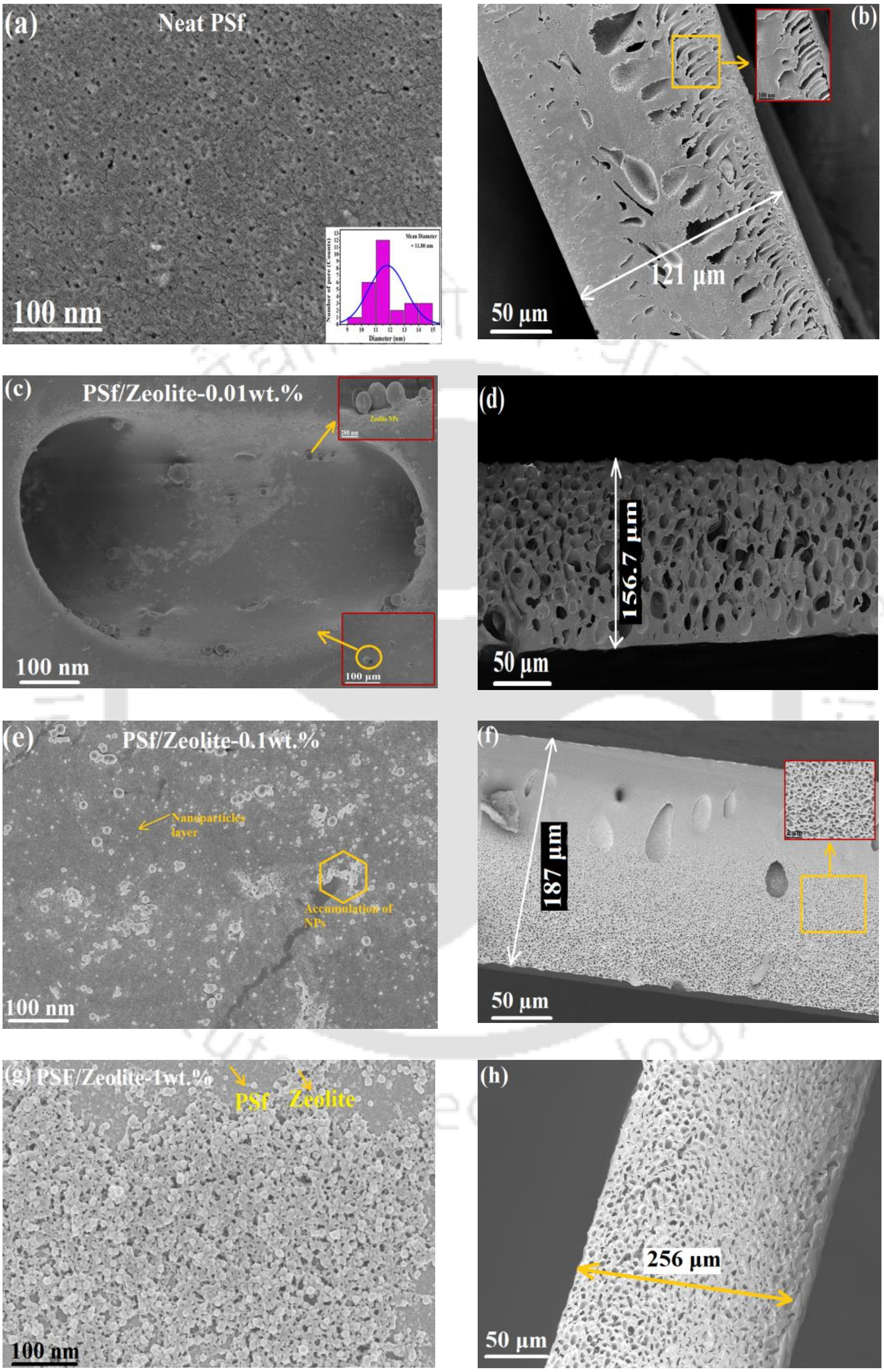

Figure 4.9: Surface (a, c, e, and g) and cross-sectional (b, d, f, and h) morphology of neat PSf and surface-coated membranes with different zeolite concentrations.

4.5.7. Atomic force microscopy (AFM) study

Figure 4.10 shows the topographical pictures of neat PSf and zeolite-coated thin film membrane which was fabricated through heat treatment followed by phase inversion technique. The peak-to-peak and/or valley-to-valley presented by ups and downs indicate the surface roughness of the composite membranes. The obtained Rq (RMS) and Ra values for all zeolite spray-coated membranes and pure PSf matrix are enlisted in Table 4.6. It shows that for pure PSf membrane, the root mean square roughness Rq (RMS) and average roughness (R_a) was found to be 2.76±0.48 and 2.24±0.4 nm, respectively. Table 4.6 also shows the surface roughness of other membranes which reveals that the R_a value of all modified membranes increased with zeolite concentration, which was in good agreement with the FESEM data.

Table 4.6 exhibits the zeta potential value for all fabricated membrane samples. The zeta potential of all membranes was obtained at pH 7.2. The sulfonic group present in the membrane had a significant effect on the membrane's negative charge and alters the zeta potential value from -19.8 mV to -20.6, -22.7, and -28.1 mV (Figure 4.11) in the presence of 0.01, 0.1, and 1 wt.% zeolite NPs, respectively. In other words, it can be anticipated that, at higher negatively charged zeolite (imposed by trivalent atoms like aluminium, in tetrahedral coordination of zeolite network [29]) concentration, the zeta value of the membranes will increase. Notably, the zeta value for prepared Y-type zeolite was found to be -64.5 mV (Figure 4.11).

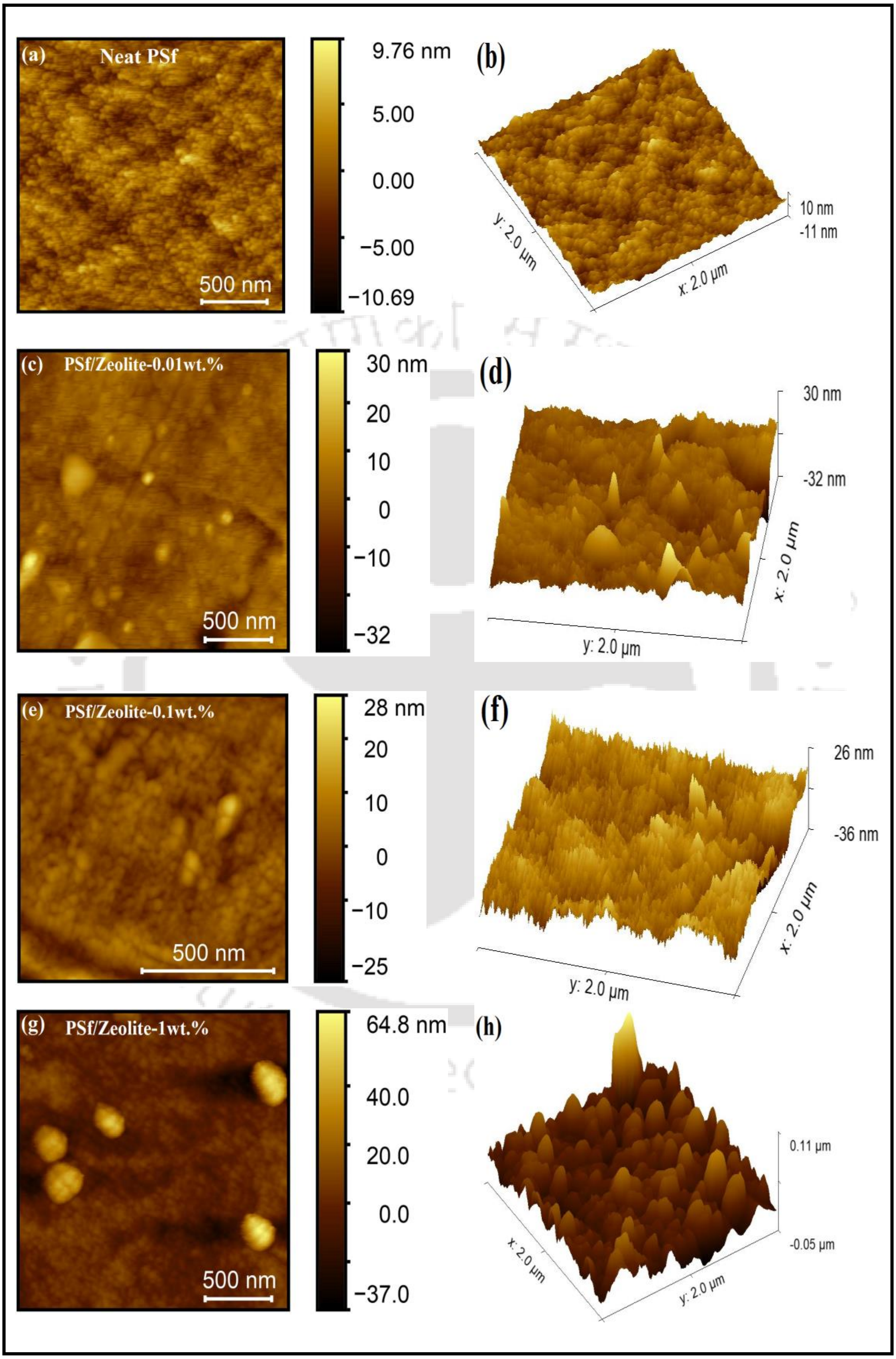

Figure 4.10: Three-dimensional and surface images of atomic force microscopy (AFM) for surface roughness analysis of prepared membranes.

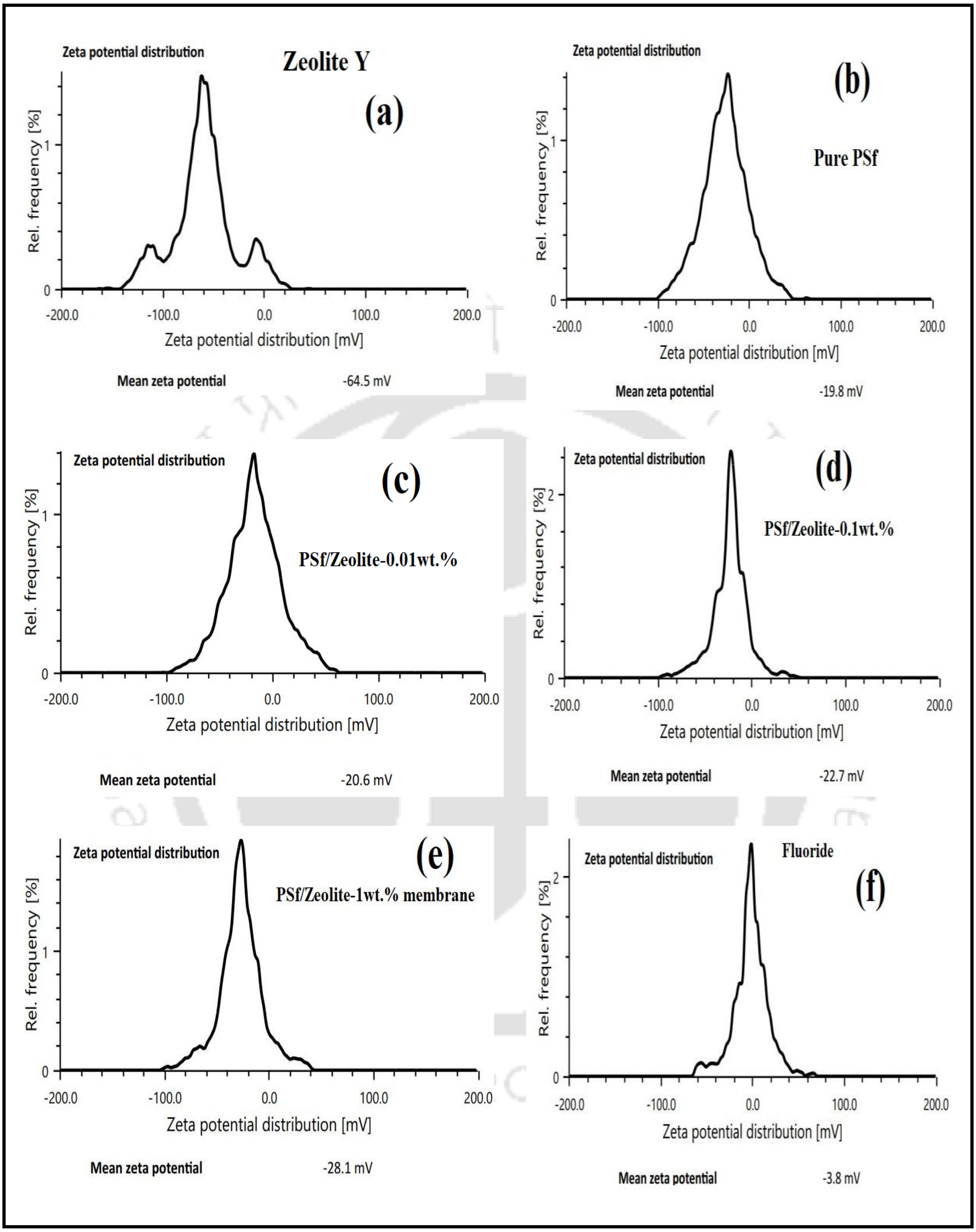

Figure 4.11: Zeta potential of (a) Neat PSf, (b) PSf/Zeolite-0.01wt.%, (c) PSf/Zeolite-0.1wt.%, (d) PSf/Zeolite-1wt.%, membrane, (e) fluoride ion and (f) prepared faujasite type zeolite Y.

Table 4.6: Surface roughness and zeta potential values of all synthesized membranes.

Membrane sample	Surface roughness		Zeta potential (mV)
	R_q (RMS) (nm)	R_a (nm)	
Pure PSf	2.76±0.48	2.24±0.41	-19.8
PSf/Zeolite-0.01wt.%	4.017±1.34	3.09±0.76	-20.6
PSf/Zeolite-0.1wt.%	4.40±1.11	3.40±0.75	-22.7
PSf/Zeolite-1wt.%	14.8±3.8	11.54±3.14	-28.1

4.5.8. Pure water flux and fluoride rejection study of all the membranes

4.5.8.1. Pure water flux of all synthesized membranes

The pure water flux of neat PSf and zeolite NPs coated membrane was carried out at 1.37 bar for 60 minutes. As depicted in Figure 4.12a, the water flux increases with the zeolite concentration. The increasing flux was denoted due to the enhancement of hydrophilicity and porosity (see Table 4.5) of the fabricated membranes. Based on the contact angle result as depicted in Figure 4.5c, the membranes' hydrophilicity was found to increase, which resulted in better water flux. Due to the increased hydrophilicity and improved porous structure, NP-layered membranes tend to attract water molecules and make water penetration easier than that of neat PSf membrane and resulting in higher water flux. The equilibrium water flux for all synthesized membranes was observed at ~50 minutes, as illustrated in Figure 4.12a. The highest water flux was found to be 28.83 L/m^{2}h for PSf/Zeolite-1wt.% membrane when compared with others.

4.5.8.2. Fluoride elimination through a cross-flow spray-coated membrane ultrafiltration process

The de-fluoridation performance of all fabricated membranes is shown in Figure 4.12b. The fluoride removal experiments were carried out at room temperature and with a transmembrane pressure of 1.37 bar. For every batch of experiments synthetic 5 ppm fluoride (F^-) solution was introduced to the dead-end filtration set-up, as illustrated in Figure 4.2. The fluoride rejection of neat PSf membrane was found to be 6.33%, however, the fluoride removal got enhanced with the higher zeolite content modified membrane. The fluoride rejection mechanism obeys the electrostatic repulsive forces that appear between negatively charged zeolite surface and negatively charged fluoride ions. Zeolite is an aluminosilicate mineral that contained $[SiO_4]^{4-}$ and $[AlO_4]^{5-}$ and creates a three-dimensional network structure carrying a negative charge [30], which results in a negative surface charge. Hence, a higher zeolite-loaded membrane resulted in a higher negative surface charge. The zeta value for as-synthetic membranes increased with higher zeolite Y concentration, as shown in Table 4.6, and thus the PSf/Zeolite-1wt% membrane was found to have the highest negative surface charge -28.1 mV. The highest fluoride removal for all membranes was attained at nearly 20 minutes, except PSf/Zeolite-1wt.% membrane.

4.5.8.3. Permeate fluoride concentration after de-fluoridation experiment over all synthesized membranes

The permeate fluoride concentrations after ultrafiltration experiments through all the fabricated membranes are presented in Figure 4.12c. The permeate fluoride concentration was found to be lowest at 1.83 mg/L when PSf/Zeolite-1wt.% membrane was utilized for the de-fluoridation study. However, the fluoride concentration of permeate was relatively higher for other zeolite wt.% membranes. Moreover, fluoride concentration data shown in Figure 4.12c suggested that the fluoride concentration on permeate side is higher than 1.5 mg/L (the permissible limit according to WHO).

The fluoride rejection results, as shown in Figures 4.12b and 4.12c, revealed that, in comparison to other synthesized membranes, the PSf/Zeolite-1wt.% membrane has remarkably reduced fluoride content from the synthetic fluoride solution. However, the permeate fluoride concentration (1.83 mg/L) was beyond the permissible limit (Figure 4.12c). The reason might be the formation of a non-uniform zeolite layer on the membrane matrix (Figure 4.13) that allow hydrated fluoride ions (0.34 nm) [31] to pass through the pores to permeate side. According to this performance, 1 wt.% zeolite-modified PSf membrane could reject 13.36 mg fluoride per m^2 area. Therefore, in the next study, membrane PSf/Zeolite-1wt.% was only considered for fluoride removal at different operating pressure and discussed in the subsequent sections.

4.5.8.4. Effect of TMP on PWF and fluoride removal over PSf/Zeolite-1wt.% membrane in the ultrafiltration operation

The fluoride rejection behavior and permeate flux of PSf/Zeolite-1wt.% membrane was observed at two different transmembrane pressure in a batch mode experimental run, as illustrated in Figure 4.14. The bar chart, as shown in Figure 4.12d exhibits the highest obtained value of permeate flux and fluoride rejection at two different pressure, respectively. A decrease in fluoride rejection or increase of fluoride concentration at permeate side was observed with a change in TMP from 2.7 to 4.2 bar. The reason might be, a reduction in repulsive force due to increasing the dispersion force at considerably greater transmembrane pressure [32].

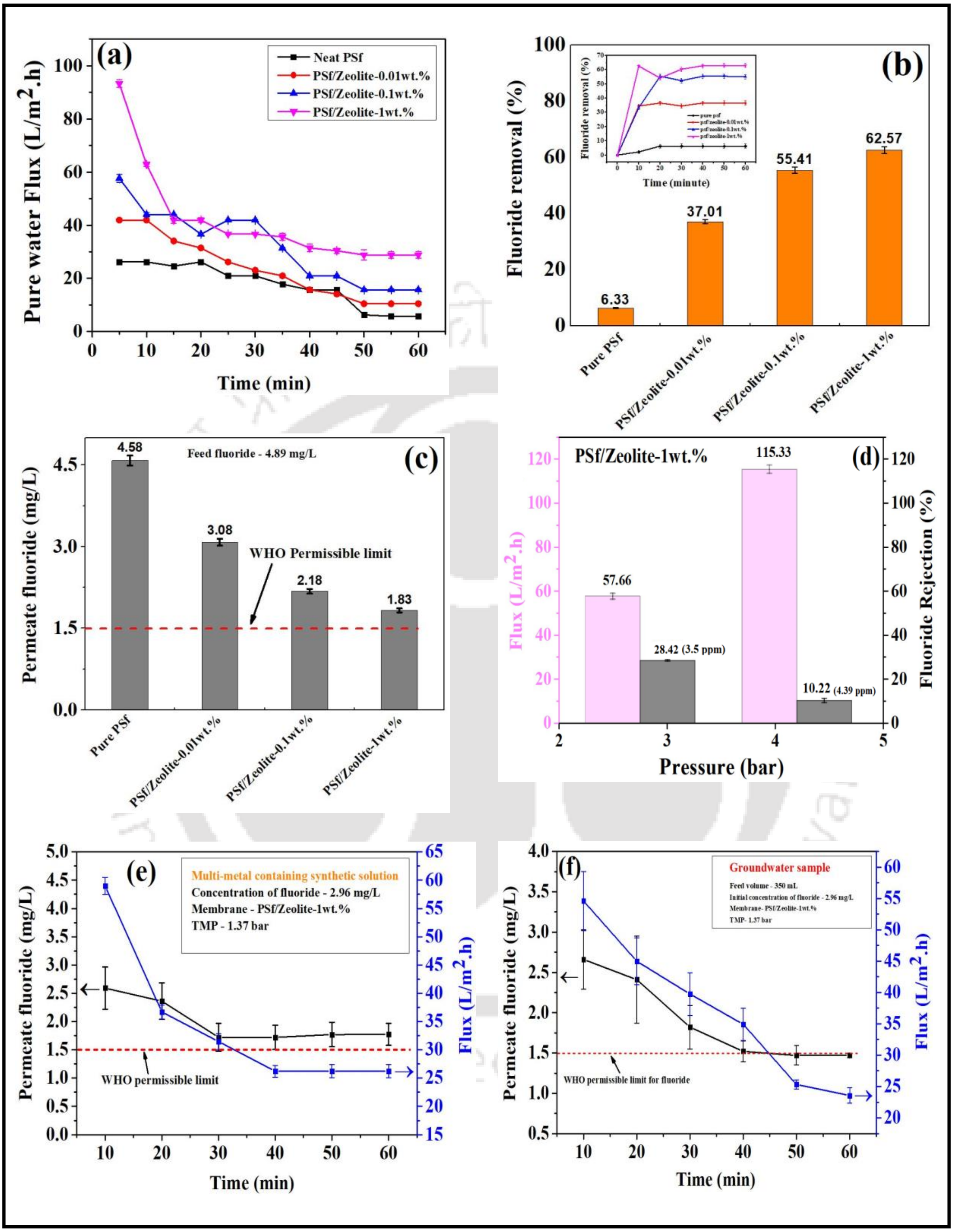

Figure 4.12: (a) Pure water flux of virgin PSf and zeolite-modified membranes (b) fluoride removal for all fabricated membranes, (c) permeate fluoride concentration and WHO permissible limit, (d) fluoride rejection at different TMP over PSf/Zeolite-1wt.% membrane, (e) fluoride rejection from multi-metal containing synthetic solution, and (f) permeate fluoride concentration after groundwater sample filtration (results are average of three replicates) at 1.37 bar (20 psi).

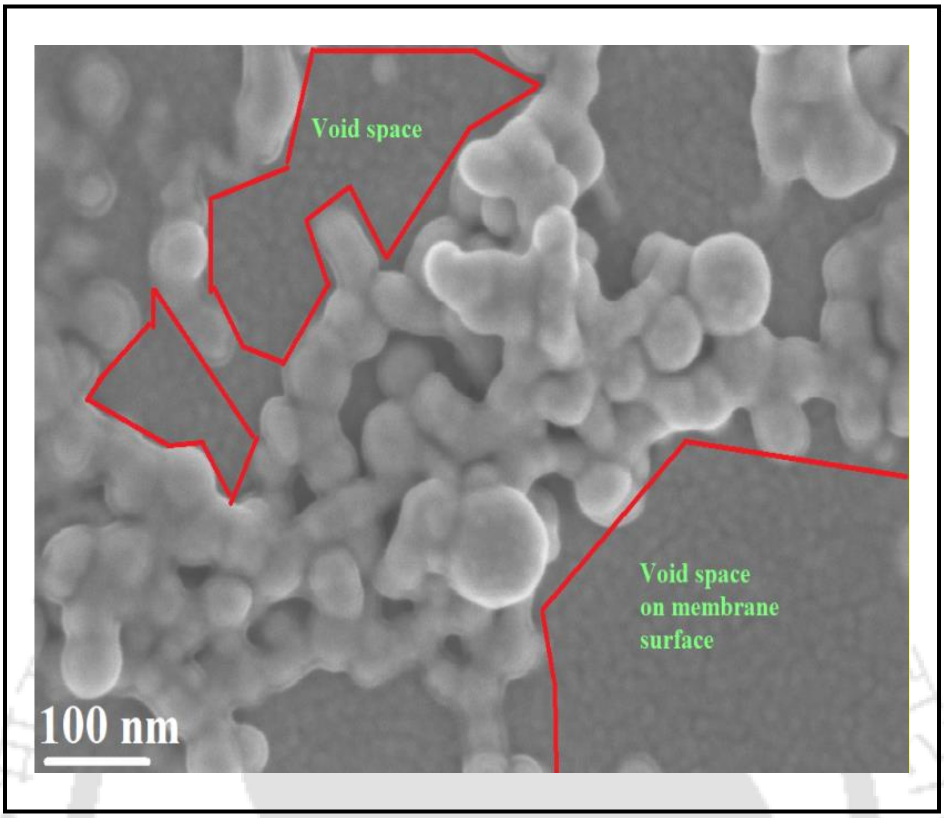

Figure 4.13: Flat sheet membrane with an uneven coating of zeolite nanoparticles. Red marked indicates the non-coated region on the membrane matrix.

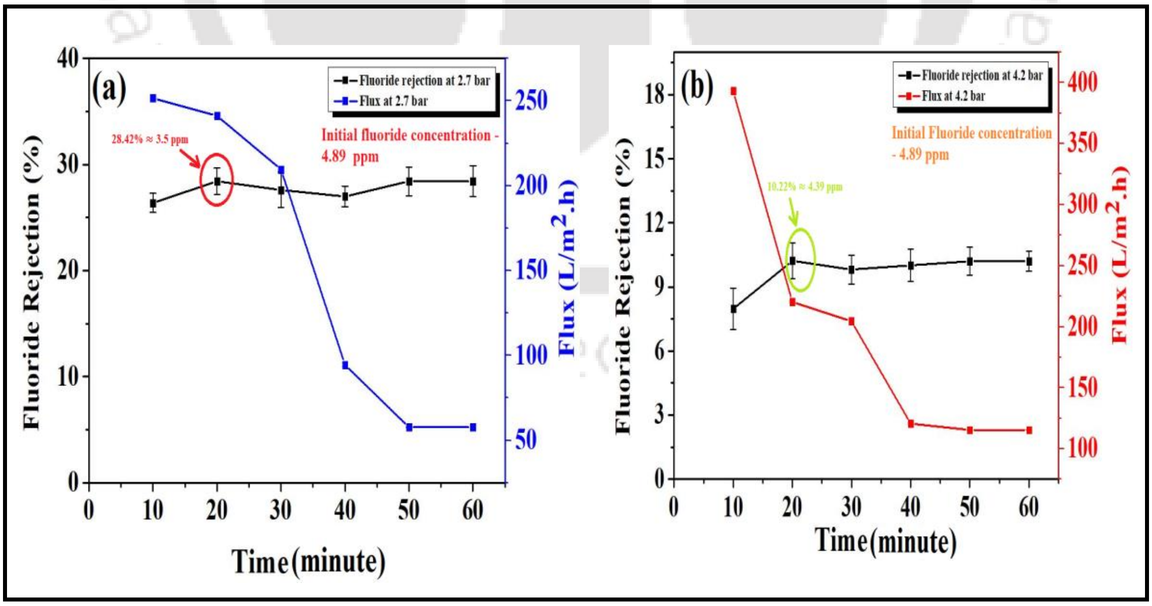

Figure 4.14: Fluoride rejection and permeate flux (a) at 2.7 bar and (b) at 4.2 bar.

4.5.8.4.1. De-fluoridation Investigation

De-fluoridation experiments were carried out with fluoride-contained groundwater to examine the impact of other ions and the practical applicability of the PSf/Zeolite-1wt.% membrane. The groundwater sample (approximately 5 L) was collected from Bhuragaon, Kaki Hojai, Assam, India. The conductivity, TDS, and pH of the water sample were found to be 473 µS/cm, 325 ppm, and 8.9, respectively. It was also found that apart from fluoride the groundwater sample contained several cations (Ca^{2+}, Mg^{2+}, Mn^{2+}, Cr^{6+}, Na^{2+}, K^{+}, Fe^{2+}) and anions (SO_4^-, Cl^-, PO_4^{3-}). The concentration of each ion is tabulated in Table 4.7, which demonstrates that the obtained values are below the WHO-permissible limit except for fluoride, chromium, and manganese. The subsequent sections described the membrane selection for the removal performance of the other elements over the opted membrane sample. For all experiments, the ideal pressure throughout is kept at 1.37 bar, taking into account the cost-effectiveness of the ultrafiltration process.

Table 4.7: Components present in collected groundwater samples.

	Components present in the sample	Concentration (mg/L)
 **Groundwater sample**	Iron (Fe^{2+})	Below detection level
	Fluoride (F^-)	2.96±0.07
	Magnesium (Mg^{2+})	16±0.08
	Manganese (Mn^{2+})	0.96±0.04
	Sulfate (SO_4^{2-})	29.69±0.14
	Chromium (Cr^{6+})	3.13±0.19
	Sodium (Na^{2+})	9.02±1.4
	Potassium (K^+)	2.7±1.12
	Chloride (Cl^-)	3.096±0.05
	Calcium (Ca^{2+})	10.15±0.04
	Nitrate (NO_3^-)	0.347±0.24
	Phosphate (PO_4^{3-})	0.231±0.06
	TDS	325

4.5.8.4.2. Fluoride rejection study from groundwater sample

Prior to proceeding with the fluoride rejection from groundwater, we prepared a synthetic solution containing fluoride, chromium, and manganese at the same concentration level as the groundwater. This batch mode experiment was conducted for a period of 60 minutes to obtain a rough idea of fluoride rejection from the groundwater sample using a synthesized PSf/Zeolite-1wt.% membrane. Figure 4.12e depicts the fluoride rejection behavior from a multi-metal synthetic water system. Results revealed that with time the fluoride rejection was increased gradually and the highest rejection was found to be at 41.21% after 60 minutes with a permeation flux of 26.21 L/m^{2}h. Therefore, the fluoride concentration at permeate was measured as 1.74 mg/L (Figure 4.12e).

The de-fluoridation of the groundwater sample has been shown in Figure 4.12f. It is observed that the permeate fluoride concentration gradually decreases with time. Fluoride concentration at permeate after 10 minutes was found to be 2.66 mg/L and reached equilibrium at 50 minutes with a concentration of 1.47 mg/L, which is equivalent to 50.33% fluoride rejection. It was found that the permeate fluoride concentration also reaches below the WHO permissible limit. The results compared with the fluoride rejection study for the multi-metal system, reveals that the highest fluoride rejection was obtained on the membrane surface for the groundwater sample. This could be attributed to (i) the zeta potential value for PSf/Zeolite-1wt.% membrane was found to be -28 mV (Table 4.6). Therefore, it can be assumed that both the zeolite and membrane surface will contribute a negative charge that can easily adsorb cations from the contaminated water. Considering our case, the cations present in groundwater get easily adsorbed on the zeolite surface and membrane matrix, resulting in cake-layer formation, that led to pore blocking and decay in permeation flux (23.59 L/m^{2}h) which is less than pure water flux of unused PSf/Zeolite-1wt.% membrane's flux (28.83 L/m^{2}h). This mechanism can be attributed to higher fluoride rejection as compared with the rejection results achieved after filtration of multi-metal synthetic solution over the functionalized PSf/Zeolite-1wt.% membrane; (ii) the mechanism can also be explained by electrostatic interaction between the membrane surface and solutes: repulsion charge exists between negatively charged solutes and membrane surface. There are no charge interactions between neutral solutes and the membrane surface, whereas positively charged solutes encourage charge attraction. As a result, there are more positively charged solutes at the membrane as well as zeolite surface than in the bulk solution (because they are drawn to the membrane that is negatively charged), which lowers the measured rejection values. For negatively charged ions (fluoride in this study), the opposite holds: the repulsive charge causes a lesser density of negatively charged solutes to accumulate at the membrane surface, leading to a higher rejection. This mechanism is known as “charge concentration polarization” [33]. The possible mechanism of fluoride rejection and other heavy metals removal from groundwater sample has been illustrated in Figure 4.15.

The total fluoride ion rejection was experimented utilizing PSf/Zeolite-1wt.% membrane and it was found that the fabricated membrane can reject ~6.5 mg fluoride per m^2 membrane area (6.50 mg F^-/m^2). The fluoride rejection investigation demonstrates that unequal distribution of negatively charged zeolite on the membrane surface leads to decay in fluoride rejection, which causes increased fluoride concentration at permeate section. Thus, a significant problem in the fabrication of surface-coated membranes is the uniform distribution of nanoparticles.

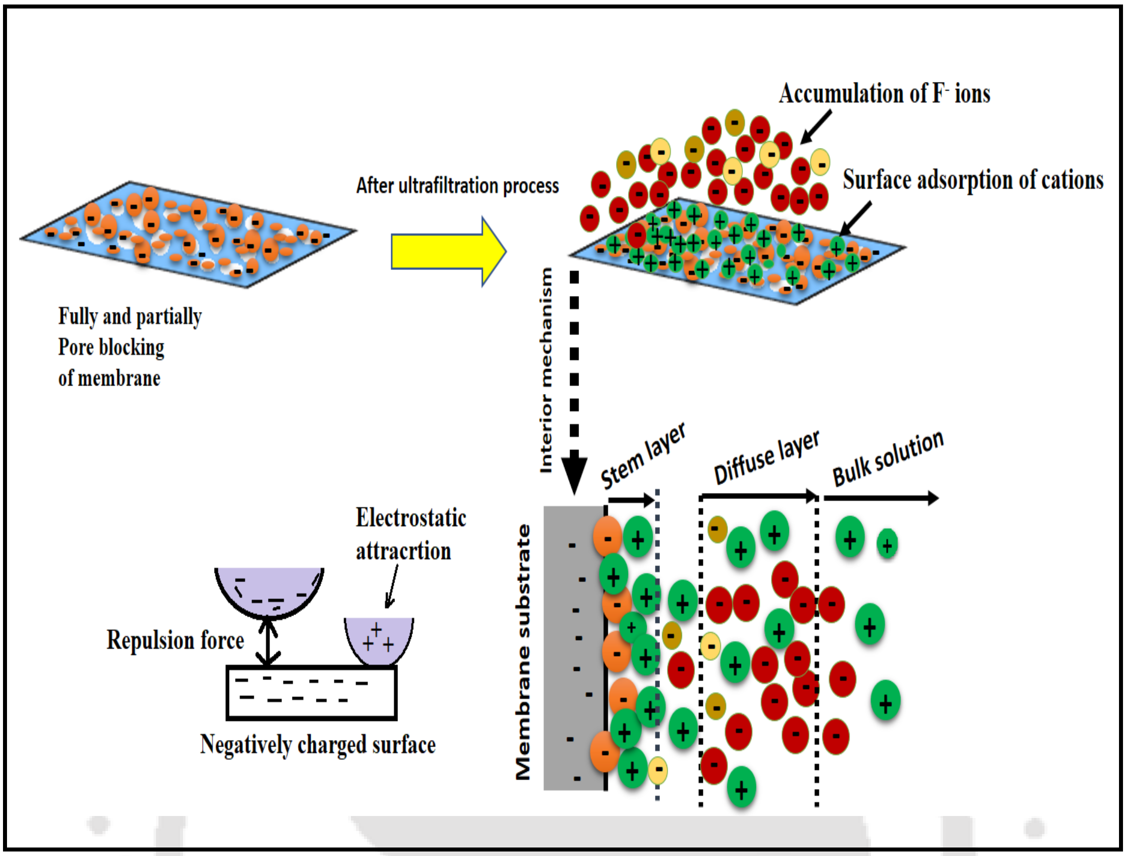

Figure 4.15: Possible mechanism of fluoride rejection and other heavy metals adsorption over fabricated PSf/Zeolite-1wt.% membrane.

4.6. Membrane selection for the heavy metal ions removal

The adsorption study of manganese (Mn^{2+}) and chromium (Cr^{6+}) (as mentioned in Table 4.7) was carried out in order to obtain a suitable membrane for metal ions removal from the collected water sample. Before this investigation, an aqueous stock solution of manganese and chromium of 1000 mg/L was prepared in distilled water. By successive dilution, the necessary concentration for each working solution was obtained. The removal of manganese and chromium metal ions was conducted utilizing the prepared membranes with the same experimental conditions (as discussed previously for F^- removal study), and shown in Figure 4.16. The synthetic solution of manganese and chromium was prepared according to their concentration present in the groundwater sample, as illustrated in Table 4.7. The results achieved from the study revealed that 1wt.% zeolite-coated PSf membrane has shown a higher metal ions removal capacity than others. For manganese, the highest removal percentage was found to be 100%, whereas, 60.66% chromium removal was found over the fabricated PSf/Zeolite-1wt.% membrane.

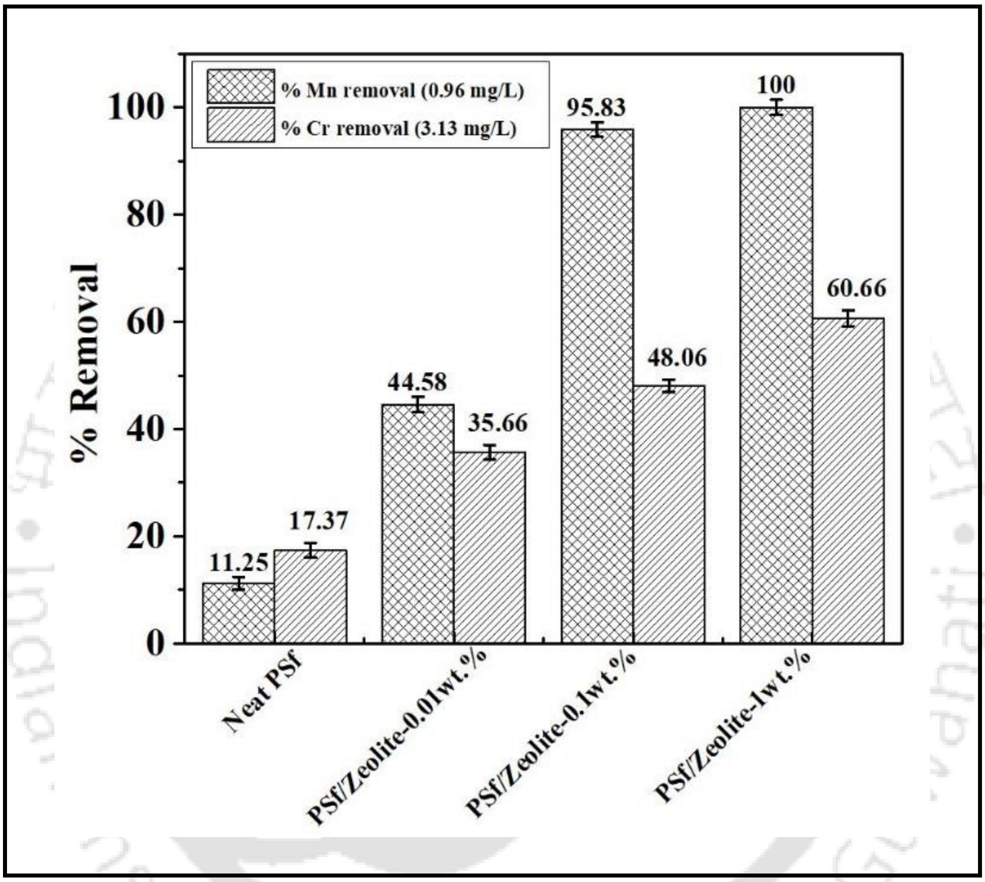

Figure 4.16: Metal ions removal percentage from synthesized membranes.

From the above study, it was concluded that membrane PSf/Zeolite-1wt.% showed a significant impact on metal ions removal. Henceforth, this membrane has opted for the next studies, which illustrate the removal behavior of manganese and chromium from multi-metal-containing synthetic solution and contaminated groundwater sample.

4.6.1. Manganese and chromium removal study from synthetic multi-metal containing solution and groundwater sample using PSf/Zeolite-1wt.% membrane

Figure 4.17, illustrates the manganese (Mn^{2+}) and chromium (Cr^{6+}) removal study from multi-metal containing synthetic solutions and groundwater sample, respectively, at 1.37 bar. From Figures 4.17a and b, it is observed that the manganese concentration decreased gradually with time, which is attributed to the surface adsorption on the membrane or in other words, the electrostatic attraction occurred between positively charged manganese ions with negatively charged zeolite particles present on the membrane's surface. After the ultrafiltration operation, the manganese concentration was found to be in the range of 0.37-0.395 mg/L for multi-metal and groundwater samples, respectively. The permeate manganese concentration was found to be 0.5 mg/L (below the permissible limit according to WHO). It was also noted that (Figure 4.17 a and b), during the ultrafiltration process, the manganese concentration at permeate side dropped below its permissible limit within 10-20 minutes of operation for the multi-metal solution. When the ultrafiltration study was carried out with ground water samples the operation time was found to be 30-40 minutes for attaining concentration below permissible limit. The difference in time taken to reach the permissible limit for groundwater samples is presumably due to the competitiveness of other cations present (e.g., Na^{2+}, K^{+}, Mg^{2+}, Cr^{6+}), which may hinder the adsorption process of manganese on the membrane surface.

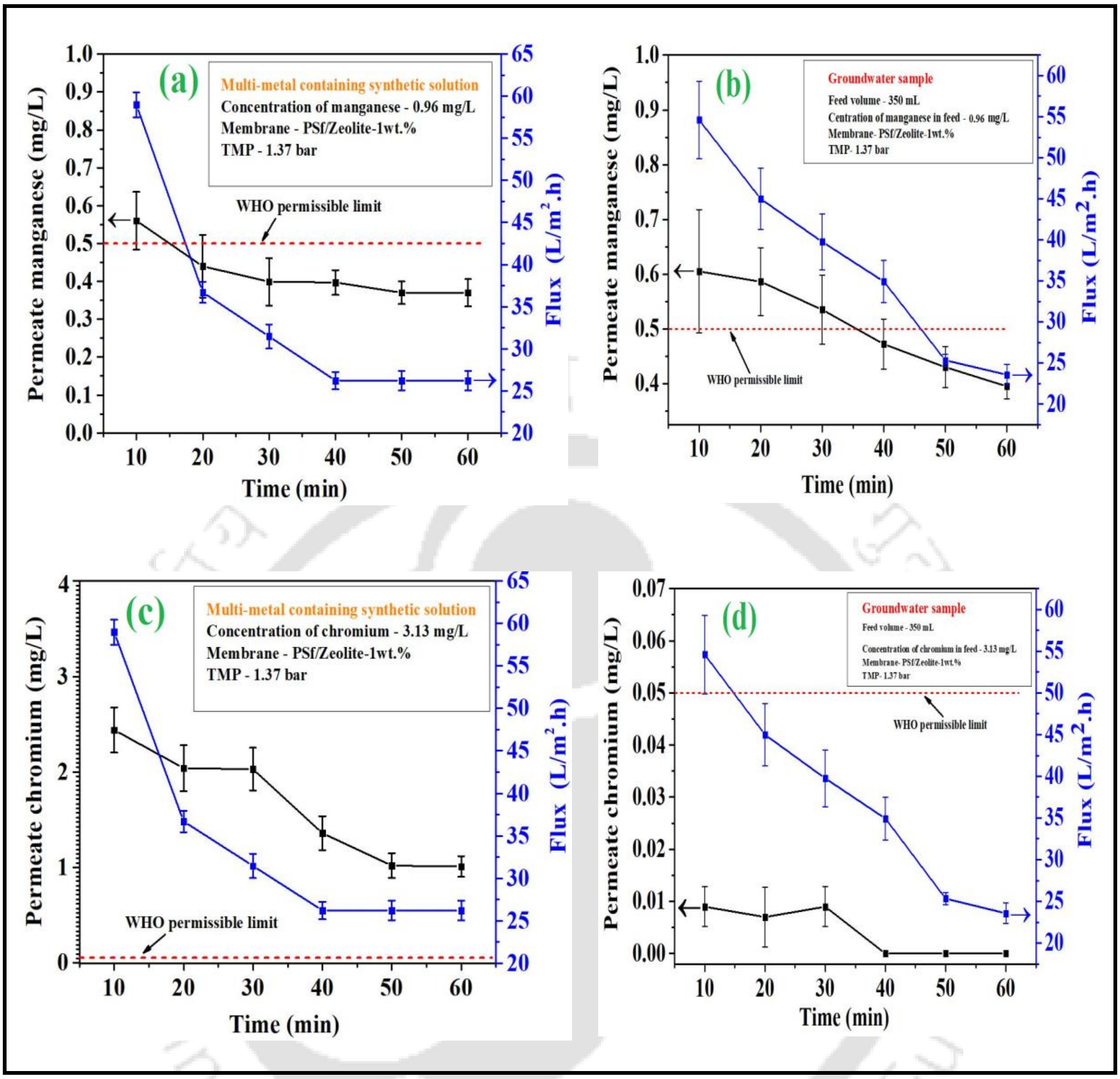

Figure 4.17: (a), (b) manganese and (c), (d) chromium metal ions removal from synthetic multi-metal-containing solution and groundwater sample using PSf/Zeolite-1wt.% membrane.

The chromium removal study was illustrated in Figure 4.17 c and d, respectively, keeping all process parameters same. As shown in Figure 4.17c, drastic chromium removal was observed resulting in a decrease in permeate chromium concentration (1.02 mg/L). The reason can be explained by the adsorptive surface characteristic of the membrane and the formation of an adsorbate monolayer on the membrane's surface. The permeate chromium concentration was found to be beyond the permissible limit due to (i) saturation of the active site of zeolite nanoparticles by chromium ions and (ii) channeling of chromium through the membrane pores containing less zeolite-coated region.

On the other hand, a ‘zero’ concentration of chromium was obtained at permeate side, as shown in Figure 4.17d, which implies 100% chromium was removed. The results can be explained by (i) adsorption of Cr^{6+} and other adsorbates (in groundwater sample) due to electrostatic interaction with the adsorptive membrane surface, which results in cake layer formation on the membrane surface which leads to pore blocking and hinders the chromium permeation through the pores (as chromium has bigger hydrodynamic radius among others), (ii) the electrostatic repulsion based chromium removal can also be considered after the sufficient extent of Cr^{6+} adsorption on the skin layer, leading to accumulation of Cr^{6+} ions at diffusion layer and bulk solution. It is also notable that the electrostatic repulsion-based rejection phenomenon will be more plausible when sufficient adsorption of the targeted cations will take place on the membrane skin layer [34]. This reason can be attributed to the drastic reduction of Cr^{6+} in the groundwater sample. The mechanism of this removal study has been represented in Figure 4.15.

As stated earlier, the permeate flux for a multi-metal solution was comparatively higher than the flux obtained for groundwater samples, which is because of the formation of several ionic layers on the membrane surface, resulting in reduced penetration of water molecules through the pores. According to the results, PSf/Zeolite-1wt.% membrane could filter 2722 gallons of groundwater per m^2 of area per hour at the permeate rate of 23.59 L/m^2h. Notably, after washing with DI water the membrane flux was moderately increased to 24.63 L/m^2h. This value was used to find the flux recovery ratio and total fouling of the selected membrane, which is provided in the following section.

Table 4.8 represents the concentration of elements before and after groundwater treatment. The permissible limit of all elements is shown in Table 4.8, in accordance with the Bureau of Indian Standards (BIS) standards (2012) [35]. It was also found that the concentration of other essential elements was reduced after the process and enlisted in Table 4.8.

Table 4.8: The concentration of fluoride and other heavy metals in groundwater sample before and after the ultrafiltration process.

Elements and other parameters	Before treatment (mg/L)	After treatment (mg/L)	Permissible limit (mg/L)
F^-	**2.96±0.07**	1.47±0.08	1.5
Fe^{2+}	Below detection level	-	0.3-1
Mg^{2+}	16	11.04	30-100
Mn^{2+}	**0.96±0.04**	0.395±0.02	0.1-0.5
SO_4^{2-}	29.69	24.17	200
Cr^{6+}	**3.13±0.19**	0.00	0.05 (no relaxation)
Ca^{2+}	10.15	7.34	75-200
Na^{2+}	9.02	5.67	200
K^+	2.7	2.4	200
Cl^-	3.096	1.37	250-1000
NO_3^-	0.347	0.277	45 (no relaxation)
PO_4^{3-}	0.231	0.231	1.0
TDS	325.66±0.54	265±0.37	500
Conductivity	47.5±0.236 μS/cm	45.07±0.354	-
Salt	232±0.012	137±0.02	-
pH	8.9±0.5	8.15±0.09	6.5-8.5

4.6.2. Adsorption isotherm analysis

In the UF chamber, Cr^{6+} and Mn^{2+} concentrations were varied from 2 to 4 and 0.5 to 1.5 mg/L, respectively, to examine the adsorption isotherm with a fixed membrane weight of 0.54 g. As shown in Figure 4.18a, the equilibrium adsorption time for Mn was reached at 30 minutes with 100% removal. It was also found that C_e/Q_e value shows 'zero' while considering the highest removal, i.e., 100%, by which no isotherm data could be fitted. Hence, adsorption behaviour was only considered for up to 30 minutes which is shown in Figure 4.18b. It was found that no isotherm model was fitted with the obtained adsorption data except the Langmuir isotherm. It shows that Langmuir isotherm fits better with an R^2 value of 0.99 for chromium as compared with manganese (R^2 = 0.96), according to Figures 4.18c and 4.18d. The highest adsorption capacity was measured as 2.37 and 1.18 mg/g for Cr^{6+} and Mn^{2+}, respectively. The isotherm results indicate that the adsorption mechanism followed physisorption which results in monolayer formation on the membrane surface.

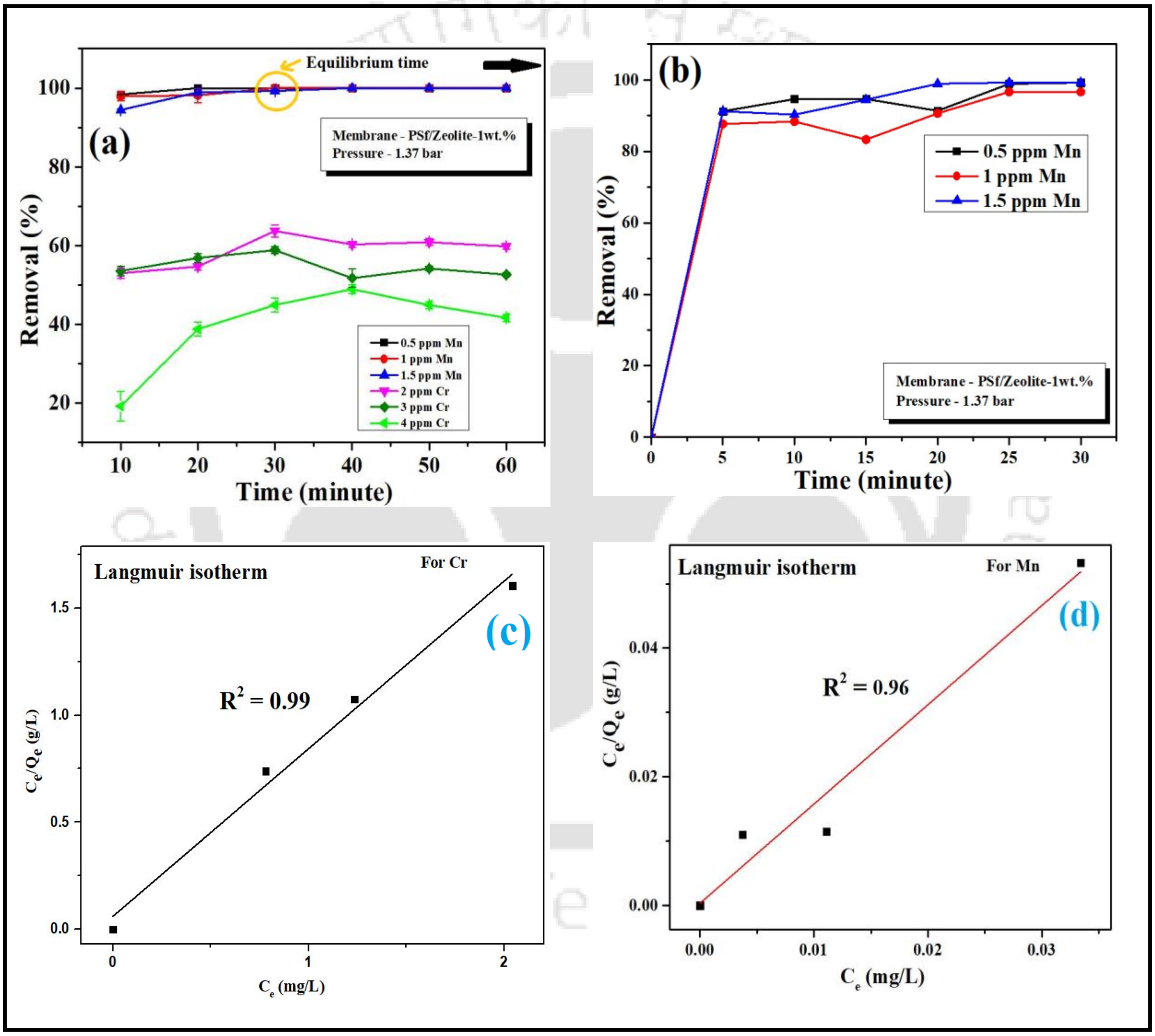

Figure 4.18: (a) Removal % of Mn^{2+} and Cr^{6+} within different concentration ranges, (b) removal behaviour of Mn^{2+} for first 30 minutes where concentration reached equilibrium for 60 minutes operation time, (c) Langmuir isotherm for Cr^{6+} and (d) for Mn^{2+}, respectively (working pressure-1.37 bar; Membrane-PSf/Zeolite-1wt.%).

4.6.3. Total fouling (Rt) and flux recovery ratio (FRR) of membrane PSf/Zeolite-1wt.%

Total fouling and its mechanisms are determined by membrane surface properties such as hydrophilicity and surface charge. It was also reported that adding polyethylene glycol (PEG) or polyacrylonitrile (PAN) to the PSf membrane increases its surface hydrophilicity [36]. In this study, steel slag-derived zeolite nanoparticles were incorporated into the PSf substrate in order to enhance the membrane's hydrophilicity. The chemical structure of a zeolite comprising innumerable oxygen bonding (-O) contributed to the hydrophilic by absorbing water molecules to create hydroxyl bonding [37]. According to Huang et al. [38], the presence of nanoparticles on the upper layer of the membrane enhances the antifouling ability. The membrane PSf/Zeolite-1wt.% exhibits a good antifouling behavior and flux recovery ratio after the filtration process. The FRR, R_t, R_r, and R_{ir} value was calculated using equations (4.5) to (4.8), as described earlier (section 2.5.2). The total fouling and flux recovery ratio was evaluated from equations (4.5)-(4.8). According to the results, PSf membrane functionalized with zeolite nanoparticles has shown excellent flux recovery of 85.43% as compared with other literature [39,40] with less total fouling (R_t) of 3.61%.

From the fouling study, it can be envisaged that the membrane exhibits a magnificent anti-fouling character. It can be assumed that electric double-layer repulsion-based metal removal may results in good anti-fouling behavior [41].

4.7. Characterization of spent membrane

4.7.1. FESEM and EDX analysis

Figure 4.19a depicts the FESEM analysis of the used PSf/Zeolite-1wt.% membrane after the separation of the groundwater sample. Agglomerated particles were observed on the membrane. A membrane pore block was seen on the membrane surface, indicating adsorption as well as accumulation when the adsorbate-adsorbent interaction took place.

The elemental analysis of the spent membrane has been shown in Figure 4.19b. The elemental analysis shows the number of deposited elements on the membrane substrate. A significant fluoride concentration was detected, indicating the rejection of F^- ions by the membrane PSf/Zeolite-1wt.%. Furthermore, the presence of other targeted contaminants (Cr^{6+} and Mn^{2+}) confirms the successive adsorption on the zeolite-modified membrane. Results achieved from the study revealed that the fabricated PSf/Zeolite-1wt.% membrane can adsorb and reject detrimental constituents from contaminated water.

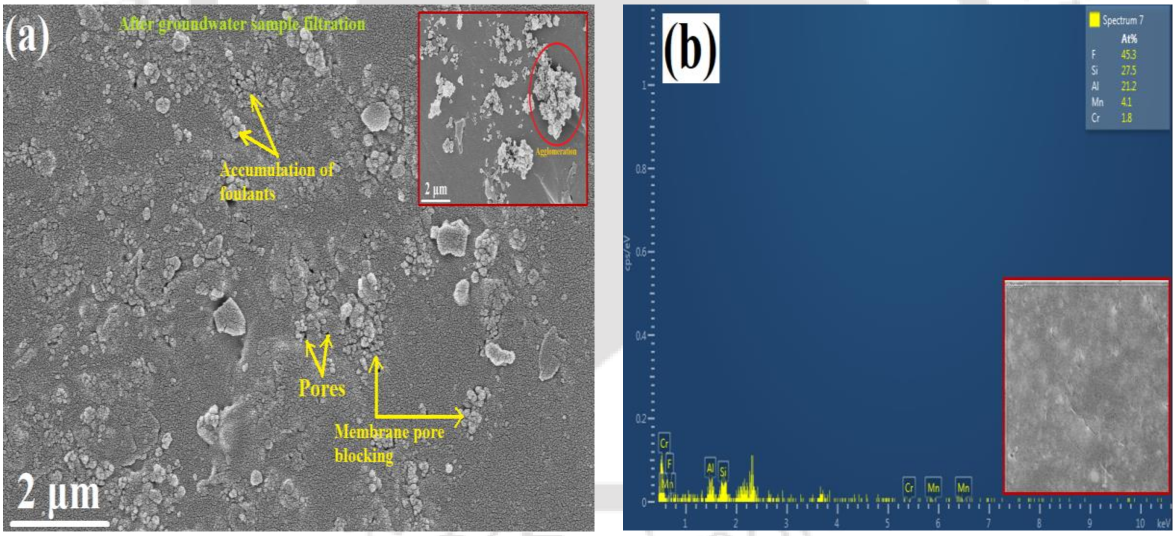

Figure 4.19: (a) FESEM and (b) EDX analysis of spent PSf/Zeolite-1wt.% membrane after groundwater sample filtration.

4.7.2. ATR-FTIR spectroscopic analysis

The ATR-FTIR spectra of unused (also provided in Figure 4.7b) and used membranes have been shown in Figure 4.20a and 4.20b, respectively. It was observed that after groundwater filtration some functional groups are shifted towards the higher wavenumber attributed to the interaction of polymer chain and adsorbates which took place during the filtration process. Table 4.9 shows the absorption bands of various functional groups for PSf/Zeolite-1wt.% membrane, before and after filtration. It reveals that the existing absorption band for the C=C and O=S=O groups in the spent membrane was shifted to higher wavenumbers at 1587 and 1149 cm^{-1} when compared to the unused membrane, presumably due to chemically bonding of the adsorbed elements with the membrane chain that occurred after the pressure-induced filtration process.

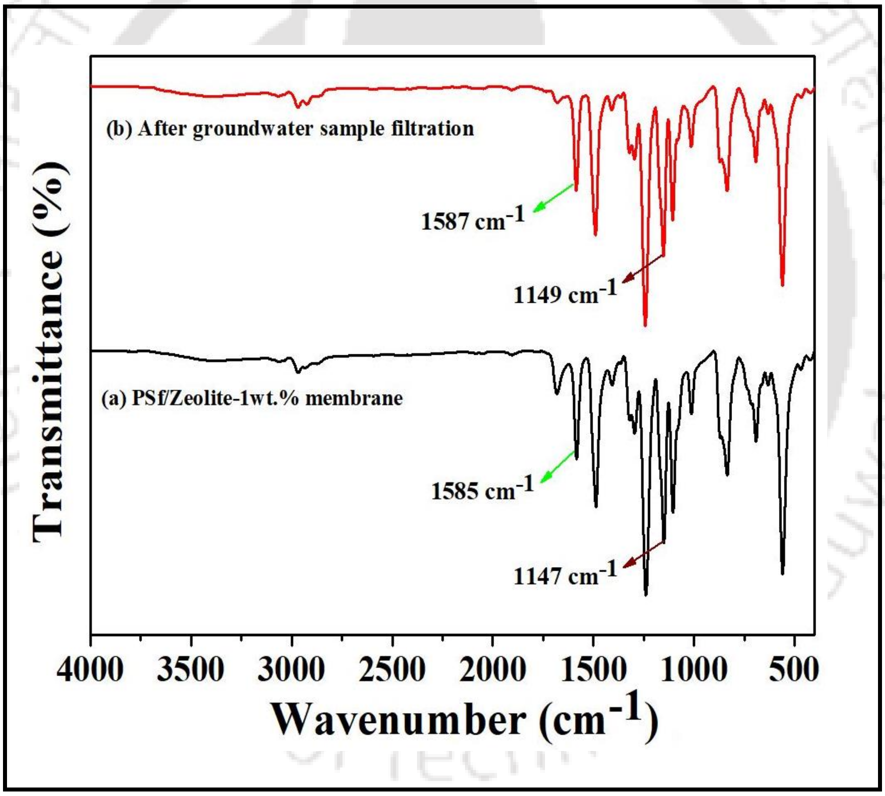

Figure 4.20: ATR-FTIR analysis of (a) unused and (b) used PSf/Zeolite-1wt.% membrane.

Table 4.9: Peak shifting and peak position of the functional groups of the used membrane.

Membrane Sample	Peak position before filtration	Peak position after filtration
PSf/Zeolite-1wt.%	1585 (C=C) 1147 (O=S=O)	1587 (C=C) 1149 (O=S=O)

4.7.3. XPS analysis of spent PSF/Zeolite-1wt.% membrane

The XPS analysis of the used membrane has been shown in Figure 4.21 and the corresponding XPS binding energies for the C 1s, N 1s, O 1s, Si 2p, and Al 2p were enlisted in Table 4.10. These results demonstrate the core level XPS Si 2p and Al 2p shifts of the spent membrane as compared with the unused membrane, as seen in Table 4.4. The findings imply the reduction in electron binding energy of 0.1 to 0.6 eV for Si 2p and 0.32 eV for Al 2p. Based on the analysis, no considerable changes were seen for C 1s XPS spectra.

Now considering the core level XPS N 1s for unused and used membrane (Table 4.4 and Table 4.10), it was found that the BEs of (C)-N= and N^- group decreased accordingly from 399.87 to 399.61 eV and 400.62 to 400.23 eV, respectively. Furthermore, two distinct peaks were observed after the deconvolution of O 1s spectra, as shown in Figure 4.21d. The O=S=O/OH^- and O-C-O group of O 1s core level was shifted towards higher BEs, in the order of 0.17 to 0.45 eV. Higher binding energy indicates a higher oxidation state due to the extra coulombic interaction between the photo-emitted electron and the ion core.

From the analysis, it can be concluded that the Si 2p and Al 2p group of the zeolite framework was shifted towards the higher binding energies. Moreover, lower binding energies of N 1s and O 1s spectra were found in the used membrane which is attributed to the surface adsorption as well as surface complexation on zeolite layered PSf substrate. Specifically, the peak shift of the hydroxyl group is strongly indicated in the involvement of oxides of chromium and manganese, which was caused by the removal of Cr^{6+} and Mn^{2+}. The results were in good agreement with the FESEM-EDX analysis of the used membrane.

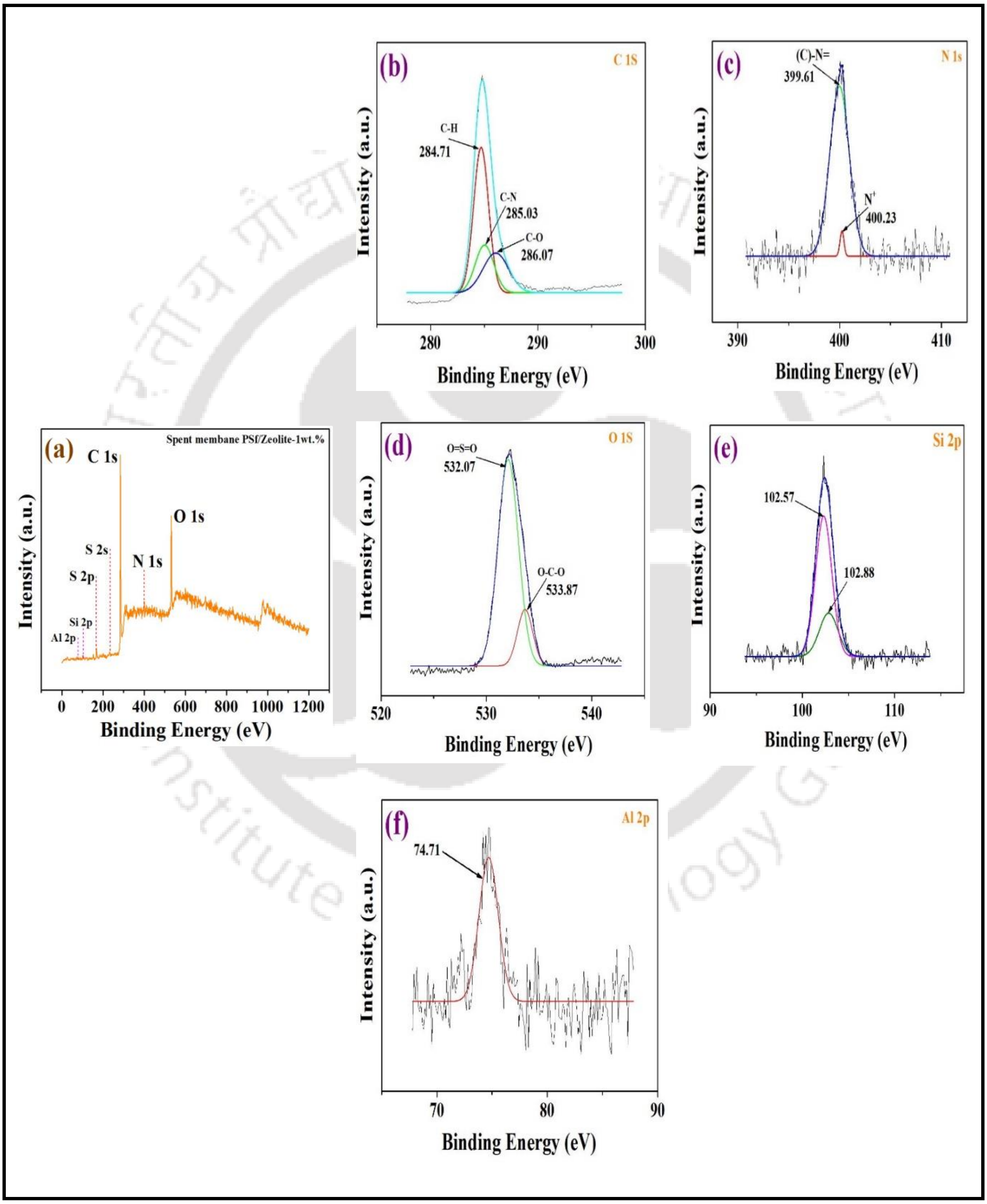

Figure 4.21: XPS spectra for the used membrane: (a) wide scan, (b) C 1s, (c) N 1s, (d) O 1s, (e) Si 2p, and (f) Al 2p spectra.

Table 4.10: XPS binding energies (eV) of the used membrane.

Spectra	Group	Spent PSf/Zeolite-1wt.%
C 1s	**C-H**	284.72
	C-N	285.03
	C-O	286.07
N 1s	**(C)-N=**	399.61
	N^-	400.23
O 1s	**$O{=}S{=}O/OH^-$**	532.07
	O-C-O	533.87
Si 2p	**-**	102.57, 102.88
Al 2p	**-**	74.71

4.7.4. Tensile strength analysis of all synthetic membranes and used PSf/Zeolite-1wt.% membrane

The stress-strain plot as depicted in Figure 4.22 exhibits the mechanical behaviour of synthesized membranes along with the used PSf/Zeolite-1wt.% membrane and Table 4.11 illustrates the corresponding mechanical values. Young's modulus was computed using the slope of the stress vs. strain curve in the linear elasticity regime of uniaxial deformation, whereas the ultimate tensile strength was approximated using the highest tensile stress obtained at the breakpoint. The strain is stated as the ratio of the change in length to the total length of the samples, and the stress is a function of the force applied to the area of the cross-section. It is assumed that the concentration of zeolite materials has a profound effect on Young’s modulus and tensile strength. Zeolite coating on the membrane firstly increases the tensile strength and Young’s modulus from 0.95 to 4.06 MPa and 17.61 to 141.62 MPa, respectively. The improved mechanical strength can be ascribed to the development of sponge-like structures and excellent mechanical characteristics of synthetic zeolite. Thereafter, these values were decreased by 0.1wt.% zeolite concentration (Table 4.11) that is presumably due to aggregation and weak interface of nanolayers. The obtained results revealed that membrane PSf/Zeolite-1wt.% has the highest tensile strength and Young's modulus that can withstand greater stresses without considerable deformation.

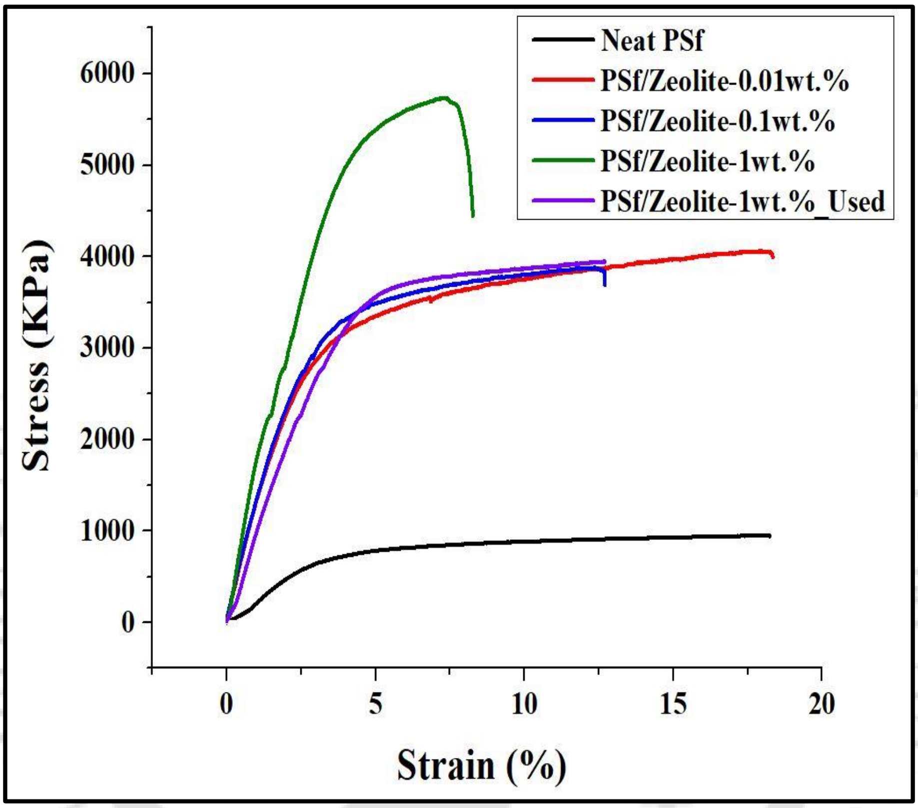

Figure 4.22: Stress-strain plot of all fabricated membranes and used PSf/Zeolite-1wt.% membrane.

According to the results, due to abrasion during the filtration process, the membranes became more fragile (lowering the elongation and tensile strength). The tensile strength and elongation of the used membranes were found to be 4.38 MPa and 28.34%. Additionally, backwashing with a chemical agent like HCl has the potential to degrade the PSf as well as to remove membrane fouling.

Table 4.11: Mechanical properties of all fabricated membranes and used membrane.

Membrane Samples	Tensile strength (MPa)	Elongation at strength (%)	Elongation at break (%)	Tensile strength at maximum point (MPa)	Young's modulus (MPa)
PSf	0.95	12.77	18.18	18.23	17.61
PSf/Zeolite-0.01wt.%	4.06	15.04	17.90	18.34	141.62
PSf/Zeolite-0.1wt.%	3.88	9.62	12.34	12.69	141.23
PSf/Zeolite-1wt.%	5.73	4.80	7.88	8.99	184.79
PSf/Zeolite-1wt.% (after 4th cycle)	4.31	32.60	36.58	36.81	113.06

4.7.5. Regeneration of the used PSf/Zeolite-1wt.% membrane

In order to investigate the reusability of the PSf/Zeolite-1wt.% membrane, a regeneration experiment was conducted by passing a 3 pH HCl solution through the dead-end filtration set-up. For membrane regeneration, utilizing pH 3 was found to be optimum. The regeneration process took place after each filtration cycle. Solution at a much lower pH may damage the membrane structure and the membrane cannot be further reutilized [42]. During the regeneration process, H^+ ions produced by HCl replace the Cr^{6+} and Mn^{2+} ions adsorbed by functional groups of zeolite Y, resulting in the regeneration of the active adsorption site of the zeolite as well as the membrane. Figure 4.23a depicts the percent removal of Cr^{6+} and Mn^{2+} and F^- rejection behavior during four regeneration cycles. The results obtained after cycle 1 shows that only manganese concentration at permeate was below the permissible limit except for chromium and fluoride with a permeation flux of 20.96 L/m^{2}h. A drastic decrease in fluoride rejection was seen after the first cycle. It was also observed that for cycle 2 and cycle 3 the water flux was found to be at 41.93 and 52.42 L/m^{2}h, respectively, which may be due to the creation of void space on the membrane surface caused by regeneration that lead to leach out of ZNPs from the membrane surface. A small amount of zeolite particles was noticed on the regenerated membrane surface, as depicted in Figure 4.23b. Another reason for higher flux might be the membrane swelling (Figure 4.23b) which could lead to a sudden increase in the membrane's pores size and result in high water permeation. It was also seen from Figure 4.23a that the water flux for the last cycle declined to 51.37 L/m^{2}h which is presumably due to reverse fouling of the F^-, Mn^{2+}, and Cr^{6+} ions.

This regeneration study demonstrates the degradation of polymer substrate after membrane regeneration. Membrane swelling causes the creation of big pores and increases water permeability, which may adversely affect pollutant removal.

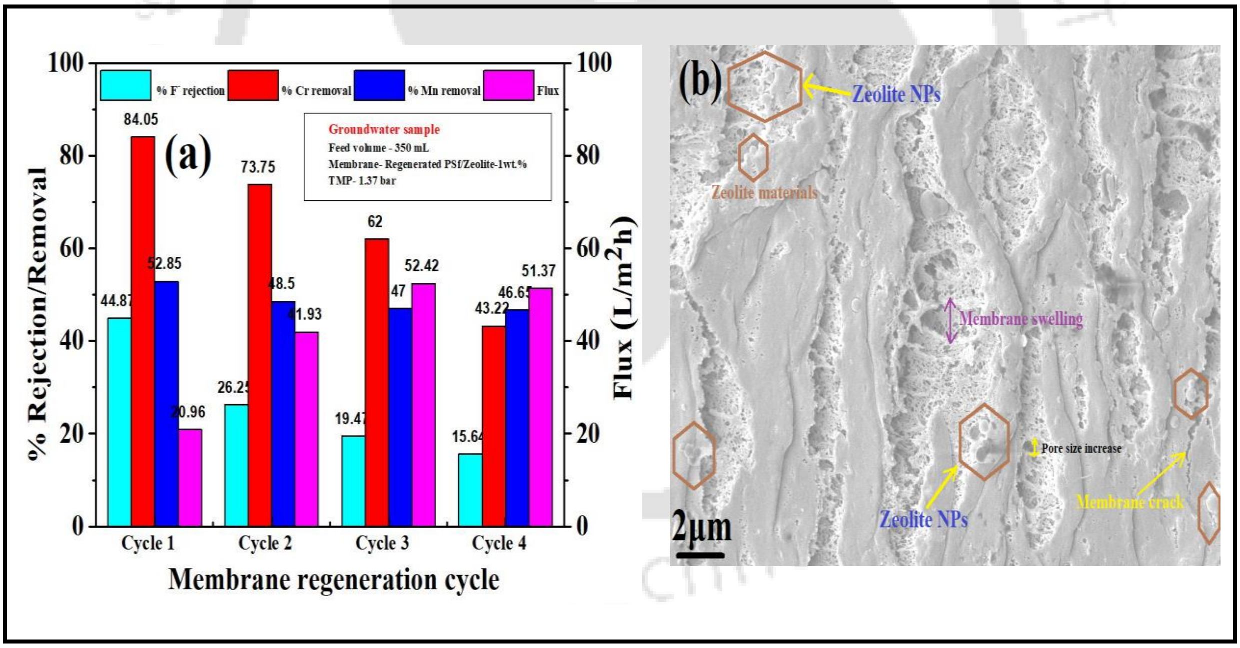

Figure 4.23: (a) Cr^{6+}, Mn^{2+} removal, and F^- rejection performance of regenerated membrane and (b) FESEM image of the regenerated membrane after cycle 4.

4.8. Cost analysis of prepared membrane

According to Das et al. [43], the cost analysis of the membrane was performed to evaluate the total cost of materials required to synthesize a 1wt.% zeolite-coated PSf membrane with a surface area of 1 m^2. The total synthesis cost of 1 m^2 of the zeolite-modified membrane was estimated to be 131.04 USD (detail of cost analysis is provided in Table 4.12). It was observed that the 1wt.% zeolite-coated PSf membrane had a flux of 23.59 L/m^2h when utilized for treating groundwater contaminated with F^-, Mn^{2+}, Cr^{6+}. Though water flux studies are shown only for 1 hour, but the prepared 1wt% zeolite-coated PSf membrane was found to provide stable results when utilized for 3 hours during 1st cycle. It was estimated that the cost of treating groundwater contaminated with F^-, Mn^{2+}, Cr^{6+} was ~ 0.022 USD/L. According to this result, the fabricated membrane is cost-effective considering the desirable performance of the membrane.

Table 4.12: Cost estimation to prepare PSf/Zeolite-1wt.% membrane for ultrafiltration studies.

Sl. No.	Material used	Amount taken	Price (INR)	
1	**Zeolite**	100 mg	11	
2	**NMP**	8 mL	12.8	
3	**PSf**	1.9 g	133	
Total price				156.8 (INR)
Area of membrane				160 cm^2
Overall cost per m^2 area of zeolite-coated membrane **1 m^2 = 10000 cm^2**				(156.8/160)×10000 = 9800 (INR)
Overhead charge =10% of the overall cost				980 (INR)
Net cost for membrane preparation per m^2 = Overall cost + Overhead charge				9800+980 (INR) = 10,780 (INR) = 131.04 USD

Summary

Nano-sized Y-type zeolite (59.07 nm) was prepared from steel industry solid waste LD-slag. The zeolite nanolayered membrane was fabricated by heat treatment followed by a phase inversion technique. FESEM images captured from membrane surfaces reveal the graft of zeolite particles, and cross-sectional images demonstrate the formation of a honeycomb-like pore structure in the membrane. Porosity, mean pore radius, and EWC were increased with zeolite concentration. The maximum PWF was achieved from PSf/Zeolite-1wt.% membrane sample. Ultrafiltration test was conducted to extract fluoride, manganese, and chromium from the groundwater sample over the modified PSf/Zeolite-1wt.% membrane. All synthesized membranes possess good thermal and mechanical durability. The cost of treating groundwater contaminated with F^-, Mn^{2+}, Cr^{6+} was ~ 0.022 USD/L.

References

[1] J.-F. Li, Z.-L. Xu, H. Yang, L.-Y. Yu, M. Liu, Effect of TiO2 nanoparticles on the surface morphology and performance of microporous PES membrane, Appl. Surf. Sci. 255 (2009) 4725–4732. https://doi.org/https://doi.org/10.1016/j.apsusc.2008.07.139.

[2] R.A. Rachman, U.T.I. Martia, W. Aulia, R.M. Iqbal, N. Widiastuti, F. Kurniawan, Combination of microbial fuel cell and zeolite Na-Y adsorption for chromium removal, AIP Conf. Proc. 2049 (2018). https://doi.org/10.1063/1.5082478.

[3] S. Chand, B. Paul, M. Kumar, A comparative study of physicochemical and mineralogical properties of ld slag from some selected steel plants in India, J. Environ. Sci. Technol. 9 (2016) 75–87. https://doi.org/10.3923/jest.2016.75.87.

[4] M. Dehghani, A. Tadjarodi, S. Chamani, Synthesis and Characterization of Magnetic Zeolite Y − Palladium − Nickel Ferrite by Ultrasonic Irradiation and Investigating Its Catalytic Activity in Suzuki − Miyaura Cross-Coupling Reactions, (2019). https://doi.org/10.1021/acsomega.9b00666.

[5] K.S. Ambili, J. Thomas, Synthesis of hybrid materials by immobilizing para-aminobenzoic acid complexes of Eu^{3+} and Tb^{3+} in zeolite Y and their luminescent properties, J. Porous Mater. 27 (2020) 755–764. https://doi.org/10.1007/s10934-019-00857-0.

[6] N.S. Samanta, P.P. Das, P. Mondal, U. Bora, M.K. Purkait, Physico-chemical and adsorption study of hydrothermally treated zeolite A and FAU-type zeolite X prepared from LD (Linz–Donawitz) slag of the steel industry, Int. J. Environ. Anal. Chem. (2022) 1–23. https://doi.org/10.1080/03067319.2022.2079082.

[7] T.W. Duan, B. Yan, Photophysical properties of metal ion functionalized NaY zeolite, Photochem. Photobiol. 90 (2014) 503–510. https://doi.org/10.1111/php.12235.

[8] H. Ramezani, S.N. Azizi, G. Cravotto, Improved removal of methylene blue on

modified hierarchical zeolite Y: Achieved by a “destructive-constructive” method, Green Process. Synth. 8 (2019) 730–741. https://doi.org/10.1515/gps-2019-0043.

[9] S. Dhara, N.S. Samanta, R. Uppaluri, M.K. Purkait, High-purity alkaline lignin extraction from Saccharum ravannae and optimization of lignin recovery through response surface methodology, Int. J. Biol. Macromol. (2023) 123594. https://doi.org/https://doi.org/10.1016/j.ijbiomac.2023.123594.

[10] M. Kalhor, S. Banibairami, S.A. Mirshokraie, Ni@zeolite-Y nanoporous; a valuable and efficient nanocatalyst for the synthesis of N-benzimidazole-1,3-thiazolidinones, Green Chem. Lett. Rev. 11 (2018) 334–344. https://doi.org/10.1080/17518253.2018.1499968.

[11] N.S. Samanta, S. Banerjee, P. Mondal, Anweshan, U. Bora, M.K. Purkait, Preparation and characterization of zeolite from waste Linz-Donawitz (LD) process slag of steel industry for removal of Fe^{3+} from drinking water, Adv. Powder Technol. 32 (2021) 3372–3387. https://doi.org/10.1016/j.apt.2021.07.023.

[12] D. Kim, J.S. Bae, T.E. Hong, K.N. Hui, S. Kim, C.H. Kim, J.C. Park, Color-Tunable and Highly Luminous N3--DopedBa2-xCaxSiO4-δN2/3δ:Eu2+ (0.0≤ x≤1.0) Phosphors for White NUV-LED, ACS Appl. Mater. Interfaces. 8 (2016) 17371–17381. https://doi.org/10.1021/acsami.6b02778.

[13] Y. Okamoto, M. Ogawa, A. Maezawa, T. Imanaka, Electronic structure of zeolites studied by X-Ray photoelectron spectroscopy, J. Catal. 112 (1988) 427–436. https://doi.org/https://doi.org/10.1016/0021-9517(88)90157-1.

[14] S. Ye, J. Sun, X. Yi, Y. Wang, Q. Zhang, Interaction between the exchanged Mn^{2+} and Yb^{3+} ions confined in zeolite-Y and their luminescence behaviours, Sci. Rep. 7 (2017) 1–9. https://doi.org/10.1038/srep46219.

[15] C. Belviso, F. Cavalcante, A. Lettino, S. Fiore, Effects of ultrasonic treatment on

zeolite synthesized from coal fly ash, Ultrason. Sonochem. 18 (2011) 661–668. https://doi.org/10.1016/j.ultsonch.2010.08.011.

[16] D. Nasirian, I. Salahshoori, M. Sadeghi, N. Rashidi, M. Hassanzadeganroudsari, L. Badrinezhad, S. Ghasemi, Y. Azizian-Kalandaragh, A. Nematollahzadeh, Investigation of the gas permeability properties from polysulfone/polyethylene glycol composite membrane, Polym. Bull. 75 (2018) 469–484. https://doi.org/10.1007/s00289-019-03031-3.

[17] M.- Al, B. Seoane, V. Sebastián, C. Téllez, J. Coronas, CrystEngComm Crystallization in THF : the possibility of one-pot synthesis of mixed matrix membranes containing MOF, 68 (2013) 9483–9490. https://doi.org/10.1039/c3ce40847g.

[18] A. Mushtaq, H. Bin Mukhtar, A.M. Shariff, FTIR study of enhanced polymeric blend membrane with amines, Res. J. Appl. Sci. Eng. Technol. 7 (2014) 1811–1820. https://doi.org/10.19026/rjaset.7.466.

[19] B.M. Ganesh, A.M. Isloor, A.F. Ismail, Enhanced hydrophilicity and salt rejection study of graphene oxide-polysulfone mixed matrix membrane, Desalination. 313 (2013) 199–207. https://doi.org/https://doi.org/10.1016/j.desal.2012.11.037.

[20] M.M. Rahman, N. Hasnida, W.B. Wan Nik, Preparation of Zeolite Y Using Local Raw Material Rice Husk as a Silica Source, J. Sci. Res. 1 (2009) 285–291. https://doi.org/10.3329/jsr.v1i2.1777.

[21] M. Ionita, A.M. Pandele, L. Crica, L. Pilan, Improving the thermal and mechanical properties of polysulfone by incorporation of graphene oxide, Compos. Part B Eng. 59 (2014) 133–139. https://doi.org/https://doi.org/10.1016/j.compositesb.2013.11.018.

[22] T. Anjum, R. Tamime, A.L. Khan, Mixed-matrix membranes comprising of polysulfone and porous uio-66, zeolite 4a, and their combination: Preparation, removal of humic acid, and antifouling properties, Membranes (Basel). 10 (2020) 1–21.

https://doi.org/10.3390/membranes10120393.

[23] K. Tsutsumi, T. Kawai, T. Yanagihara, Adsorption Characteristics of Hydrophobic Zeolites, in: T. Hattori, T.B.T.-S. in S.S. and C. Yashima (Eds.), Zeolites Microporous Cryst., Elsevier, 1994: pp. 217–224. https://doi.org/https://doi.org/10.1016/S0167-2991(08)63260-7.

[24] S.C. Rodrigues, R. Whitley, A. Mendes, Preparation and characterization of carbon molecular sieve membranes based on resorcinol–formaldehyde resin, J. Memb. Sci. 459 (2014) 207–216. https://doi.org/https://doi.org/10.1016/j.memsci.2014.02.013.

[25] B. Zhang, L. Ma, S. Deng, C. Xie, X. Qiu, Shelf-life of pacific white shrimp (Litopenaeus vannamei) as affected by weakly acidic electrolyzed water ice-glazing and modified atmosphere packaging, Food Control. 51 (2015) 114–121. https://doi.org/https://doi.org/10.1016/j.foodcont.2014.11.016.

[26] T. Xiang, R. Wang, W.F. Zhao, S.D. Sun, C.S. Zhao, Covalent deposition of zwitterionic polymer and citric acid by click chemistry-enabled layer-by-layer assembly for improving the blood compatibility of polysulfone membrane, Langmuir. 30 (2014) 5115–5125. https://doi.org/10.1021/la5001705.

[27] A.M.C. Tuncel, F.M.A.M. Pandele, C.B.C. Orbeci, L.B.A. Palla, Synthesis and characterization of polysulfone – TiO 2 decorated MWCNT composite membranes by sonochemical method, Appl. Phys. A. 126 (2020) 1–9. https://doi.org/10.1007/s00339-020-3408-9.

[28] V. Vatanpour, M. Esmaeili, M.H.D.A. Farahani, Fouling reduction and retention increment of polyethersulfone nanofiltration membranes embedded by amine-functionalized multi-walled carbon nanotubes, J. Memb. Sci. 466 (2014) 70–81. https://doi.org/https://doi.org/10.1016/j.memsci.2014.04.031.

[29] G.-T. Vuong, T.-O. Do, A New Route for the Synthesis of Uniform Nanozeolites with

Hydrophobic External Surface in Organic Solvent Medium, J. Am. Chem. Soc. 129 (2007) 3810–3811. https://doi.org/10.1021/ja069058p.

[30] N.S. Samanta, P.P. Das, P. Mondal, M. Changmai, M.K. Purkait, Critical review on the synthesis and advancement of industrial and biomass waste-based zeolites and their applications in gas adsorption and biomedical studies, J. Indian Chem. Soc. 99 (2022) 100761. https://doi.org/https://doi.org/10.1016/j.jics.2022.100761.

[31] J. Shen, A. Schäfer, Removal of fluoride and uranium by nanofiltration and reverse osmosis: A review, Chemosphere. 117 (2014) 679–691. https://doi.org/https://doi.org/10.1016/j.chemosphere.2014.09.090.

[32] N. Eom, D.F. Parsons, V.S.J. Craig, Roughness in Surface Force Measurements: Extension of DLVO Theory To Describe the Forces between Hafnia Surfaces, J. Phys. Chem. B. 121 (2017) 6442–6453. https://doi.org/10.1021/acs.jpcb.7b03131.

[33] A.R.D. Verliefde, E.R. Cornelissen, S.G.J. Heijman, J.Q.J.C. Verberk, G.L. Amy, B. Van Der Bruggen, J.C. Van Dijk, The role of electrostatic interactions on the rejection of organic solutes in aqueous solutions with nanofiltration, J. Memb. Sci. 322 (2008) 52–66. https://doi.org/10.1016/j.memsci.2008.05.022.

[34] M. Chaudhary, A. Maiti, Fe – Al – Mn @ chitosan based metal oxides blended cellulose acetate mixed matrix membrane for fluoride decontamination from water : Removal mechanisms and antibacterial behavior, J. Memb. Sci. 611 (2020) 118372. https://doi.org/10.1016/j.memsci.2020.118372.

[35] A.K. Haritash, S. Gaur, S. Garg, Assessment of water quality and suitability analysis of River Ganga in Rishikesh, India, Appl. Water Sci. 6 (2016) 383–392. https://doi.org/10.1007/s13201-014-0235-1.

[36] S. Mondal, S. Kumar Majumder, Fabrication of the polysulfone-based composite ultrafiltration membranes for the adsorptive removal of heavy metal ions from their

contaminated aqueous solutions, Chem. Eng. J. 401 (2020) 126036. https://doi.org/https://doi.org/10.1016/j.cej.2020.126036.

[37] R. Saranya, G. Arthanareeswaran, A.F. Ismail, N.L. Reddy, M. V. Shankar, J. Kweon, Efficient rejection of organic compounds using functionalized ZSM-5 incorporated PPSU mixed matrix membrane, RSC Adv. 7 (2017) 15536–15552. https://doi.org/10.1039/c6ra27314a.

[38] Z. Huang, J. Liu, Y. Liu, Y. Xu, R. Li, H. Hong, L. Shen, H. Lin, B.-Q. Liao, Enhanced permeability and antifouling performance of polyether sulfone (PES) membrane via elevating magnetic Ni@MXene nanoparticles to upper layer in phase inversion process, J. Memb. Sci. 623 (2021) 119080. https://doi.org/https://doi.org/10.1016/j.memsci.2021.119080.

[39] M. Meng, B. Li, Y. Zhu, Y. Yan, Y. Feng, A novel mixed matrix polysulfone membrane for enhanced ultrafiltration and photocatalytic self-cleaning performance, J. Colloid Interface Sci. 599 (2021) 178–189. https://doi.org/https://doi.org/10.1016/j.jcis.2021.04.082.

[40] H. Zhao, L. Wu, Z. Zhou, L. Zhang, H. Chen, Improving the antifouling property of polysulfone ultrafiltration membrane by incorporation of isocyanate-treated graphene oxide, Phys. Chem. Chem. Phys. 15 (2013) 9084–9092. https://doi.org/10.1039/C3CP50955A.

[41] D. Rana, T. Matsuura, Surface Modifications for Antifouling Membranes, Chem. Rev. 110 (2010) 2448–2471. https://doi.org/10.1021/cr800208y.

[42] J.J. Leam, M.R. Bilad, Y. Wibisono, M.D. Hakim Wirzal, I. Ahmed, Chapter 7 - Membrane Technology for Microalgae Harvesting, in: A.B.T.-M.C. for B.P. Yousuf (Ed.), Academic Press, 2020: pp. 97–110. https://doi.org/https://doi.org/10.1016/B978-0-12-817536-1.00007-2.

[43] I. Das, S. Das, R. Dixit, M.M. Ghangrekar, Goethite supplemented natural clay ceramic as an alternative proton exchange membrane and its application in microbial fuel cell, Ionics (Kiel). 26 (2020) 3061–3072. https://doi.org/10.1007/s11581-020-03472-1.

Chapter 5

Synthesis of precipitated calcium carbonate from LD-slag using CO_2

The precipitated calcium carbonate ($CaCO_3$) was prepared from CaO-rich LD-slag by CO_2 sequestration where table sugar was added as a promoter. The carbonation was carried out within the temperature range of 25-55°C. Three types of $CaCO_3$ polymorphs were detected by several characterization techniques like field emission scanning electron microscope (FESEM), field emission transmission electron microscopy (FETEM), X-ray diffraction (XRD), and Fourier transform infrared (FTIR) analysis. Thermogravimetric analysis (TGA) of the obtained sample was recorded in order to examine the thermal stability. The formation of precipitated calcium carbonate (PCC) without sugar was also carried out with the same temperature range (25-55°C). The chemical analysis of with and without sugar $CaCO_3$ samples was investigated by X-ray photoelectron spectroscopy (XPS).

5.1. Experimental

5.1.1. Materials and Method

5.1.1.1. Precipitated Calcium Carbonate Production

LD-slag was collected from TATA Steel Limited, Jamshedpur, India. Table sugar and CO_2 gas were procured from the market and Assam air products ltd., India, respectively. The carbonation experiment was conducted in a 500 mL sequestration chamber equipped with a mechanical agitator. Prior to the process, the LD-slag was calcined at a high temperature (550°C) and then acid leached with 0.1M HCl at room temperature for 1 hour to remove an excess amount of carbonaceous and undesirable components from the slag. About 4 g of LD-

---

Content of this chapter is published as below:

N. S .Samanta, Anweshan, Piyal Mondal, Utpal Bora, M K Purkait, Synthesis of precipitated calcium carbonate from LD-slag using CO_2, Mater. Today Commun. (2023) 106588. https://doi.org/10.1016/j.mtcomm.2023.106588.

slag was taken from the processed slag and mixed with 2 g of table sugar to conduct the experiment. The mixture of LD-slag and table sugar powder was kept in the reaction chamber containing 100 mL of deionized (DI) water. The speed of the stirrer was set at 300 rpm and the reaction temperature was varied from 25 to 55°C. After attaining the required temperature, CO_2 gas was continually purged to the reaction at a 50 mL/minute flow rate. The carbonation reaction was carried out for 2 hours. After the reaction, the solution was then filtered and thoroughly washed with hot water maintained at 100°C for three times to remove the excess amount of sugar from the obtained sample. The thicker sample was then placed in a petri dish and allowed to dry for 12 hours at 80°C. The experimental setup and reaction conditions for the synthesis of $CaCO_3$ from CaO-enriched LD-slag have been presented in Figure 5.1.

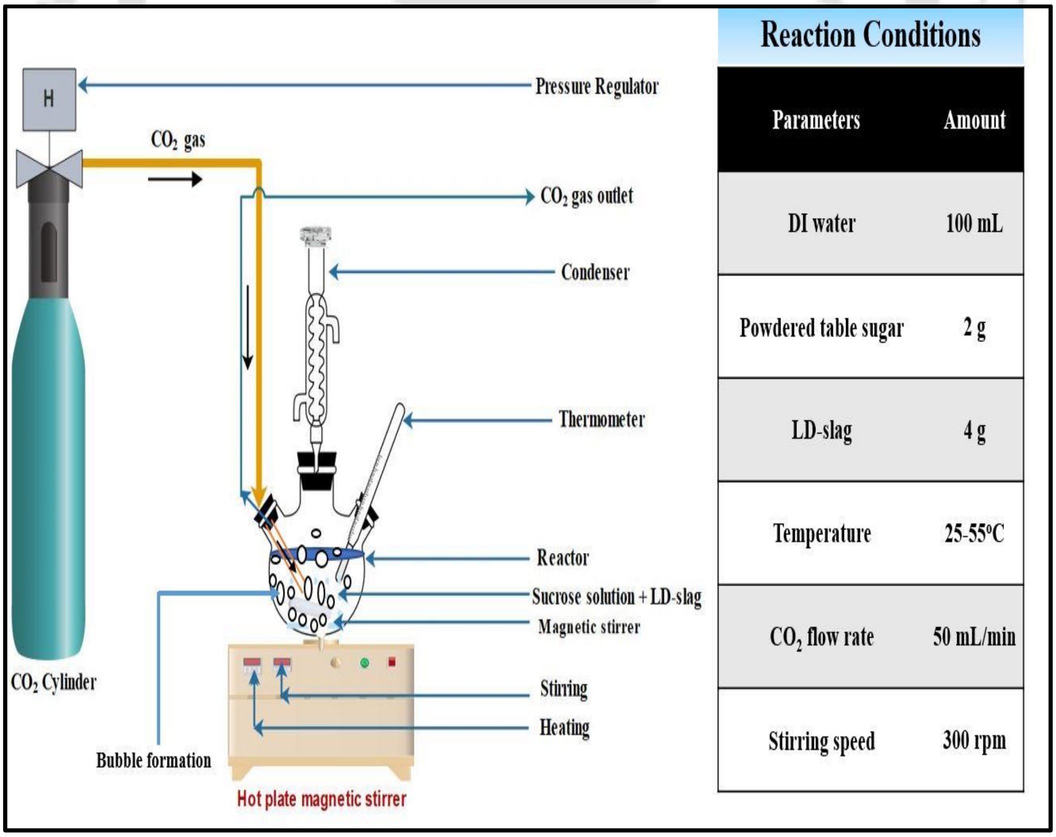

Reaction Conditions

Parameters	Amount
DI water	100 mL
Powdered table sugar	2 g
LD-slag	4 g
Temperature	25-55°C
CO_2 flow rate	50 mL/min
Stirring speed	300 rpm

Figure 5.1: Experimental setup and reaction conditions for the production of precipitated $CaCO_3$ from CaO-rich LD-slag.

5.1.1.2. CaO conversion

A 4 g of LD-slag by composition should have 49.15% CaO which means when calculated it would have 1.96 g of CaO. After reaction with carbon dioxide carbonates will be formed that precipitated carbonate went taken off and weighed which gives the amount of $CaCO_3$ thus if we divide the amount of precipitated carbonate by the theoretically calculated amount of CaO present in the LD-slag it will give us the amount of CaO conversion.

5.1.1.3. Hypothesis test (t-test)

A t-test compares the means of two samples using statistical evaluation. It is used in hypothesis testing, where the null hypothesis is that there is no difference between the group means, and the alternate hypothesis is that there is a difference between the two. The hypothesis result is said to be significant if the p-value from the t-test is less than 0.05. The results are not significant if the p-value is higher than 0.05.

5.1.1.4. Concentration of carbonate (CO_3^{2-}) ions measurement

The concentration of carbonate ions in the solution was determined via back titration. A 500 mL solution of 0.01M HCl was prepared from 37% pure HCl (procured from Merck, Germany), added to 20 mL of which was then added to the 50 mL sample solution kept in a flask. Any carbonate ions in the water are reacted with by the acid to create carbon dioxide gas. The reaction will be followed as below:

$$HCl + CaCO_3 \rightarrow NaCl + CO_{2\,(G)} \uparrow + H_2O \qquad (5.1)$$

Any unreacted acid will stay in the solution together with the salt produced by the calcium chloride reaction once the reaction has finished. The remaining acid in the solution was titrated with a solution of 0.01M NaOH and was prepared from dissolving NaOH pellets (purchased from Merck, Germany) in DI water and using a phenolphthalein indicator. The quantity of acid remaining in the solution, or the amount of acid that did not interact with the carbonate ions, will be revealed by titration. The amount of reacted acid will be evaluated by subtracting the amount of unreacted acid from the known excess. The concentration of CO_3^{2-} ions in the solution will be calculated from the known amount of acid that was added to the solution in the first place.

5.1.1.5. Characterization techniques

Powder X-ray diffractions were performed using a Bucker X-ray D8 analyzer. Scanning was carried out in the range of 2θ =10-60° at 0.05°/sec in continuous mode. XRD results were obtained employing (Cu $K\alpha$ = 0.15406 nm) radiation. The X-ray source was performed at 40 kV and 5 mA.

X-ray photoelectron spectroscopy (XPS) analysis of synthesized precipitated calcium carbonate was carried out by an RBD upgraded PHI-5000 Versa Probe III system (PerkinElmer) utilizing a monochromatic Al K-alpha x-ray source at pass energy of 55 eV.

FESEM analysis was used for morphological analysis of reacted samples. The internal, as well as external surface morphology, was carried out by FESEM (ZESIS, Model 1430 VP) instrument. Prior to analysis, the reacted samples were dried in a hot air oven at 70°C to 80°C and coated with gold plating. Energy dispersive x-ray spectroscopy (EDX) was used to characterize the elemental composition and chemical analysis of synthetic PCC. The preparation of the sample was the same as the FESEM analysis, which was stated earlier. Field emission transmission electron microscopic (FETEM) studies of prepared samples were done by a FETEM analyzer (Model, JEOL JEM 2100F). Fourier transforms infrared (FTIR) spectroscopic analysis of synthesized $CaCO_3$ was conducted utilizing an FTIR analyzer (Perkin Elmer, Singapore, and Model: Spectrum two). The scanning range was set from 400 to 4000 cm^{-1} with the highest resolution of 0.5 cm^{-1}. The UV-Vis diffuse reflectance spectrum (200-700 nm) of the obtained $CaCO_3$ samples was achieved by employing a UV-Vis spectrophotometer facilitated with a deuterium for UV light and a tungsten lamp for visible light (UV-2600, Shimadzu, Singapore).

A thermal durability test of the obtained $CaCO_3$ sample was performed by a TGA analyzer (Make: NETZSCH, Model: TG209 F1), type of crucible: DSC/TG pan Al_2O_3. Argon was employed as a protective gas at 20 and 60 mL/minute flow rates, respectively. The testing temperature was set at a range of 25-1000°C with a 10°C/minute heating rate. Differential Scanning Calorimetry (DSC) analysis was operated to observe the degradation temperatures and melting point of the $CaCO_3$ existing in the samples (Make: Mettler Toledo, Model: DSC1 STARe System). The operational temperature was the same as the TGA analysis, mentioned earlier. A flame photometer (Make: Systronics, Model: 128) was employed for quantitative analysis of Ca^{2+} as well as $Ca(OH)_2$ ions in reaction and standard solutions. All sets of the sample were tested at an ambient temperature (25°C).

5.2. Results and discussion

5.2.1. Characterization of raw LD-slag and solid samples

5.2.1.1. X-ray Diffraction (XRD) Study

XRD pattern of LD-slag and all samples reacted at different temperatures (25 to 55°C), is shown in Figure 5.2a. It was observed that the principal calcite phase was formed by the carbonation process with a trace amount of vaterite and aragonite phases. Peak values at 2θ = 27.03°, 29.48°, 32.78°, 35.9°, 39.5°, 42.83°, 43.2°, 45.8°, 48.5°, and 61.8° correspond to the (1 1 2), (1 0 4), (1 1 4), (1 1 0), (1 1 3), (2 2 0), (2 0 2), (2 2 1), (1 1 6) and (1 2 2) lattice plane of calcium carbonate, respectively [1]. The crystalline plane of (1 0 4), (1 1 6), (1 1 3), and (1 1 0) represent the calcite (JCPDS card No. 05-0586) phase [2], and (2 2 0), (2 2 1), and (2 4 1) assign the crystalline plane of aragonite (JCPDS card No. 41-1475) phase [3]. In addition, peaks displayed at 2θ = 27.03° and 32.78 corresponds to the crystalline plane of (1 1

2) and (1 1 4) which are found to be in good agreement with the existence of vaterite (JCPDS card No. 33-0268) polymorph in the produced sample [4–6]. Moreover, peaks at 2θ = 34.2° (0 1 1) and 64.55° (1 0 3) well matched with crystalline peaks of $Ca(OH)_2$ particles [7], which revealed the presence of unreacted $Ca(OH)_2$ in the sample. Hence, it was confirmed from the XRD analysis that mostly calcite and aragonite polymorphs dominated the precipitated calcium carbonate, whereas the vaterite phase was observed in very small amounts along with amorphous $Ca(OH)_2$.

The crystallinity index (CI) or % crystallinity of all the prepared samples was calculated using equation (5.2), as given below.

$$\text{Crystallinity index } (\%) = \frac{Area\ of\ all\ crystalline\ peks}{Area\ of\ all\ crystalline\ and\ amorphous\ peaks} \tag{5.2}$$

The crystallinity index of synthesized samples with sugar was found to be within the range of ~80 to 90% (Table 5.1 and Figure 5.3). The crystallinity of a material has a significant impact on its physical characteristics. The more crystalline a material, the more consistently its atoms are arranged in a periodically repeating geometric array. The hardness and density of a material rise as crystallinity increases [8]. As a result, the analysis confirmed that sample 1 (S_1) has the maximum stability and hardness among others.

From XRD analysis, it can be concluded that three types of $CaCO_3$ polymorphs namely calcite, vaterite, and aragonite, were detected in the prepared samples. The unreacted $Ca(OH)_2$ was also observed in the prepared sample. The XRD analysis further verified that calcite and aragonite phases predominate in PCC samples, with vaterite and amorphous $Ca(OH)_2$ appearing in trace levels. The crystallinity of all as-synthesized samples was estimated from XRD analysis and found to be within the range of 80-90%.

5.2.1.2. Fourier Transform Infrared (FTIR) Study

The FTIR spectra of steel slag as well as prepared samples (S_1, S_2, S_3, and S_4, respectively, produced within temperature from 25 to 55°C), as illustrated in Figure 5.2b, demonstrates various peaks corresponding to different functional groups including carbonyl, hydroxyl, and carbonate groups, which validates successful formation of $CaCO_3$. The peaks that arrived in the range 3500-3420 cm^{-1} (displayed by dotted lines) for all reacted samples correspond to the existence of the hydroxyl (–OH) group due to the moisture absorbance affinity of the samples [9–14]. The broad transmittance peak displayed at 3644 cm^{-1} is attributed to the hydroxyl stretching vibration of CaO. Furthermore, the strong vibration peak at 1779 and 2504 cm^{-1} was ascribed to the deformation mode of C-O stretching modes of carbonate (CO_3^{2-}) ion ($\nu_4+\nu_3$ bending mode of CO_3^{2-} ion) [3,15]. Also, the peak band at 872 cm^{-1} (ν_2, out-of-plane bending) and 712 cm^{-1} (ν_4, doubly degenerated planer bending) reveal the presence of calcite phase in precipitated calcium carbonate (PCC) [16,17]. Another notable aspect of the increasing trend of peak intensity at 872 and 712 cm^{-1} is presumably due to the crystal growth of calcite polymorph with temperature [18]. Whereas, the peak at 1083 cm^{-1} is designated to the aragonite phase [19], as the temperature increases the intensity of the peak appears at 1083 cm^{-1} also increases which implies that the aragonite phase is mostly dominated at a higher temperature in carbonation reaction [20].

Results achieved from FTIR data demonstrate that distinct peaks appeared at different wavelengths, revealing $CaCO_3$ polymorphs for every sample. Moreover, the increasing trend of the calcite phase (at 872 cm^{-1}) with temperature is probably due to the precipitation of more calcite phases in precipitated calcium carbonate.

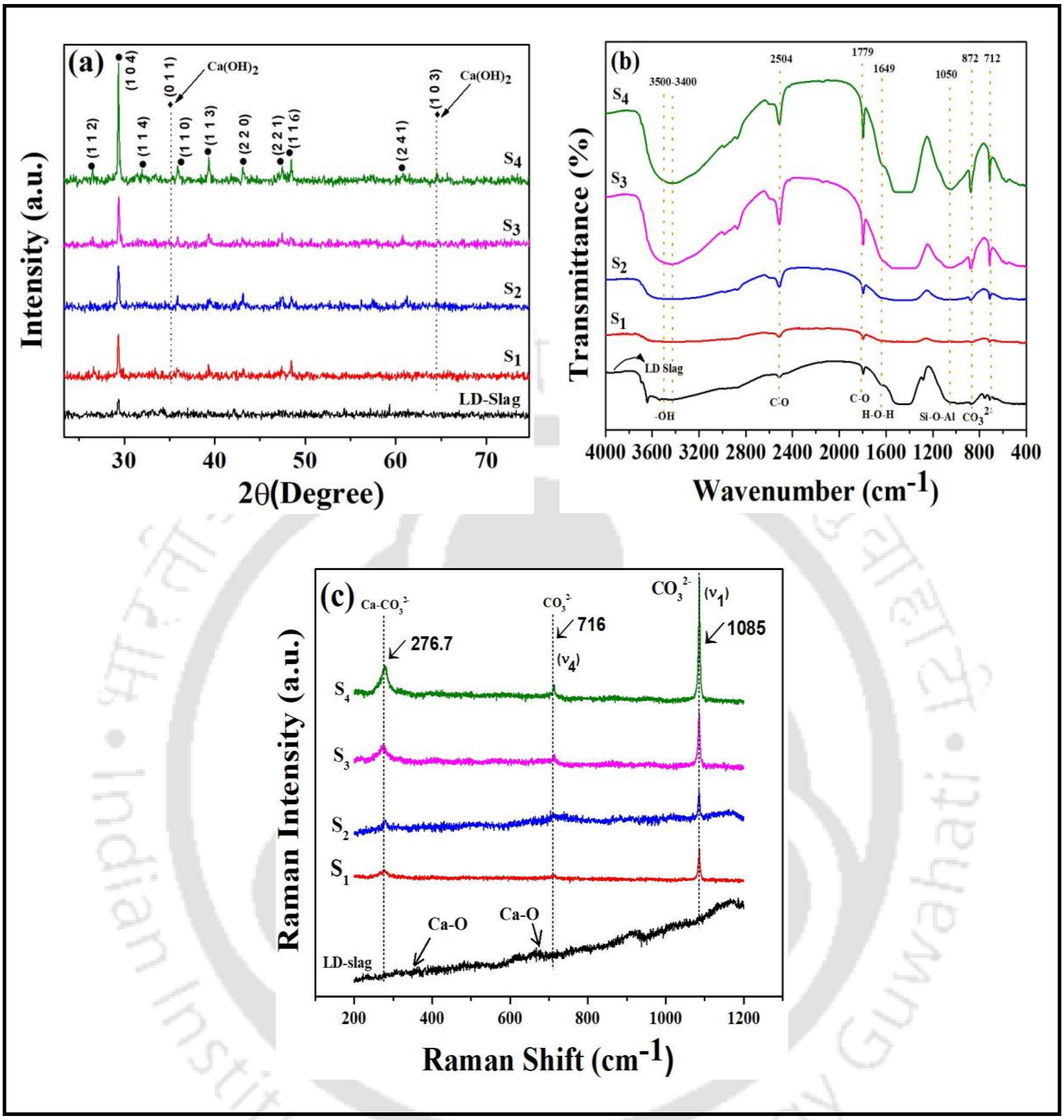

Figure 5.2: (a) XRD (b) FTIR, and (c) Raman spectroscopic analysis of $CaCO_3$ powder samples. Captions S_1, S_2, S_3, and S_4 indicate samples 1, 2, 3, and 4 reacted at 25, 35, 45, and 55°C, respectively.

5.2.1.3. Raman Analysis

The Raman spectrum of calcite, aragonite, and vaterite phases of synthetic $CaCO_3$ along with LD-slag are shown in Figure 5.2c. No distinct peaks are found in the slag sample. However, the Ca-O characteristic bonds were found at 365 and 678 cm^{-1}, respectively, which attributes to the existence of CaO in the used slag. The vibrations mode of PCC ions is divided into four categories: i) symmetric stretching mode (ν_1) ii) asymmetric stretching mode (ν_3) iii) out-of-plane bending mode (ν_2) and iv) in-plane bending mode (ν_4). A Low-frequency Raman peak was observed at 287 cm^{-1} where CO_3^{2-} ions and Ca^+ ions vibrate together, which reveals the presence of an aragonite polymorph [18]. The strong vibration band at 1085 cm^{-1} and less intense peak at 712 cm^{-1} can be assigned to the symmetric stretching (ν_1) and in-plane stretching mode (ν_4) of the carbonate groups, respectively [21]. Moreover, from a number of Raman analyses, the phase analysis of $CaCO_3$ reveals that calcite and aragonite are observed at 1086 and 1085 cm^{-1} [22], and somewhere the phases are shifted to 1085 and 1086 cm^{-1}, respectively [22,23]. Hence, the peak appearance for both phases is relatively the same, therefore we may consider that both phases are present at 1085 cm^{-1} in this study. However, the disappearance of the vaterite phase might be overlapping the highly intense peak of calcite and aragonite phases [21,24].

From Raman analysis, it is implied that no distinct peaks appeared for LD-slag, whereas, the intense peak was observed for calcium and carbonate groups which attribute to the presence of calcium carbonate in the powder PCC samples.

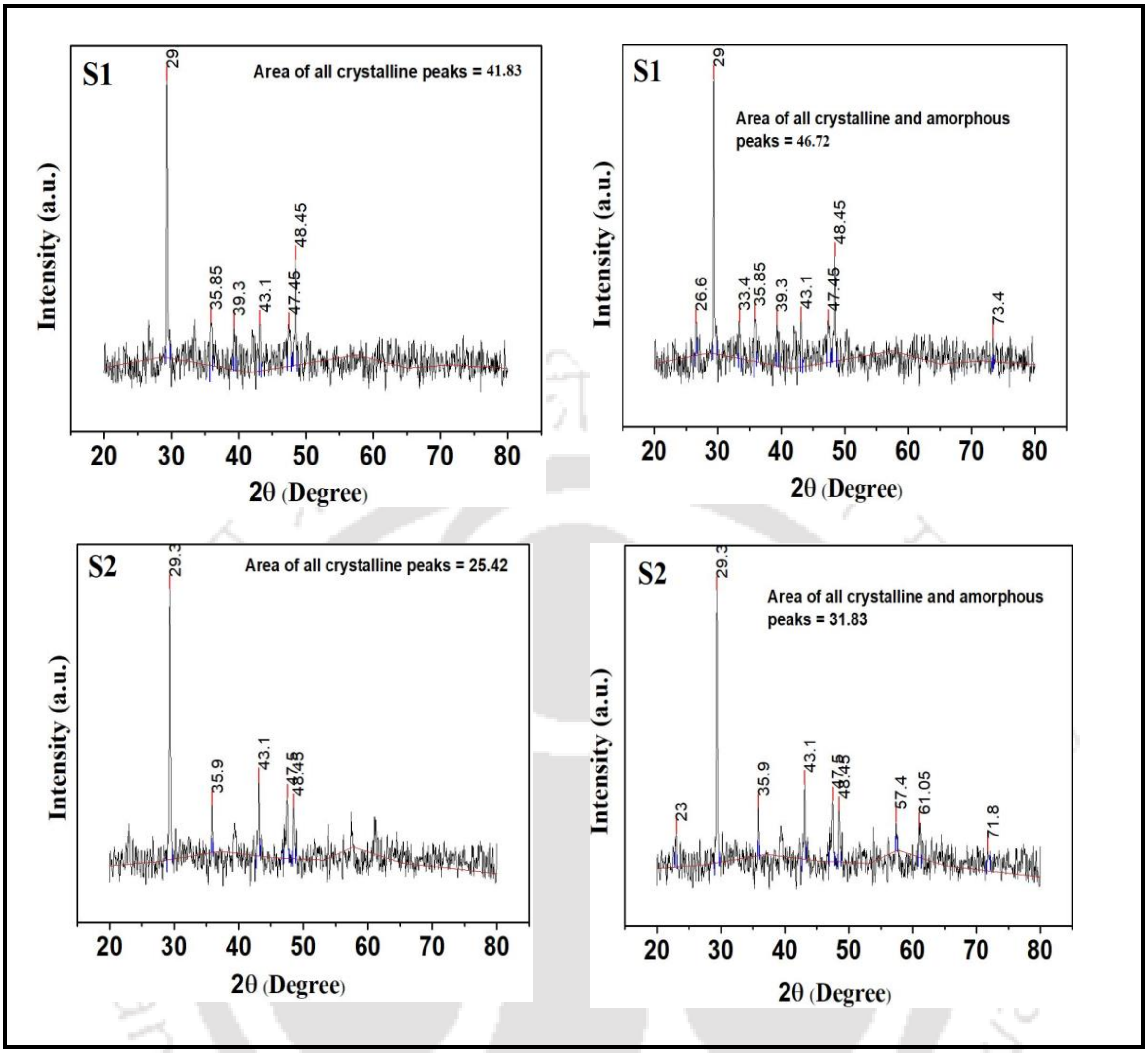
S1
Area of all crystalline peaks = 41.83
29
35.85
39.3
43.1
47.45
48.45
Intensity (a.u.)
20 30 40 50 60 70 80
2θ (Degree)
S1
Area of all crystalline and amorphous peaks = 46.72
29
26.6
33.4
35.85
39.3
43.1
47.45
48.45
73.4
Intensity (a.u.)
20 30 40 50 60 70 80
2θ (Degree)
S2
Area of all crystalline peaks = 25.42
29.3
35.9
43.1
47.5
48.45
Intensity (a.u.)
20 30 40 50 60 70 80
2θ (Degree)
S2
Area of all crystalline and amorphous peaks = 31.83
29.3
23
35.9
43.1
47.5
48.45
57.4
61.05
71.8
Intensity (a.u.)
20 30 40 50 60 70 80
2θ (Degree)

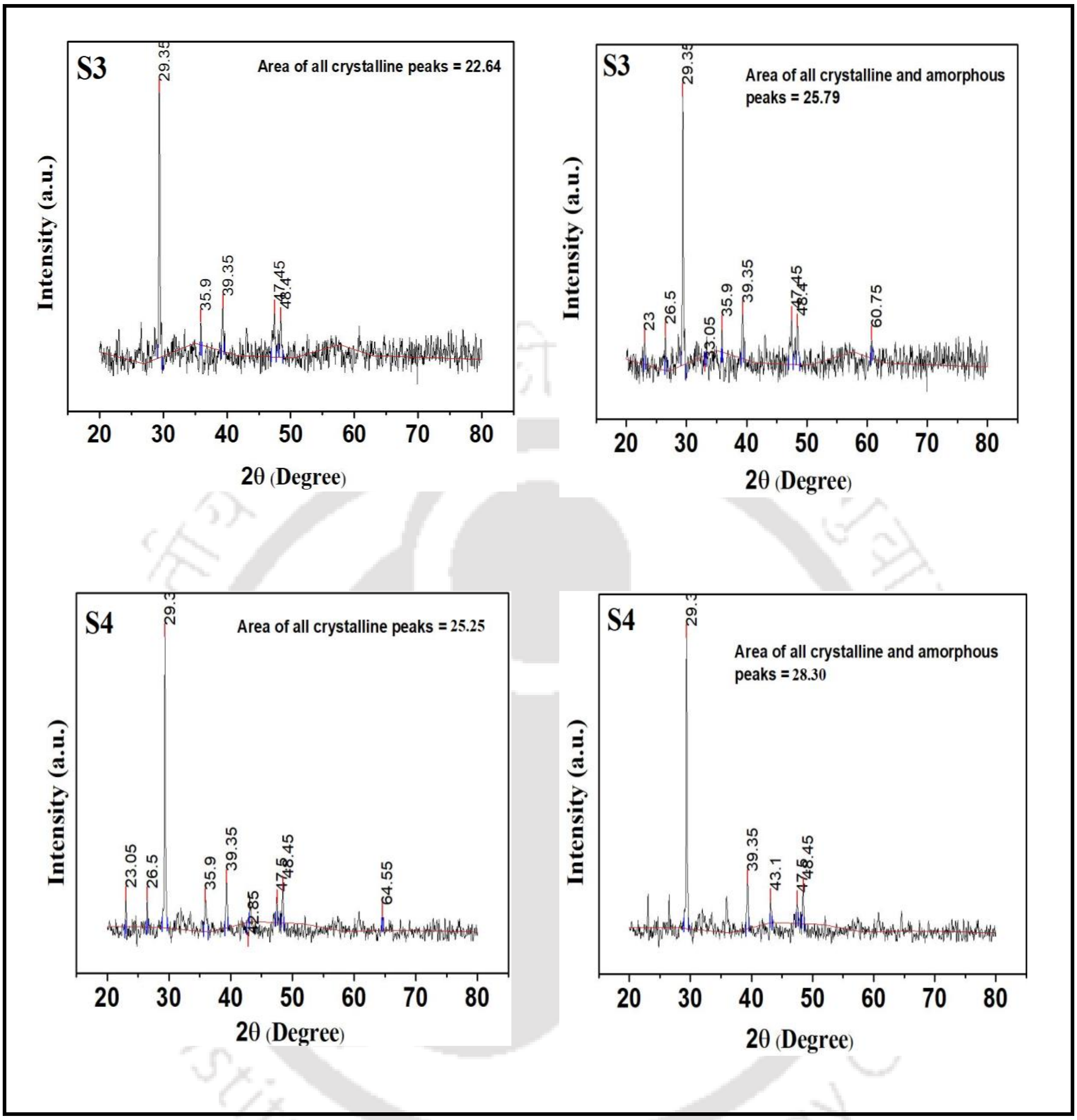
S3
Area of all crystalline peaks = 22.64
Intensity (a.u.)
2θ (Degree)
29.35
35.9
39.35
47.45
48.4
20 30 40 50 60 70 80
S3
Area of all crystalline and amorphous peaks = 25.79
Intensity (a.u.)
2θ (Degree)
23
26.5
29.35
33.05
35.9
39.35
47.45
48.4
60.75
20 30 40 50 60 70 80
S4
Area of all crystalline peaks = 25.25
Intensity (a.u.)
2θ (Degree)
23.05
26.5
29.3
35.9
39.35
42.85
47.5
48.45
64.55
20 30 40 50 60 70 80
S4
Area of all crystalline and amorphous peaks = 28.30
Intensity (a.u.)
2θ (Degree)
29.3
39.35
43.1
47.5
48.45
20 30 40 50 60 70 80

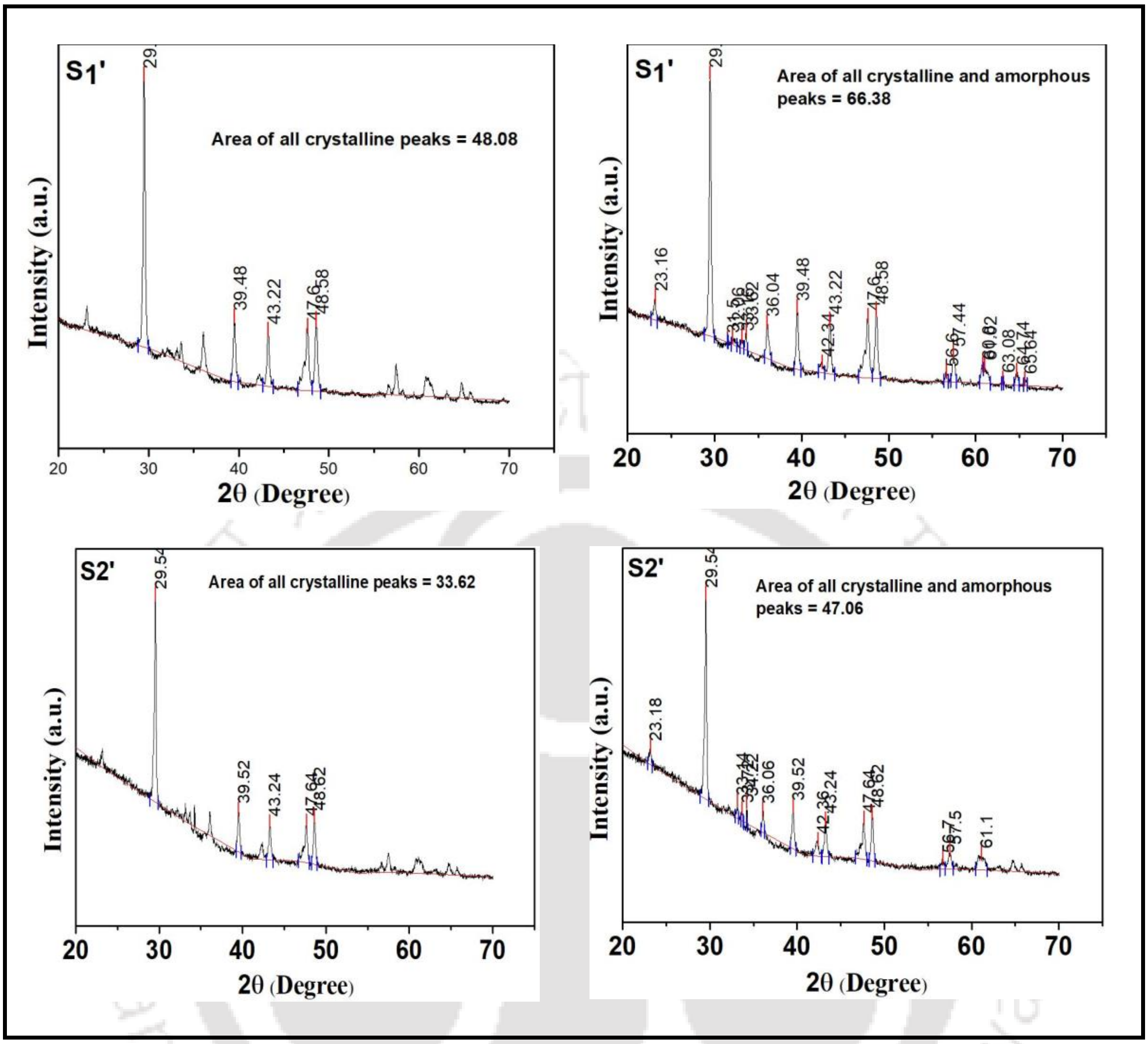
S1'
Area of all crystalline peaks = 48.08
29.
39.48
43.22
47.6
48.58
Intensity (a.u.)
2θ (Degree)
20
30
40
50
60
70
S1'
Area of all crystalline and amorphous peaks = 66.38
29.
23.16
31.56
33.62
36.04
39.48
42.34
43.22
47.6
48.58
56.6
57.44
63.08
65.64
S2'
Area of all crystalline peaks = 33.62
29.54
39.52
43.24
47.64
48.62
S2'
Area of all crystalline and amorphous peaks = 47.06
29.54
23.18
34.22
36.06
39.52
42.36
43.24
47.64
48.62
56.7
57.5
61.1

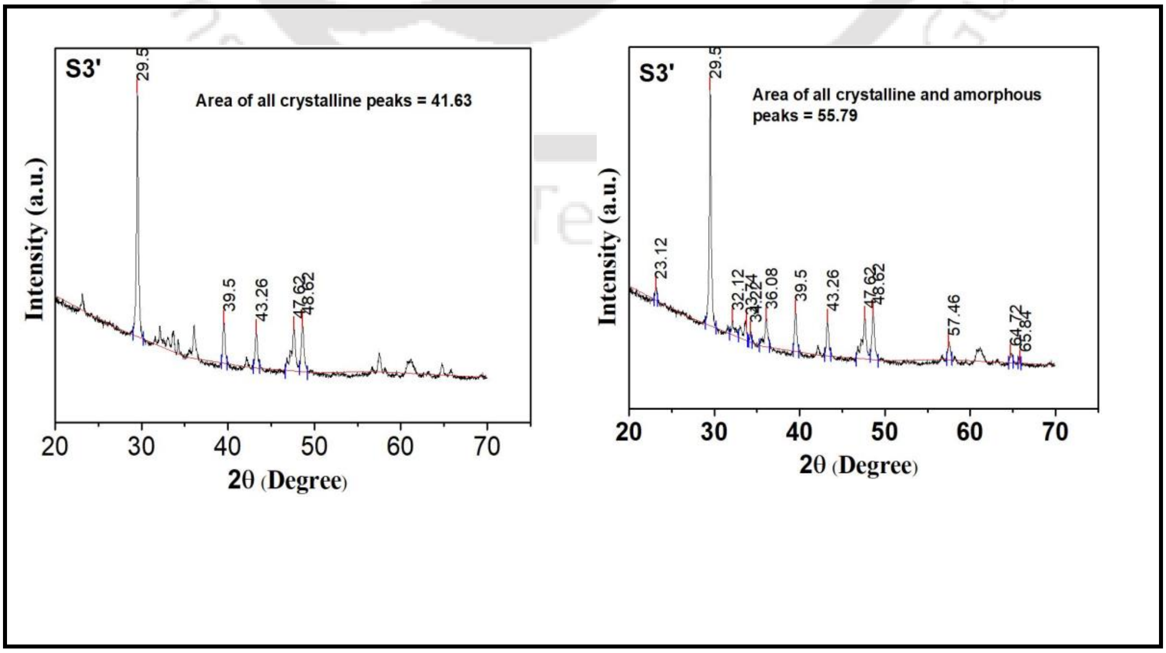
S3'
Area of all crystalline peaks = 41.63
29.5
39.5
43.26
47.62
48.62
Intensity (a.u.)
2θ (Degree)
20
30
40
50
60
70
S3'
Area of all crystalline and amorphous peaks = 55.79
29.5
23.12
32.12
36.08
39.5
43.26
47.62
48.62
57.46
64.72
65.84

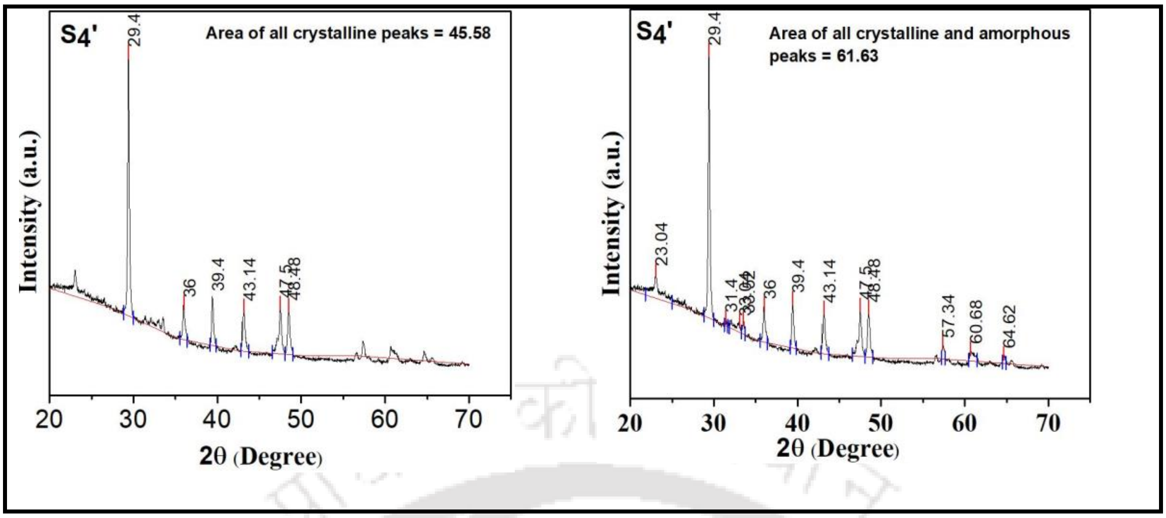

Figure 5.3: The area under the curve of all crystalline and crystalline-amorphous phases of samples synthesized with and without sugar.

Table 5.1: Crystallinity index (CI) value obtained from XRD peaks of all synthetic PCC powder samples.

With sugar	CI (%)	Without sugar	CI (%)
S_1	89.53	**S_1'**	72.43
S_2	79.86	**S_2'**	71.44
S_3	87.78	**S_3'**	74.61
S_4	89.22	**S_4'**	74.20

5.2.1.4. Field Emission Scanning Electron Microscopy (FESEM) Study

The morphological analysis of slag powder has been shown in Figure 5.4. The granular and amorphous nature of the sample was observed. It was also observed from the FESEM image that some particles have an angular-shaped structure with a flaky appearance.

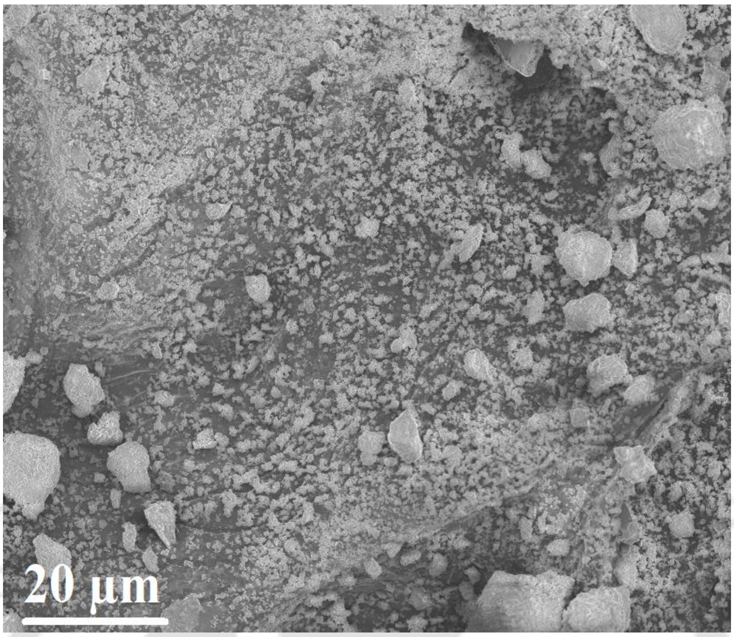

Figure 5.4: FESEM image of steel industry processed LD-slag.

The morphology of precipitated calcium carbonate products derived from reactions at different temperatures is shown by FESEM (Figure 5.5). The results revealed that distinct cubical morphologies are calcite which is precipitated at low temperatures ranging from 25 to 35°C for samples 1 and 2, respectively, as shown in Figure 5.5a-c, while disc, plate, and hollow-cone architecture type unstable vaterite [25] are observed at 45°C in sample 3, as displayed in Figure 5.5d-f. From Figure 5.5h, it was observed that spindle-type aragonite [26] dominated at the highest temperature in synthetic $CaCO_3$ polymorph. At 55°C, the flake-like aragonite [26] phase was found to be dominant (Figure 5.5i), which was accompanied by residues of hollow-four-sided calcite pyramids [25] in sample 4, as illustrated in Figure 5.5g. It is apparent from FESEM analysis that most stable calcite phases precipitated first at low temperatures (25-35°C), whereas less stable vaterite and aragonite phases appeared at 45 and 55°C, respectively. The binary mixture of aragonite and calcite phase was observed at 55°C. Such phenomenon was attributed to the fact that, as the temperature raised from 45 to 55°C, the aragonite phase soon got transformed into a stable calcite phase. The reason might be the sugar-induced aggregation of colloid particles in the crystallization process, as evident from hypothesis testing (Figure 5.13).

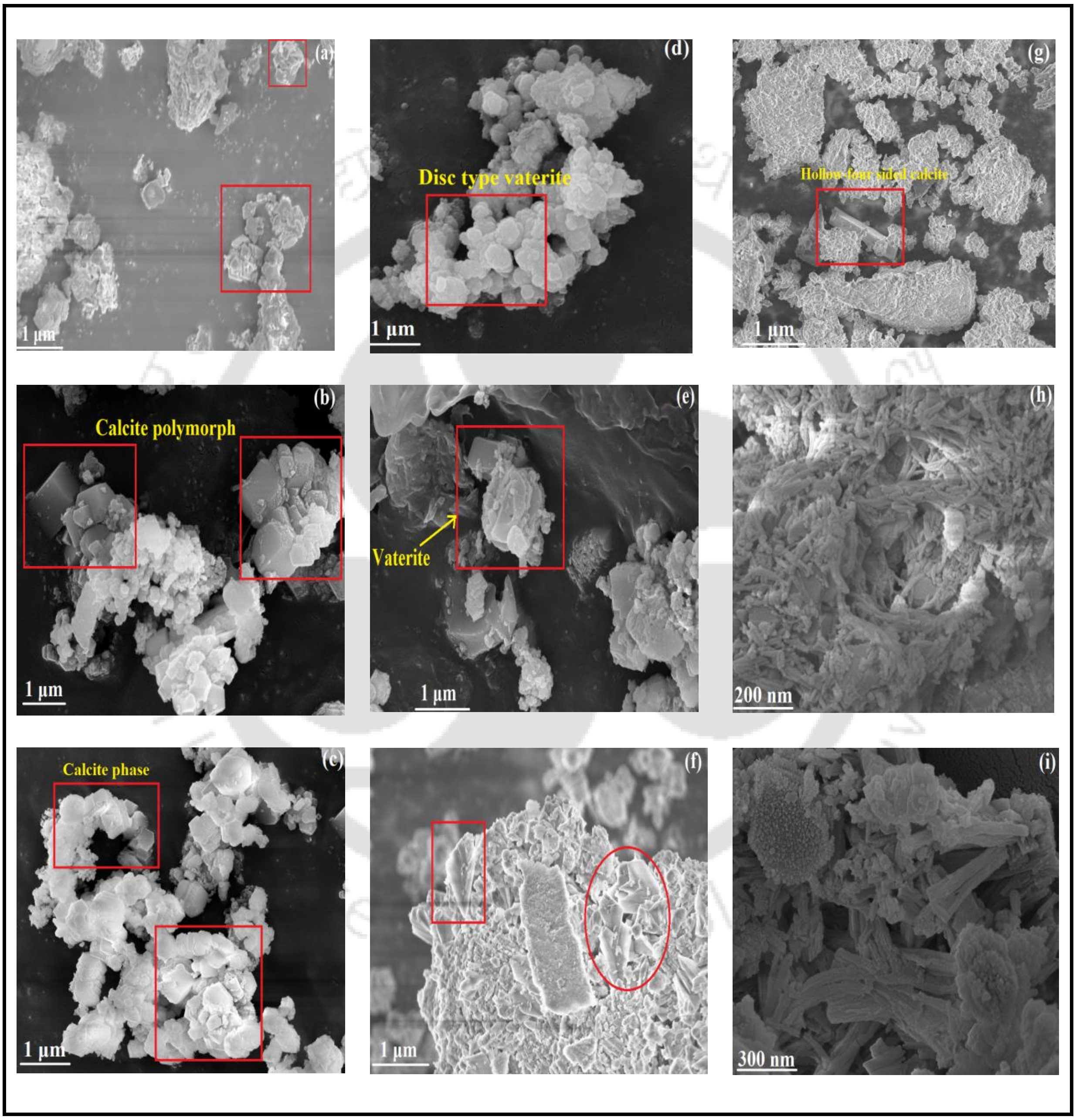

Figure 5.5: FESEM images of synthesized calcium carbonate polymorphs (a)-(c) for samples 1 and 2, (d)-(f) for sample 3, and (g)-(i) for sample 4.

According to the FESEM results, it can be attributed that, room temperature (25°C) is acceptable to achieve the highly crystalline calcite polymorph, however, other phases like vaterite and aragonite can be produced at comparatively higher temperatures under the given reaction conditions, taking LD-slag as the raw material.

5.2.1.5. Energy Dispersive X-ray (EDX) Study

The results of the elemental analysis of LD-slag and reacted samples are shown in Figure 5.6a-e. The EDX analysis of four reacted samples along with unreacted LD-slag are enlisted in Table 5.2**.** The weight percentage of calcium was found to increase as the temperature of the carbonation reaction was increased from 25 to 55°C, as shown in Table 5.2. From Table 5.2 it also can be seen that the amount of calcium weight percentage was 32.7 wt.% for LD-slag, whereas for samples 1, 2, 3, and 4 the calcium concentration was found to be 35.6, 53.8, 61.8, and 81.6 wt.%, respectively. The results indicate that the reaction progressed more at higher temperatures and it resulted in more $CaCO_3$ formation with respect to other compounds, which decreases the weight percentage of other elements present thus resulting in a higher Ca weight percentage.

5.2.1.6. Field Emission Transmission Electron Microscopy (FETEM) Study

The FETEM analysis of LD-slag has been shown in Figure 5.7. From the image, it was observed that slag particles were amorphous and agglomeration-type. In addition, the halo ring pattern found in selected area electron diffraction (SAED) (at inset) reveals the amorphous nature of the slag material.

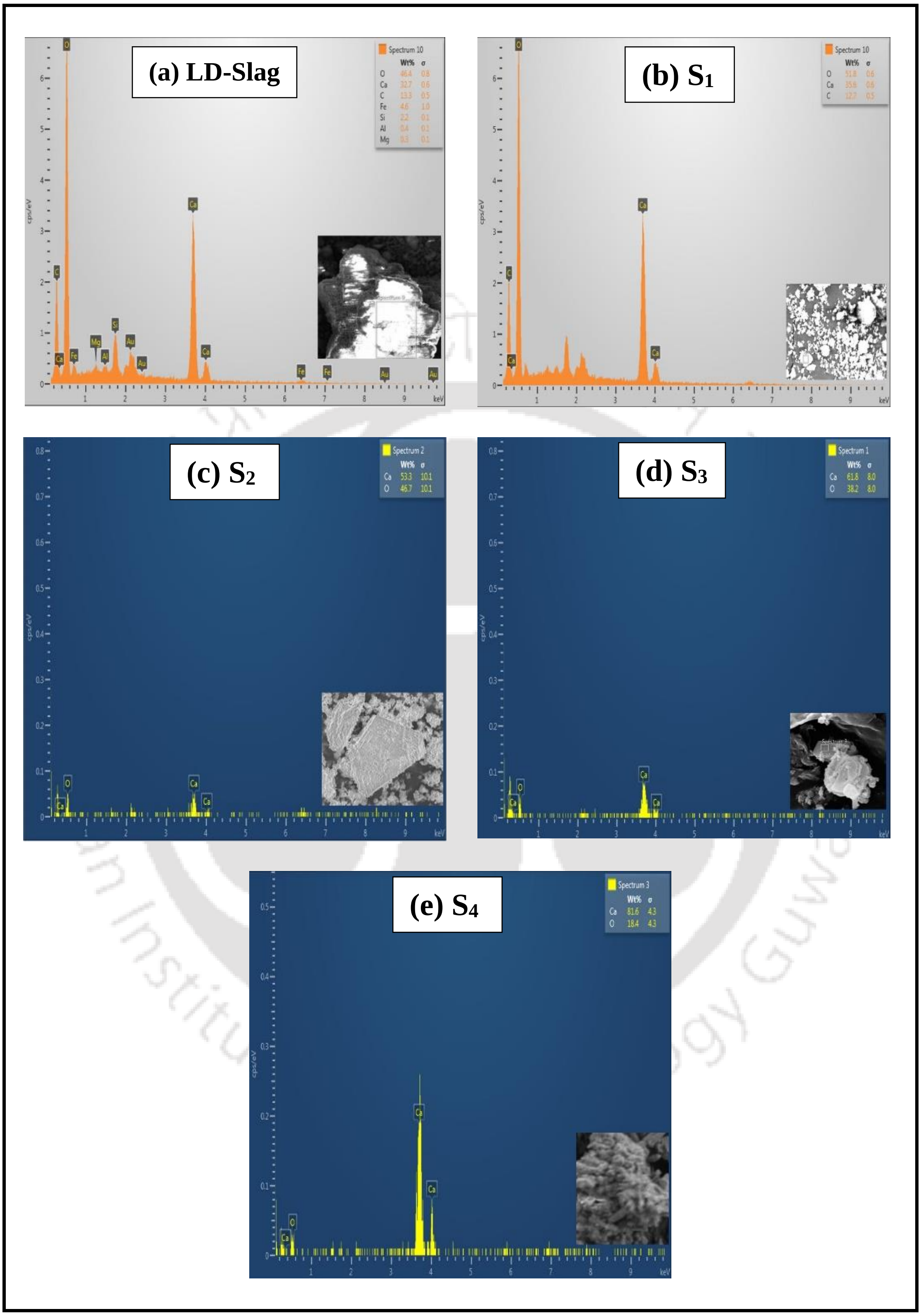

Figure 5.6: EDX spectroscopic analysis of (a) LD-slag; (b) sample S_1; (c) sample S_2; (d) sample S_3 and (e) sample S_4, respectively. The quantitative analysis of the major component Ca^{2+} is enlisted in Table 5.2.

Table 5.2: Shows the EDX spectrum of all reacted samples.

Elements	Wt.%
LD-slag	
Calcium (Ca)	32.7
Oxygen (O)	46.4
Sample 1 (S_1)	
Calcium (Ca)	35.6
Oxygen (O)	51.8
Sample 2 (S_2)	
Calcium (Ca)	53.8
Oxygen (O)	46.7
Sample 3 (S_3)	
Calcium (Ca)	61.8
Oxygen (O)	38.2
Sample 4 (S_4)	
Calcium (Ca)	81.6
Oxygen (O)	18.4

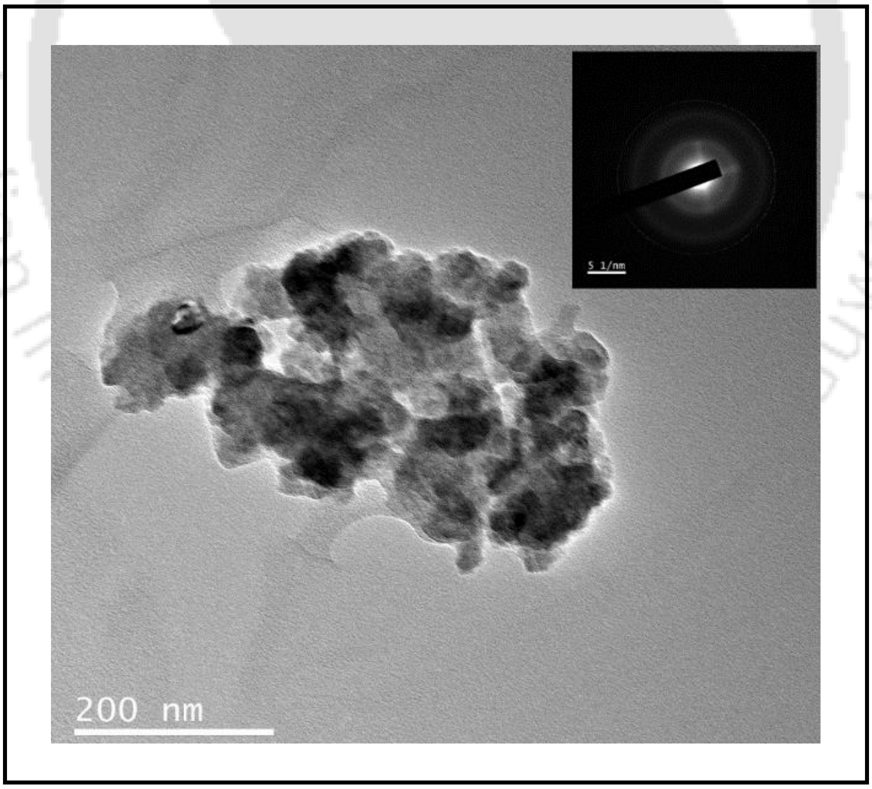

Figure 5.7: FETEM and SAED (selected area electron diffraction) analysis of LD-slag.

The results of the FETEM analysis of as-synthesized $CaCO_3$ samples are shown in Figure 5.8. This microscopic analysis exhibits the different crystalline shapes such as vaterite, calcite, and aragonite of the $CaCO_3$ polymorphs at different magnification ranges. Here, Figure 5.8a-c refers to samples 1 and 2, Figure 5.8d-f refers to sample 3, and Figure 5.8g-i to sample 4, respectively. The results of the FETEM analysis revealed that orthorhombic-cross sectional, irregular acicular, needle [27], and rod-type aragonite $CaCO_3$ phase [28] prevailed at high temperature ~55°C in sample 4 (Figure 5.8g-i). A similar needle-shaped aragonite phase of the synthesized $CaCO_3$ was also obtained in previous work carried out by Fellner et al. [27]. FETEM images of the plate-like vaterite [29] phase (Figure 5.8d) at 45°C were perceived with a minor amount of irregular aragonite (Figure 5.8e inset) and calcite phase (Figure 5.8f), respectively. At lower temperatures (25 to 35°C), the calcite polymorph [30] of $CaCO_3$ particles was obtained, as displayed in Figure 5.8a-c, for S_1 and S_2, respectively. Wherein, the rhombohedron-like calcite phase was observed in the FETEM image, as illustrated in Figure 5.8b [31].

From FETEM analysis, agglomeration and amorphous phase of raw LD-slag were observed. FETEM images confirmed the geometrical shape of synthetic $CaCO_3$ polymorphs produced from waste LD-slag in a CO_2 environment and the presence of sugar as a promoter.

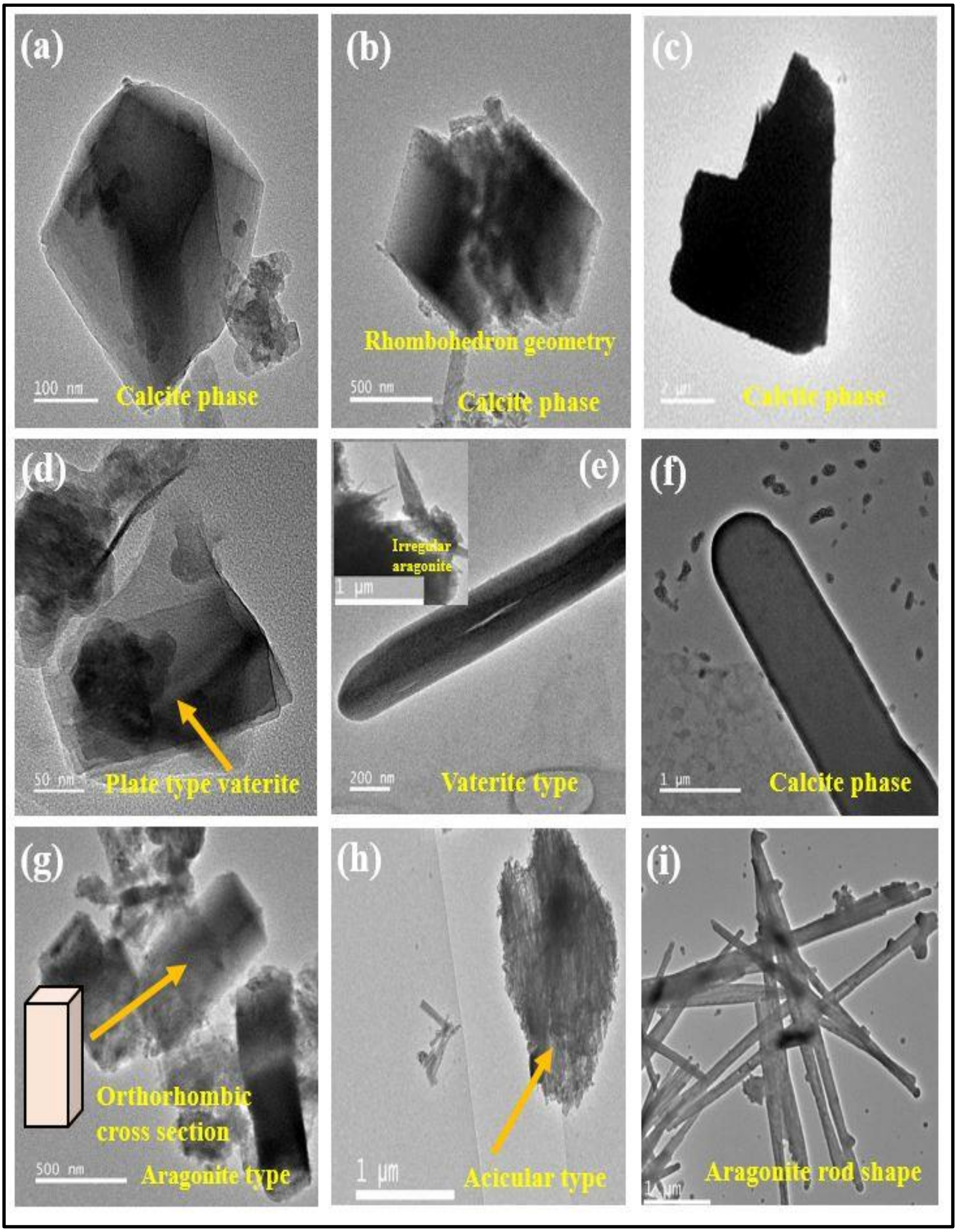

Figure 5.8: FETEM images of $CaCO_3$ polymorphs: (a)-(c) indicates for S_1 and S_2, (d)-(f) for S_3, and (g)-(i) for S_4, respectively.

5.2.1.7. SAED and HRTEM characterization

The corresponding selected area electron diffraction (SAED) and HRTEM patterns of PCC polymorphs are presented in Figure 5.9. Relevant SAED of three types of $CaCO_3$ phases are given in Figure 5.9a inset, which illustrates that the first ring with a small spot reveals polycrystalline material, which means the polymorphs have a more crystalline plane with a bright spot near the first ring indicating the crystalline nature of the $CaCO_3$ specimen and the other small spot found in the diffusing ring next to the first ring assigned for unreacted amorphous material or impurities present in reacted $CaCO_3$ material, which aggregates the presence of amorphous aragonite [32]. In addition, the well-defined crystalline plane of (1 0 4), (1 1 0), and (1 1 3) of the SAED pattern (Figure 5.9a), agreed with the presence of calcite phase in the precipitated sample [32,33]. Figure 5.9b shows the lattice spacing of $CaCO_3$ crystals, which was found to be around 0.31 nm [34]. The SAED pattern of the obtained sample revealed the polycrystalline nature of the $CaCO_3$ sample.

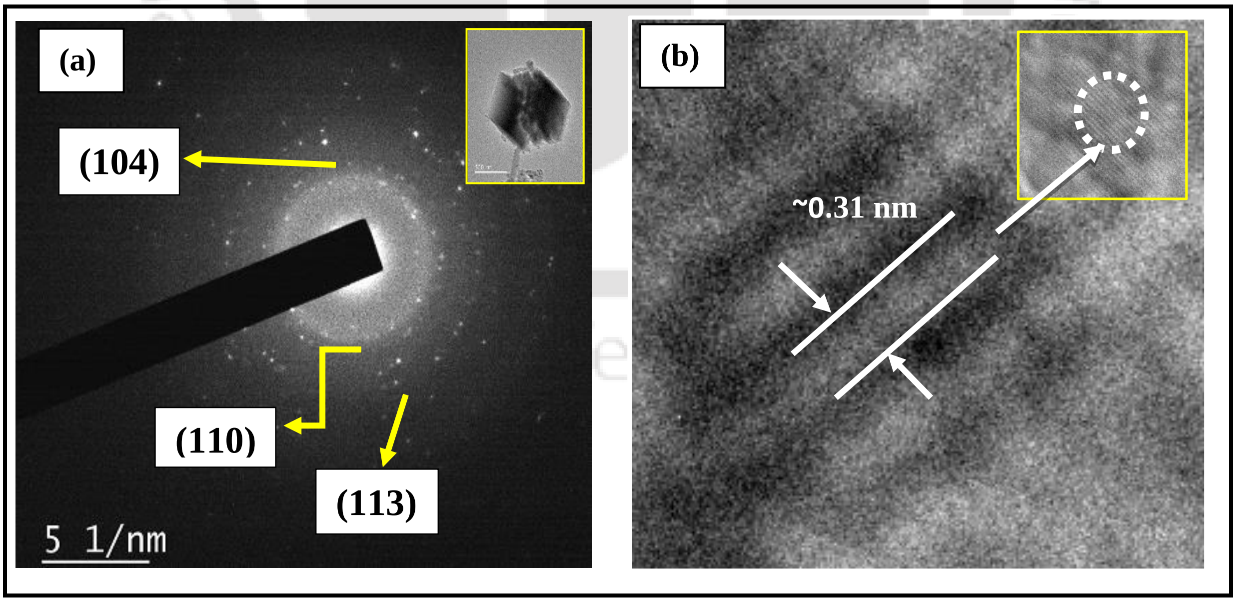

Figure 5.9: (a) The SAED pattern of calcite phase (b) crystal size of $CaCO_3$ polymorph synthesized at 55°C, and the inserted is the corresponding HRTEM pattern.

5.2.1.8. UV-Visible DRS analysis of PCC samples

In this study, UV-spectroscopy for solid samples was used to determine the whiteness value of the obtained PCC samples. It is well known that opaque substances have negligible transmittance, so any wavelength of light falling on them is either absorbed or reflected. A substance considered to be of white color must reflect all wavelengths of the electromagnetic spectrum within the visible range, i.e., from 400-700 nm. As seen in the reflectance plot of the lab-grade $CaCO_3$ (purity ≥99.0%, Sigma Aldrich), in Figure 5.10, the reflectance of the pure $CaCO_3$ is 98.84%, and the percentage reflectance against wavelength is plotted for all prepared $CaCO_3$ samples for comparison. It is observed that with an increase in reaction temperature, the precipitated calcium carbonate has an increasing reflectance. Thus, it can be set that the sample obtained reaction temperature of 55°C is more intensely reflecting light than the sample obtained at other temperatures. However, the reflectance of the obtained PCC is skewed towards the higher (reddish) wavelength (Figure 5.10). So, the obtained PCC sample has a reduced whiteness value than the lab-grade $CaCO_3$.

The PCC sample obtained at 55°C exhibits higher reflectance among other samples, which reveals the highest whiteness value of that sample. The whiteness of $CaCO_3$ can be increased by sintering it at high temperatures, typically above 800°C. However, the exact temperature required to achieve the desired whiteness may vary depending on the initial quality of the $CaCO_3$, the sintering conditions, and other factors.

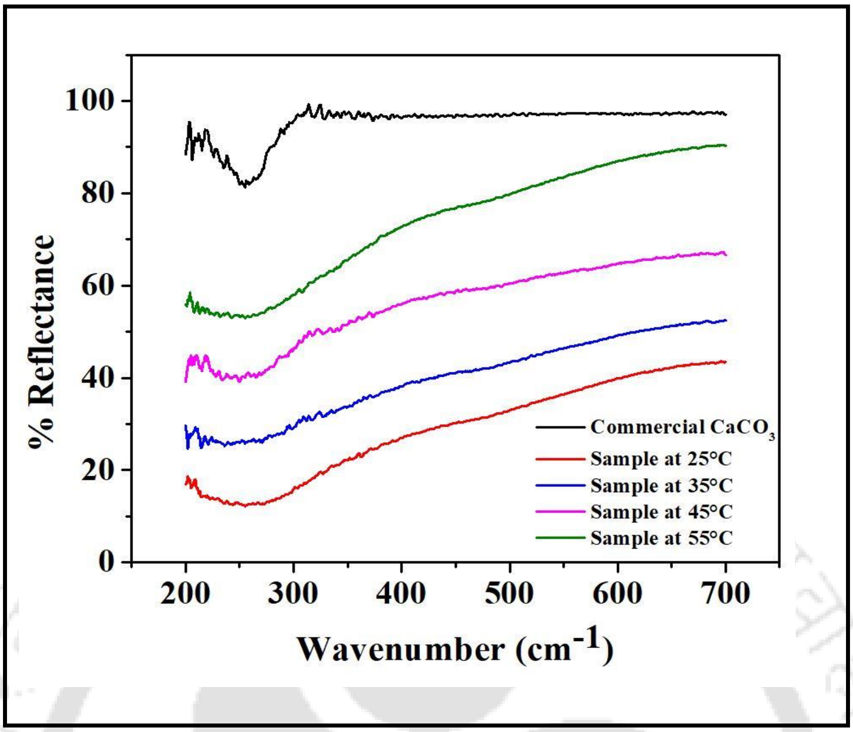

Figure 5.10: UV-Vis DRS plot of $CaCO_3$ samples prepared at different reaction temperatures (25-55°C).

5.2.1.9. Thermal analysis

The TGA thermograph of PCC (reacted at 55°C), as shown in Figure 5.11 confirmed the existence of $CaCO_3$ after the aqueous phase reaction of LD-slag with CO_2. It may be found from Figure 5.11a that the thermal degradation of $CaCO_3$ was a two-stage weight loss process. In the first stage, the mass loss began around 25°C and continued up to 640°C with a weight loss of 15.17%, indicating that the $CaCO_3$ mineral is stable up to that temperature range (640°C). The second mass loss is obtained in the temperature range of 640 to 795°C with a mass loss of 16.69%, demonstrating the decomposition of $CaCO_3$ to carbon dioxide (CO_2) and CaO [35]. Differential scanning calorimetry (DSC) was used to examine the thermal behavior of the $CaCO_3$ sample, as illustrated in Figure 5.11b. The DSC thermal analysis of the $CaCO_3$ polymorph was performed at temperatures ranging from 25 to 1000°C. The endothermic band occurred at 360°C and 570°C in the DSC heating curve (Figure 5.11b) and is aggregated with the result [36]. Furthermore, another endothermic signal observed at

794.9 ~ 795°C revealed the disintegration of calcium carbonate and the release of CO_2 and CaO [37]. The DSC result of the PCC sample formed at 55°C indicates that the endothermic peaks only appeared for the vaterite phase rather than other phases like calcite and aragonite which implied less stability of the vaterite polymorph present in the PCC sample.

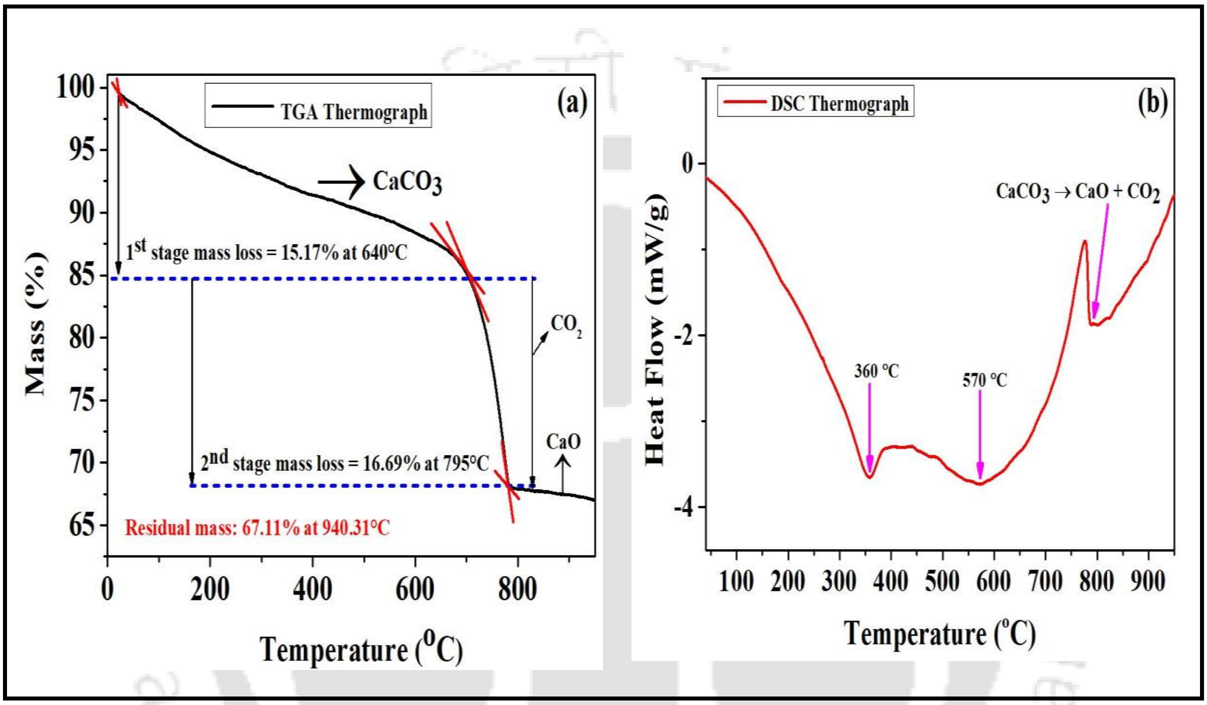

Figure 5.11: (a) TGA and (b) DSC analysis of precipitated calcium carbonate sample obtained at 55°C.

TGA analysis of precipitated calcium carbonate can reveal information about its thermal characteristics, such as breakdown and carbonation behavior. These discoveries might be helpful for various applications, including understanding its stability, investigating reaction kinetics, and improving production methods.

5.2.1.10. CaO conversion and $CaCO_3$ formation

The CaO conversion has been elucidated in section 5.1.3. Figure 5.12a and 5.12b illustrates the CaO conversion and $CaCO_3$ formation with and without sugar at various reaction temperature. The highest CaO conversion and $CaCO_3$ formation were found to be 85.83%

and 1.7 g at 55°C, as shown in Figure 5.12a and Figure 5.12a (inset), respectively. As can be seen in Figure 5.12b, the CaO conversion as well as the $CaCO_3$ formation declined to ± 39-40% when the reaction was carried out without sugar. The reason could be less $Ca(OH)_2$ concentration in the reaction mixture.

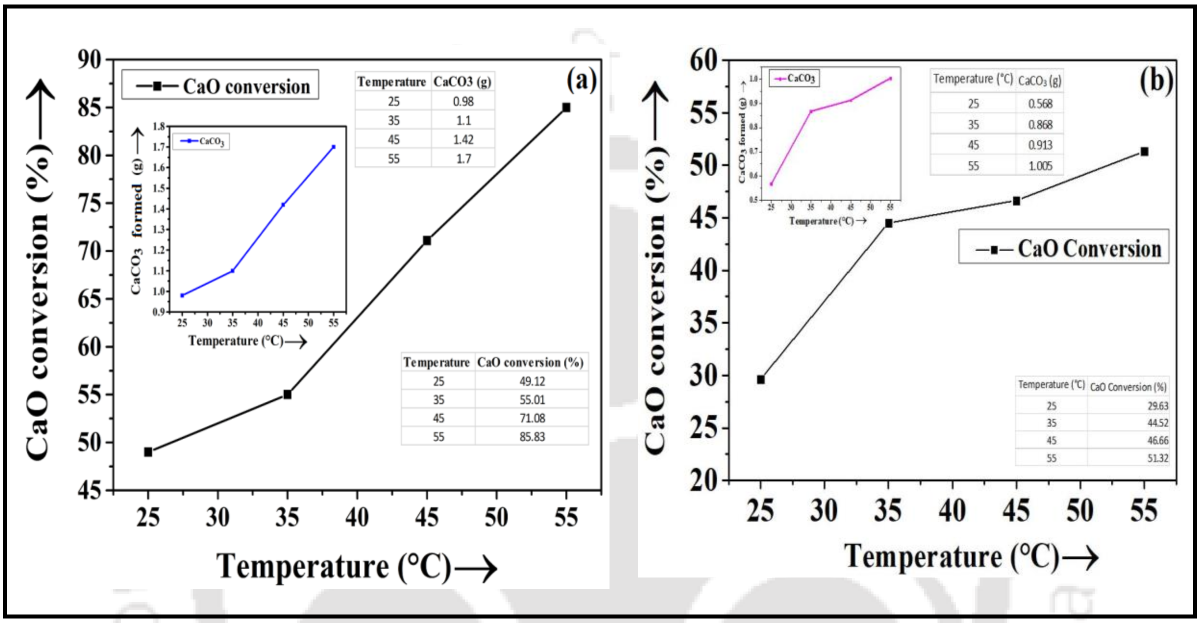

Temperature	CaCO3 (g)
25	0.98
35	1.1
45	1.42
55	1.7

Temperature	CaO conversion (%)
25	49.12
35	55.01
45	71.08
55	85.83

Temperature (°C)	$CaCO_3$ (g)
25	0.568
35	0.868
45	0.913
55	1.005

Temperature (°C)	CaO Conversion (%)
25	29.63
35	44.52
45	46.66
55	51.32

Figure 5.12: (a) CaO conversion and $CaCO_3$ formation at different temperatures with table sugar and (b) without sugar.

The aforementioned study showed that the highest CaO conversion and $CaCO_3$ formation were attained at 55°C. High temperatures may facilitate the production of more calcium carbonate, practical constraints or concerns may exist depending on the individual process or application. Excessive heat might cause undesirable reactions, breakdowns, or changes in the physical characteristics of the materials obtained after the reaction.

5.3. Influence of table sugar on the carbonation reaction

It was suggested that in the presence of sugar, a large concentration of $Ca(OH)_2$ is converted, resulting in an increased amount of precipitated calcium carbonate under the CO_2 bubbling method [38,39]. Literature is scant to establish the hypothesis. Therefore, the Null hypothesis is reported here (Figure 5.13) as there will be no difference in the mean value of the two distributions of the $Ca(OH)_2$ concentration in solution with and without table sugar as a promoter. The alternate hypothesis is that there will be a notable difference between the two means of the distributions of the $Ca(OH)_2$ concentration in solution with and without table sugar. In this study, five samples are taken from the experimental data carried out with and without table sugar. As the sample size is low "t" statistics are considered instead of the "z" distribution. In this case, the mean of with and without table sugar is 1912.64 and 522.12 with a standard deviation of 56.20 and 26.83, respectively. In addition, it is found that the degree of freedom (DF value) was 8. Furthermore, the difference of the means to has a greater significance, hence, considering 0.005 as "α" for this test. From the "t" distribution table it was also found that the "t" statistics for the given parameters and conditions is 49.92. The corresponding p-value was estimated to be 1.43×10^{-11}. As the p-value is drastically lower than α then the Null hypothesis could be rejected with good conviction. The alternate hypothesis can be adapted for further investigation i.e. the inclusion of table sugar solution enhances the formation of $Ca(OH)_2$ in a relatively quick time which enhances the rate kinetics for the production of $CaCO_3$.

The hypothesis test is evident that the addition of powdered sugar enhances the $Ca(OH)_2$ concentration which may result in high $CaCO_3$ formation.

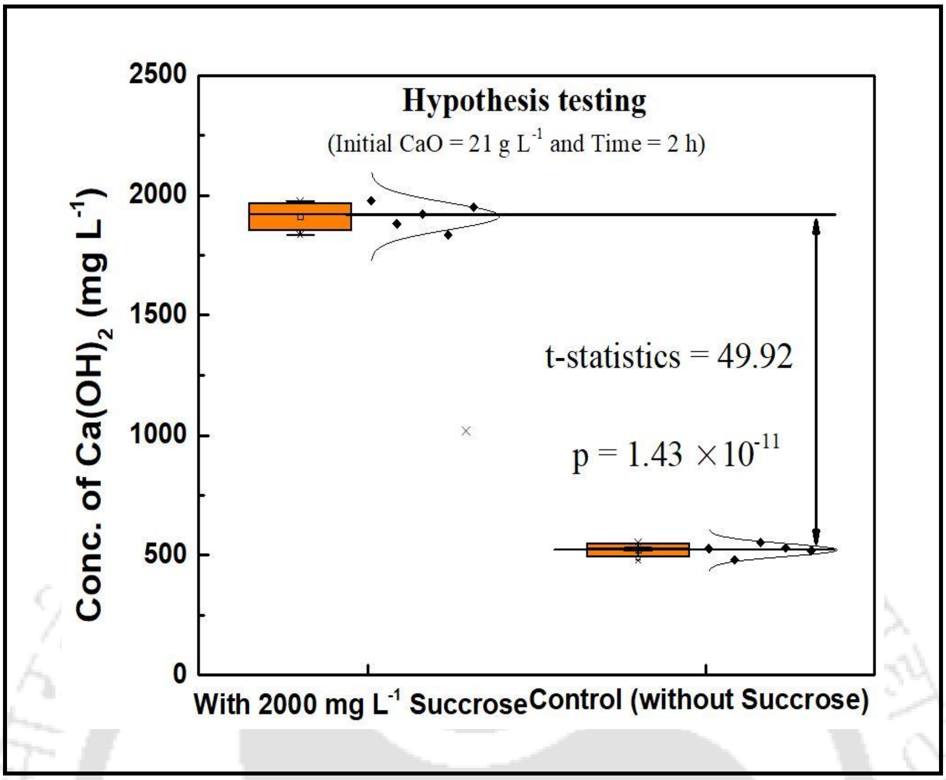

Figure 5.13: Hypothesis testing (t-value) to establish the influence of table sugar for enhancing $Ca(OH)_2$ concentration.

In-depth analysis revealed that the increase in $Ca(OH)_2$ concentration depends not only on the presence of sugar but also on the temperature. The Arrhenius equation was used in order to establish the hypothesis. As shown in Figure 5.14 and equation 3, the frequency or pre-exponential factor increases exponentially with reaction temperature, suggesting a higher degree of collision between reactant molecules, resulting in a high reaction rate and calcium hydroxide concentration. The activation energy for this reaction was found to be 42646±53 J mol^{-1}. Other derived parameters are mentioned in Table 5.3.

The activation energy and pre-exponential factor or frequency factor (A) was calculated from the Arrhenius equation, as given in equation (5.3)

$$K = (k_0\, T^n)\exp(\frac{-E_a}{RT}) \tag{5.3}$$

Where, $A = KT^n$, A represents the pre-exponential factor or frequency factor; E_a represents activation energy (KJ/mol); R is gas constant (J/mol K), and T is the temperature (K).

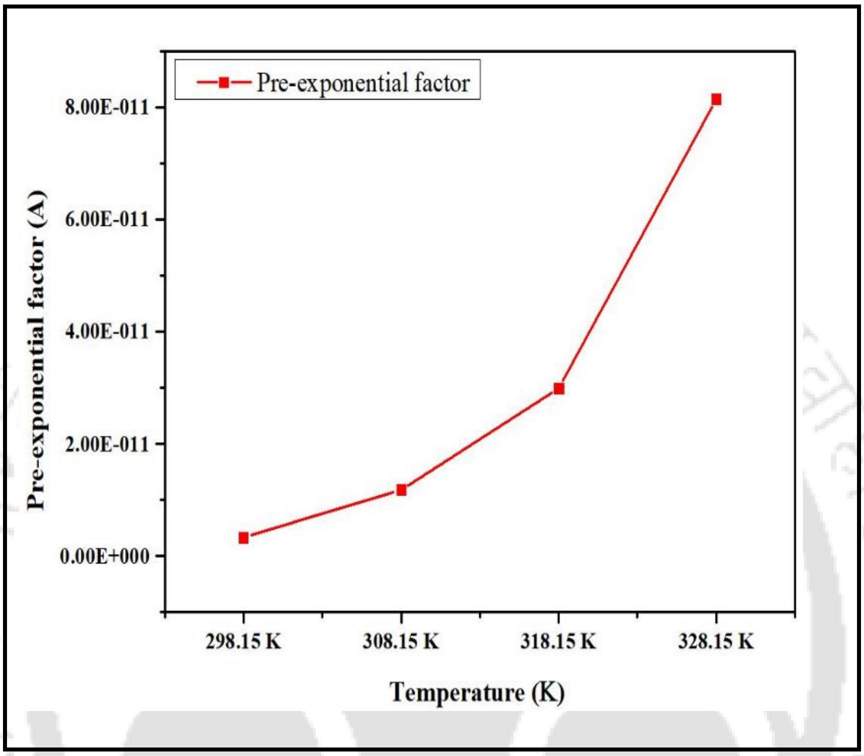

Figure 5.14: Graph for pre-exponential factor vs temperature (the value was estimated from equation 3).

Table 5.3: Represents the value of k, n, activation energy which is obtained from the Arrhenius equation, as mentioned in equation (3).

k_0	n	E_a (KJ/mol)	R (J/mol K)
3×10^{-93}	32.80	42646±53	8.3145

5.4. Kinetic models

The curves related to different kinetic models such as zero-order, pseudo-first-order, and pseudo-second-order are shown in Figure 5.15 to investigate the reaction kinetics of the $Ca(OH)_2$ production.

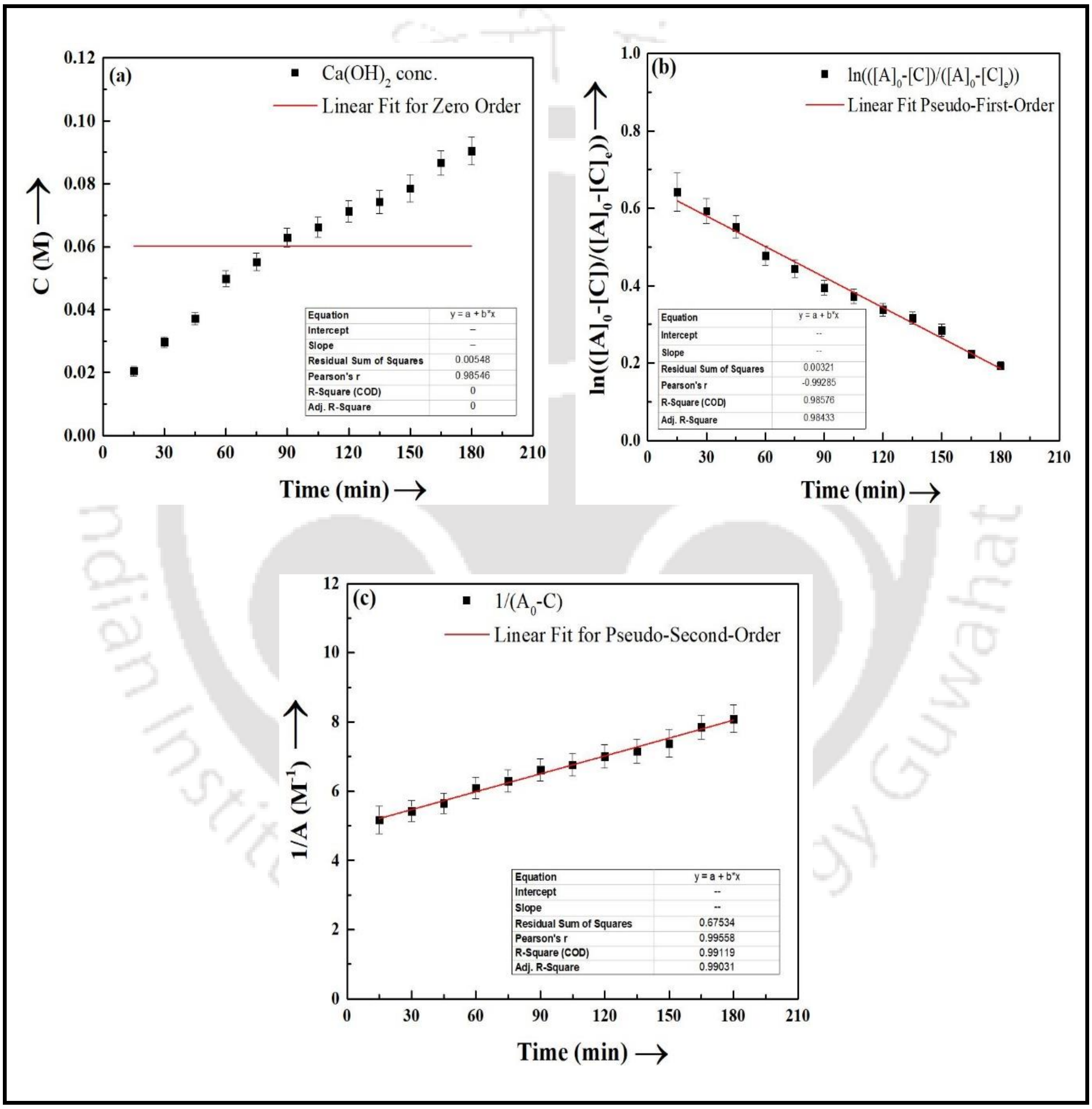

Figure 5.15: Different kinetic models (a) zero-order, (b) pseudo-first-order, and (c) pseudo-second-order.

The kinetic models imply that the increase in the concentration of calcium ions in the solution when sugar is added as a promoter is because of the mechanism provided in the following section. We find in the mechanism that the concentration of calcium ions is directly proportional to the concentration of CaO squared times the concentration of H_2O squared. However, since water is in excess so a considerable concentration change does not take place, thereby, the kinetic rate is directly proportional to the second power of the CaO concentration, thus, this becomes a pseudo-second-order reaction (Figure 5.15c). This also has been found in our analysis which is given in Figure 5.15 wherein, the rate kinetic models are tested for each model of zero-order, pseudo-first, and pseudo-second-order which confirms that the earlier presented mechanism suits the best. Table 5.4 displays the results for kinetic models estimated for $Ca(OH)_2$ formation with the inclusion of table sugar. As can be seen from Table 5.4, the rate constant for the pseudo-first and second-order model was estimated as 0.0048 and 0.0005, respectively.

Table 5.4: Different kinetic variables were obtained from the zero, pseudo-first, and pseudo-second-order models.

	Values		
Order of reaction	**Parameters**		
	R^2	**Intercept**	**K values**
Zero-order kinetic model: $C = -K_t + C_o$	0	0.060	$K_t = 0$
Pseudo-first-order kinetic model: $C_t = C_e(1 - e^{-k_1 t})$	0.985	0.685	$k_1 = 0.0048$
Pseudo-second-order kinetic model: $C_t = \frac{C_e^2 K_2 t}{(1+C_e K_2 t)}$	0.991	4.94	$k_2 = 0.0005$

5.4.1. Reaction mechanism

The reaction pathway for the dissolution of calcium oxide (CaO), in water in the presence of sucrose ($C_{12}H_{22}O_{11}$) can be

$$CaO + H_2O \xrightarrow{K_{SP}} Ca(OH)_2 \tag{5.4}$$

$$Ca(OH)_2 + C_{12}H_{22}O_{11} \underset{k_{-1}}{\overset{k_1}{\rightleftharpoons}} C_{12}H_{22}O_{11}.CaO + H_2O \tag{5.5}$$

$$Ca(OH)_2 + C_{12}H_{22}O_{11}.CaO \underset{k_{-2}}{\overset{k_2}{\rightleftharpoons}} C_{12}H_{22}O_{11}.2CaO + H_2O \tag{5.6}$$

$$C_{12}H_{22}O_{11}.2CaO + 2H_2O \underset{k_{-3}}{\overset{k_3}{\rightleftharpoons}} C_{12}H_{22}O_{11} + 2Ca^{2+}(aq) + 4OH^-(aq) \tag{5.7}$$

Overall:

$$CaO + Ca(OH)_2 + H_2O \xrightarrow[sucrose\ solution]{K_{obs}} 2Ca^{2+}(aq) + 4OH^-(aq)$$

5.4.1.1. Reaction Kinetics

The kinetic parameters of the overall reaction are derived from the aforementioned mechanism. The concentration of $Ca(OH)_2$ is derived from equation (5.4)

$$K_{sp} = \frac{[Ca(OH)_2]}{[CaO].[H_2O]}$$

$$Or, [Ca(OH)_2] = K_{sp}.[CaO].[H_2O] \tag{5.8}$$

Similarly, the concentration of the other intermediates is estimated from equations (5.5), (5.6), and (5.7), respectively

$$K_a = \frac{k_1}{k_{-1}} = \frac{[C_{12}H_{22}O_{11}.CaO].[H_2O]}{[C_{12}H_{22}O_{11}].[Ca(OH)_2]}$$

$$Or, [C_{12}H_{22}O_{11}.CaO] = K_a.\frac{[C_{12}H_{22}O_{11}].[Ca(OH)_2]}{[H_2O]}$$

$$Or, [C_{12}H_{22}O_{11}.CaO] = K_{sp}.K_a.[C_{12}H_{22}O_{11}].[CaO] \tag{5.9}$$

$$\text{Again,} \quad K_b = \frac{K_2}{K_{-2}} = \frac{[C_{12}H_{22}O_{11}.2CaO].[H_2O]}{[C_{12}H_{22}O_{11}.CaO].[Ca(OH)_2]}$$

$$Or, [C_{12}H_{22}O_{11}.2CaO] = K_b.\frac{[C_{12}H_{22}O_{11}.CaO].[Ca(OH)_2]}{[H_2O]}$$

$$Or, [C_{12}H_{22}O_{11}.2CaO] = {K_{sp}}^2.K_a.K_b.[C_{12}H_{22}O_{11}].[CaO]^2 \qquad (5.10)$$

$$Now, Kc = \frac{K_3}{K_{-3}} = \frac{[C_{12}H_{22}O_{11}].[Ca^{2+}]^2.[OH^-]^4}{[C_{12}H_{22}O_{11}.2CaO].[H_2O]^2}$$

$$or, K_c = \frac{1}{K_{sp}^2.K_a.K_b}.\frac{[Ca^{2+}]^2.[OH^-]^4}{[CaO]^2.[H_2O]^2}$$

$$or, K_c = \left(\frac{\mathbf{1}}{\boldsymbol{K_{sp}\sqrt{K_aK_b}}}.\frac{\boldsymbol{[Ca^{2+}].[OH^-]^2}}{\boldsymbol{[CaO].[H_2O]}}\right)^{\mathbf{2}}$$

$$[Ca^{2+}].[OH^-]^2 = \boldsymbol{K_{sp}.\sqrt{K_{a.}\,K_{b.}K_{c.}}.[CaO].[H_2O]} \qquad (5.11)$$

From equation (5.8) we can establish the rate law as,

$$-r_A = K.[CaO].[Ca(OH)_2].[H_2O] \qquad (5.12)$$

$$Also, r_p = K.[Ca^{2+}]^2.[OH^-]^4 \qquad (5.13)$$

$$And, -r_A = r_p$$

$$K.[CaO].[Ca(OH)_2].[H_2O] = K.[Ca^{2+}]^2.[OH^-]^4$$

$$Or, [CaO].[Ca(OH)_2].[H_2O] = K_{sp}^2.K_{a.}\,K_{b.}K_{c.}[CaO]^2.[H_2O]^2 \qquad (5.14)$$

$$Or, [Ca(OH)_2] = K_{sp}^2.K_{a.}\,K_{b.}K_{c.}[CaO].[H_2O] \qquad (5.15)$$

Putting the concentration of calcium hydroxide obtained from equation (5.16) in equation (5.13). We get,

$$-r_A = K.K_{sp}^2.K_{a.}\,K_{b.}K_{c.}[CaO]^2.[H_2O]^2 \qquad (5.16)$$

As the following reaction takes place in aqueous media, i.e., water is in extreme abundance, we can neglect the change in its concentration. The resultant equation thus becomes a pseudo-second-order reaction,

$$-r_A = K.K_{sp}^2.K_{a.}\,K_{b.}K_{c.}[CaO]^2 \qquad (5.17)$$

Thus, by comparing equations (5.8) and (5.18), we obtain,

$$K_{obs} = K.K_{sp}^{2}.K_{a.}\,K_{b.}K_{c.} \qquad (5.18)$$

5.5. Efficiency of CO_2 sequestration in this operation

The CO_2 sequestration efficiency was determined in order to estimate the process's capacity. The CO_2 sequestration efficiency value was obtained from equation (5.19) and which is nearly (~) 17%. This value has also been verified from TGA (Figure 5.11), as CO_2 evolve from TGA is around 16.69% which is very close to the efficiency value obtained from equation (5.19). And dissolved CO_3^{2-} ions in the water contribute to the remaining carbon dioxide concentration as well as efficiency.

$$\%\,Efficiency = \left(\frac{CO_2 in\ precipitated\ CaCO_3 + {CO_3}^{2-}\ in\ aqueous\ solution}{Moles\ of\ CO_2 in}\right) \times 100 \qquad (5.19)$$

As can be seen in Figure 5.16, the maximum dissolution of CO_2 (mol/L) was reached at first 30 minutes and thereafter it reached equilibrium with time. It is also seen from the same figure that the CO_3^{2-} concentration profile is following the CO_2 dissolve curve wherein, the highest CO_3^{2-} concentration was achieved at 30 minutes and then got equilibrium with the time. Table 5.5 illustrates a study on CO_2 sequestration efficiency, which reveals that the efficiency of CO_2 sequestration in this study is found to be better than many other reported data. Chen et al., 2022 [40], achieved an efficiency of 16.5% with a CO_2 flow rate of 200 mL/mil, which is four times the CO_2 flow rate in this study. Revathy et al. 2016 [41], and Hou et al., 2020 [42] achieved an efficiency of 27% and 18.9%, respectively, in a pressurized environment, thereby increasing the energy demand of the process.

It was estimated that on a w/w basis, 2 g of CO_2 sequestrated in 4 g of LD-slag which gives a 500 g CO_2 sequestration per kilogram of LD-slag. The details calculation are here:

One mole of CO_2 occupies a volume of 22.4 L which equals 985.6 L of CO_2. According to our study, the CO_2 flow rate was 50 mL/minute which gives the consumption of 3.04 L CO_2

per hour and which will also give 6.08 L CO_2 per 2 hours. Then, the gram of CO_2 intake was (6.08×1.97 (density of CO_2, g/L)) which gives 11.97 g of CO_2. This study estimated 17% CO_2 sequestration per 4 g of slag which equals 2.03 g of CO_2 per 4 g of LD-slag. According to this, 1 kg LD-slag could capture 500 g of carbon dioxide gas.

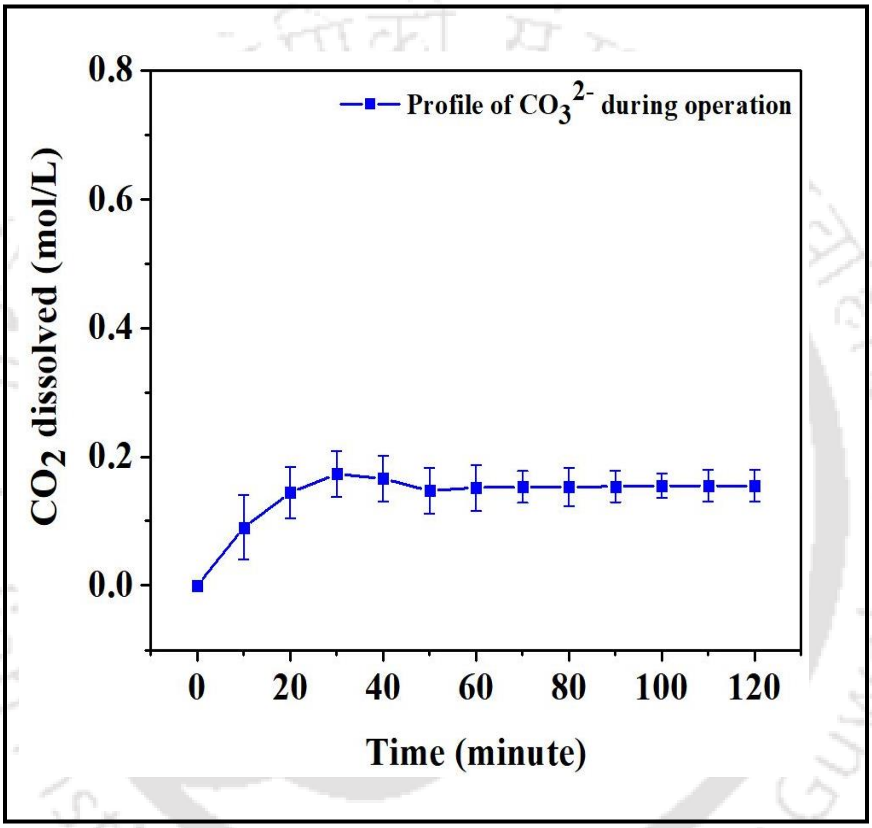

Figure 5.16: CO_3^{2-} concentration profile with time during the process of CO_2 dissolution.

Table 5.5: CO_2 sequestration Efficiency comparison study.

Purity of CO_2 gas (%)	Alkaline waste source/Application	Process parameters used	CO_2 sequestration efficiency (in %)	References
100	Municipal solid waste incineration fly ash (MSWI FA) for CO_2 sequestration.	Temperature: at ambient; CO_2 flow rate: 200 mL/minute; Reaction time: 60 minutes	16.5	[40]
100	Industrial raw materials limestone and sandstone for CO_2 sequestration	Temperature: ambient; limestone: sandstone (78.2:21.8, w/w); Reaction time: 60 minutes	6.75	[43]
100	Industrial steel slag for CO_2 sequestration	Temperature: room temperature; Pressure: 6 bar; Sequestration time: 3 hours; liquid to solid ratio: 10	27	[44]
100	Rankinite ($3CaO·2SiO_2$ or C_3S_2) used as clinker	Temperature: room temperature; Pressure: 57.4 MPa; Sequestration time: 3 days	18.9	[42]
100	**Steel industry processed LD-slag was taken to synthesize precipitated calcium carbonate (PCC)**	**Temperature: 25-55°C; CO_2 flow rate: 50 mL/minute; Sequestration time: 2 hours; Pressure: atmospheric pressure**	**17**	**This work**

5.6. Characterization of PCC samples synthesized without sugar

5.6.1. FESEM analysis

Figure 5.17 shows the morphological analysis of PCC samples, produced within a temperature range from 25-55°C. From Figure 5.17a it was observed that the non-identical and agglomerated calcite phase appeared at ambient temperature (25°C). The FESEM images also revealed that, as the reaction temperature is increased from 35 to 55°C, the crystal structure of synthesized precipitated calcium carbonate is rhombohedron calcite, which is the most stable form of $CaCO_3$ polymorph, as shown in Figure 5.17b-d. One can also notice that the flake-like aragonite phase also appeared when the reaction was carried out at 55°C, as shown in Figure 5.17d. The morphological analysis of synthetic PCC samples without sugar indicates that the supersaturation is not taking place due to $Ca(OH)_2$ deficiency in the absence of table sugar, thereby resulting in low interaction between Ca^{2+} and CO_3^{2-} [1,38] ions.

The FESEM analysis of as-synthesized sugar-activated $CaCO_3$ crystals (Figure 5.5) and without sugar (Figure 5.17) concludes that the shape and orientation of calcium carbonate formed in the different samples are due to the formation of various kinetics of $CaCO_3$ particles in different Ca^{2+} concentration solutions. $CaCO_3$ particles develop slowly but uniformly at low Ca^{2+} concentrations due to the limited quantity of Ca^{2+} in the unit volume. These particles are subsequently absorbed by surfaces and combine to form larger particles. Surface chemistry causes crystals to develop gradually after reaching a threshold size. High amounts of $CaCO_3$ are produced in a short period once CO_2 formed CO_3^{2-} by dissolving in a high Ca^{2+} concentration solution, which leads to the formation of a dynamic crystal structure. The findings are also evident that calcite polymorphs are formed in high Ca^{2+} concentrations [4].

In our study, therefore, calcite crystals are formed at 25°C with sugar (Figure 5.5a-c), whereas, prominent calcite phases appeared at 55°C in the sample without sugar. It was also stated that less stable vaterite and aragonite will be formed at lower Ca^{2+} concentrations [45]. The study therefore also revealed that the vaterite and aragonite were formed at lower Ca^{2+} supersaturation in solution. Therefore, it is also noticeable from Figure 5.17 that calcite polymorph is strongly dominated rather than other polymorphs i.e., vaterite and aragonite in the LD-slag processed PCC samples.

FESEM images of without sugar samples demonstrate that only the calcite phase was dominated in all synthesized PCC samples at all temperatures. However, the presence of aragonite and calcite was noticed in the $CaCO_3$ sample when the reaction was carried out at 55°C. From the investigation, it is also evident that increasing temperature leads to the formation of better crystallinity of the calcite polymorph.

5.6.2. FETEM analysis

Figure 5.18 exhibits the FETEM images with the SAED pattern without sugar-synthesized PCC samples. In the SAED pattern as shown in Figure 5.18e, a ring-like pattern was observed which reveals that the agglomeration takes place in the sample, indicating a collection of tiny crystalline particles with random crystallographic orientations (polycrystalline sample) [46]. The corresponding SAED patterns of other FETEM images reveal spots superimposed on the diffuse ring. The spots are attributed to the single crystal wherein halo ring images appeared in this image, demonstrating the amorphous nature [47] of the sample. Therefore, the sample obtained after the reaction is polycrystalline in nature which indicates that the $CaCO_3$ polymorphs formed by the carbonation reaction are mostly crystalline but composed of several sub-crystals [48]. In addition, the presence of agglomerated rhombohedron calcite phase was also clearly seen, as illustrated in Figure 5.18c.

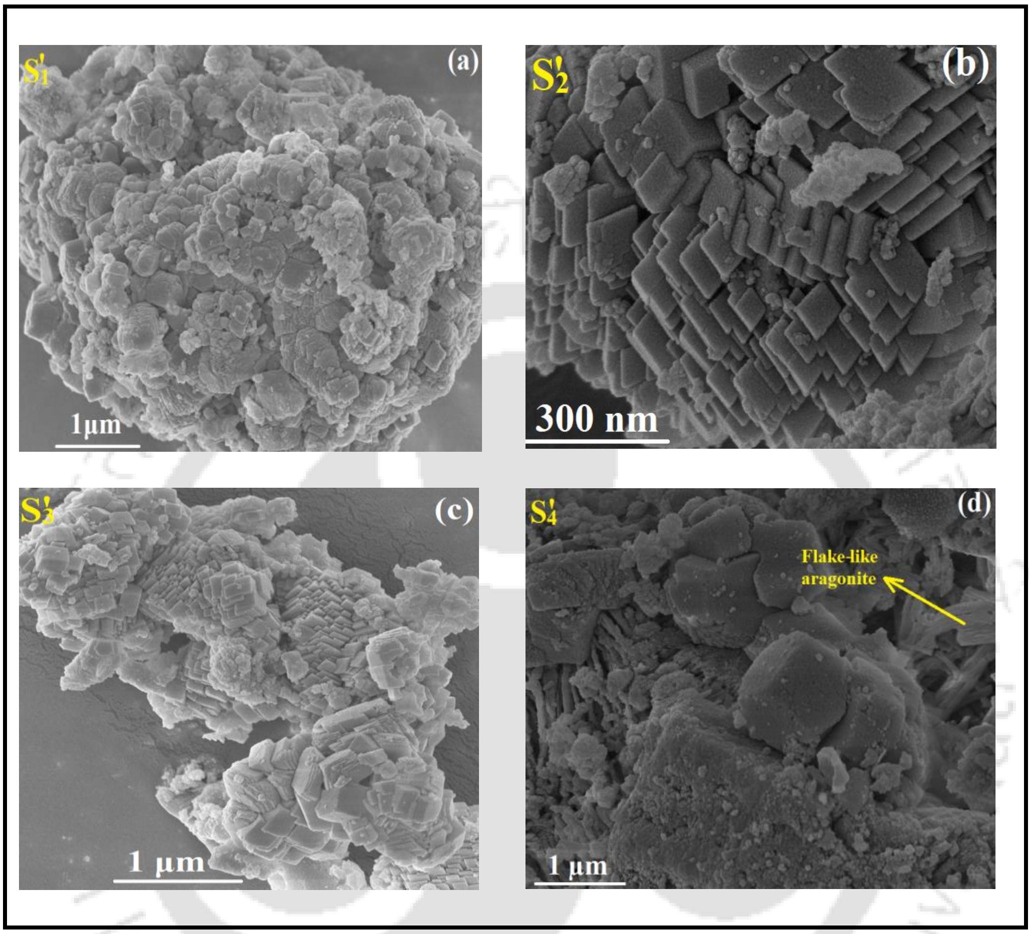

Figure 5.17: FESEM images of four samples synthesized without sugar. Where S_1', S_2', S_3', and S_4' represents sample produced without sugar within the temperature ranging from 25-55°C.

A conclusion can be made by comparing both the FETEM analysis of synthetic $CaCO_3$ polymorph as displayed in Figure 5.8 and Figure 5.18 that, precipitated calcium carbonate produced in sugar solution has dominated its uniform crystalline polymorphs namely calcite, vaterite, and aragonite when CO_2 gas was purged into the aqueous mixture, as depicted in Figure 5.8. Notably, a crystalline calcite phase was observed (for S_4') in Figure 5.18 along with flake-shaped aragonite (Figure 5.18d) when the reaction was conducted without sugar and obtained results are in good agreement with FESEM analysis (Figure 5.17d). The above results may be due to the high solubility of hydrated lime ($Ca(OH)_2$) in sugar solution [39] rather than only aqueous media, leading to nucleation formation and resulting in the production of different $CaCO_3$ polymorphs.

5.6.3. XRD analysis

The XRD pattern of without sugar PCC samples has been illustrated in Figure 5.19. Results achieved from analysis reveal the presence of only calcite (JCPDS file No. 05-0586) phase in the synthesized sample. No vaterite phase has appeared in the XRD profile. However, the appearance of a very small peak at 2θ of ~ 42.8° is ascribed to the presence of the aragonite phase which corresponds to the crystalline plane of (2 2 0) of the obtained sample. The absence of vaterite is presumably due to dominating of the calcite phase in the final sample. Samples that were synthesized without sugar had a crystallinity index within the range of 71 to 74% (Table 5.1, Figure 5.3). Comparing CI data, it can be seen that produced sample with sugar was shown a higher CI value rather than PCC samples synthesized without sugar.

It is well known that the crystallinity index (CI) of a material has been used to describe the relative amount of crystalline material present in the sample, which contains both crystalline (ordered) and amorphous (less ordered) regions. The crystallinity result indicates that the sugar-activated samples comprised more crystalline calcite and less crystalline vaterite and aragonite phases than samples synthesized without sugar. Moreover, the CI data also demonstrates that sample 3 (S_3') obtained without a sugar solution mixture exhibits higher crystallinity (74.61%, (Figure 5.3)) among others.

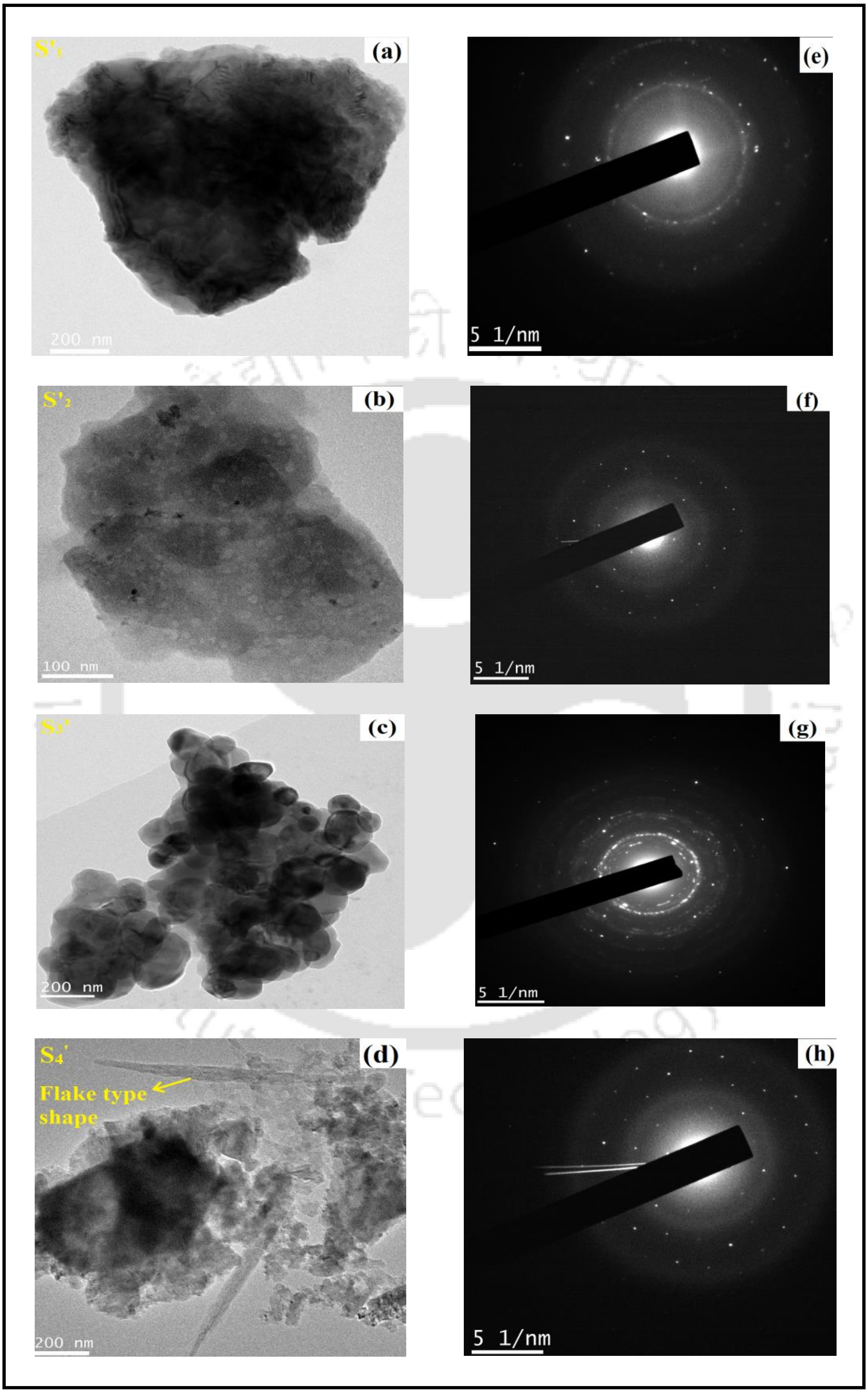

Figure 5.18: (a) to (d) TEM images and (e) to (h) SAED patterns of sample S_1', S_2', S_3', and S_4', reacted at temperatures ranging from 25 to 55°C without sugar.

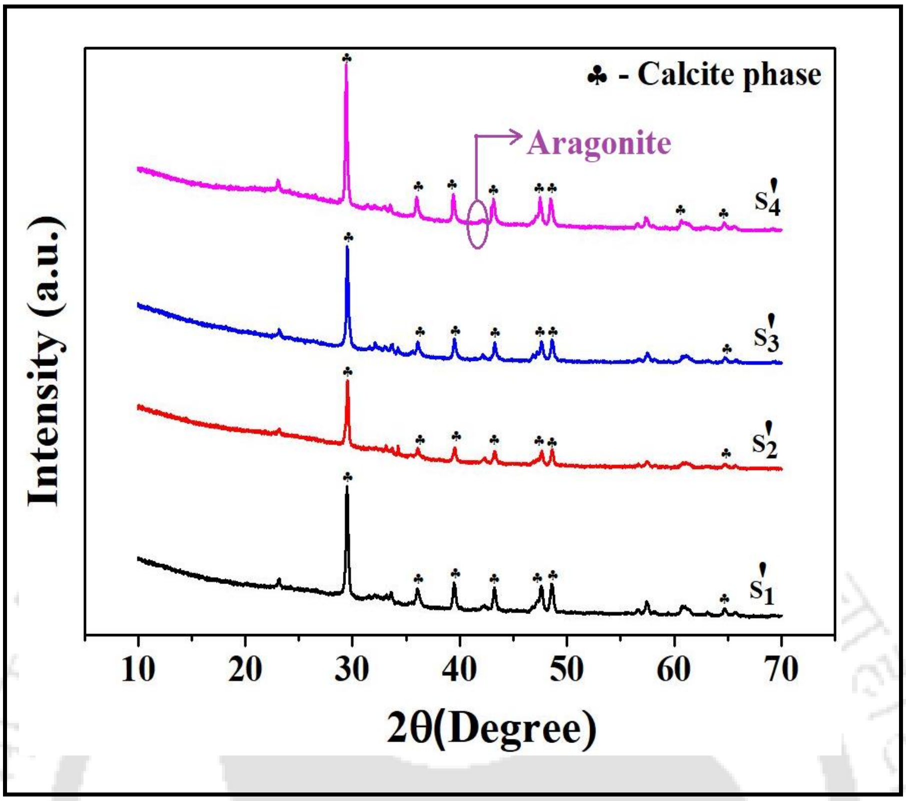

Figure 5.19: XRD pattern of calcium carbonate powder synthesized without sugar.

The XRD profiles of the without sugar sample revealed that only the calcite phase of precipitated calcium carbonate was observed. The crystallinity index (CI) value was calculated from the peaks that appeared in the XRD analysis and it was found that sample S_3' exhibited better CI among others.

5.6.4. XPS analysis of with-sugar and without-sugar synthesized $CaCO_3$ samples

Figure 5.20a and 5.20b shows the XPS wide-scan spectrum of synthetic PCC, reacted with and without sugar. All three elements i.e. C, Ca, and O, were found in both synthesized $CaCO_3$ samples. Table 5.6 represents the corresponding atomic concentrations of both the $CaCO_3$ powders achieved from the XPS survey. As is shown in Table 5.6, the atomic concentration of Ca 2p spectra in the $CaCO_3$ (reacted with sugar) surface is higher than without sugar-synthesized precipitated calcium carbonate.

As shown in Figures 5.21A and 5.21B, the high-resolution XPS spectra of as-synthesized $CaCO_3$ samples were carried out to analyze the C 1s, Ca 2p, and O 1s, elemental peak in three polymorphs i.e., calcite, vaterite, and aragonite. In Figure 5.21A, the adventitious carbon peak appeared at 284.6 eV, and the binding energy (BE) of a standard C 1s peak at 289.3±0.2 eV coincided with CO_3 in the $CaCO_3$ surface. The binding energies (BEs) and peak intensities of calcite, vaterite, and aragonite were identical. The CO_3 peak intensity for calcite and vaterite was high, whereas, aragonite yielded lower values. The binding energies for all three phases are different, and the higher BE only occurred for the aragonite phase. The BE 284.6 eV related to an adventitious carbon center deduced from sample contamination during air exposure [49]. The Ca 2p spectra of the $CaCO_3$ powder samples with high energy resolution revealed two binding energies for Ca $2p_{1/2}$ and Ca $2p_{3/2}$, as depicted in Figure 5.21A. The Ca $2p_{3/2}$ and Ca $2p_{1/2}$ peaks for calcite, vaterite, and aragonite phases reflected binding energies of 346.5, 346.6, 347.2 and 350.2, 350.1, and 350.5 eV, respectively. Comparing all three types of polymorphs, the Ca $2p_{3/2}$ core level is found to be at a low BE on calcite surfaces, which implies that the electron density in calcite around calcium atoms in the surface zone is considerably high [50]. However, there was a 3.5±0.1 eV difference in the chemical shifts of the Ca $2p_{3/2}$ and Ca $2p_{1/2}$ core levels in the three polymorphs of the synthetic $CaCO_3$ sample. These results are almost in good agreement with other work [49]. As is shown in Figure 5.21A, the O 1s core-level BE position of calcite, vaterite, and aragonite, appears at 531.2, 531.1, and 531.3 eV, respectively (Table 5.7). The shoulder peaks for all the polymorphs are discernible and the peaks are segregated at the high energy resolution, with a BE of 532.9±0.2 eV. Table 5.7 illustrates XPS parameters for Ca 2p, C 1s, and O 1s core levels obtained from the with sugar synthesized $CaCO_3$ sample.

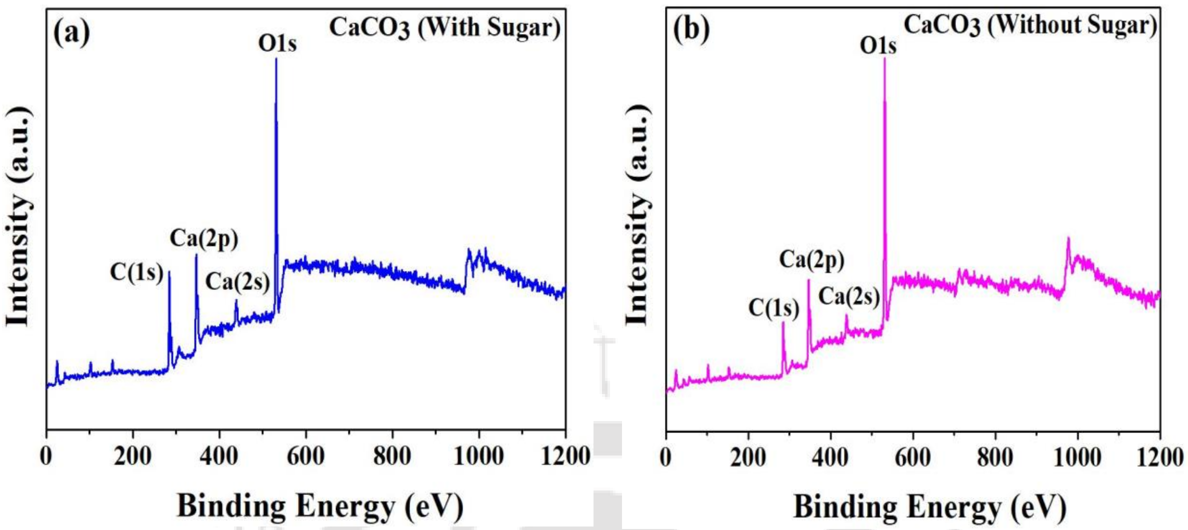

Figure 5.20: (a) and (b) XPS wide-scan of calcium carbonate demonstrating that C, Ca, and O, are the three compositional constituents present in the obtained samples.

Table 5.6: Atomic elemental concentration (at. %) for the $CaCO_3$ surface.

Sample	**$CaCO_3$ (sugar activated)**			
Constituents	**Ca 2p**	**C 1s**	**O 1s**	**N 1s**
Concentration (at %)	8.93	45.72	45.12	0.24
Sample	**$CaCO_3$ (without sugar)**			
Constituents	**Ca 2p**	**C 1s**	**O 1s**	**N 1s**
Concentration (at %)	7.28	33.37	55.20	4.15

The high-resolution XPS spectra of Ca 2p, C 1s, and O 1s core levels from the three $CaCO_3$ surfaces are shown in Figure 5.21B. No drastic change of the Ca 2p, C 1s, and O 1s core-levels binding energies from three polymorphs of the $CaCO_3$ (without sugar) sample is observed as compared with the BE position of three polymorphs found in the $CaCO_3$ (with sugar) sample, as shown in Table 5.8. Comparing Ca $2p_{3/2}$ core level peak intensity appeared from calcite, vaterite, and aragonite surface of both $CaCO_3$ samples, as presented in Figures 5.21A and 5.21B, it was seen that the higher peak intensity of the Ca $2p_{3/2}$ core level is observed in sugar activated $CaCO_3$ sample, implying the higher Ca concentration on the surface.

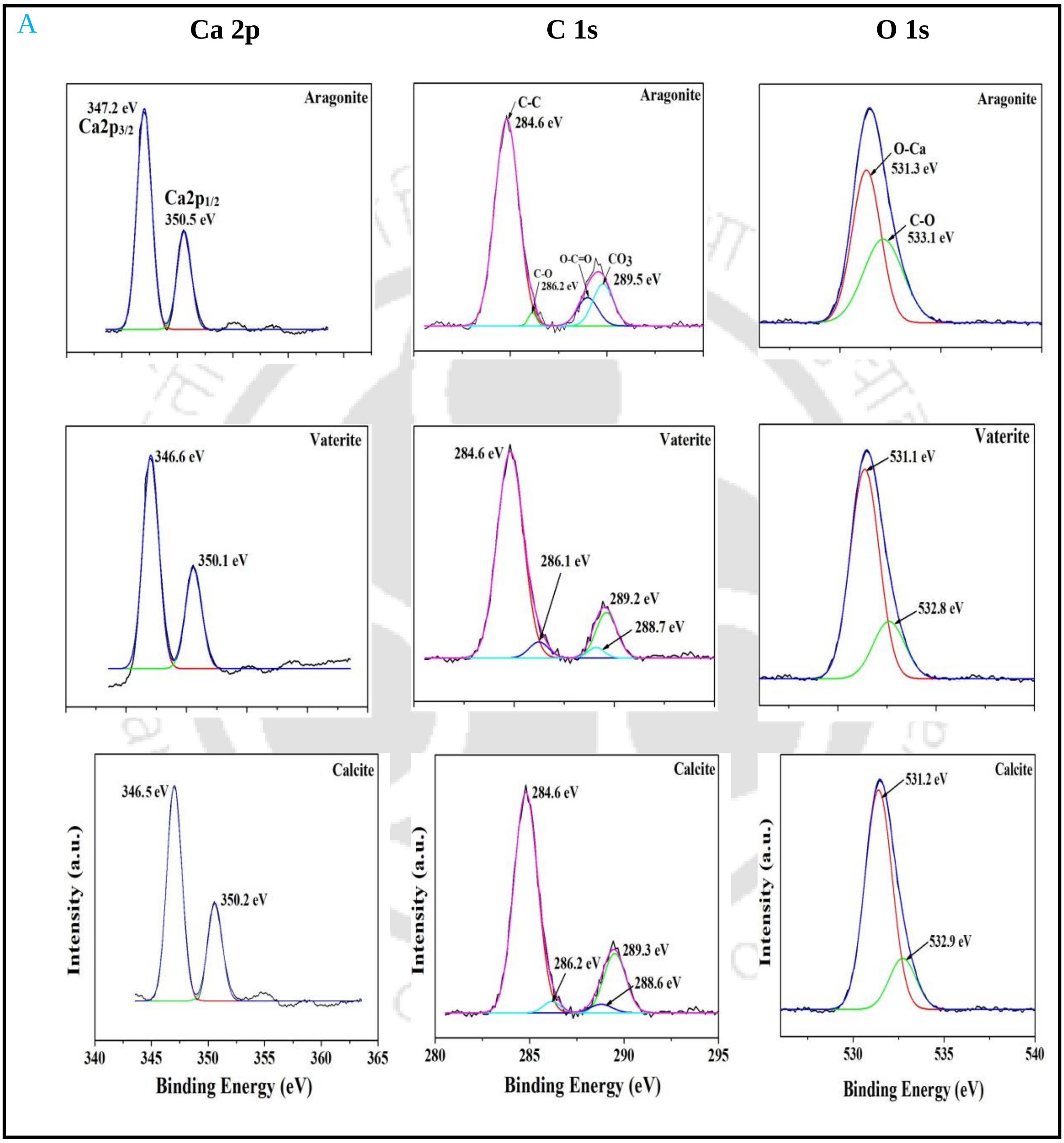

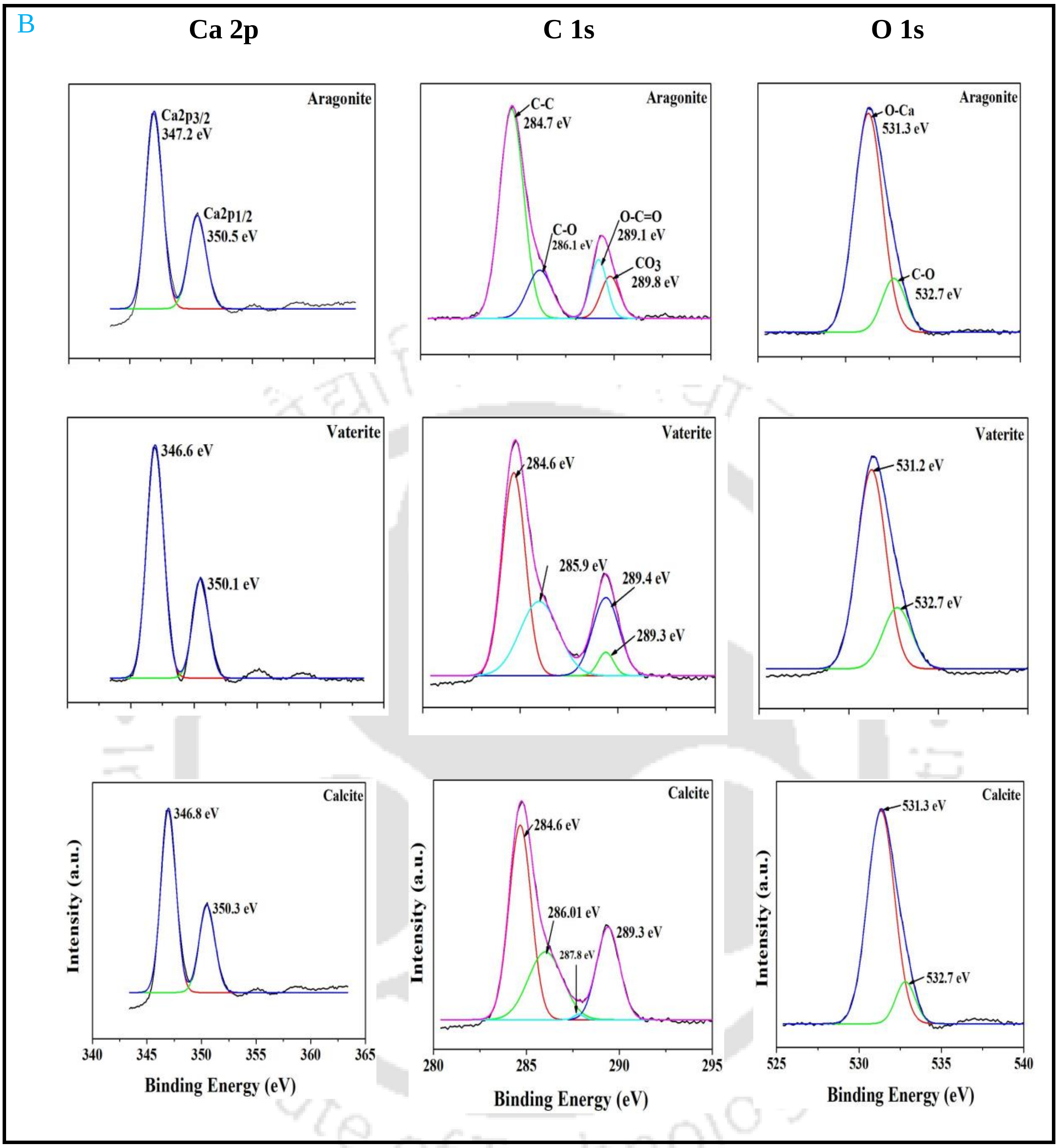

Figure 5.21: XPS high-resolution spectra of calcite, vaterite, and aragonite phases of (A) calcium carbonate synthesized with sugar and (B) calcium carbonate synthesized without sugar.

One can notice that the corresponding peak intensity of the C-C bond in the C 1s core level is relatively higher (Figure 5.21A) rather than in other samples, presumably due to the interaction between Ca and carbon-bonded sugar.

Table 5.7: XPS parameters for Ca 2p, C 1s, and O 1s core levels from the polymorphs of synthetic $CaCO_3$ sample, activated with sugar.

		Calcite	Vaterite	Aragonite
Ca 2p	**Ca $2p_{3/2}$**	346.5	346.6	347.2
	Ca $2p_{1/2}$	350.2	350.1	350.5
C 1s	**C-C**	284.6	284.6	284.6
	C-O	286.2	286.1	286.2
	O-C=O	288.6	288.7	288.5
	CO_3	289.3	289.2	289.5
O 1s	**O-Ca**	531.2	531.1	531.3
	C-O	532.9	532.8	533.1

Table 5.8: XPS parameters for Ca 2p, C 1s, and O 1s core levels from the polymorphs without sugar sample.

		Calcite	Vaterite	Aragonite
Ca 2p	**Ca $2p_{3/2}$**	346.8	346.6	347.2
	Ca $2p_{1/2}$	350.3	350.1	350.5
C 1s	**C-C**	284.6	284.6	284.7
	C-O	286.01	285.9	286.1
	O-C=O	287.8	289.3	289.1
	CO_3	289.3	289.4	289.8
O 1s	**O-Ca**	531.3	531.2	531.3
	C-O	532.7	532.7	532.7

5.7. Cost analysis of PCC production from LD-slag

A techno-economic analysis (TEA) is investigated in order to examine the techno-economic feasibility of the proposed PCC synthesis. Table 5.9 displays the TEA’s primary financial metrics as well as the costs of the associated electricity. In every batch of reaction, 4 g LD-slag was associated wherein, 1.96 g of CaO was present in weight because LD-slag only comprised nearly ~49.15% of CaO of the total slag mass. It was also estimated that a maximum of 1.7 g precipitated calcium carbonate was obtained at the highest temperature. It is also seen from Table 5.9 that 3.50 USD (~295.65 INR) is required to obtain 1.7 g of pure $CaCO_3$ from 4 g of alkaline steel slag. It was also estimated that to prepare 100 g of pure $CaCO_3$ 3.62 USD is required which is very close to the amount required for 1.7 g of pure $CaCO_3$ i.e., 3.50 USD.

The above cost analysis demonstrates that the synthesis of PCC was a cost-effective process since the price of 100 g pure calcium carbonate (Sigma-Aldrich) is ~ 46.19 USD.

Table 5.9: Cost analysis of LD-slag derived precipitated calcium carbonate.

Sl. no.	Raw Materials	Values	Price (INR)	Instrument used	Unit	Electric charge/Unit	Price (INR)
1.	**LD-slag**	4 g	0.00	Dryer	36	5.9	212.4
2.	**Table sugar dust**	2 g	0.07	Hot plate magnetic stirrer	1.1		6.49
3.	**CO_2 gas**	13.46 g	48.60				
4.	**DI water**	99.8 g (100 mL)	0.39				
			(A) TOTAL = 49.89				(B) TOTAL =218.89
Overall cost for PCC formation=(A+B)= 268.78 INR				**Overhead charge = 10% of overall cost = 0.1×268.78 = 26.87 INR**			
Net cost for PCC production = (Overall cost + Overhead charge) = 268.78+26.87 = 295.65 INR = 3.50 $							

Summary

Production of $CaCO_3$ from LD-slag was found to be cost-effective by CO_2 sequestration. Table sugar was added as a promoter that enhances the production of $CaCO_3$ in the precipitated sample. Three polymorphs of $CaCO_3$ such as calcite, vaterite, and aragonite were detected in the obtained samples. Whereas, only the calcite phase was dominated in the without sugar-reacted sample. But, at higher temperature mixture of calcite and aragonite were noticed. From the experiment, the CO_2 sequestration was found to be ~17%.

References

[1] H. Wei, Q. Shen, Y. Zhao, D. Wang, D. Xu, Crystallization habit of calcium carbonate in the presence of sodium dodecyl sulfate and/or polypyrrolidone, J. Cryst. Growth. 260 (2004) 511–516. https://doi.org/10.1016/j.jcrysgro.2003.08.047.

[2] M.M.M.G.P.G. Mantilaka, R.M.G. Rajapakse, D.G.G.P. Karunaratne, H.M.T.G.A. Pitawala, Preparation of amorphous calcium carbonate nanoparticles from impure dolomitic marble with the aid of poly(acrylic acid) as a stabilizer, Adv. Powder Technol. 25 (2014) 591–598. https://doi.org/https://doi.org/10.1016/j.apt.2013.09.008.

[3] R. Ylme, Carbonation of Portland Cement Studied by Diffuse Reflection Fourier Transform Infrared Spectroscopy, 7 (2013) 119–125. https://doi.org/10.1007/s40069-013-0039-y.

[4] H. Deng, X. Wang, C. Du, X. Shen, F. Cui, CrystEngComm Combined effect of ion concentration and functional groups on surface chemistry modulated $CaCO_3$ crystallization, (2012) 6647–6653. https://doi.org/10.1039/c2ce25731a.

[5] M.E.I. Saraya, H. Hassan, A. Latif, Preparation of Vaterite Calcium Carbonate in the Form of Spherical Nano-size Particles with the Aid of Polycarboxylate Superplasticizer as a Capping Agent, 4 (2016) 44–51. https://doi.org/10.12691/ajn-4-2-3.

[6] M.C. Reis, M.F.B. Sousa, F. Alobaid, C.A. Bertran, Y. Wang, A two-fluid model for calcium carbonate precipitation in highly supersaturated solutions, Adv. Powder Technol. 29 (2018) 1571–1581. https://doi.org/10.1016/j.apt.2018.03.022.

[7] S. Tanpure, V. Ghanwat, B. Shinde, K. Tanpure, S. Lawande, The Eggshell Waste Transformed Green and Efficient Synthesis of K-Ca(OH)2 Catalyst for Room Temperature Synthesis of Chalcones, Polycycl. Aromat. Compd. 0 (2020) 1–19. https://doi.org/10.1080/10406638.2020.1776740.

[8] No Title, (n.d.). https://www.doitpoms.ac.uk/tlplib/polymerbasics/crystallinity.php.

[9] S.I. Kuriyavar, R. Vetrivel, S.G. Hegde, A. V. Ramaswamy, D. Chakrabarty, S. Mahapatra, Insights into the formation of hydroxyl ions in calcium carbonate: Temperature dependent FTIR and molecular modelling studies, J. Mater. Chem. 10 (2000) 1835–1840. https://doi.org/10.1039/b001837f.

[10] P.P. Das, Anweshan, M.K. Purkait, Treatment of cold rolling mill (CRM) effluent of steel industry, Sep. Purif. Technol. 274 (2021) 119083. https://doi.org/https://doi.org/10.1016/j.seppur.2021.119083.

[11] N.S. Samanta, P.P. Das, P. Mondal, U. Bora, M.K. Purkait, Physico-chemical and adsorption study of hydrothermally treated zeolite A and FAU-type zeolite X prepared from LD (Linz–Donawitz) slag of the steel industry, Int. J. Environ. Anal. Chem. (2022) 1–23. https://doi.org/10.1080/03067319.2022.2079082.

[12] P.K. Patel, L.M. Pandey, R.V.S. Uppaluri, Adsorptive removal of Zn, Fe, and Pb from Zn dominant simulated industrial wastewater solution using polyvinyl alcohol grafted chitosan variant resins, Chem. Eng. J. (2023) 141563. https://doi.org/https://doi.org/10.1016/j.cej.2023.141563.

[13] P.K. Patel, S. Nagireddi, R.V.S. Uppaluri, L.M. Pandey, Batch adsorption characteristics of Dowex Marathon MSA commercial resin for Au(III) removal from synthetic electroless plating solutions, Mater. Today Proc. (2022). https://doi.org/https://doi.org/10.1016/j.matpr.2022.06.258.

[14] S. Dhara, N.S. Samanta, R. Uppaluri, M.K. Purkait, High-purity alkaline lignin extraction from Saccharum ravannae and optimization of lignin recovery through response surface methodology, Int. J. Biol. Macromol. (2023) 123594. https://doi.org/https://doi.org/10.1016/j.ijbiomac.2023.123594.

[15] Z. Zhang, Y. Xie, X. Xu, H. Pan, R. Tang, Transformation of amorphous calcium

carbonate into aragonite, J. Cryst. Growth. 343 (2012) 62–67. https://doi.org/10.1016/j.jcrysgro.2012.01.025.

[16] B. Myszka, M. Schüßler, K. Hurle, B. Demmert, R. Detsch, A.R. Boccaccini, S.E. Wolf, Phase-specific bioactivity and altered Ostwald ripening pathways of calcium carbonate polymorphs in simulated body fluid, RSC Adv. 9 (2019) 18232–18244. https://doi.org/10.1039/c9ra01473j.

[17] E.A. Ofudje, A. Rajendran, A.I. Adeogun, M.A. Idowu, S.O. Kareem, D.K. Pattanayak, Synthesis of organic derived hydroxyapatite scaffold from pig bone waste for tissue engineering applications, Adv. Powder Technol. 29 (2018) 1–8. https://doi.org/https://doi.org/10.1016/j.apt.2017.09.008.

[18] S. Gopi, V.K. Subramanian, K. Palanisamy, Aragonite–calcite–vaterite: A temperature influenced sequential polymorphic transformation of CaCO3 in the presence of DTPA, Mater. Res. Bull. 48 (2013) 1906–1912. https://doi.org/https://doi.org/10.1016/j.materresbull.2013.01.048.

[19] H. Guo, Z. Qin, P. Qian, P. Yu, S. Cui, W. Wang, Crystallization of aragonite $CaCO_3$ with complex structures, Adv. Powder Technol. 22 (2011) 777–783. https://doi.org/10.1016/j.apt.2010.11.004.

[20] K. Chong, C. Chia, S. Zakaria, Polymorphs calcium carbonate on temperature reaction Polymorphs Calcium Carbonate on Temperature Reaction, 52 (2017) 3–8. https://doi.org/10.1063/1.4895169.

[21] G. Nehrke, H. Poigner, D. Wilhelms-Dick, T. Brey, D. Abele, Coexistence of three calcium carbonate polymorphs in the shell of the Antarctic clam Laternula elliptica, Geochemistry, Geophys. Geosystems. 13 (2012). https://doi.org/10.1029/2011GC003996.

[22] U. Wehrmeister, D.E. Jacob, A.L. Soldati, T. Häger, W. Hofmeister, Vaterite in

freshwater cultured pearls from China and Japan, J. Gemmol. 30 (2007) 399–412. https://doi.org/10.15506/jog.2007.30.7.399.

[23] F.C. Donnelly, F. Purcell-Milton, V. Framont, O. Cleary, P.W. Dunne, Y.K. Gun’ko, Synthesis of $CaCO_3$ nano- and micro-particles by dry ice carbonation, Chem. Commun. 53 (2017) 6657–6660. https://doi.org/10.1039/c7cc01420a.

[24] G.P.S. Smith, K.C. Gordon, S.E. Holroyd, Raman spectroscopic quantification of calcium carbonate in spiked milk powder samples, Vib. Spectrosc. 67 (2013) 87–91. https://doi.org/10.1016/j.vibspec.2013.04.005.

[25] Y. Oaki, R. Adachi, H. Imai, Self-organization of hollow-cone carbonate crystals through molecular control with an acid organic polymer, Polym. J. 44 (2012) 612–619. https://doi.org/10.1038/pj.2012.29.

[26] R. Ševčík, P. Šašek, A. Viani, Physical and nanomechanical properties of the synthetic anhydrous crystalline $CaCO_3$ polymorphs: vaterite, aragonite and calcite, J. Mater. Sci. 53 (2018) 4022–4033. https://doi.org/10.1007/s10853-017-1884-x.

[27] P. Fellner, J. Jurišová, L. Pach, Preparation of needle-like aragonite particles from calcium nitrate solution, 4 (2011) 3–10.

[28] S. Maleki Dizaj, M. Barzegar-Jalali, M.H. Zarrintan, K. Adibkia, F. Lotfipour, Calcium carbonate nanoparticles as cancer drug delivery system, Expert Opin. Drug Deliv. 12 (2015) 1649–1660. https://doi.org/10.1517/17425247.2015.1049530.

[29] M.H. Nielsen, S. Aloni, J.J. De Yoreo, In situ TEM imaging of CaCO3 nucleation reveals coexistence of direct and indirect pathways, Science (80-.). 345 (2014) 1158–1162. https://doi.org/10.1126/science.1254051.

[30] V. Vergaro, E. Carata, E. Panzarini, F. Baldassare, L. Dini, G. Ciccarella, Synthesis of calcium carbonate nanocrystals and their potential application as vessels for drug delivery, AIP Conf. Proc. 1667 (2015). https://doi.org/10.1063/1.4922570.

[31] A. Barhoum, H. Rahier, R.E. Abou-Zaied, M. Rehan, T. Dufour, G. Hill, A. Dufresne, Effect of cationic and anionic surfactants on the application of calcium carbonate nanoparticles in paper coating, ACS Appl. Mater. Interfaces. 6 (2014) 2734–2744. https://doi.org/10.1021/am405278j.

[32] M. Nakayama, S. Kajiyama, T. Nishimura, T. Kato, Liquid-crystalline calcium carbonate: biomimetic synthesis and alignment of nanorod calcite, Chem. Sci. 6 (2015) 6230–6234. https://doi.org/10.1039/C5SC01820J.

[33] R.R. Menon, J. Luo, X. Chen, H. Zhou, Z. Liu, G. Zhou, N. Zhang, C. Jin, N. Brunswick, E. Program, E. Therapeutics, N. Brunswick, Screening of Fungi for the Application of Self-Healing Concrete, (n.d.) 1–21.

[34] J. Jiang, Q. Zheng, D. Hou, Y. Yan, H. Chen, W. She, S. Wu, D. Guo, W. Sun, Calcite crystallization in the cement system: Morphological diversity, growth mechanism and shape evolution, Phys. Chem. Chem. Phys. 20 (2018) 14174–14181. https://doi.org/10.1039/c8cp01979g.

[35] X.-G. Li, Y. Lv, B.-G. Ma, W.-Q. Wang, S.-W. Jian, Decomposition kinetic characteristics of calcium carbonate containing organic acids by TGA, Arab. J. Chem. 10 (2017) S2534–S2538. https://doi.org/https://doi.org/10.1016/j.arabjc.2013.09.026.

[36] D. Konopacka-Łyskawa, Synthesis methods and favorable conditions for spherical vaterite precipitation: A review, Crystals. 9 (2019). https://doi.org/10.3390/cryst9040223.

[37] M.-A. Popescu, R. Isopescu, C. Matei, G. Fagarasan, V. Plesu, Thermal decomposition of calcium carbonate polymorphs precipitated in the presence of ammonia and alkylamines, Adv. Powder Technol. 25 (2014) 500–507. https://doi.org/https://doi.org/10.1016/j.apt.2013.08.003.

[38] D. Konopacka-Łyskawa, N. Czaplicka, B. Kościelska, M. Łapiński, J. Gębicki,

Influence of selected saccharides on the precipitation of calcium-vaterite mixtures by the CO_2 bubbling method, Crystals. 9 (2019). https://doi.org/10.3390/cryst9020117.

[39] S. Dzuhri, N.Y. Yuhana, O. Anuar, I. Nasharudin, O. Rohaya, Synthesis of Precipitated Calcium Carbonate from Industrial Waste Carbide Lime by Using Sucrose as Promoter, (2014) 204–210.

[40] J. Chen, X. Lin, M. Li, T. Mao, X. Li, J. Yan, Heavy metal solidification and CO_2 sequestration from MSWI fly ash by calcium carbonate oligomer regulation, J. Clean. Prod. 359 (2022) 132044. https://doi.org/10.1016/j.jclepro.2022.132044.

[41] R. Revathy, T. Dananjayan, P. Kandasamy, R. Andimuthu, Direct mineral carbonation of coal fly ash for CO_2 sequestration, J. Clean. Prod. 112 (2016) 4173–4182. https://doi.org/10.1016/j.jclepro.2015.05.145.

[42] G. Hou, J. Chen, B. Lu, S. Chen, E. Cui, H.M. Naguib, M. Guo, Q. Zhang, Cement and Concrete Research Composition design and pilot study of an advanced energy-saving and low- carbon rankinite clinker, Cem. Concr. Res. 127 (2020) 105926. https://doi.org/10.1016/j.cemconres.2019.105926.

[43] X. Chang, S. Liu, C. Zhang, P. Shen, D. Xuan, X. Guan, C. Shi, Carbonation-hardening properties and ITZ microstructure of low-calcium CO2 sequestration binder mortar, Constr. Build. Mater. 336 (2022) 127589. https://doi.org/10.1016/j.conbuildmat.2022.127589.

[44] T.D. Rushendra Revathy, K. Palanivelu, A. Ramachandran, Direct mineral carbonation of steelmaking slag for CO_2 sequestration at room temperature, Environ. Sci. Pollut. Res. 23 (2016) 7349–7359. https://doi.org/10.1007/s11356-015-5893-5.

[45] B. Njegić-Džakula, G. Falini, L. Brečević, Ž. Skoko, D. Kralj, Effects of initial supersaturation on spontaneous precipitation of calcium carbonate in the presence of charged poly-l-amino acids, J. Colloid Interface Sci. 343 (2010) 553–563.

https://doi.org/https://doi.org/10.1016/j.jcis.2009.12.010.

[46] A. Related, T.H.C. Lines, P. Kuropka, M. Dobrzynski, B. Bazanow, D. Stygar, T. Gebarowski, A. Leskow, M. Tarnowska, K. Szyszka, M. Malecka, N. Nowak, W. Strek, R.J. Wiglusz, file:///C:/Users/Mithilesh/Desktop/NILADRI/MANUCRIPT 3_slag to caco3/References/First_Glass_Electrode_and_its_Creators_F_Haber_and.pdf, (2021).

[47] B. Marczewska, K. Marczewski, First glass electrode and its creators F. haber and Z. klemensiewicz - on 100th anniversary, Zeitschrift Fur Phys. Chemie. 224 (2010) 795–799. https://doi.org/10.1524/zpch.2010.5505.

[48] C.H. Weng, C.C. Huang, C.S. Yeh, H.Y. Lei, G. Bin Lee, Synthesis of hexagonal gold nanoparticles using a microfluidic reaction system, J. Micromechanics Microengineering. 18 (2008). https://doi.org/10.1088/0960-1317/18/3/035019.

[49] D.H. Chu, M. Vinoba, M. Bhagiyalakshmi, I.I. Hyun Baek, S.C. Nam, Y. Yoon, S.H. Kim, S.K. Jeong, CO_2 mineralization into different polymorphs of $CaCO_3$ using an aqueous-CO_2 system, RSC Adv. 3 (2013) 21722–21729. https://doi.org/10.1039/C3RA44007A.

[50] M. Ni, B.D. Ratner, J. Wiley, Differentiating calcium carbonate polymorphs by surface analysis techniques–an XPS and TOF-SIMS study, (2008). https://doi.org/10.1002/sia.2904.

Chapter 6

Conclusion and scope of future work

This chapter comprises two segments; the first segment is conclusions, which include the results drawn from several works presented in this thesis. The second and last section discusses the ideas for future work.

6.1. Conclusions

The thesis deals with the preparation and characterization of zeolites and precipitated calcium carbonate using steel industry LD-slag as a precursor material. Zeolite type A and X were prepared via fusion-facilitated hydrothermal treatment, wherein, zeolite Y was synthesized via ultrasound irradiation followed by a fusion-assisted hydrothermal process. Synthesized zeolite A was employed for iron removal from drinking water and zeolite X was used for the expulsion of cationic dye (methylene blue) from wastewater. Thermal stability and framework stability of as-synthesized zeolite A and X were examined at various pH and treatment times. Disintegration of zeolite framework was noticed at very low pH and 3 days treatment time but no drastic changes were observed at neutral and high basic conditions. Thermal stability analysis demonstrates that A-type zeolite exhibits comparatively high thermal stability than zeolite X. Nano-sized zeolite Y was coated on PSf substrate via heat treatment followed by a phase inversion technique to prepare zeolite nano-layered membrane. The modified membrane was employed in the ultrafiltration process to treat the groundwater sample. It was found that zeolite-coated membrane is highly capable to reject detrimental components like fluoride (F^-), chromium (Cr^{6+}), and manganese (Mn^{2+}). On the other hand, CaO-enriched LD-slag was found to be a potential raw material for the production of precipitated calcium carbonate by CO_2 sequestration. The major conclusions from the different studies are presented below.

Preparation and Characterization of Zeolite from Waste Linz-Donawitz (LD) process slag of Steel Industry for Removal of Fe^{3+} from Drinking Water (Refer Chapter 2):

Fusion-assisted hydrothermal treatment was used to prepare zeolite A from LD-slag and the synthetic zeolite was employed for Fe^{3+} removal from drinking water on the basis of the following details are found:

- Cubical shape zeolite A was observed from the FESEM analysis of the obtained sample (Refer to page 40).
- BET surface area was reported as 15.1025 m^2/g with a mesoporous structure with pore volume ranging from 6.76 to 15.4 nm, respectively (Refer page 43).
- A maximum adsorption capacity of 27.55 mg/g was obtained at a 1.4 g/L adsorbent dosage, with 99.99% Fe^{3+} ion removal (Refer page 51).
- Zeolite A exhibits high stability at neutral and basic pH but shows less stability at acidic media after 3 days of treatment time (Refer to page 47).
- The batch experiment data of Fe^{3+} ion uptake onto zeolite A best fitted for the Langmuir isotherm model (Refer to page 62).

Physico-chemical and adsorption study of hydrothermally treated zeolite A and FAU-type zeolite X prepared from LD (Linz-Donawitz) slag of the steel industry (Refer Chapter 3):

Physico-chemical study of as-synthesized zeolite A and X was examined at various pH and treatment times and the following details are found:

- Zeolite A exhibits the highest degree of thermal and morphological stability as compared to X-type zeolite (Refer to pages 83-88).

- BET analysis demonstrates that A-type zeolite has a higher surface area than zeolite X and the pores of both the samples were found to be in the mesoporous range (Refer page 92).
- Zeolite A showed a maximum adsorption capacity of 25.30 mg/g with the highest removal of 98.13% as compared to zeolite X (Refer page 96).
- The isotherm data obtained from experiments are nicely fitted in the Langmuir model with a maximum Langmuir monolayer adsorption capacity of 20 and 25.40 mg/g over zeolite A and X, respectively (Refer to page 103).

Fabrication of LD-slag derived Zeolite Y coated Polysulfone (PSf) membrane for decontamination of groundwater (Refer Chapter 4):

LD-slag-based zeolite Y-coated PSf membrane was fabricated for wastewater treatment and on the basis of that the following details are found:

- The average particle size of the zeolite material was found to be 59.07 nm (Refer to Figure 4.3g).
- The temperature 60°C was found to be the most suited drying temperature among others (Refer to Figure 4.6).
- Morphology assessment revealed the agglomeration of nanoparticles on the membrane surface at 1wt.% zeolite concentration. Cross-sectional images of surface-modified membranes demonstrate closely packed holes that resemble a honeycomb structure (Refer to Figure 4.9).
- The addition of zeolite Y enhances the surface roughness and zeta potential of the PSf membrane (Refer to Table 4.6).
- Increasing zeolite concentration made the membranes more hydrophilic in nature which results in enhanced pure water flux. The highest flux of water was found to

be 28.83 L/m^{2}h at 1.37 bar for PSf/Zeolite-1wt.% membrane which is higher as compared to other fabricated membranes (Refer Figure 4.12a).

- After 1-hour ultrafiltration process the permeate fluoride, chromium, and manganese concentration were found to be 1.47, 0.00, and 0.39 mg/L (Refer Table 4.8).
- The highest adsorption capacity was measured as 2.37 and 1.18 mg/g for Cr^{6+} and Mn^{2+}, respectively (Refer to page 169).

Synthesis of precipitated calcium carbonate from LD-slag using CO_2

Carbon dioxide gas was sequestrated with the LD-slag and the following details are found:

- The CO_2 sequestration efficiency in this study was found to be ~17% (Refer to page 221).
- Table sugar was added as a promoter. With sugar, the CaO conversion was found to be 85.83%, whereas, CaO conversion as well as the $CaCO_3$ formation declined to ± 39-40% when the reaction was carried out without sugar (Refer to page 212).
- The hypothesis test revealed that the higher $Ca(OH)_2$ conversion occurred from CaO in the sugar solution, noting that the formation of higher Ca ions concentrations, resulted in higher $CaCO_3$ production (Refer Figure 5.13).
- Three types of $CaCO_3$ polymorphs were detected namely calcite, vaterite, and aragonite when the reaction was carried out with sugar (Refer to Figure 5.5).
- Only the calcite phase was dominated when the reaction was conducted without sugar, however, at a higher reaction temperature (55°C) mixture of calcite and aragonite phases were observed (Refer Figure 5.17).

6.2. Recommendations for future work

This section highlights some of the new areas of research, that can be carried out to further the preparation and applicability of LD-slag-based zeolite. Some of the important areas of recommended research are suggested as an extension of the present study:

- Zeolites possess a range of acidic or basic sites on their surface. These sites can participate in acid-base catalysis, promoting various chemical reactions. So, LD-slag-derived zeolite can be studied for catalytic applications.
- The synthesis of various zeolite types from LD-slag and their photo-catalytic application in dye degradation has not been studied yet. Further research can focus on this.
- LD-slag-based zeolites and their composites for wastewater treatment can be investigated.
- A Composite of LD-slag derived geo-polymer and zeolite and its application towards wastewater treatment is suggested for future study.

Appendix

A. Error analysis

The errors in experimentally measured quantities and in parameters calculated from those measurements are important in that they determine the accuracy of calculation and predictions using those quantities. There are two types of errors viz. systematic error and random error. Systematic errors are the results of faulty assumptions or improper experimental measuring techniques. In this work, care was taken in eliminating systematic errors by appropriately designing the experiments and adopting qualified methods for the analysis of the data. On the other hand, random errors result from variations in the precision of measuring parameters and the slight variations that occur in successive measurements made by the same observer under nearly identical conditions. Random errors cannot be eliminated. The focus of the error analysis presented in this section is on random errors.

In most of the experiments performed in this work, the quantities that are measured directly are concentrations and permeate flow rates which are used to determine the rejection (%) and permeate flux, respectively.

A.1. Error in the measurement of fluoride concentration in permeate

Fluoride concentration in the aqueous phase was calculated by measuring the value obtained from the fluoride ion meter. A calibration curve was prepared by taking standard fluoride concentrations of 1 and 10 mg/L. The obtained slope value from the calibration curve would be in the range of -53 to -54 eV and the permeate fluoride concentration was determined from the slope value.

Thus, every measurement of fluoride concentration in permeation is associated with an error of 0.05 % whose effect on rejection values of fluoride can be ignored.

A.2. Error in the measurement of permeate flux

The errors in the values of permeate flux are related to the errors in the measurements used to calculate those values. In this section, statistical analysis is used for the estimation of uncertainty associated with the values of permeate flux. Determination of standard deviation is generally considered to be one of the best methods to estimate uncertainty which is based on the following method:

If $u_1\ u_2$......................., u_N are the N results of the measurements of a particular quantity u, then the mean value of u (i.e.$\bar{u}$), is defined by

$$\bar{u} = \frac{u_1 + u_2 + \dots\dots\dots\dots + u_N}{N} = \frac{1}{N}\sum_{i=1}^{N} u_i \tag{A.1}$$

The uncertainty in the result is usually expressed as "root-mean-squared-deviation", which is denoted as Δu, which is computed using the following Equation. (A.2):

$$\Delta u = \sqrt{\frac{(u_1 - \bar{u})^2 + (u_2 - \bar{u})^2 + \dots\dots\dots\dots + (u_N - \bar{u})^2}{N-1}} \tag{A.2}$$

In the present work, all the membranes were cleaned thoroughly following each experiment. Besides, before each experiment, the performance of all the membranes was checked through pure water flux (PWF) measurement; hence uncertainties involved in the PWF measurements are reported here. The uncertainties involved in different experimental measurements for (PWF) for membranes PSf, PSf/Zeolite-0.1wt.%, and PSf/Zeolite-1wt.% and shown in Table A.1.

Table A.1. Values of uncertainties estimated in PWF measurements for membranes PSf, PSf/Zeolite-0.1wt.%, and PSf/Zeolite-1wt.%.

Membranes	Pure Water Flux (L/m^{2}h)					
	Run 1	Run 2	Run 3	$\bar{u}$	Δu	Uncertainties (%)
PSf	5.76	6.12	6	5.96	0.18	0.08
PSf/Zeolite-0.1wt.%	15.7	16.25	15.2	15.71	0.52	0.27
PSf/Zeolite-1wt.%	28.83	30.40	29.7	29.64	0.39	0.38